To the Graduate Council:

I am submitting herewith a thesis written by Norman S. Weinberg entitled "Experimental Optical Radiation Data in the Wake Flow Fields of Ablating Reentry Vehicles." I recommend that it be accepted in partial fulfillment of the requirements for the degree of Master of Science, with a major in Mechanical Engineering.

F. Shahrokhi, Major Professor

We have read this thesis
and recommend its acceptance:

Conley Powell

H C Reddy

Accepted for the Council:

L Evans Roth
Vice Chancellor
Graduate Studies and Research

Thesis
77
.W432
cop. 2

EXPERIMENTAL OPTICAL RADIATION DATA IN THE WAKE FLOW FIELDS OF ABLATING REENTRY VEHICLES

A Thesis

Presented for the

Master of Science

Degree

The University of Tennessee, Knoxville

Norman S. Weinberg

December 1977

1390090

ACKNOWLEDGMENTS

The author wishes to express his appreciation to the officials of ARO, Inc.; Headquarters, AEDC, Arnold Air Force Station, Tennessee; and Foreign Technology Division, Air Force Systems Command, Wright-Patterson Air Force Base, Ohio, for their permission to use experimental work for this thesis.

Appreciation is expressed to his advisor, Dr. F. Shahrokhi, Professor and Director of the Remote Sensing Division, and to the other members of his committee, Dr. T. C. Powell, Assistant Professor, Mechanical and Aerospace Engineering, and Dr. K. C. Reddy, Professor of Mathematics.

Appreciation is also extended to Mrs. Jeannie Harper for her kind cooperation in typing the final copy of this thesis.

The work reported herein was sponsored by the Arnold Engineering Development Center, Air Force Systems Command, under Contract F40600-77-C-0001 with ARO, Inc., a Sverdrup Corporation company. The work was performed in the Projects Section of the Aeroballistics Branch of the von Karman Gas Dynamics Facility.

ABSTRACT

The purpose of this study was to analyze experimental optical radiation data (visible and infrared) in the wake flow fields of ablating scale models of reentry vehicles. Theories exist that relate the nose radius of a blunted vehicle to a characteristic distance behind the vehicle where the logarithmic decay of the optical intensity changes slope. Data, obtained during a test sponsored by the Foreign Technology Division, were analyzed using the existing theories to assess theory validity with the acquired data. Effects of wavelength and model parameters were addressed. A modification to the existing method by which the characteristic distance is determined was evaluated; the modified method treated logarithmic distance, instead of linear distance. It was found that one of the theories predicted the actual nose radius very well from both visible and infrared data. The modified method for determining distance was useful for both visible and infrared data. The results obtained using the theoretical equations applied to all the model configurations tested; no model parametric effects were noted. Well controlled data from specific model configurations are required to further refine the prediction techniques.

TABLE OF CONTENTS

CHAPTER		PAGE
I.	INTRODUCTION	1
II.	EXPERIMENTAL METHOD	5
	Test Unit	5
	Models	5
	Radiometer Description	11
	Radiometer Calibration	15
III.	TECHNICAL APPROACH	22
	Test Data Reduction	22
	Correlation Theories	25
	Data Curve Fits	29
IV.	EXPERIMENTAL DATA AND RESULTS	37
	General Log-Linear Plotted Data	37
	Visible Log-Linear Plotted Data	41
	Infrared Log-Linear Plotted Data	60
	Log-Log Plotted Data	61
	Data Summary and Results	61
V.	CONCLUSIONS AND RECOMMENDATIONS	86
BIBLIOGRAPHY		89
APPENDIXES		92
A.	FIELD OF VIEW GEOMETRY	93
B.	UNCERTAINTY ANALYSIS	96
	Introduction	96

CHAPTER PAGE

Calculation of Uncertainty of Visible Radiometer Data. 97

Calculation of Uncertainty of Infrared Radiometer Data. 106

C. LOG INTENSITY VERSUS DISTANCE DATA 110

D. LOG INTENSITY VERSUS LOG DISTANCE DATA 151

VITA 192

LIST OF TABLES

TABLE		PAGE
I.	Model Properties	8
II.	Summary of Test Conditions	38
III.	Range Air Data	39
IV.	Drag Coefficient Data	40
V.	Visible Data, Log-Linear Plots	58
VI.	Infrared Data, Log-Linear Plots	62
VII.	Visible Data, Log-Log Plots	66
VIII.	Infrared Data, Log-Log Plots	69
IX.	Data Summary	79
B- I.	Errors	99

LIST OF FIGURES

FIGURE		PAGE
1.	Model Schematics.	6
2.	Photograph of Models.	9
3.	Image Converter Camera Photograph	10
4.	Radiometer Installation in Range G.	12
5.	Typical Visible Radiometer Range Installation.	13
6.	Typical Infrared Radiometer Range Installation.	14
7.	Radiometer Relative Spectral Response Characteristics	16
8.	Visible Radiometer Calibration Apparatus. . . .	18
9.	Infrared Radiometer Calibration Apparatus . . .	20
10.	Wake Kink Phenomenon.	27
11.	Shot 4402, 0.5 to 0.7 μm Residuals.	44
12.	Shot 4498, 0.7 to 0.8 μm Residuals.	45
13.	Shot 4502, 0.7 to 0.8 μm Residuals.	46
14.	Shot 4659, 0.5 to 0.7 μm Residuals.	47
15.	Shot 4232, 0.5 to 0.7 μm Residuals.	48
16.	Shot 4398, 0.5 to 0.7 μm Residuals.	49
17.	Shot 4503, 0.5 to 0.7 μm Residuals.	50
18.	Shot 4503, 0.7 to 0.8 μm Residuals.	51
19.	Shot 4660, 0.7 to 0.8 μm Residuals.	52
20.	Shot 4810, 0.7 to 0.9 μm Residuals.	56

FIGURE PAGE

21. Visible Data Summary, Log-Linear Plots. 73

22. Infrared Data Summary, Method 1, Log-Linear Plots. 74

23. Infrared Data Summary, Method 2, Log-Linear Plots. 75

24. Visible Data Summary, Log-Log Plots 76

25. Infrared Data Summary, Method 1, Log-Log Plots 77

26. Infrared Data Summary, Method 2, Log-Log Plots 78

A- 1. Field of View Schematic 94

NOMENCLATURE

A	Ablating model
C_D	Total drag coefficient
C Ph	Carbon Phenolic
H-C-F	Hemisphere-cylinder-flare
ℓ	Model length
m	Model mass
M_∞	Mach number
NA	Non-ablating model
P_∞	Range free-stream pressure
r_B	Base radius of model
r_C	Calculated nose radius of model
r_N	Nose radius of model
r_1	Nose radius calculated by Bauer's equation
r_2	Nose radius calculated by Textoris' and Stankevics' equation
r_3	Nose radius calculated by Heyda's equation
Δr	Tolerance associated with calculated nose radius
Si Ph	Silica phenolic
T_∞	Range free-stream temperature
V_∞	Model velocity
X_K	Kink distance
α	Model angle of attack
$\bar{\alpha}$	Average angle of attack

θ_c	Cone half-angle
3DQP	Three-dimensional quartz phenolic

CHAPTER I

INTRODUCTION

Fluid dynamics of the wake behind a hypersonic body has been of much interest in the past 15 years. The main interest is to attempt to give accounts of the different phenomena involved in the production of the wake and their possible use in predicting the geometry, weight, and flight characteristics of the object causing the wake. Numerous hypersonic wake studies have been conducted. Lykoudis [1],[1] who has studied many of the theoretical and experimental investigations that had been performed (prior to 1965), reviewed wake phenomena results and made reference to over 180 papers. He states, "from an experimental point of view, the hypersonic wake flow has been investigated only to a limited extent." He recommends that extensive experimental investigation be conducted in the near flow field. Two other prominent theoreticians in this field were Steiger [2], who reviewed hypersonic wake fluid dynamics and auxiliary theoretical and experimental studies in near wake regions, and Gold [3], who discussed near wake theories.

---

[1]Numbers in brackets refer to similarly numbered references in the Bibliography.

While the fluid dynamics of wakes was under study in the 1960's, little attention was paid to optical radiation from wakes. Reis [4] believed that emphasis on shock layer radiation partly precluded research on wake radiation. It was indicated at that time that wake radiation from a hypersonic blunt body could be appreciable, and that there should be a strong correlation between wake radiation and fluid dynamics of the wake. Reis reviewed blunt-body wake phenomenology that related to wake radiation. He also reported on results that showed there was considerable radiation in the wakes behind hypersonic spheres, and that the wake radiation appeared to be closely coupled to the overall fluid dynamic character of the wake. Reis mentioned the difficulty and complexity associated with the analysis of the fluid dynamics and chemistry of hypersonic wake flows. He emphasized the importance of obtaining experimental data by stating that,

> The numerous theoretical techniques and computational codes that have been developed to calculate hypersonic wake flows often lack a complete enough set of experimental observables so as to validate their accuracy.

More complication is added when an ablative body is considered. Here the gaseous by-products from the ablated material react with air in the boundary layer and in the near wake.

In recent years the understanding of hypersonic wake radiation phenomenon has been of growing concern. One of the main reasons for this concern is from a military

need, as it is well known that the radiation history of a reentry vehicle is highly dependent upon the vehicle configuration. It, thereby, seems reasonable that having obtained a vehicle's radiation history, one could obtain knowledge of the vehicle configuration.

There have been many experimental techniques for making radiation measurements in hypersonic wakes. These techniques involve use of free-flight ballistic ranges and tunnel-type facilities, vehicle-borne systems, and remote observations from ground-based or air-borne platforms. Burns and Riethof [5] reviewed a number of diagnostic applications of radiation measurements in hypersonic wakes within the three basic measurement situations aforementioned.

The free-flight ballistic range is a primary laboratory facility which has been used for measuring the radiation intensity and its distribution in the wake. Many techniques have been developed to obtain wake radiation. Taylor, et al. [6], described several techniques for investigating the wake generated by hypersonic projectiles in a ballistic range, and they also described some experiments conducted. Optical measurement of radiation history is of prime use in understanding wake phenomena. Rapid expansion in the electro-optics industry has generated many optical radiation measurement devices [7].

A test program, Project V41G-23A, was conducted by the Arnold Engineering Development Center (AEDC), Air Force Systems Command (AFSC), Arnold Air Force Station, Tennessee, under the sponsorship of the Foreign Technology Division (FTD), AFSC, Wright-Patterson Air Force Base, Ohio. One of the main objectives of this test program was to obtain optical radiation intensity data (visible and infrared) from the wakes behind ablating blunted reentry vehicle shapes.

The purpose of this study is to analyze the experimental radiometric data obtained during the FTD tests to:

1. Assess the validity of the "Bauer Kink" phenomenon with regard to the acquired data.
   a. Determine the effects of various model parameters on the "Bauer Kink."
   b. Assess the effect of wavelength on the "Bauer Kink."
2. Evaluate two modified versions of the "Bauer Kink" equation.
3. Determine if other modifications to the "Bauer Kink" phenomenon could be useful.

CHAPTER II

EXPERIMENTAL METHOD

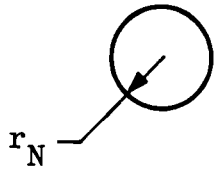
I. TEST UNIT

The Hyperballistic Range (G) can be used as a free-flight test unit; it is a 1,000-foot-long, 10-foot-diameter steel tank. A blast chamber which absorbs the expanding muzzle gases makes up the initial 85 feet of the range, and it is in this chamber that the test model is separated from the sabot which adapts it to the bore of the launcher.

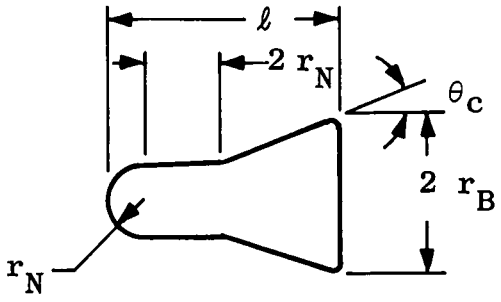
Range pressures and temperatures were monitored at gaging stations along the length of the range. Situated at 20-foot intervals (10-foot intervals in the uprange portion) along the range are 53 dual-axis spark shadowgraphs. Optical axes at each shadowgraph station are mutually orthogonal with the range centerline.

II. MODELS

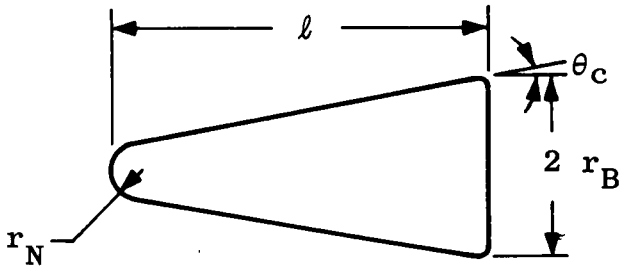
The wake radiation sources were models launched out of the Range G two-stage light gas gun. The models for the FTD test were 10-degree half-angle non-ablative blunt cones; 10-degree, 12-degree, and 14-degree half-angle ablative blunt cones; ablative spheres and an ablative hemisphere-cylinder-flare (Figure 1). All the cones had a bluntness ratio (nose radius/base radius) of 0.333. Specific details



Sphere



Hemisphere-Cylinder-Flare



Hemisphere-Cone

Figure 1. Model schematics.

of each model are contained in Table I. A photograph of some cone models, including a sabot, is shown in Figure 2.

Nominal launch velocity was 19,000 feet per second (Mach 16.8), and the range free-stream gas was air. Range conditions were generally chosen such that when PD scaling (pressure times base diameter) was applied, the tests simulated full-scale reentry wake conditions for a 3-foot-diameter cone at 100,000-foot altitude.

Figure 3 shows a photograph of a model and its wake taken during the FTD test. An image-converter camera recorded the self-luminous model and wake with a 1-μsec exposure time. The optical density of the black-and-white developed negative was read by utilizing a visual color display system.

Basically, the data color system is a closed-circuit television network consisting of a camera and a color monitor console. The signal from the camera is directly proportional to the optical density of the picture it is viewing. The amplifiers of the system break the continuous camera signal into a maximum of 32 color steps. Thus, a black-and-white picture is converted to a color picture on the screen of the system. The screen is photographed to record the isodensity contours, resulting in the displayed photograph. Radiometers viewed the model and its wake and recorded spatially resolved absolute radiant intensity.

Table I. Model Properties

Shot No.	Model Material: Model	Nose	Base	Model Dimensions: r_N (in.)	r_B (in.)	θ_c (deg)	ℓ (in.)	m (gm)
4232	Cone	Cu	Al	0.333	1.00	10	4.09	170
4271	Cone	Cu	Ti	0.316	0.95	10	3.89	150
4398	Cone	3DQP	Si Ph	0.167	0.50	10	2.04	21.3
4400	Cone	3DQP	Si Ph	0.250	0.75	10	3.06	100
4401	Cone	Cu	Ti	0.316	0.95	10	3.89	165
4402	Cone	3DQP	Si Ph	0.316	0.95	10	3.89	165
4403	Cone	Cu	Al	0.250	0.75	10	3.06	99.5
4498	Sphere	3DQP	3DQP	0.330	0.33	--	0.66	4.55
4500	Cone	3DQP	Si Ph	0.250	0.75	10	3.06	99.6
4502	Cone	3DQP	Si Ph	0.250	0.75	10	3.06	98.6
4503	Cone	C Ph	C Ph	0.250	0.75	10	3.06	98.5
4504	Cone	3DQP	Si Ph	0.167	0.50	10	2.04	22.3
4505	Cone	3DQP	Si Ph	0.316	0.95	10	3.89	152
4506	H-C-F	3DQP	3DQP	0.230	0.50	20	1.43	12.1
4657	Sphere	3DQP	3DQP	0.330	0.33	--	0.66	4.29
4659	Cone	3DQP	Si Ph	0.250	0.75	12	2.58	79.2
4660	Cone	3DQP	Si Ph	0.250	0.75	10	3.06	98.3
4810	Cone	3DQP	Si Ph	0.250	0.75	14	2.23	95.6

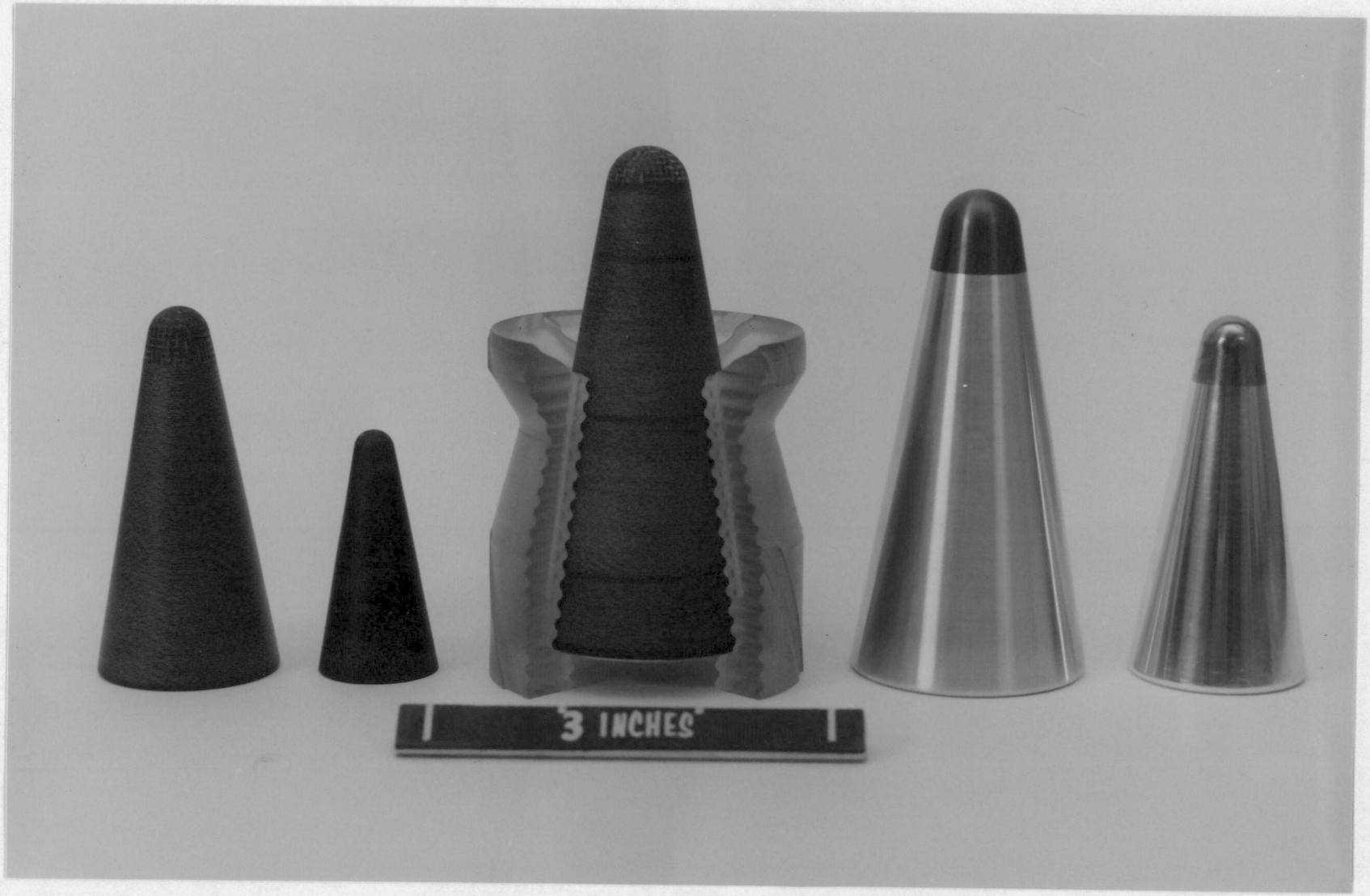


Figure 2. Photograph of models.



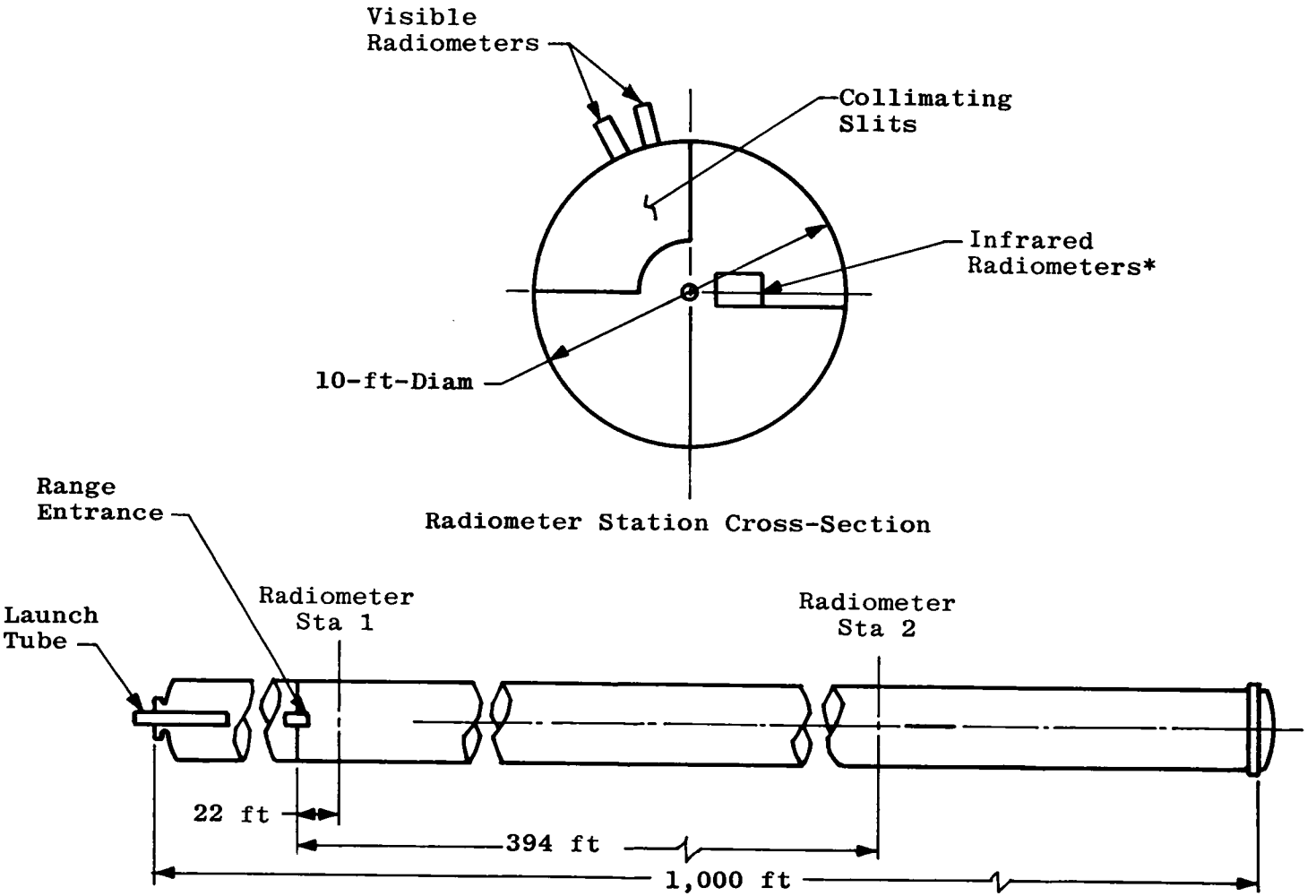
Figure 3. Image converter camera photograph.

III. RADIOMETER DESCRIPTION

Ten wideband radiometers were used to measure spatial distribution of wake intensity along the flight axis. Each of the radiometer stations (Figure 4) was comprised of two visible and three near infrared radiometers.

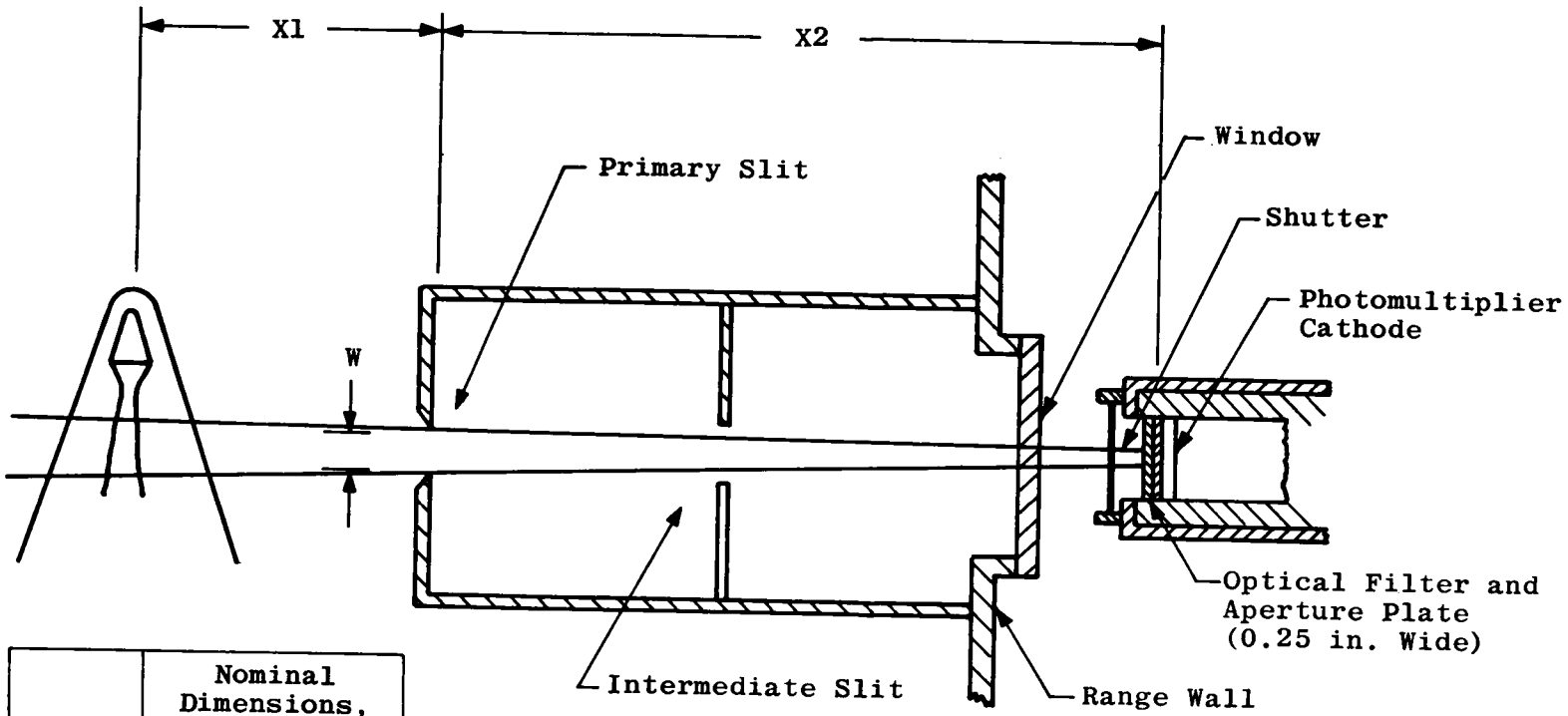
The visible radiometers (Figure 5) consist of a photomultiplier tube with a 44-mm-diameter cathode, a divider circuit for establishing proper tube bias precision switch selectable anode load resistors for converting the tube output current signal to a voltage signal, and a holder for optical filters. An 11.75-inch-long by 4.50-inch-diameter aluminum cylinder housed the photomultiplier tube, bias and load circuitry, and optical filter holder. An external precision-regulated power supply provided voltage to the internal bias circuit. A camera shutter was attached to the front of the cylinder and was used for calibration/capping purposes (generated a light pulse for calibration and served to keep the photomultiplier tube in a dark environment when not in use). A mask was usually installed in the optical filter holder to define the exposed area of the photomultiplier cathode. The mask for the FTD test contained a rectangular aperture (0.25-inch horizontal by 1.00-inch vertical).

The infrared radiometers (Figure 6) were photovoltaic indium antimonide (InSb) detectors, each with a



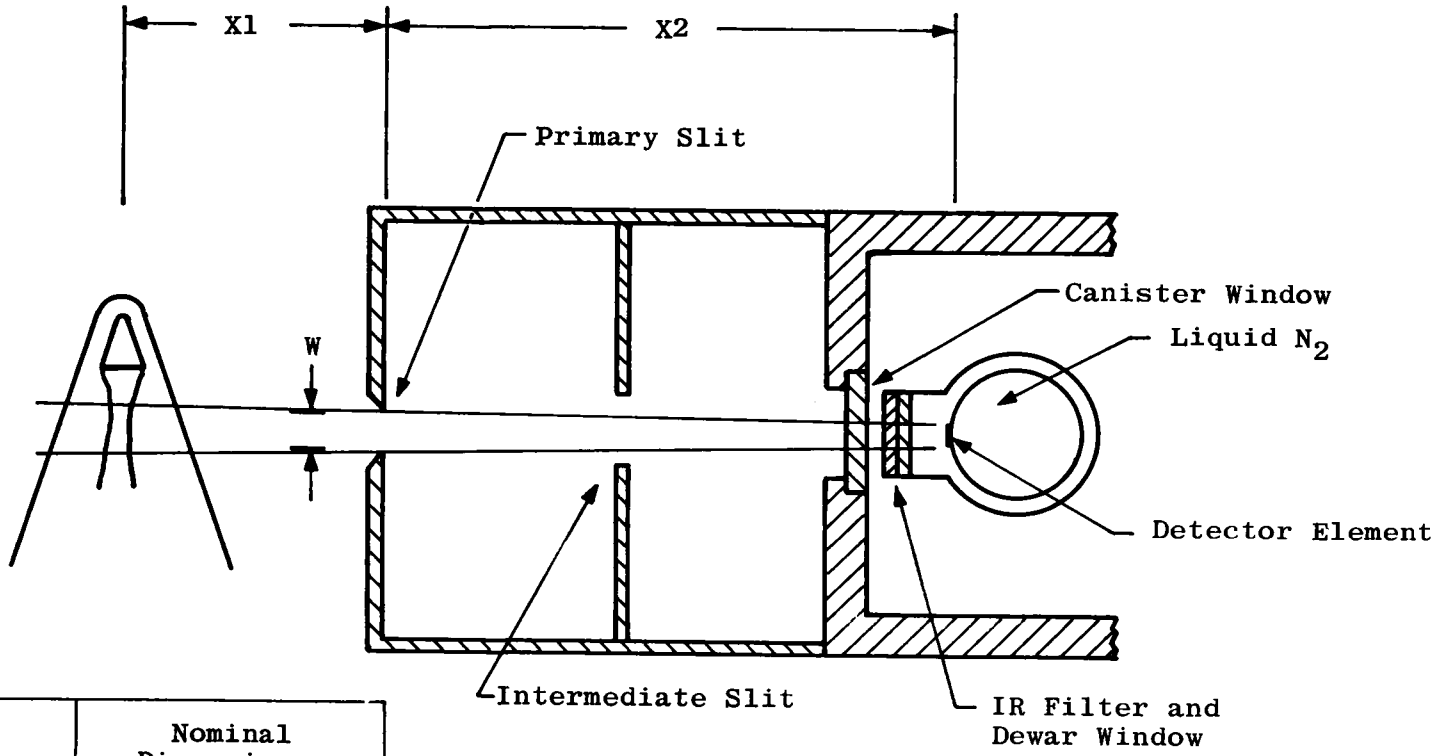
*Radiometer Sta 1 has an infrared radiometer outside the enclosure.

Figure 4. Radiometer installation in Range G.



Radiometer Sta	Nominal Dimensions, in.		
	X1	X2	W
1	12	55	0.25
2	18	49	0.25

Figure 5. Typical visible radiometer range installation.



Radiometer Sta	Nominal Dimensions, in.		
	X1	X2	W
1	12.0	7.2	0.50
1	11.3	8.2	0.25
2	17.4	7.4	0.33

Figure 6. Typical infrared radiometer range installation.

2.5-mm-diameter element. The infrared detectors, bandpass filters, and liquid nitrogen dewars were installed in canisters whose interiors were vented to atmosphere.

A slit system was used to define the radiometer field of view (Figures 5 and 6). Past range experience has indicated that slit systems are superior to lens systems in regard to rejection of optical noise (i.e., unwanted reflections). This was of extreme importance for the FTD test because of the possible interference of intense model radiation with the low-level wake radiation of interest. Past experience has also indicated that more precise absolute measurements can be obtained with a slit system, and data reduction is simplified.

The visible radiometers viewed the model flight path through plexiglass windows, whereas the infrared radiometers viewed through calcium fluoride (CaF_2) windows.

IV. RADIOMETER CALIBRATION

Relative spectral responses of the radiometers were determined from the manufacturer's specifications for filter transmissions and photomultiplier cathode responses; response characteristics are shown in Figure 7. The radiometers had filters in place during calibration.

For the visible radiometers, a calibrated 650-watt quartz iodide lamp was used. A standard lamp power supply provided a precision regulated current to the calibration lamp. The radiometers were calibrated at a nominal

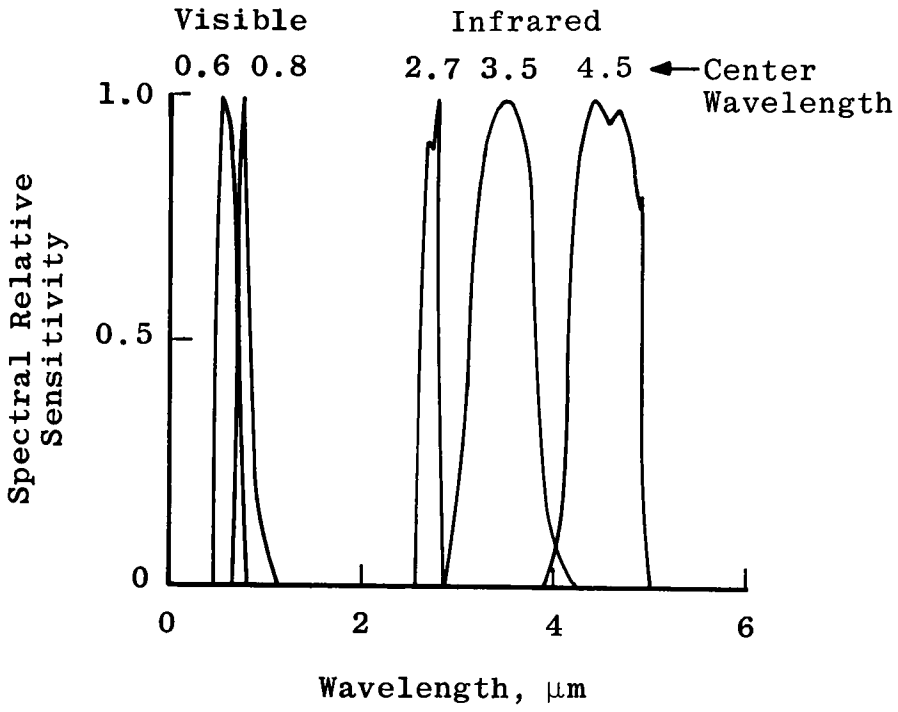


Figure 7. Radiometer relative spectral response characteristics.

distance of 12 feet. A schematic of the calibration apparatus is shown in Figure 8.

The measured output signal from the visible radiometer is

$$V_c = K A_D \int_0^\infty R(\lambda) I_\lambda \, d\lambda \, \frac{d_c^2}{d_d^2} , \qquad (1)$$

where

V_c = measured radiometer output, volts,

K = calibration constant of the filtered radiometer, volts/watt,

A_D = detector area, cm^2,

$R(\lambda)$ = relative spectral response of the radiometer, including installed filter $[R(\lambda)_{max} = 1]$,

I_λ = spectral irradiance of the quartz iodide lamp, watts/cm^2-μm,

λ = wavelength, μm,

d_c = lamp irradiance calibration distance, cm,

d_d = distance from lamp to radiometer, inch.

Equation (1) was used to measure each visible radiometer calibration constant.

For the infrared radiometers, a blackbody was used. They were calibrated at a nominal distance of 24 inches, and a temperature of 1200°K was typically used; the

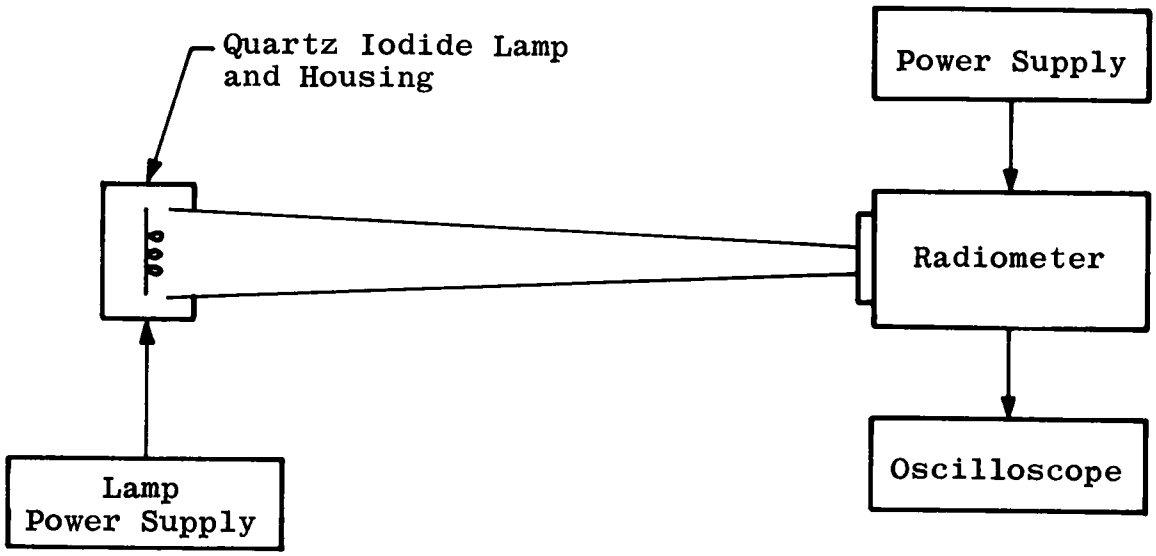


Figure 8. Visible radiometer calibration apparatus.

blackbody temperature was determined by an internal thermocouple. A schematic of the calibration apparatus is shown in Figure 9.

The measured output signal from the infrared radiometer is

$$V_c = \frac{K A_D}{d^2} \int_0^\infty R(\lambda) J_\lambda \, d\lambda \ , \qquad (2)$$

where

d = distance from blackbody to radiometer, cm,

J_λ = radiant intensity of the blackbody source, watts/sr-μm.

From [8], Eq. (2-5),

$$J_\lambda = \frac{A_{bb}}{\pi} W_\lambda \ ,$$

where

A_{bb} = blackbody aperture area, cm^2,

W_λ = blackbody spectral radiant emittance, watts/cm^2-μm.

From [8], Eq. (2-8),

$$W_\lambda = \frac{C_1}{\lambda^5} \frac{1}{e^{C_2/\lambda T} - 1} \ ,$$

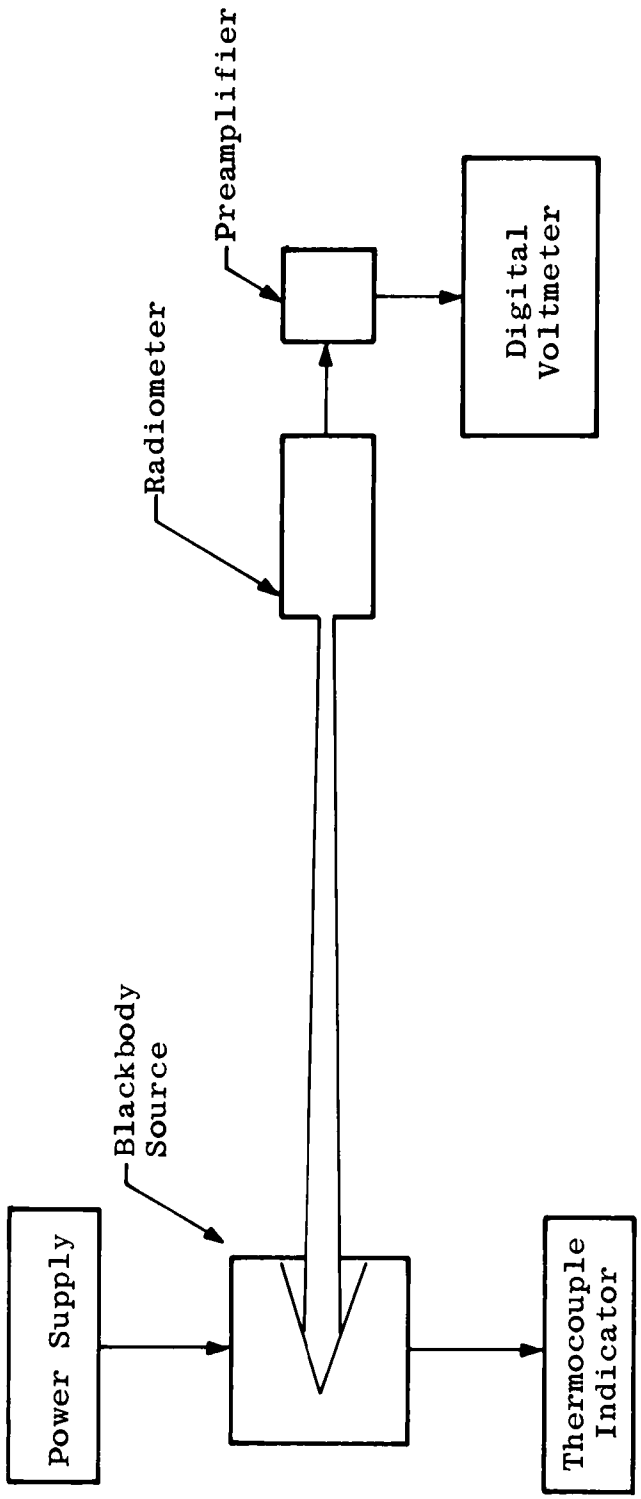


Figure 9. Infrared radiometer calibration apparatus.

where

$$C_1 = 3.7415 \cdot 10^4 \text{ watts-}\mu m^4/cm^2,$$

$$C_2 = 1.43879 \cdot 10^4 \ \mu m\text{-}°K,$$

$$T = \text{absolute temperature, } °K.$$

Equation (2) was used to measure each infrared-radiometer calibration constant.

CHAPTER III

TECHNICAL APPROACH

I. TEST DATA REDUCTION

Data reduction activities for the radiometers consisted of deriving the desired wake radiant intensity measurements from oscilloscope traces of various output voltages as a function of time. The oscilloscope traces were read on a film reader, which is basically a manually operated analog/digital device, and computer cards containing the digital data were punched automatically. Computer programs were written which utilized the calibration data and film reader output to calculate the final data from the equation given below:

$$J_{OBS} = \frac{V_S/K}{(A_D/d_s^2)\, f_w}, \qquad (3)$$

where

J_{OBS} = wake radiant intensity that is sensed or observed by the radiometer per unit solid angle per cm of wake axial length, watts/sr-cm,

K = calibration constant, volts/watt,

A_D = detector area, $inch^2$,

d_s = wake to radiometer distance, inch,

f_w = wake axial field of view, cm,

V_S = amplitude signal read from oscilloscope, volts.

Measurement of the calibration constant was addressed in Chapter II, Section IV. The wake to radiometer distance was obtained after model position was measured from the Range G shadowgraph systems; model dispersion was negligible at the first radiometer station. The axial field of view was calculated in accordance with the method given in Appendix A.

Timing data from the oscilloscope traces were converted to distance by the following equation:

$$X = TV ,$$

where

T = time read from oscilloscope, seconds,

V = velocity determined from shadowgraph system, feet/second.

The method and equations used to determine the measurement uncertainty of the radiometric data are given in Appendix B.

To calculate the drag coefficient, C_D, the measurements of forces on a body in free flight can be obtained from Newton's Second Law, normally expressed as

$$F = ma .$$

With the forces being the drag forces, F = -D, and using the definition of C_D, i.e.,

$$D = C_D \, q \, A = C_D \left(\frac{1}{2} \rho V^2 \right) A \ ,$$

then

$$- C_D \, q \, A = ma \ .$$

Letting the acceleration, A, be $\ddot{X}$, and the velocity, V, be $\dot{X}$, the differential equation governing the longitudinal motion of a model down the range is written as

$$\ddot{X} = - \frac{\rho A}{2m} (\dot{X})^2 \, C_D \ , \tag{4}$$

where, for zero amplitude motion,

$$C_D = C_{D_o} + C_{D_V} (V_\infty - V_m) \ .$$

Applying the technique of [9], which is a least-squares method employing differential corrections, Eq. (4) is fitted to the time-position data to determine values of the unknown coefficients, C_{D_o} and C_{D_V}; an existing range computer program was used. The C_{D_V} term accounts for changes in C_D that are linear with velocity. For a model experiencing yawing motion, C_{D_o} is now the drag coefficient corresponding to the mean amplitude of the yawing motion. To obtain a reliable zero yaw angle drag coefficient for models experiencing yawing motion, shots of the same model

configuration made at similar test conditions but experiencing different amplitude levels are required. During the FTD test program, few shots provided measurable angular motion histories, because of severe shadowgraph film fogging (resulting from model ablation) and because the yaw levels were generally low.

II. CORRELATION THEORIES

Bauer of Lincoln Laboratory first observed the phenomenon that the decay of radiation in the near wake of blunt reentry bodies exhibits two distinct rates [10]. He suggested a method for measuring the location of the discontinuity between the two rates, by which the wake radiation intensity is plotted against axial distance along the wake on log-linear paper. Then the data are fitted with two straight lines, the intersection of which is the location of the discontinuity, which has come to be known as the "Bauer Kink." This means the wake decay rate is exponential.

In accordance with the results of Lees and Kubuta [11], the decay of pressure with wake distance for a hemisphere-cylinder was derived to be:

$$\frac{P(X)}{P_\infty} = 0.133\ M_\infty^2\ \frac{r_N}{X} + 0.405\ , \qquad (5)$$

where

$P(X)$ = pressure as a function of distance, X,

P_∞ = free-stream pressure,

M_∞ = free-stream Mach number,

r_N = nose radius of the hemisphere-cylinder,

X = distance from the nose.

Bauer set $P(X) = P_\infty$, and Eq. (5) became

$$X_{P_\infty} = \frac{M_\infty^2 \, r_N}{4.5} = X_K \ , \qquad (6)$$

which is the Bauer Kink formula which correlates the nose radius of a hemisphere-cylinder to the distance at which the pressure has become ambient; this distance is the pressure relaxation point, or wake kink. This is shown schematically in Figure 10, where on a log-linear plot, the wake intensity decay rate is represented by two straight lines of different slopes. Even though the Bauer formula was derived for blunted cylinders, Bauer applied it to blunted cone data with satisfactory results.

Improved versions of Eq. (6) have been suggested by Textoris and Stankevics [10], and by Heyda [12]. Both these versions introduce a shape-dependent factor into the kink formula. Textoris, after looking at some experimental data, speculated that the kink distance was most likely related to an effective nose radius rather than the actual

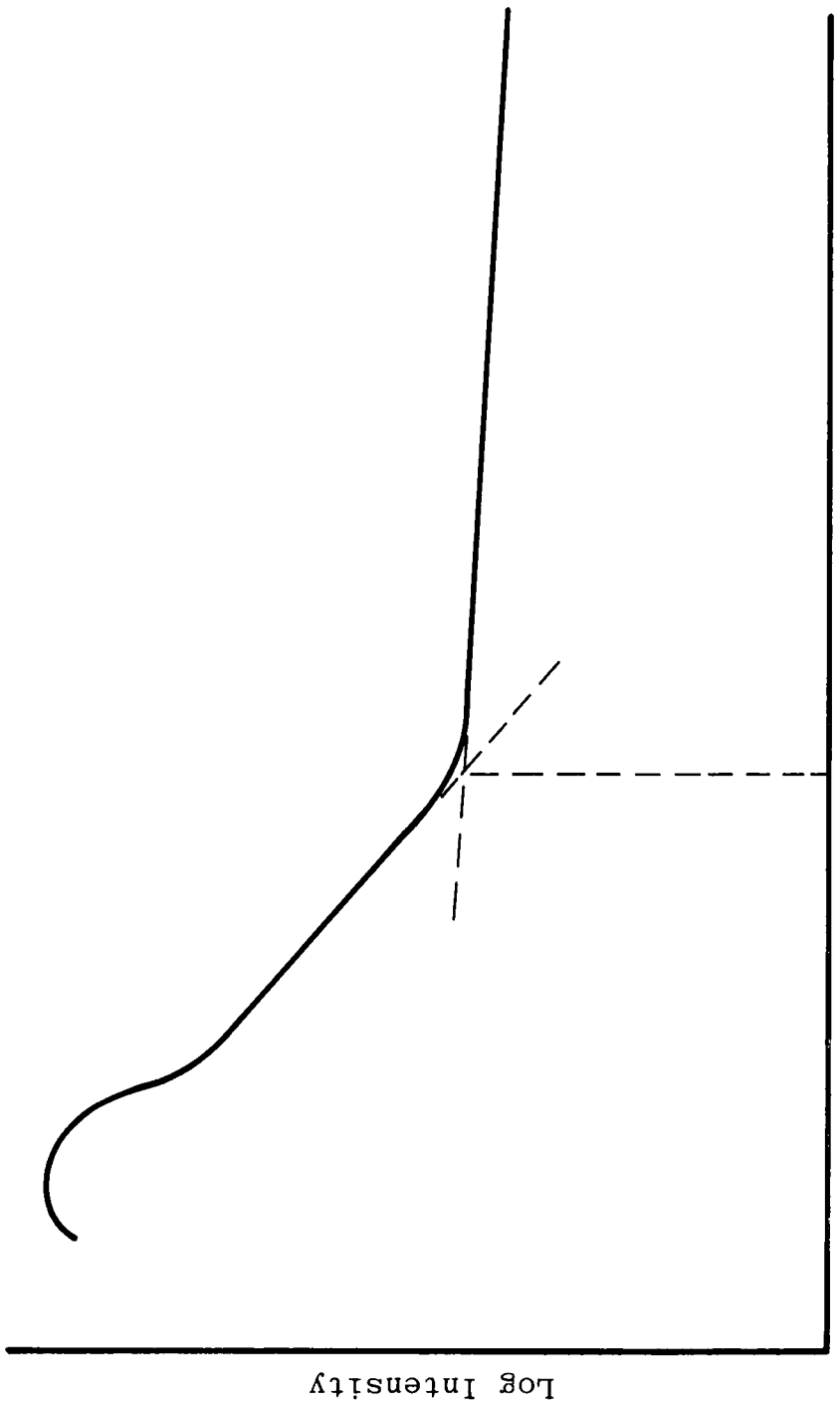


Figure 10. Wake kink phenomenon.

nose radius. By defining an effective nose radius as such:

$$r_{eff} = \sqrt{C_D A/\pi} \ ,$$

where

C_D = drag coefficient,

A = area upon which drag coefficient is based,

Textoris introduced the following revised formula:

$$X_K = \frac{r_{eff} \ M_\infty^2}{4.5} \ , \tag{7}$$

where

$$r_{eff} = \sqrt{C_{D_B}} \ r_B \ ,$$

with

r_B = model base radius,

C_{D_B} = drag coefficient based upon model base radius.

The term r_{eff} is also referred to as the drag radius. Textoris applied Eq. (7) to some experimental data with satisfactory results.

Heyda [12] derived the following kink distance equation:

$$\frac{X_K}{r_N} = 0.4 \ C_D^{1/2} \ M_\infty^2 \ , \tag{8}$$

by utilizing the following equations of Lykoudis [13]:

$$\text{(a)}\quad \sin^2 \delta = \frac{1}{1 + \dfrac{R^{2(1-m)/m}}{m^2 A^{2/m}}} , \tag{9}$$

where δ = shock-wave angle,

R = function defining bow shock wave, as defined below:

$$R = A X^m = 1.27 C_D^{1/4} X^{1/2} \tag{10}$$

(on a per unit body radius basis),

i.e., $A = 1.27 C_D^{1/4}$

$m = 1/2$.

$$\text{(b)}\quad \sin \delta = \frac{1}{M_\infty} , \tag{11}$$

where the pressure first becomes ambient (at $X = X_K$).

Combining Eqs. (9), (10), and (11), and letting $M_\infty^2 - 1 = M_\infty^2$, and noting that $X = X/r_N$ when considering a nose radius that is not unity, one obtains Eq. (8).

IV. DATA CURVE FITS

The method of least squares is used to fit the radiometric wake data to obtain two straight lines of different slopes, as suggested by Bauer. A computer

program was written for a least-squares polynomial fit, details of which follow.

Consider the problem of fitting a given number of function values, J_i (wake radiant intensity J_{OBS}), to a polynomial of m^{th} degree. Let the dependent values be designated D_i (distance X) and let the weighting factors be W_i (one minus the uncertainty associated with the intensity, $1 - (S_{J_{OBS}}/100)/J_{OBS}$). The polynomial takes the form:

$$J = K_o + K_1 D + K_2 D^2 + \ldots + K_m D^m \quad . \tag{12}$$

The objective is to find the values of K_o, K_1,...K_m which make the graph of Eq. (12) pass as near as possible to each of the n points (J_1,D_1), (J_2,D_2),...(J_n,D_n); or stated otherwise, find an equation of the form of Eq. (12) which will be satisfied as nearly as possible by each of the n pairs of values (J_1,D_1), (J_2,D_2),...(J_n,D_n). Substituting into Eq. (12) each of the n pairs of values in turn results in the following residual equations:

$$\begin{aligned}
S_1 &= K_o + K_1 D_1 + K_2 D_2^2 + \ldots + K_m D_1^m - J_1 \\
S_2 &= K_o + K_1 D_2 + K_2 D_2^2 + \ldots + K_m D_2^m - J_2 \\
&\vdots \\
S_n &= K_o + K_1 D_n + K_2 D_n^2 + \ldots + K_m D_n^m - J_n \quad .
\end{aligned}$$

The principle of least squares for measurements of unequal weight is that the best values of the unknown constants, K_o, K_1, K_2,...K_m, are those which make the sum of the weighted squares of the residuals a minimum. Hence,

$$S = \sum_{i=1}^{n} W_i S_i^2 \tag{13}$$

is to be a minimum, where

$$S_i = K_o + K_1 D_i + K_2 D_i^2 + \ldots + K_m D_i^m - J_i \ .$$

To obtain the minimum value of S, which is now a function of m+1 variables, K_o, K_1,...K_m, set the following m+1 first partial derivatives to zero:

$$\frac{\partial S}{\partial K_o} = \sum_{i=1}^{n} 2 W_i S_i = 0$$

$$\frac{\partial S}{\partial K_1} = \sum_{i=1}^{n} 2 D_i W_i S_i = 0$$

$$\vdots$$

$$\frac{\partial S}{\partial K_m} = \sum_{i=1}^{n} 2 D_i^m W_i S_i = 0 \ .$$

The following m+1 simultaneous linear equations are then obtained:

$$
\begin{aligned}
&K_o \Sigma W_i + K_1 \Sigma W_i D_i + K_2 \Sigma W_i D_i^2 + \ldots \\
&\qquad + K_m \Sigma W_i D_i^m - \Sigma W_i J_i = 0 \\
&K_o \Sigma W_i D_i + K_1 \Sigma W_i D_i^2 + K_2 \Sigma W_i D_i^3 + \ldots \\
&\qquad + K_m \Sigma W_i D_i^{m+1} - \Sigma W_i D_i J_i = 0 \\
&K_o \Sigma W_i D_i^2 + K_1 \Sigma W_i D_i^3 + K_2 \Sigma W_i D_i^4 + \ldots \\
&\qquad + K_m \Sigma W_i D_i^{m+2} - \Sigma W_i D_i^2 J_i = 0 \\
&\vdots \\
&K_o \Sigma W_i D_i^m + K_1 \Sigma W_i D_i^{m+1} + K_2 \Sigma W_i D_i^{m+2} + \ldots \\
&\qquad + K_m \Sigma W_i D_i^{m+m} - \Sigma W_i D_i^m J_i = 0 \ ,
\end{aligned}
$$

where the summation, Σ, is for i=1 to n.

It is convenient to express the above equations in matrix notation,

$$[A]\ [K] = [B]\ , \qquad (14)$$

where

$$[A] = \begin{bmatrix} \Sigma W_i & \Sigma W_i D_i & \Sigma W_i D_i^2 & \cdots & \Sigma W_i D_i^m \\ \Sigma W_i D_i & \Sigma W_i D_i^2 & \Sigma W_i D_i^3 & \cdots & \Sigma W_i D_i^{m+1} \\ \vdots & & & & \\ \Sigma W_i D_i^m & \Sigma W_i D_i^{m+1} & \Sigma W_i D_i^{m+2} & \cdots & \Sigma W_i D_i^{2m} \end{bmatrix},$$

$$[K] = \begin{bmatrix} K_o \\ K_1 \\ \vdots \\ K_m \end{bmatrix}, \quad [B] = \begin{bmatrix} \Sigma W_i J_i \\ \Sigma W_i D_i J_i \\ \vdots \\ \Sigma W_i D_i^m J_i \end{bmatrix}.$$

To solve Eq. (14) for the unknown K coefficients, an existing range computer program, which fitted a polynomial through a given number of unweighted points, was modified. Modification included the capability to fit weighted points. The curve fit routines employ the least-squares method and solve simultaneous equations, represented by Eq. (14), algebraically.

The method just discussed is for a polynomial fit. The specified equations will be simplified for a straight line fit, as only straight line fits were considered in this study; however, the computer programs used can perform polynomial fits.

To find the equation of the straight line which comes nearest to passing through n weighted points, let the equation of the line be

$$J = K_o + K_1 D \ .$$

In accordance with Eq. (14), with m=2 (second order equation),

$$\begin{bmatrix} a_{11} & a_{12} \\ a_{21} & a_{22} \end{bmatrix} \begin{bmatrix} K_o \\ K_1 \end{bmatrix} = \begin{bmatrix} b_1 \\ b_2 \end{bmatrix} \ , \qquad (15)$$

where

$$a_{11} = \Sigma W_i, \quad a_{12} = a_{21} = \Sigma W_i D_i, \quad a_{22} = \Sigma W_i D_i^2 \ ,$$

$$b_1 = \Sigma W_i J_i, \quad b_2 = \Sigma W_i D_i J_i \ .$$

To solve Eq. (15) for K_o and K_1, the following method was employed in the computer program.

From Eq. (15),

$$a_{11} K_o + a_{12} K_1 = b_1 \ , \qquad (16)$$

$$a_{21} K_o + a_{22} K_1 = b_2 \ . \qquad (17)$$

Dividing Eq. (16) by a_{11},

$$K_o + \frac{a_{12}}{a_{11}} K_1 = \frac{b_1}{a_{11}} . \qquad (18)$$

Multiplying Eq. (18) by a_{21}, subtracting it from Eq. (17), and solving for K_1,

$$K_1 = \frac{b_2 - a_{21} (b_1 / a_{11})}{a_{22} - a_{21} (a_{12}/a_{11})} .$$

Substituting K_1 into Eq. (18), K_o can be determined,

$$K_o = \frac{b_1}{a_{11}} - \frac{a_{12}}{a_{11}} K_1 .$$

Then the residuals are summed by Eq. (13), where,

$$S_i = K_o + K_1 D_i - J_i$$

and

$$(D_i, J_i)$$

are the data points.

For the "Bauer Kink" phenomenon, the first few radiometric wake data points were fit with one least-squares straight line and the remaining data points were fit with another least-squares straight line. The residuals between the data and the straight line fits were calculated and then summed by Eq. (13). Additional

straight line curve fits were made by sequentially adding the next data point to the first group of points and deleting it from the second group of data points. The best fit was deemed to occur when the residuals reached a minimum value.

CHAPTER IV

EXPERIMENTAL DATA AND RESULTS

Useful radiometric data were obtained from 18 shots; a summary of the test conditions is shown in Table II. It is to be noted that three shots had copper nosetips and metal bases (non-ablative). For all the data reported herein, the test gas was at room temperature. No special effort was made to lower either water vapor content or vacuum pump-induced contamination, with one exception; Shot 4660 had dry air pumped into the evacuated range. Range air was sampled and dewpoint measurements were made prior to each shot. Test gas constituency is given in Table III. Drag coefficient data are presented in Table IV.

I. GENERAL LOG-LINEAR PLOTTED DATA

The radiometric data on oscilloscope traces were reduced by the method described in Chapter III, Section I. The reduced data were plotted in accordance with the Bauer method; that is, radiation intensity data (J_{OBS}) on a log scale versus distance data (X) on a linear scale. The data are given in Appendix C. Data in the 4.0 to 5.0 μm wavelength are not given, as intensity did not decay with distance; thereby, the data could not be used to obtain kink distances.

Table II. Summary of Test Conditions

Model/ Type	r_N (in.)	P_∞ (torr)	Sta. 1 V_∞ (fps)	Sta. 2 V_∞ (fps)	Shot No.	Remarks
Cone/NA	0.333	149	18,850	--	4232	Model bulged.
	0.316	179	18,800	--	4271	
	0.316	161	18,700	18,150	4401	
	0.250	200	18,700	17,950	4403	
Cone/A	0.316	159	18,600	18,100	4402	Part of sleeve off.
	0.316	66	18,700	18,450	4505	Part of sleeve off.
	0.250	314	19,150	--	4502	
	0.250	201	18,800	18,100	4400	Part of wake not observed by Sta. 2 infrared radiometers because of model dispersion.
	0.250	200	18,950	18,350	4503	
	0.250	201	18,750	18,050	4660	Dry air shot.
	0.250	86	18,750	--	4500	
	0.167	300	18,400	--	4398	
	0.167	127	18,550	--	4504	Part of sleeve off.
Cone A/12°	0.250	200	18,250	17,450	4659	Part of wake not observed by Sta. 2 infrared radiometers because of model dispersion.
Cone A/14°	0.250	199	18,900	18,100	4810	
Sphere/A	0.330	199	17,200	--	4498	
	0.330	193	19,000	--	4657	
H-C-F/A	0.230	201	18,600	--	4506	

Table III. Range Air Data

Shot No.	CO_2 (%)	O_2 + Ar (%)	N_2 (%)	CO (%)	H_2 (%)	ppm HC as CH_4	T_∞ (°F)		Dewpoint Temp. (°F)	
							Sta. 1	Sta. 2	Sta. 1	Sta. 2
4232	<0.02	21.9	78.7	<0.03	<0.01	6	75		<25	
4271	<0.04	22.0	78.7	<0.02	<0.01	13	73		--	
4398	<0.04	22.3	79.6	<0.02	<0.01	3	75		38	
4400	<0.04	22.1	79.6	<0.02	<0.01	2	76	76	34	31
4401	<0.04	20.8	76.7	<0.02	<0.01	2	75		31	
4402	<0.04	20.9	76.6	<0.02	<0.01	6	76	76	32	28
4403	<0.04	21.5	77.0	<0.02	<0.01	2	75		34	
4498	<0.04	21.6	77.1	<0.03	<0.01	7	74		<25	
4500	<0.04	19.9	77.4	<0.03	<0.01	10	66		<25	
4502	<0.04	21.7	77.8	<0.02	<0.01	2	73		40	
4503	<0.04	21.8	77.9	<0.02	<0.01	2	72	73	30	26
4504	<0.02	21.1	78.3	<0.02	<0.01	1	70		26	
4505	<0.02	20.5	79.1	<0.02	<0.01	1	68	73	<25	<25
4506	<0.02	21.2	77.3	<0.02	<0.01	1	69		33	
4657	<0.04	22.0	78.5	<0.02	0.05	6	73		17	
4659	<0.04	21.9	78.1	<0.02	<0.01	2	74	72	26	28
4660	<0.04	21.7	78.1	<0.02	<0.01	2	74	72	-11	<25
4810	--	20.7	75.0	<0.02	<0.01	--	75		<25	

Table IV. Drag Coefficient Data

Shot No.	Radiometer Sta.	M_∞	C_D	α (deg)	$\bar{\alpha}$ (deg)
4232	1	16.6	0.166	2	2
4271	1	16.6	0.162	1	1
4398	1	16.2	0.181	4	7
4400	1	16.6	0.170	0	0
4400	2	15.9	0.174	0	--
4401	1	16.5	0.168	1	1
4402	2	15.9	0.176	1	--
4403	1	16.5	0.170	1	1
4498	1	15.2	1.16	N/A	N/A
4500	1	16.7	0.153	2	2
4502	1	16.9	0.169	1	1
4503	1	16.8	0.165	1	1
4503	2	16.2	0.168	1	--
4504	1	16.4	0.185	1	1
4505	2	16.3	0.166	4	--
4506	1	16.5	0.308	9	8
4657	1	16.8	0.934	N/A	N/A
4659	1	16.1	0.185	0	0
4659	2	15.4	0.190	3	--
4660	1	16.6	0.170	1	1
4660	2	16.0	0.187	6	--
4810	1	16.7	0.193	2	2
4810	2	16.0	0.201	2	--

The intensity/distance data were then curve fitted by the least-squares method detailed in Chapter III, Section IV. Details of the methodology used to obtain kink distances involved engineering judgment and individual decisions at different stages; thereby, a detailed discussion of the techniques used follows. The initial problem was to decide what data were to be used for the curve fit of two straight lines to yield kink distances. The wake data to be fitted were thought to have the characteristic shape depicted in Figure 10, page 27.

II. VISIBLE LOG-LINEAR PLOTTED DATA

For the visible radiometric data, the wake data starting at a distance of about 10 inches exhibited the Figure 10 shape. Initially, body radiation intensity decayed (refer to page 111 of Appendix C, distance about 2 inches); then generally, came wake intensity rises and decays (page 111 of Appendix C, distance about 2 to 11 inches); finally, a gradual wake intensity decay occurred. The data to be fitted for kink distance determination were chosen to be those data in the gradual wake intensity decay regime, generally starting at about 10 inches, which is in agreement with the Figure 10 kink distance determination. The initial task then was to define exactly where the wake kink data were to begin. To do this, the Chapter III, Section IV, least-squares method was used to curve fit the intensity decay data by two straight lines. The beginning

of the intensity decay data to be analyzed started at the intensity decay point where there were essentially no further intensity rises (page 111 of Appendix C, distance about 8 inches), except for small oscillatory rises and decays in the wake. After fitting the two straight lines, the data of the second straight line were deemed to be the wake kink data, that is, the data to be used for kink distance determination. These wake kink data were then analyzed with the same Section IV method. The distance where the change in slope of the two straight line curve fits occurred defined the kink distance.

Curve fitting of the visible radiometric data thereby consisted of the following two steps:

Step 1. Fitting the intensity decay data to two straight lines to determine the wake kink data.

Step 2. Fitting the wake kink data to two straight lines to determine the kink distance.

For each of the above steps, the first three data points were fit with one straight line and the remaining data points were fit with another straight line. Sequentially, the next data point was added to the first group of points and deleted from the second group of points, until the second group of points consisted of three data points. When the sum of the residuals squared (SRS) for a particular shot and radiometer was analyzed, it was observed that in many cases the minimum value of the SRS

was very close to the next highest value. It was also observed that in most cases a plot of SRS versus distance did not show a one-time trend of residuals decreasing to a minimum and then increasing again; but rather, a few transition points (where the slope of the curve is zero) were obtained.

Figures 11 through 19 present typical curves of SRS versus distance for the wake kink data. Figure 11 has one transition point area, defined by two data points; whereas the other figures have more than one transition point area. Since the acquisition of data and their reduction are neither 100 percent precise nor repeatable, it was felt that if there were more than one transition data point, and the SRS of the transition points differed by only a small amount, it was not justified to consider only the minimum point. It was thereby chosen to define a minimum residual range, consisting of the minimum SRS up to 90 percent of the minimum SRS; this range is depicted on Figures 11 through 19. The decision to consider a range of "minimum" SRS points instead of one minimum SRS point adds to the complexity of the data reduction/analysis. Considering a range of minimum SRS points obviously results in a corresponding range of distance points. For the initial fit of two straight lines to determine the wake kink data (Step 1), the range of minimum SRS usually dictates more than one distance at which to start wake kink data. For example, referring to Shot 4232, 0.5 to 0.7 μm

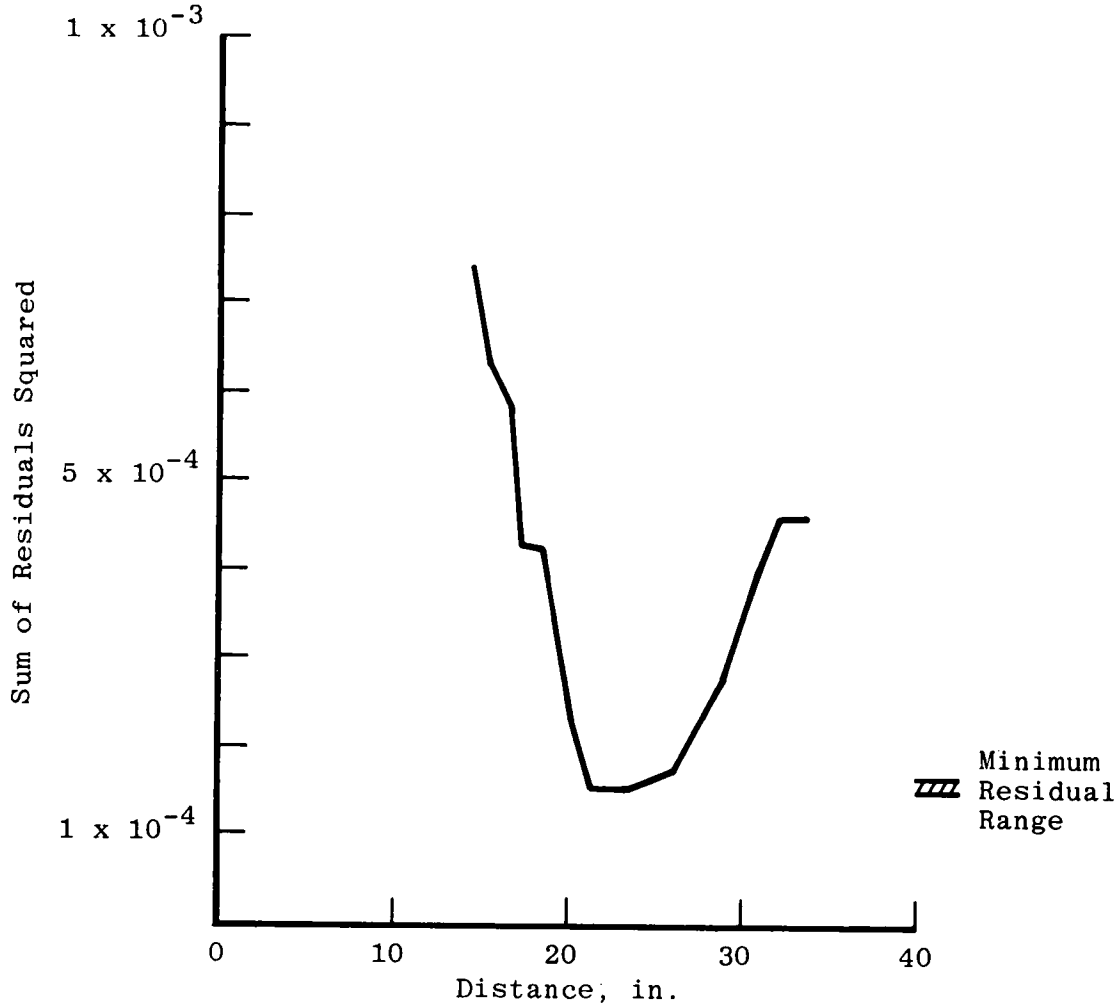


Figure 11. Shot 4402, 0.5 to 0.7 μm residuals.

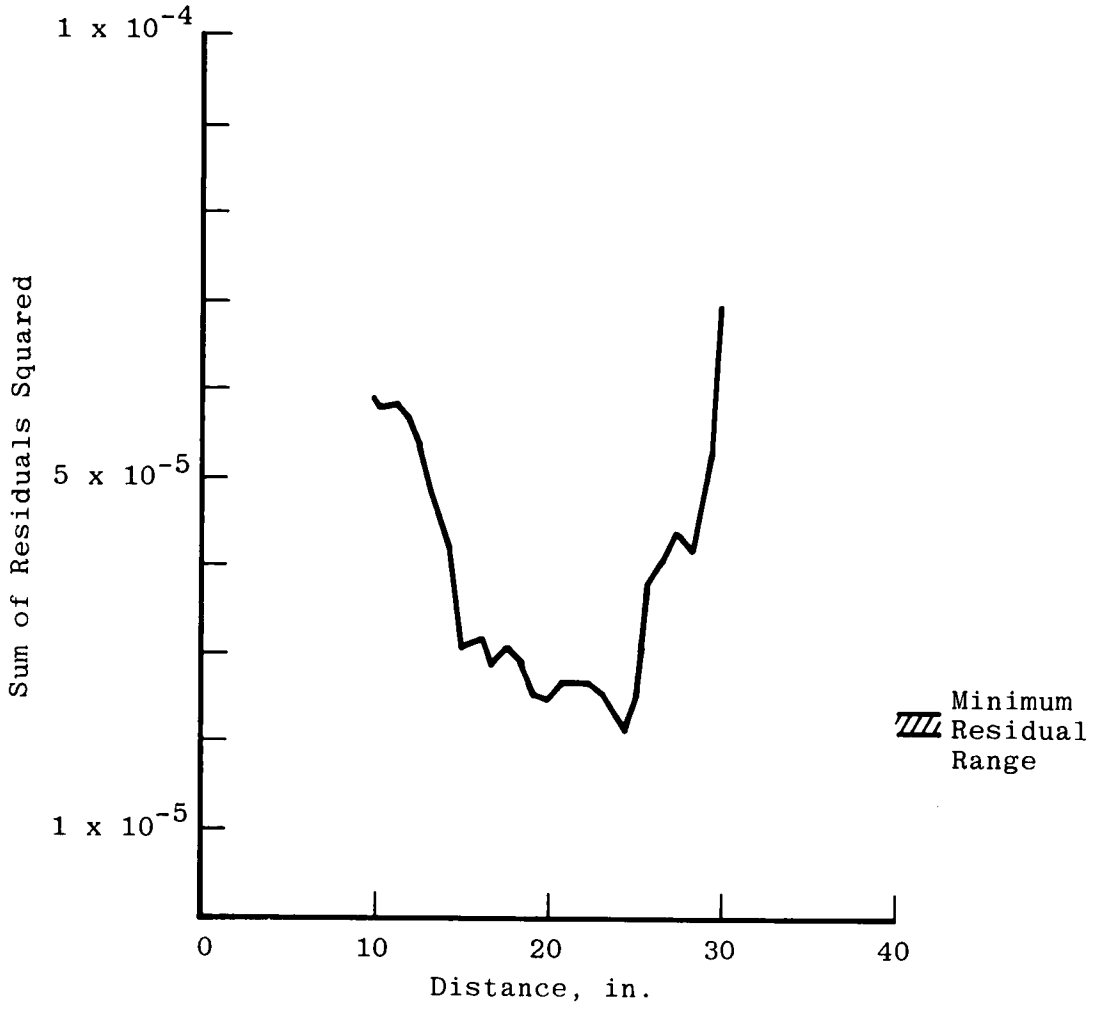


Figure 12. Shot 4498, 0.7 to 0.8 μm residuals.

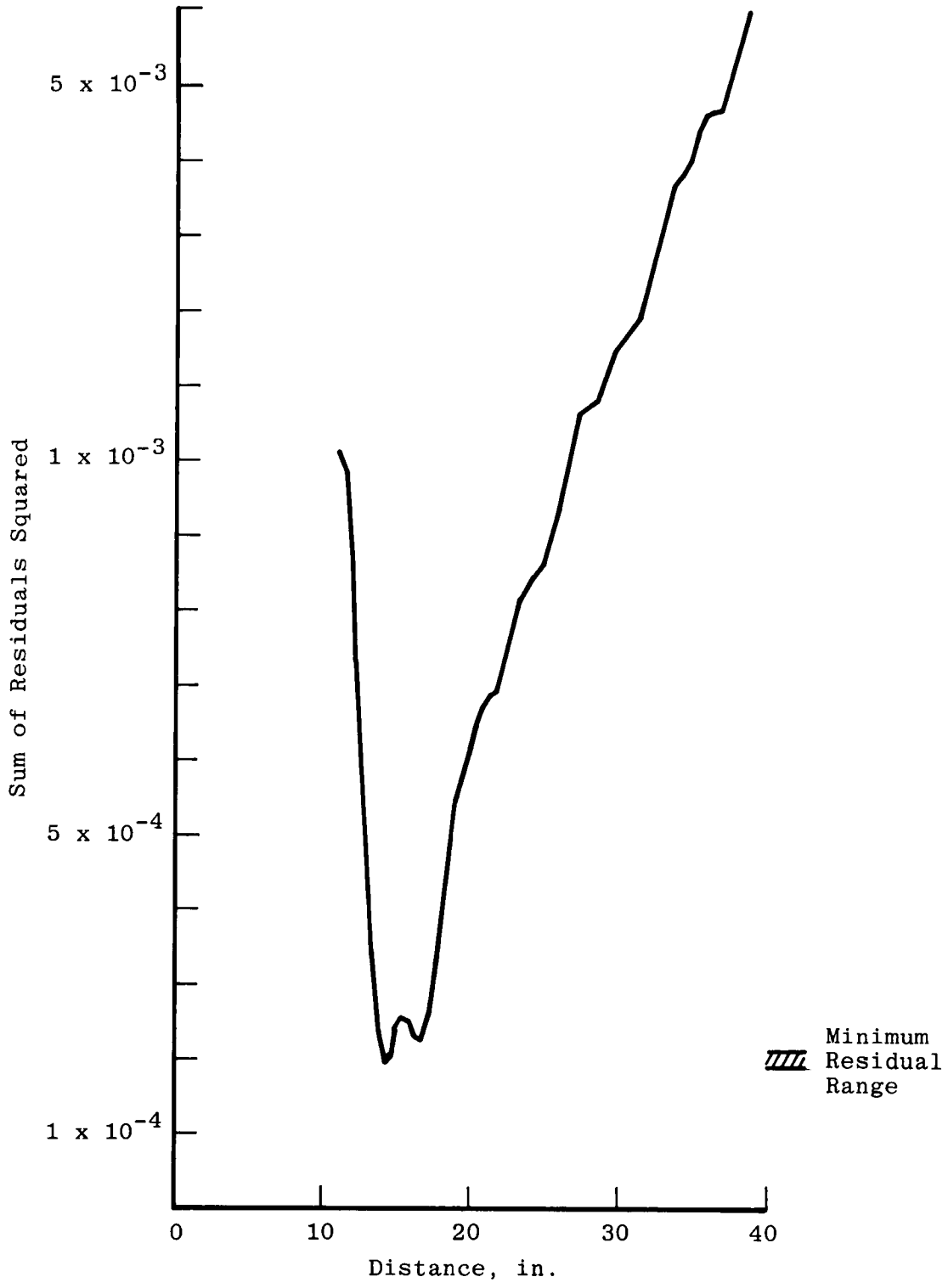


Figure 13. Shot 4502, 0.7 to 0.8 μm residuals.

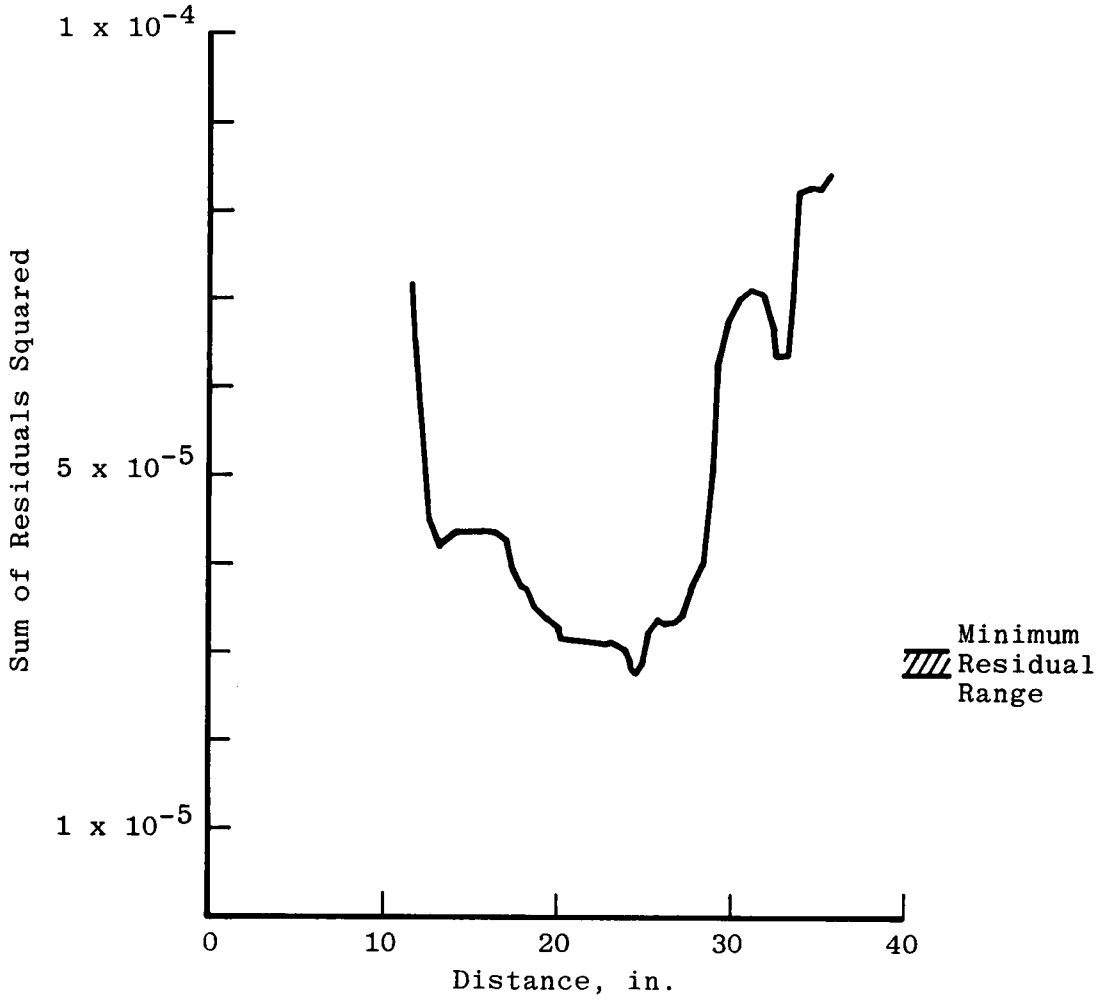


Figure 14. Shot 4659, 0.5 to 0.7 μm residuals.

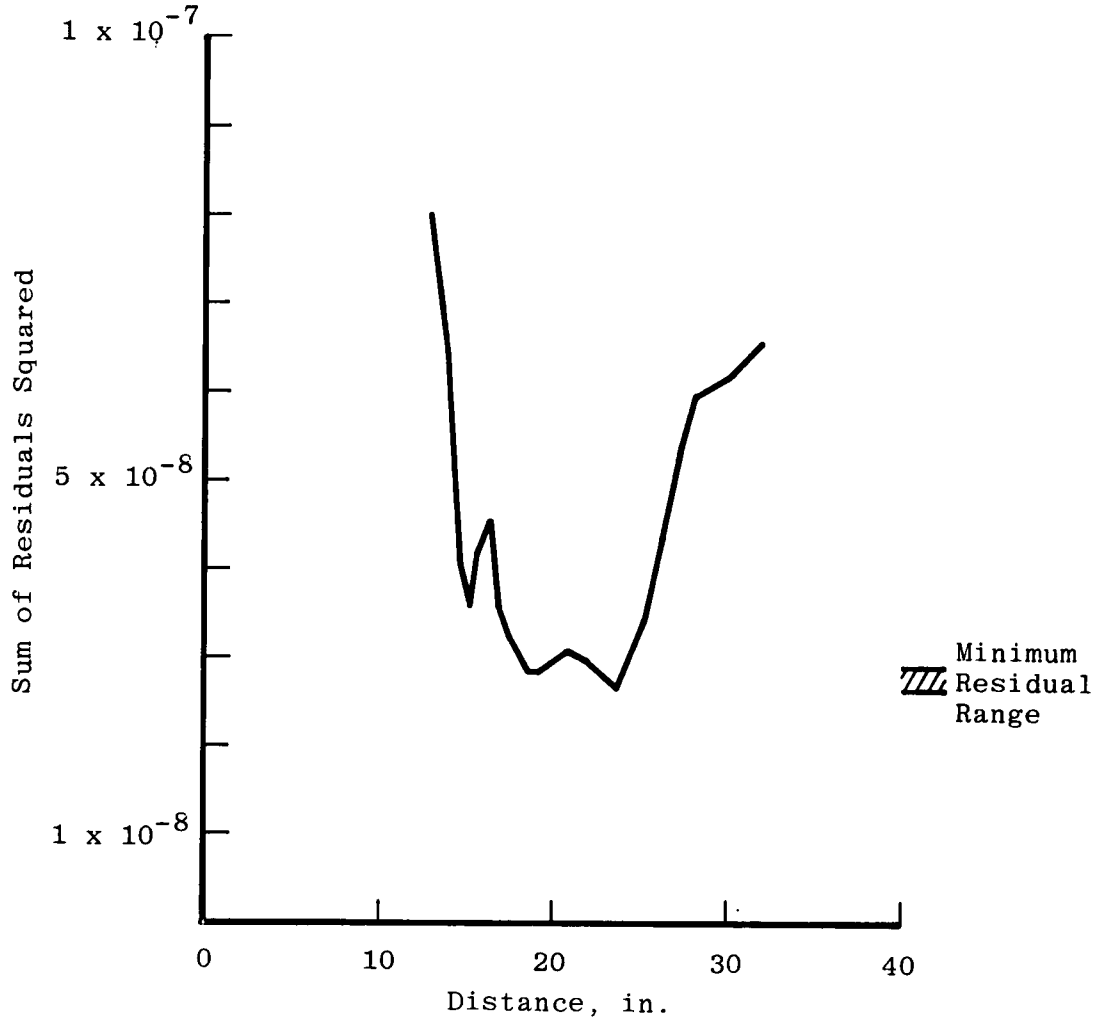


Figure 15. Shot 4232, 0.5 to 0.7 μm residuals.

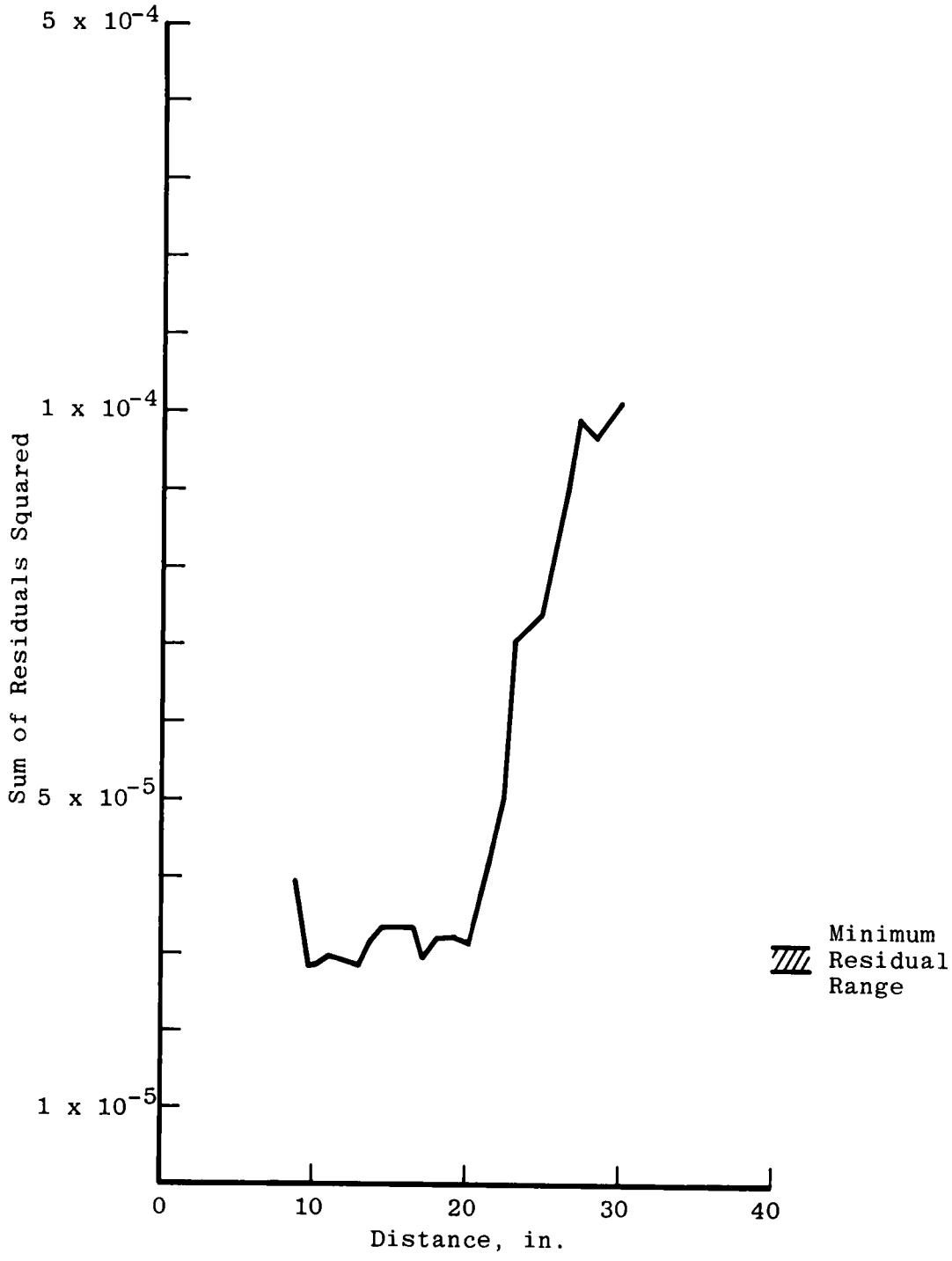


Figure 16. Shot 4398, 0.5 to 0.7 μm residuals.

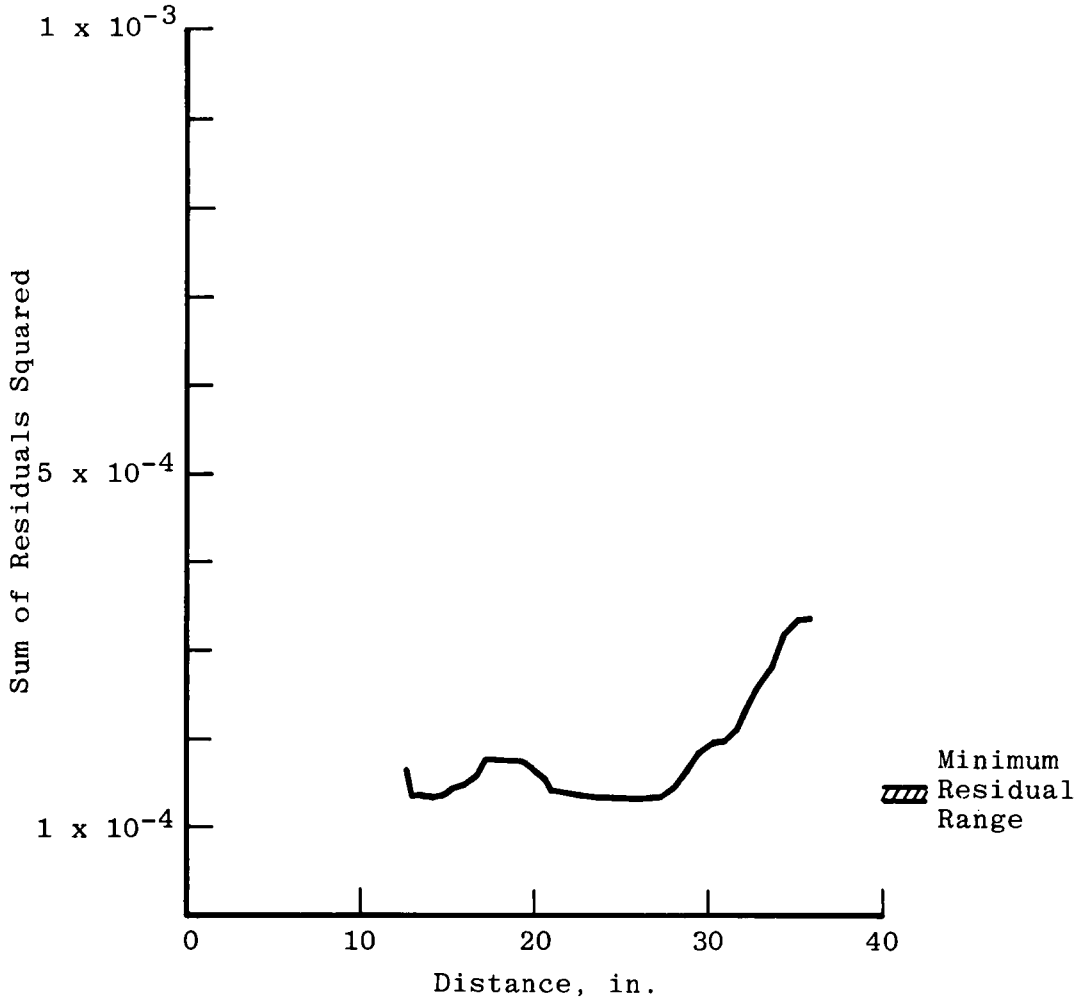


Figure 17. Shot 4503, 0.5 to 0.7 μm residuals.

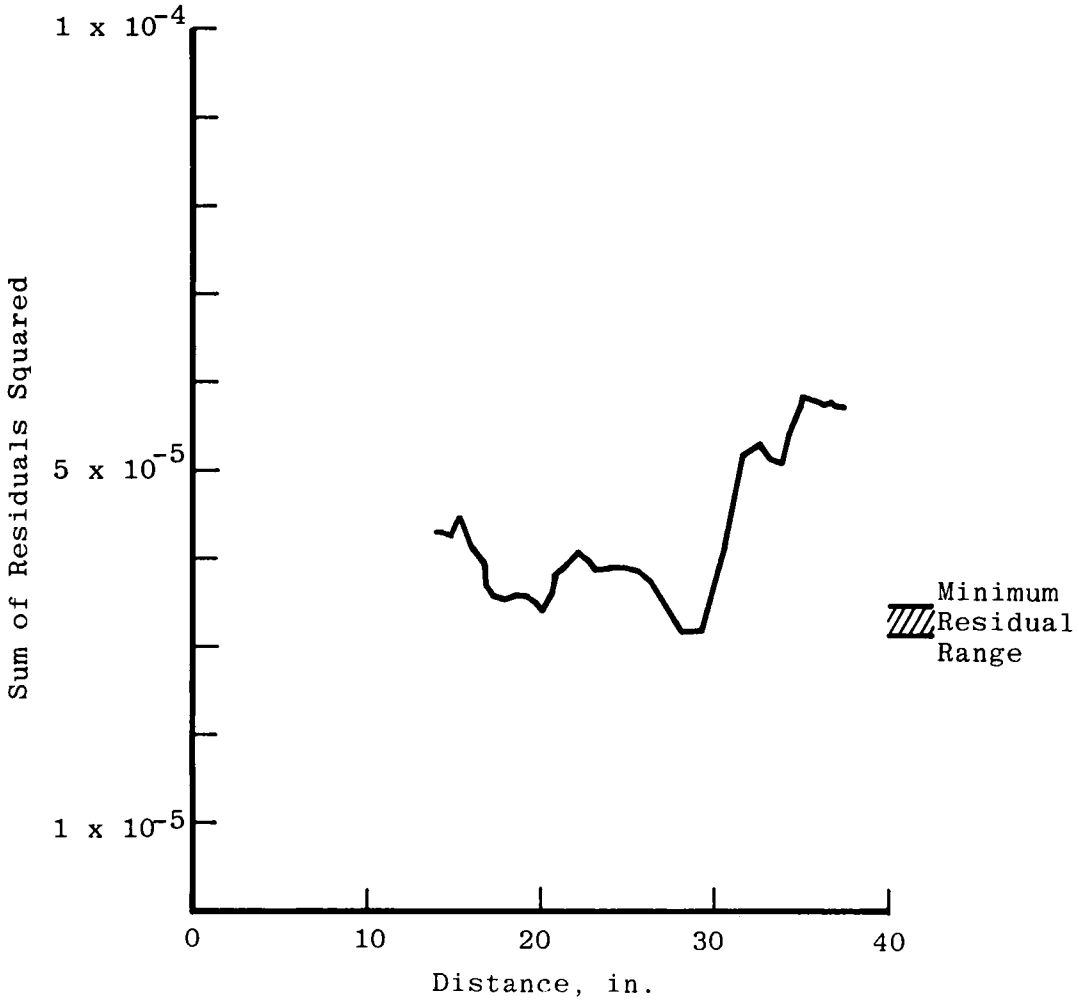


Figure 18. Shot 4503, 0.7 to 0.8 μm residuals.

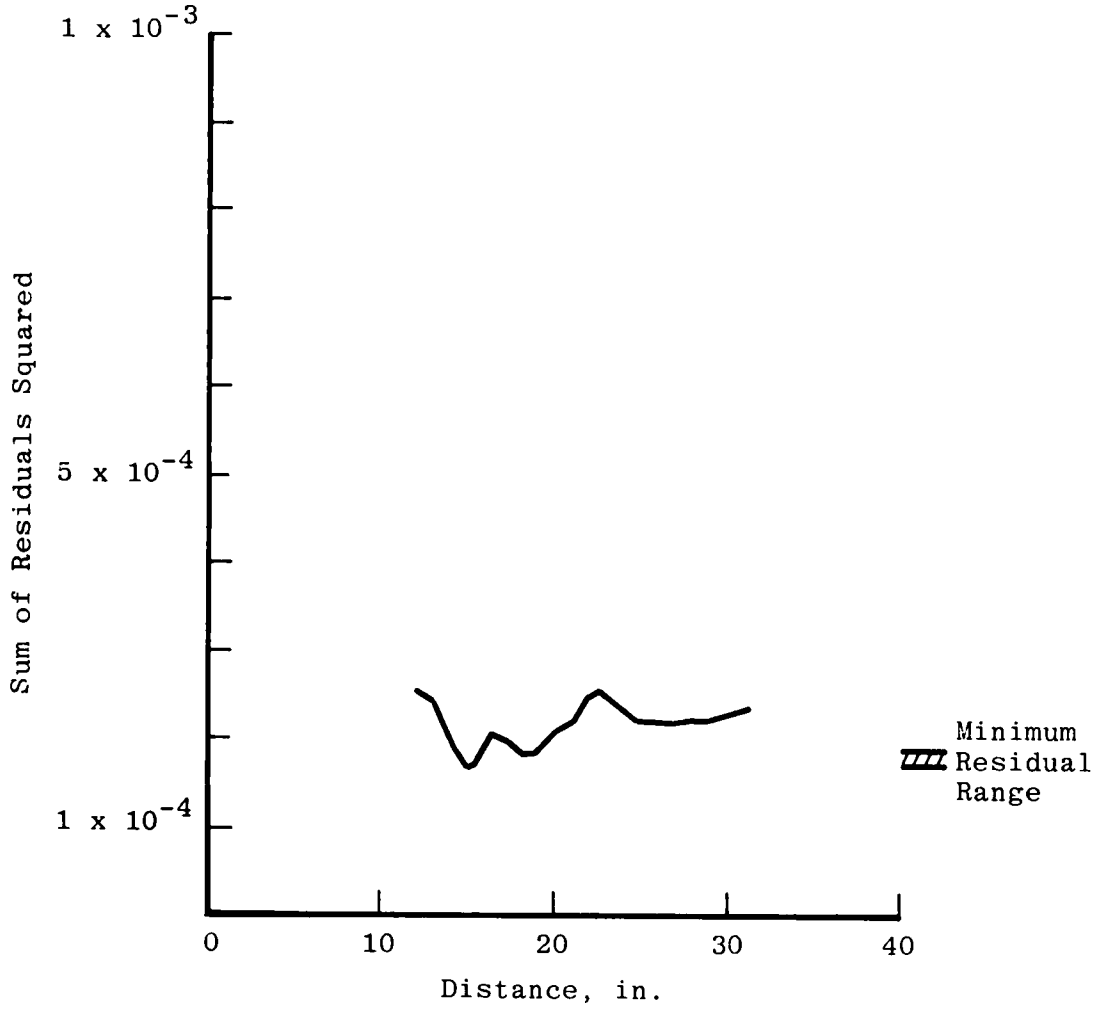


Figure 19. Shot 4660, 0.7 to 0.8 μm residuals.

bandpass (Appendix C, page 111), the minimum SRS range encompassed a distance range 9.6 to 12.0 inches, which made the first straight line include four, five, six, or seven points. The final fit of two straight lines to determine the wake kink distance (Step 2) consisted of four cases, each of which obtained two straight lines; the first fit consisted of 26 wake kink points, and the last one consisted of 23 wake kink points. The first fit gave kink distances of 21.8 and 23.6 inches; the second fit (refer to Figure 15) gave 18.4, 19.2, and 23.6 inches; the third fit gave 18.4, 19.2, and 23.6 inches also; and the fourth fit gave 23.6 inches. The judgment was made to consider only the first kink distances and not the later ones that occurred at least two data points and 2 inches or more later. Thereby, the distances 18.4 and 19.2 inches were considered, but the 21.8- and 23.6-inch distances were not considered. This judgment was used for all cases. All kink distances obtained in the minimum residual range on Figures 11 through 14 were considered, whereas only the initial kink distances obtained on Figures 15 through 19 were considered. Other decisions made during the determination of the kink distances included the following:

1. During Step 1, if the minimum residual range included an SRS point obtained from a straight line of the first three points, then not only was Step 2 conducted with the initial three points deleted, but also with the first one

and then the first two points deleted. For example, for Shot 4400, 0.7 to 0.9 μm bandpass (Appendix C, page 118), the minimum residual range occurred with the first three, four, and five points forming the first straight line. When the wake kink data points were curve fitted, there were five cases run; the first case included all the intensity decay data points less one, the second case--all points less two, and so forth, and the last case--all points less five.

2. In fitting the wake kink data (Step 2), in some cases the minimum residual range included an SRS point obtained from a straight line of the first three points, and in other cases this did not occur. When both occurrences happened for one shot and one bandpass, the kink distances obtained from straight lines from the first three points and sequential points were not considered, but rather, later kink distances were used. For example, for Shot 4810, 0.7 to 0.9 μm bandpass (Appendix C, page 149), the wake kink distance was to be determined from two cases; Case 1--all intensity decay data less six points, and Case 2--all intensity decay data less seven points. The SRS's of

these two cases are shown on Figure 20. The best initial straight lines (minimum SRS's) of Case 1 included ones comprised of the first three points and subsequent points (distance range 9.1 to 11.2 inches) and one comprised of the first 24 points (distance 18.4 inches). Case 2 resulted in the best initial straight lines being those comprised of the first 21 to 23 points (distance range 17.7 to 18.4 inches). The kink distances of 9.1 to 11.2 inches were not used, as they were deemed not to be representative minimums (there was not a decrease in residuals followed by an increase).

Once the kink distances were determined, the kink distance range was specified as such:

1. The minimum kink distance value was lowered to that value midway between it and the previous data point distance to yield a minimum possible kink distance.
2. The maximum kink distance value was increased to that value midway between it and the following data point distance to yield a maximum possible kink distance.
3. The minimum and maximum possible kink distances were averaged, and the mean value plus and

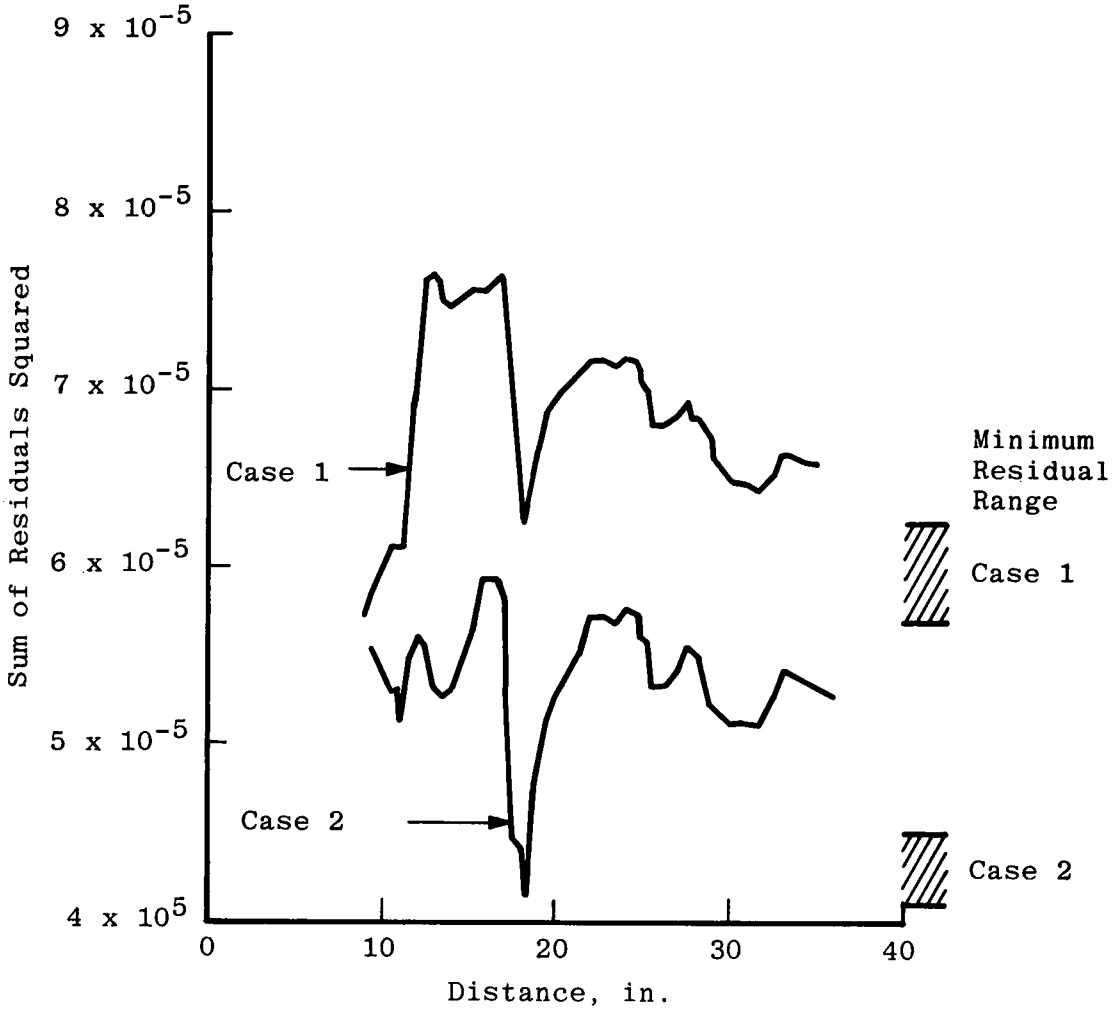


Figure 20. Shot 4810, 0.7 to 0.9 μm residuals.

minus the difference between the mean value and the maximum or minimum value was specified.

The kink distance, X_K, ranges are specified on Table V. In two cases, not all the visible radiometric data were recorded; in these cases the Step 1 curve fitting was not accomplished, and all the existing data points were deemed to be all wake kink data points, upon which only the Step 2 curve fitting was conducted. On Table V, Data Reduction Method 1 refers to the conduct of curve fitting Steps 1 and 2, and Data Reduction Method 2 refers to curve fitting Step 2 only.

To calculate the nose radius from the determined kink distance, X_K, the correlation theory equations of Chapter III, Section II, were used as such:

1. From the Bauer kink formula, Eq. (6),

$$r_1 = r_N = \frac{4.5\ X_K}{M_\infty^2} .$$

2. From the Textoris/Stankevics formula, Eq. (7),

$$r_2 = \frac{4.5\ X_K}{M_\infty^2} \frac{\psi}{\sqrt{C_{D_B}}} ,$$

where

$$\psi = \frac{r_N}{r_B} .$$

Table V. Visible Data, Log-Linear Plots

Shot No.	Radiometer Sta.	Bandpass (μm)	Data Reduction Method[a]	X_K (in.)	$r_c \pm \Delta r$(in.)			r_N (in.)	r_c(percent of r_N)		
					r_1	r_2	r_3		r_1	r_2	r_3
4232	1	0.5 to 0.7	1	18.8±0.9	.307±.015	.251±.012	.419±.020	.333	-7.8	-24.6	25.8
	1	0.7 to 0.8	1	19.3±0.5	.315±.008	.258±.007	.430±.011	.333	-5.4	-22.5	29.1
4271	1	0.5 to 0.7	1	15.4±0.7	.251±.011	.208±.009	.347±.016	.316	-20.6	-34.2	9.8
	1	0.7 to 0.8	1	15.4±1.0	.251±.016	.208±.014	.347±.023	.316	-20.6	-34.2	9.8
4398	1	0.5 to 0.7	1	11.3±2.1	.194±.036	.152±.028	.253±.047	.167	16.2	-9.0	51.5
	1	0.7 to 0.8	2	11.1±1.8	.190±.031	.149±.024	.249±.040	.167	13.8	-10.8	49.1
4400	1	0.5 to 0.7	1	18.4±6.2	.300±.101	.243±.082	.405±.136	.250	20.0	-2.8	62.0
	1	0.7 to 0.8	2	23.1±6.3	.377±.103	.305±.083	.508±.139	.250	50.8	22.0	103.2
	2	0.5 to 0.7	1	19.7±1.6	.351±.029	.280±.023	.467±.038	.250	40.4	12.0	86.8
	2	0.7 to 0.9	1	13.0±2.4	.231±.043	.185±.034	.309±.057	.250	-7.6	-26.0	23.6
4401	1	0.5 to 0.7	1	16.5±2.1	.273±.035	.222±.028	.370±.047	.316	-13.6	-29.7	17.1
4402	2	0.5 to 0.7	1	23.1±2.3	.411±.041	.327±.033	.545±.054	.316	30.0	3.4	72.5
	2	0.7 to 0.9	1	20.1±0.5	.358±.009	.284±.007	.473±.012	.316	13.3	-10.1	49.7
4403	1	0.5 to 0.7	1	17.4±2.2	.288±.036	.233±.029	.388±.049	.250	15.2	-6.8	55.2
	1	0.7 to 0.8	1	15.5±3.4	.256±.056	.207±.045	.345±.076	.250	2.4	-17.2	38.0
4498	1	0.5 to 0.7	1	21.3±3.9	.415±.076	.385±.070	.213±.039	.330	25.8	16.7	-35.5
	1	0.7 to 0.8	1	24.2±0.5	.471±.010	.437±.009	.243±.005	.330	42.7	32.4	-26.4
4500	1	0.5 to 0.7	1	16.9±0.3	.272±.005	.232±.004	.387±.007	.250	8.8	-7.2	54.8
	1	0.7 to 0.8	1	18.2±0.5	.293±.008	.250±.007	.416±.011	.250	17.2	0.0	66.4

Table V. (continued)

Shot No.	Radiometer Sta.	Bandpass (μm)	Data Reduction Method[a]	X_K (in.)	$r_c \pm \Delta r$ (in.)			r_N (in.)	r_c (percent of r_N)		
					r_1	r_2	r_3		r_1	r_2	r_3
4502	1	0.5 to 0.7	1	13.7±0.2	.216±.003	.175±.003	.292±.004	.250	-13.6	-30.0	16.8
	1	0.7 to 0.8	1	14.4±0.4	.227±.006	.184±.005	.307±.009	.250	-9.2	-26.4	22.8
4503	1	0.5 to 0.7	1	14.2±1.4	.226±.022	.185±.018	.308±.030	.250	-9.6	-26.0	23.2
	1	0.7 to 0.8	1	20.1±0.2	.320±.003	.263±.003	.438±.004	.250	28.0	5.2	75.2
	2	0.5 to 0.7	1	31.7±1.3	.544±.022	.442±.018	.737±.030	.250	117.6	76.8	194.8
4504	1	0.5 to 0.7	1	23.0±0.5	.385±.008	.298±.006	.497±.011	.167	130.5	78.4	197.6
	1	0.7 to 0.8	1	21.3±0.6	.356±.010	.277±.008	.461±.013	.167	113.2	65.9	176.0
4505	2	0.5 to 0.7	1	25.8±2.2	.437±.037	.358±.031	.597±.051	.316	38.3	13.3	88.9
	2	0.7 to 0.9	1	21.6±1.8	.366±.031	.299±.025	.498±.042	.316	15.8	-5.4	57.6
4506	1	0.5 to 0.7	1	11.4±0.8	.188±.013	.156±.011	.188±.013	.230	-18.3	-50.9	-18.3
	1	0.7 to 0.8	1	12.0±1.9	.198±.031	.164±.026	.198±.031	.230	-13.9	-48.3	-13.9
4657	1	0.5 to 0.7	1	13.2±1.5	.210±.024	.217±.025	.120±.014	.330	-36.4	-34.2	-63.6
	1	0.7 to 0.8	1	14.6±2.9	.233±.046	.240±.048	.133±.026	.330	-29.4	-27.3	-59.7
4659	1	0.5 to 0.7	1	24.4±0.6	.424±.010	.329±.008	.548±.013	.250	69.6	31.6	119.2
	1	0.7 to 0.8	1	28.2±1.3	.490±.023	.380±.018	.633±.029	.250	96.0	52.0	153.2
4660	1	0.7 to 0.8	1	15.3±0.7	.250±.011	.202±.009	.337±.015	.250	0.0	-19.2	34.8
4810	1	0.5 to 0.7	1	27.5±2.5	.444±.040	.337±.031	.562±.051	.250	77.6	34.8	124.8
	1	0.7 to 0.8	1	29.3±5.0	.473±.081	.359±.061	.598±.102	.250	89.2	43.6	139.2
	2	0.7 to 0.9	1	18.3±0.4	.322±.007	.239±.005	.398±.009	.250	28.8	-4.4	59.2

[a] 1: three straight line curve fits; 2: two straight line curve fits.

3. From the Heyda formula, Eq. (8),

$$r_3 = r_N = \frac{X_K}{0.4\ C_D^{1/2}\ M_\infty^2} .$$

By using the above nose radius equations and the X_K specified on Table V, the r_1, r_2, and r_3 values of Table V, under the "$r_c \pm \Delta r$(in.)" heading, were obtained.

III. INFRARED LOG-LINEAR PLOTTED DATA

The infrared radiometric data did not follow the intensity decay characteristics of the visible radiometric data. For the infrared data, a gradual wake decay occurred immediately following the initial body radiation decay (refer to Appendix C, page 114, distance about 4 inches); the visible data generally exhibited at least one additional intensity rise and decay between the body radiation decay and the gradual wake decay. The infrared wake data did exhibit the Figure 10, page 27, shape. Again, as with the visible data, the first task was to define the wake kink data points to be fitted to obtain the kink distance. Data Reduction Method 1, used for the visible data, was also used for the infrared data. Additionally, Data Reduction Method 2 was used for the infrared data; this meant that only a one-step method was used by which two straight lines were fitted to yield kink

distances. Table VI contains the kink distance results by both methods; also included are the nose radii calculations that were determined by the same equations that were used on the visible data.

IV. LOG-LOG PLOTTED DATA

The reduced radiometric data were also plotted with the radiation intensity data (J_{OBS}) on a log scale versus distance data (X) on a log scale. The log distance axis is a modification to the Bauer theory plot method. These data are given in Appendix D. The Appendix C data started at the model nosetip, whereas the Appendix D data start 1 inch after the model nosetip, so some body radiation is not shown. The intensity/distance data were curve fitted by the same methods and techniques that were used to curve fit the log-linear plotted data. Tables VII and VIII contain the visible and infrared data results, respectively.

V. DATA SUMMARY AND RESULTS

The calculated nose radius data presented in Tables V through VIII are summarized in Figures 21, 22, and 23, log-linear plotted data, and Figures 24, 25, and 26, log-log plotted data. A discussion of the figures follows, and the results are summarized in Table IX.

Table VI. Infrared Data, Log-Linear Plots

Shot No.	Radiometer Sta.	Bandpass (μm)	Data Reduction Method[a]	X_K (in.)	$r_c \pm \Delta r$ (in.)			r_N (in.)	r_c (percent of r_N)		
					r_1	r_2	r_3		r_1	r_2	r_3
4398	1	2.6 to 2.8	1	15.6±1.8	.267±.031	.209±.024	.348±.040	.167	59.9	25.1	108.4
	1	3.1 to 3.8	1	18.9±0.9	.324±.015	.254±.012	.423±.020	.167	94.0	52.1	153.3
4400	1	2.6 to 2.8	1	17.1±1.7	.268±.015	.217±.012	.362±.020	.250	7.2	-13.2	44.8
	1	3.1 to 3.8	1	28.1±2.0	.459±.033	.371±.026	.618±.044	.250	83.6	48.4	147.2
	2	2.6 to 2.8	1	15.7±0.4	.279±.007	.223±.006	.372±.009	.250	11.6	-10.8	48.8
	2	3.0 to 4.0	1	16.8±2.4	.299±.043	.239±.034	.398±.057	.250	19.6	-4.4	59.2
4402	2	2.6 to 2.8	1	14.8±1.8	.263±.032	.209±.025	.348±.042	.316	-16.8	-33.9	10.1
	2	3.0 to 4.0	1	23.9±2.0	.425±.036	.338±.028	.563±.047	.316	34.5	7.0	78.2
4498	1	2.6 to 2.8	1	10.7±1.7	.208±.033	.193±.031	.107±.017	.330	-37.0	-41.5	-67.6
	1	3.1 to 3.8	1	21.7±2.9	.423±.057	.393±.053	.218±.029	.330	28.2	19.1	-33.9
4500	1	2.6 to 2.8	1	11.1±1.1	.179±.018	.153±.015	.255±.025	.250	-28.4	-38.8	2.0
	1	3.1 to 3.8	1	14.2±1.8	.229±.029	.195±.025	.325±.041	.250	-8.4	-22.0	30.0
4502	1	2.6 to 2.8	1	14.6±3.7	.230±.058	.186±.047	.311±.079	.250	-8.0	-25.6	24.4
	1	3.1 to 3.8	1	18.7±1.7	.295±.027	.239±.022	.398±.036	.250	18.0	-4.4	59.2
4503	1	2.6 to 2.8	1	15.7±0.9	.250±.014	.205±.012	.342±.020	.250	0.0	-18.0	36.8
	1	3.1 to 3.8	1	27.0±1.9	.430±.030	.353±.025	.588±.041	.250	72.0	41.2	135.2
	2	2.6 to 2.8	1	21.0±0.9	.360±.015	.293±.013	.488±.021	.250	44.0	17.2	95.2
	2	3.0 to 4.0	1	23.6±2.2	.405±.038	.329±.031	.548±.051	.250	62.0	31.6	119.2
4504	1	2.6 to 2.8	1	10.5±2.5	.176±.042	.136±.032	.227±.054	.167	5.4	-18.6	35.9
	1	3.1 to 3.8	1	13.0±1.0	.218±.017	.169±.013	.282±.022	.167	30.5	1.2	68.9

Table VI. (continued)

Shot No.	Radiometer Sta.	Bandpass (μm)	Data Reduction Method[a]	X_K (in.)	$r_c \pm \Delta r$ (in.)			r_N (in.)	r_c (percent of r_N)		
					r_1	r_2	r_3		r_1	r_2	r_3
4505	2	2.6 to 2.8	1	13.9±0.3	.235±.005	.192±.004	.320±.007	.316	-25.6	-39.2	1.3
	2	3.0 to 4.0	1	24.4±1.8	.413±.030	.338±.025	.563±.042	.316	30.7	7.0	78.2
4506	1	2.6 to 2.8	1	10.5±1.8	.174±.030	.144±.025	.175±.030	.230	-24.3	-54.3	-23.9
	1	3.1 to 3.8	1	23.3±4.9	.385±.081	.319±.067	.385±.081	.230	67.4	38.6	67.4
4657	1	2.6 to 2.8	1	12.7±0.9	.202±.014	.209±.015	.116±.008	.330	-38.7	-36.7	-64.8
	1	3.1 to 3.8	1	13.0±2.5	.207±.040	.214±.041	.118±.023	.330	-37.3	-35.2	-64.2
4659	1	2.6 to 2.8	1	15.4±1.8	.268±.031	.208±.024	.346±.040	.250	7.2	-16.8	38.4
	1	3.1 to 3.8	1	22.1±0.9	.384±.016	.298±.012	.497±.020	.250	53.6	19.2	98.8
	2	2.6 to 2.8	1	16.3±0.4	.309±.008	.237±.006	.395±.010	.250	23.6	-5.2	58.0
	2	3.0 to 4.0	1	16.5±1.3	.313±.025	.239±.019	.398±.031	.250	25.2	-4.4	59.2
4660	1	2.6 to 2.8	1	21.0±1.4	.343±.023	.277±.018	.462±.031	.250	37.2	10.8	84.8
	1	3.1 to 3.8	1	23.2±0.9	.379±.015	.306±.012	.510±.020	.250	51.6	22.4	104.0
4810	1	2.6 to 2.8	1	18.1±3.9	.292±.063	.222±.048	.370±.080	.250	16.8	-11.2	48.0
	1	3.1 to 3.8	1	31.3±2.3	.505±.037	.384±.028	.639±.047	.250	102.0	53.6	155.6
	2	2.6 to 2.8	1	26.7±0.9	.469±.016	.349±.012	.582±.020	.250	87.6	39.6	136.8
	2	3.0 to 4.0	1	23.3±0.5	.409±.009	.304±.007	.507±.011	.250	63.6	21.6	102.8

Table VI. (continued)

Shot No.	Radiometer Sta.	Bandpass (μm)	Data Reduction Method[a]	X_K (in.)	$r_c \pm \Delta r$ (in.)			r_N (in.)	r_c (percent of r_N)		
					r_1	r_2	r_3		r_1	r_2	r_3
4398	1	2.6 to 2.8	2	6.3±0.5	.108±.009	.084±.007	.141±.011	.167	-35.3	-49.7	-15.6
	1	3.1 to 3.8	2	7.5±0.5	.129±.009	.101±.007	.168±.011	.167	-22.8	-39.5	0.6
4400	1	2.6 to 2.8	2	12.2±1.4	.199±.023	.161±.018	.269±.031	.250	-20.4	-35.6	7.6
	1	3.1 to 3.8	2	9.3±0.8	.152±.013	.123±.011	.205±.018	.250	-39.2	-50.8	-18.0
	2	2.6 to 2.8	2	9.2±0.9	.163±.016	.131±.013	.218±.021	.250	-34.8	-47.6	-12.8
	2	3.0 to 4.0	2	7.6±0.9	.135±.016	.108±.013	.180±.021	.250	-46.0	-56.8	-28.0
4402	2	2.6 to 2.8	2	11.3±1.7	.201±.030	.160±.024	.266±.040	.316	-36.4	-49.4	-15.8
	2	3.0 to 4.0	2	13.5±1.7	.240±.030	.191±.024	.318±.040	.316	-24.1	-39.6	0.6
4498	1	2.6 to 2.8	2	5.4±0.4	.105±.008	.032±.002	.054±.004	.330	-68.2	-90.3	-83.6
	1	3.1 to 3.8	2	4.4±0.4	.086±.008	.027±.002	.044±.004	.330	-73.9	-91.8	-86.7
4500	1	2.6 to 2.8	2	6.8±0.4	.110±.006	.094±.006	.156±.009	.250	-56.0	-62.4	-37.6
	1	3.1 to 3.8	2	6.9±0.5	.111±.008	.095±.007	.158±.012	.250	-55.6	-62.0	-36.8
4502	1	2.6 to 2.8	2	9.9±1.0	.156±.016	.126±.013	.211±.021	.250	-37.6	-49.6	-15.6
	1	3.1 to 3.8	2	10.9±1.7	.172±.027	.139±.022	.232±.036	.250	-31.2	-44.4	-7.2
4503	1	2.6 to 2.8	2	10.3±0.8	.164±.013	.134±.010	.224±.017	.250	-34.4	-46.4	-10.4
	1	3.1 to 3.8	2	15.0±0.9	.239±.014	.196±.012	.327±.020	.250	-4.4	-21.6	30.8
	2	2.6 to 2.8	2	10.8±1.1	.185±.019	.151±.015	.251±.026	.250	-26.0	-39.6	0.4
	2	3.0 to 4.0	2	17.5±3.1	.300±.053	.244±.043	.406±.072	.250	20.0	-2.4	62.4
4504	1	2.6 to 2.8	2	7.2±0.8	.121±.013	.093±.010	.156±.017	.167	-27.5	-44.3	-6.6
	1	3.1 to 3.8	2	9.2±1.0	.154±.017	.120±.013	.200±.022	.167	-7.8	-28.1	19.8

Table VI. (continued)

Shot No.	Radiometer Sta.	Bandpass (μm)	Data Reduction Method[a]	X_K (in.)	$r_c \pm \Delta r$(in.)			r_N (in.)	r_c(percent of r_N)		
					r_1	r_2	r_3		r_1	r_2	r_3
4505	2	2.6 to 2.8	2	9.7±0.4	.164±.007	.134±.006	.223±.009	.316	-48.1	-57.6	-29.4
	2	3.0 to 4.0	2	18.2±0.9	.308±.015	.252±.012	.420±.021	.316	-2.5	-20.3	32.9
4506	1	2.6 to 2.8	2	5.5±0.5	.091±.008	.055±.005	.092±.008	.230	-60.4	-67.4	-60.0
	1	3.1 to 3.8	2	5.4±0.4	.089±.007	.054±.004	.089±.007	.230	-61.3	-67.8	-61.3
4657	1	2.6 to 2.8	2	9.9±1.9	.177±.034	.137±.026	.229±.044	.330	-46.4	-58.5	-30.6
	1	3.1 to 3.8	2	8.3±1.1	.226±.030	.175±.023	.292±.039	.330	-31.5	-47.0	-11.5
4659	1	2.6 to 2.8	2	10.6±1.3	.184±.023	.143±.018	.238±.029	.250	-26.4	-42.8	-4.8
	1	3.1 to 3.8	2	13.0±1.3	.226±.023	.175±.018	.292±.029	.250	-9.6	-30.0	16.8
	2	2.6 to 2.8	2	10.9±0.9	.207±.017	.158±.013	.264±.022	.250	-17.2	-36.8	5.6
	2	3.0 to 4.0	2	8.1±0.4	.154±.008	.117±.006	.195±.010	.250	-38.4	-53.2	-22.0
4660	1	2.6 to 2.8	2	11.8±0.2	.193±.003	.156±.003	.260±.004	.250	-22.8	-37.6	4.0
	1	3.1 to 3.8	2	11.0±0.5	.180±.008	.145±.007	.242±.011	.250	-28.0	-42.0	-3.2
4810	1	2.6 to 2.8	2	7.8±0.5	.126±.008	.096±.006	.159±.010	.250	-49.6	-61.6	-36.4
	1	3.1 to 3.8	2	12.3±0.8	.199±.013	.151±.010	.251±.016	.250	-20.4	-39.6	0.4
	2	2.6 to 2.8	2	13.6±0.9	.239±.016	.178±.012	.296±.020	.250	-4.4	-28.8	18.4
	2	3.0 to 4.0	2	14.0±1.0	.246±.018	.183±.013	.304±.022	.250	-1.6	-26.8	21.6

[a] 1: three straight line curve fits; 2: two straight line curve fits.

Table VII. Visible Data, Log-Log Plots

Shot No.	Radiometer Sta.	Bandpass (μm)	Data Reduction Method[a]	X_K (in.)	$r_c \pm \Delta r$(in.)			r_N (in.)	r_c(percent of r_N)		
					r_1	r_2	r_3		r_1	r_2	r_3
4232	1	0.5 to 0.7	1	14.8±0.6	.242±.010	.198±.008	.330±.013	.333	-27.3	-40.5	-0.9
	1	0.7 to 0.8	1	19.3±0.5	.315±.008	.258±.007	.430±.011	.333	-5.4	-22.5	29.1
4271	1	0.5 to 0.7	1	22.0±0.9	.359±.015	.297±.012	.495±.020	.316	13.6	-6.0	56.6
	1	0.7 to 0.8	1	14.7±1.8	.240±.029	.199±.024	.332±.041	.316	-24.1	-37.0	5.1
4398	1	0.5 to 0.7	1	22.4±0.5	.384±.009	.301±.007	.502±.011	.167	129.9	80.2	200.6
	1	0.7 to 0.8	2	25.5±3.9	.437±.067	.343±.052	.571±.087	.167	161.7	105.4	241.9
4400	1	0.5 to 0.7	1	17.0±3.7	.277±.060	.150±.033	.250±.054	.250	10.8	-40.0	0.0
	1	0.7 to 0.8	2	16.3±2.5	.266±.041	.215±.033	.359±.055	.250	6.4	-14.0	43.6
	2	0.5 to 0.7	1	10.2±0.7	.182±.012	.145±.010	.242±.017	.250	-27.2	-42.0	-3.2
	2	0.7 to 0.9	1	13.0±2.4	.231±.043	.185±.034	.308±.057	.250	-7.6	-26.0	23.2
4401	1	0.5 to 0.7	1	18.7±1.4	.309±.023	.251±.019	.418±.031	.316	-2.2	-20.6	32.3
4402	2	0.5 to 0.7	1	22.5±1.7	.400±.030	.318±.024	.530±.040	.316	26.6	0.6	67.7
	2	0.7 to 0.9	1	12.4±1.0	.221±.018	.176±.014	.293±.024	.316	-30.0	-44.3	-7.2
4403	1	0.5 to 0.7	1	17.6±1.9	.291±.031	.235±.025	.392±.042	.250	16.4	-6.0	56.8
	1	0.7 to 0.8	1	17.8±1.2	.294±.020	.238±.016	.397±.027	.250	17.6	-4.8	58.8
4498	1	0.5 to 0.7	1	12.1±0.6	.236±.012	.219±.011	.122±.006	.330	-28.5	-33.6	-63.0
	1	0.7 to 0.8	1	24.2±0.5	.471±.010	.438±.009	.243±.005	.330	42.7	32.7	-26.4
4500	1	0.5 to 0.7	1	17.6±0.4	.284±.006	.242±.006	.404±.009	.250	13.6	-3.2	61.6
	1	0.7 to 0.8	1	19.3±0.5	.311±.008	.266±.007	.443±.011	.250	24.4	6.4	77.2

Table VII. (continued)

Shot No.	Radiometer Sta.	Bandpass (μm)	Data Reduction Method[a]	X_K (in.)	$r_c \pm \Delta r$ (in.)			r_N (in.)	r_c (percent of r_N)		
					r_1	r_2	r_3		r_1	r_2	r_3
4502	1	0.5 to 0.7	1	16.7±0.6	.263±.009	.213±.008	.355±.013	.250	5.2	-14.8	42.0
	1	0.7 to 0.8	1	16.9±0.5	.266±.008	.216±.006	.360±.011	.250	6.4	-13.6	44.0
4503	1	0.5 to 0.7	1	22.0±1.4	.351±.022	.288±.018	.480±.031	.250	40.4	15.2	92.0
	1	0.7 to 0.8	1	14.4±0.6	.230±.010	.189±.008	.315±.013	.250	-8.0	-24.4	26.0
	2	0.5 to 0.7	1	32.1±0.5	.550±.009	.447±.007	.745±.012	.250	120.0	78.8	198.0
4504	1	0.5 to 0.7	1	10.2±0.3	.171±.005	.133±.004	.222±.007	.167	2.4	-20.4	32.9
	1	0.7 to 0.8	1	10.0±0.4	.167±.007	.129±.005	.215±.009	.167	0.0	-22.8	28.7
4505	2	0.5 to 0.7	1	20.4±0.5	.346±.008	.283±.007	.472±.012	.316	9.5	-10.5	49.4
	2	0.7 to 0.9	1	19.3±1.1	.327±.019	.268±.015	.447±.025	.316	3.5	-15.2	41.5
4506	1	0.5 to 0.7	1	7.9±1.0	.131±.017	.108±.014	.129±.016	.230	-43.0	-53.0	-43.9
	1	0.7 to 0.8	1	19.7±2.3	.326±.038	.271±.032	.327±.038	.230	41.7	17.8	42.2
4657	1	0.5 to 0.7	1	16.1±2.0	.257±.032	.267±.033	.148±.018	.330	-22.1	-19.1	-55.2
	1	0.7 to 0.8	2	17.6±1.0	.281±.016	.290±.016	.161±.009	.330	-14.8	-12.1	-51.2

Table VII. (continued)

Shot No.	Radiometer Sta.	Bandpass (μm)	Data Reduction Method[a]	X_K (in.)	$r_c \pm \Delta r$(in.)			r_N (in.)	r_c(percent of r_N)		
					r_1	r_2	r_3		r_1	r_2	r_3
4659	1	0.5 to 0.7	1	18.4±3.7	.319±.064	.247±.050	.412±.083	.250	27.6	-1.2	64.8
	1	0.7 to 0.8	1	17.6±1.9	.306±.033	.237±.026	.395±.043	.250	22.4	-5.2	58.0
4660	1	0.7 to 0.8	1	19.2±0.7	.314±.011	.254±.009	.423±.015	.250	25.6	1.6	69.2
4810	1	0.5 to 0.7	1	16.4±1.4	.265±.023	.201±.017	.335±.029	.250	6.0	-19.6	34.0
	1	0.7 to 0.8	1	22.2±2.9	.358±.047	.272±.036	.453±.059	.250	43.2	8.8	81.2
	2	0.7 to 0.9	1	19.8±2.3	.348±.040	.258±.030	.431±.050	.250	39.2	3.2	72.4

[a] 1: three straight line curve fits; 2: two straight line curve fits.

Table VIII. Infrared Data, Log-Log Plots

Shot No.	Radiometer Sta.	Bandpass (μm)	Data Reduction Method[a]	X_K (in.)	$r_c \pm \Delta r$(in.)			r_N (in.)	r_c(percent of r_N)		
					r_1	r_2	r_3		r_1	r_2	r_3
4398	1	2.6 to 2.8	1	22.9±0.7	.392±.012	.307±.007	.511±.016	.167	134.7	83.8	206.0
4400	1	2.6 to 2.8	1	26.5±2.7	.433±.044	.350±.036	.583±.059	.250	73.2	40.0	133.2
	1	3.1 to 3.8	1	26.0±1.2	.425±.020	.344±.016	.573±.026	.250	70.0	37.6	129.2
	2	2.6 to 2.8	1	11.3±0.4	.201±.007	.161±.006	.268±.009	.250	-19.6	-35.6	7.2
	2	3.0 to 4.0	1	8.3±1.6	.148±.029	.118±.023	.197±.038	.250	-40.8	-52.8	-21.2
4402	2	2.6 to 2.8	1	15.6±2.7	.278±.048	.221±.038	.368±.064	.316	-12.0	-30.0	16.5
	2	3.0 to 4.0	1	26.9±1.0	.479±.018	.381±.014	.635±.024	.316	57.6	20.6	100.9
4498	1	2.6 to 2.8	1	10.2±2.9	.199±.057	.186±.053	.103±.029	.330	-39.7	-43.6	-68.8
	1	3.1 to 3.8	1	19.2±1.2	.374±.023	.348±.022	.193±.012	.330	13.3	5.5	-41.5
4500	1	2.6 to 2.8	1	11.1±1.1	.179±.018	.153±.015	.255±.025	.250	-28.4	-38.8	2.0
	1	3.1 to 3.8	1	22.7±2.3	.366±.037	.312±.032	.520±.053	.250	46.4	24.8	108.0
4502	1	2.6 to 2.8	1	15.5±2.8	.244±.044	.198±.036	.330±.060	.250	-2.4	-20.8	32.0
	1	3.1 to 318	1	20.4±0.9	.321±.014	.260±.011	.433±.019	.250	28.4	4.0	73.2
4503	1	2.6 to 2.8	1	15.6±2.7	.249±.043	.204±.035	.340±.059	.250	-0.4	-18.4	36.0
	1	3.1 to 3.8	1	11.8±0.8	.188±.013	.154±.010	.257±.017	.250	-24.8	-38.4	2.8
	2	2.6 to 2.8	1	26.9±2.3	.461±.039	.375±.032	.625±.053	.250	84.4	50.0	150.0
4504	1	2.6 to 2.8	1	15.2±0.8	.254±.013	.197±.010	.328±.017	.167	52.1	18.0	96.4

Table VIII. (continued)

Shot No.	Radiometer Sta.	Bandpass (μm)	Data Reduction Method[a]	X_K (in.)	$r_c \pm \Delta r$ (in.)			r_N (in.)	r_c (percent of r_N)		
					r_1	r_2	r_3		r_1	r_2	r_3
4505	2	2.6 to 2.8	1	21.9±0.4	.371±.007	.304±.006	.507±.009	.316	17.4	-3.8	60.4
	2	3.0 to 4.0	1	24.4±1.8	.413±.030	.338±.025	.563±.042	.316	30.7	7.0	78.2
4506	1	2.6 to 2.8	1	22.1±2.7	.365±.045	.303±.037	.365±.045	.230	58.7	31.7	58.7
	1	3.1 to 3.8	1	11.7±1.4	.193±.023	.160±.019	.193±.023	.230	-16.1	-30.4	-16.1
4657	1	2.6 to 2.8	1	10.4±0.5	.166±.024	.172±.025	.095±.014	.330	-49.7	-47.9	-71.2
	1	3.1 to 3.8	1	19.3±1.2	.308±.019	.318±.020	.177±.011	.330	-6.7	-3.6	-46.4
4659	1	2.6 to 2.8	1	29.9±3.1	.520±.054	.402±.042	.670±.069	.250	108.0	60.8	168.0
	1	3.1 to 3.8	1	21.2±0.9	.368±.016	.285±.028	.475±.020	.250	47.2	14.0	90.0
	2	2.6 to 2.8	1	16.3±0.4	.309±.008	.236±.006	.393±.010	.250	23.6	-5.6	57.2
	2	3.0 to 4.0	1	18.1±2.1	.343±.040	.262±.030	.437±.051	.250	37.2	4.8	74.8
4660	1	2.6 to 2.8	1	12.5±2.7	.204±.044	.165±.036	.275±.059	.250	-18.4	-34.0	10.0
	1	3.1 to 3.8	1	23.2±0.9	.379±.015	.306±.012	.510±.020	.250	51.6	22.4	104.0
4810	1	2.6 to 2.8	1	17.9±5.0	.289±.081	.219±.061	.365±.102	.250	15.6	-12.4	46.0
	1	3.1 to 3.8	1	17.6±2.1	.284±.034	.215±.026	.358±.043	.250	13.6	-14.0	43.2
	2	2.6 to 2.8	1	28.0±0.5	.492±.009	.366±.007	.610±.011	.250	96.8	46.4	144.0
	2	3.0 to 4.0	1	22.9±0.9	.426±.039	.317±.029	.528±.048	.250	70.4	26.8	111.2

Table VIII. (continued)

Shot No.	Radiometer Sta.	Bandpass (μm)	Data Reduction Method[a]	X_K (in.)	$r_c \pm \Delta r$ (in.)			r_N (in.)	r_c (percent of r_N)		
					r_1	r_2	r_3		r_1	r_2	r_3
4398	1	2.6 to 2.8	2	6.3±0.5	.108±.009	.084±.007	.141±.011	.167	-35.3	-49.7	-15.6
	1	3.1 to 3.8	2	25.2±1.8	.435±.031	.342±.024	.569±.041	.167	160.5	104.8	240.7
4400	1	2.6 to 2.8	2	16.9±3.4	.276±.056	.223±.045	.372±.075	.250	10.4	-10.8	48.8
	1	3.1 to 3.8	2	12.9±1.1	.211±.018	.171±.015	.284±.021	.250	-15.6	-31.6	13.6
	2	2.6 to 2.8	2	8.7±0.5	.155±.009	.124±.007	.206±.012	.250	-38.0	-50.4	-17.6
	2	3.0 to 4.0	2	6.3±0.4	.112±.007	.090±.006	.150±.010	.250	-55.2	-64.0	-40.0
4402	2	2.6 to 2.8	2	11.3±1.7	.201±.030	.160±.024	.267±.040	.316	-36.4	-49.4	-15.5
	2	3.0 to 4.0	2	14.3±2.5	.255±.045	.203±.035	.338±.059	.316	-19.3	-35.8	7.0
4498	1	2.6 to 2.8	2	5.8±0.8	.113±.016	.106±.015	.059±.008	.330	-65.8	-67.9	-82.1
	1	3.1 to 3.8	2	3.6±0.4	.070±.008	.065±.007	.036±.004	.330	-78.8	-80.3	-89.1
4500	1	2.6 to 2.8	2	6.8±0.4	.110±.006	.094±.006	.156±.009	.250	-56.0	-62.4	-37.6
	1	3.1 to 3.8	2	14.6±1.4	.235±.023	.201±.019	.334±.032	.250	-6.0	-19.6	33.6
4502	1	2.6 to 2.8	2	9.9±1.0	.156±.028	.126±.023	.211±.038	.250	-37.6	-49.6	-15.6
	1	3.1 to 3.8	2	10.6±0.7	.167±.011	.135±.009	.225±.015	.250	-33.2	-46.0	-10.0
4503	1	2.6 to 2.8	2	9.5±1.5	.152±.024	.124±.020	.207±.033	.250	-39.2	-50.4	-17.2
	1	3.1 to 3.8	2	6.2±0.2	.099±.003	.081±.003	.135±.004	.250	-60.4	-67.6	-46.0
	2	2.6 to 2.8	2	15.0±1.0	.257±.017	.209±.014	.349±.023	.250	2.8	-16.4	39.6
	2	3.0 to 4.0	2	25.1±1.9	.430±.033	.350±.026	.503±.044	.250	72.0	40.0	133.2
4504	1	2.6 to 2.8	2	10.6±0.9	.177±.015	.137±.012	.229±.019	.167	6.0	-18.0	37.1
	1	3.1 to 3.8	2	23.1±4.0	.386±.067	.300±.052	.500±.087	.167	131.1	79.6	199.4

Table VIII. (continued)

Shot No.	Radiometer Sta.	Bandpass (μm)	Data Reduction Method[a]	X_K (in.)	$r_c \pm \Delta r$ (in.)			r_N (in.)	r_c (percent of r_N)		
					r_1	r_2	r_3		r_1	r_2	r_3
4505	2	2.6 to 2.8	2	13.9±0.3	.235±.005	.193±.004	.322±.007	.317	-25.6	-38.9	1.9
	2	3.0 to 4.0	2	16.4±0.9	.278±.015	.227±.012	.378±.021	.316	-12.0	-28.2	19.6
4506	1	2.6 to 2.8	2	5.9±1.0	.097±.016	.081±.014	.097±.016	.230	-57.8	-64.8	-57.8
	1	3.1 to 3.8	2	7.2±0.5	.119±.003	.098±.007	.119±.003	.230	-48.3	-57.4	-48.3
4657	1	2.6 to 2.8	2	10.4±5.0	.166±.080	.172±.083	.095±.046	.330	-49.7	-47.9	-71.2
	1	3.1 to 3.8	2	5.4±0.9	.086±.014	.089±.015	.050±.008	.330	-73.9	-73.0	-84.8
4659	1	2.6 to 2.8	2	11.9±1.7	.207±.030	.160±.023	.267±.038	.250	-17.2	-36.0	6.8
	1	3.1 to 3.8	2	10.8±0.9	.187±.016	.145±.012	.242±.020	.250	-25.2	-42.0	-3.2
	2	2.6 to 2.8	2	11.8±0.8	.224±.015	.171±.012	.285±.019	.250	-10.4	-31.6	14.0
	2	3.0 to 4.0	2	7.7±0.8	.146±.015	.111±.012	.186±.019	.250	-41.6	-55.6	-25.6
4660	1	2.6 to 2.8	2	7.5±1.4	.122±.023	.099±.018	.165±.031	.250	-51.2	-60.4	-34.0
	1	3.1 to 3.8	2	12.6±3.4	.206±.056	.166±.045	.277±.075	.250	-17.6	-33.6	10.8
4810	1	2.6 to 2.8	2	8.1±0.7	.131±.011	.099±.009	.165±.014	.250	-47.6	-60.4	-34.0
	1	3.1 to 3.8	2	14.7±0.9	.237±.015	.180±.011	.299±.018	.250	-5.2	-28.0	19.6
	2	2.6 to 2.8	2	21.0±0.4	.369±.007	.275±.005	.458±.009	.250	47.6	10.0	83.2
	2	3.0 to 4.0	2	16.8±3.5	.296±.062	.220±.046	.367±.026	.250	18.4	-12.0	46.8

[a] 1: three straight line curve fits; 2: two straight line curve fits.

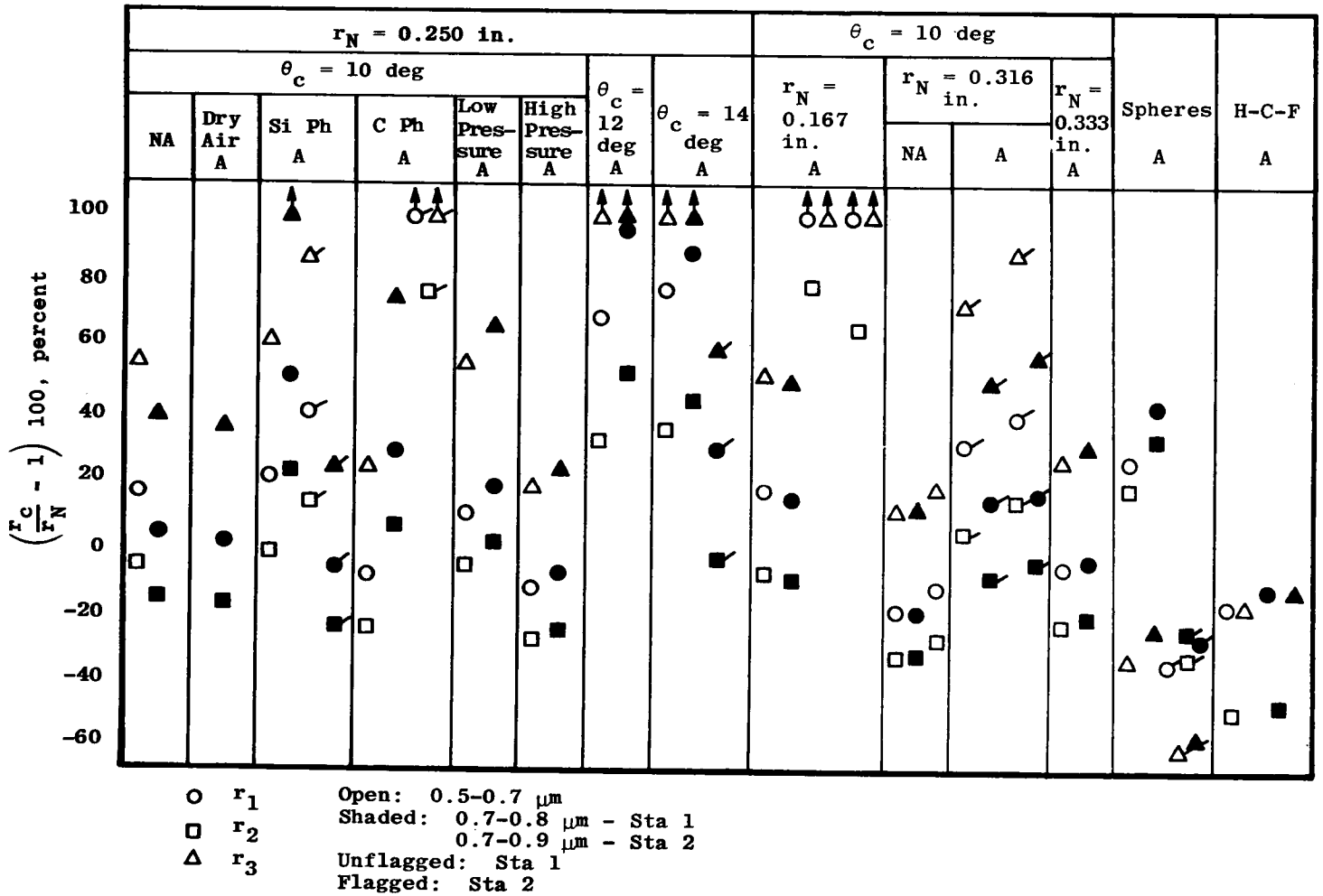


Figure 21. Visible data summary, log-linear plots.

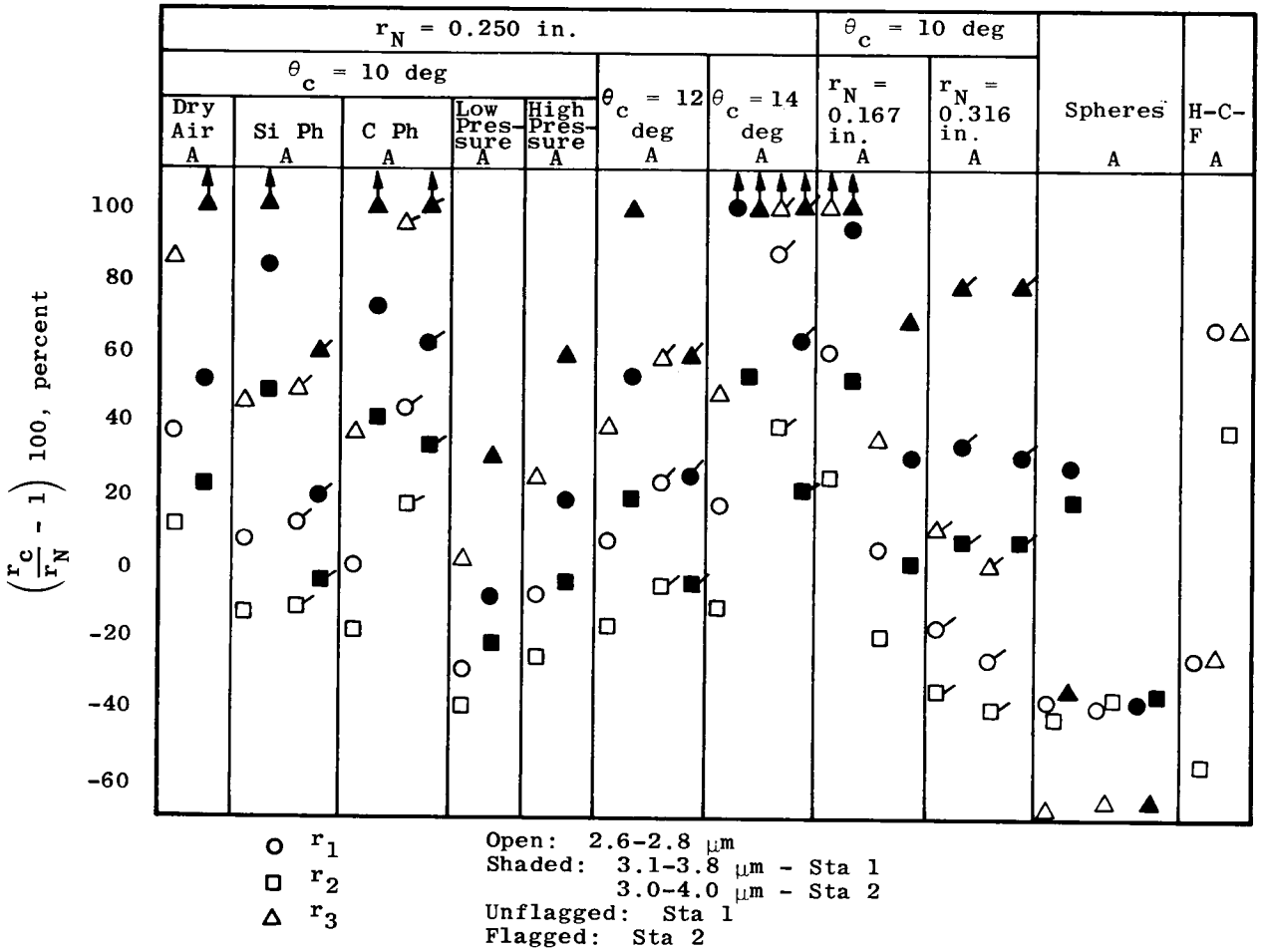


Figure 22. Infrared data summary, Method 1, log-linear plots.

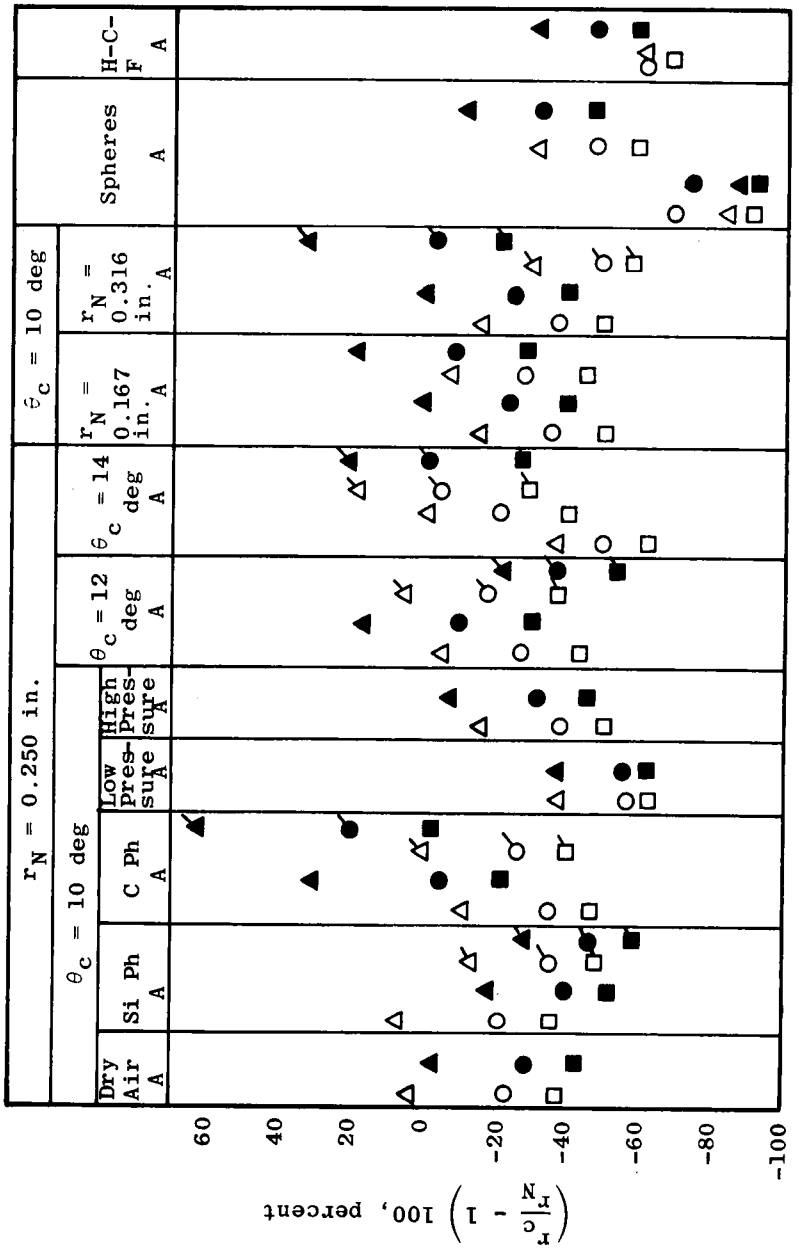


Figure 23. Infrared data summary, Method 2, log-linear plots.

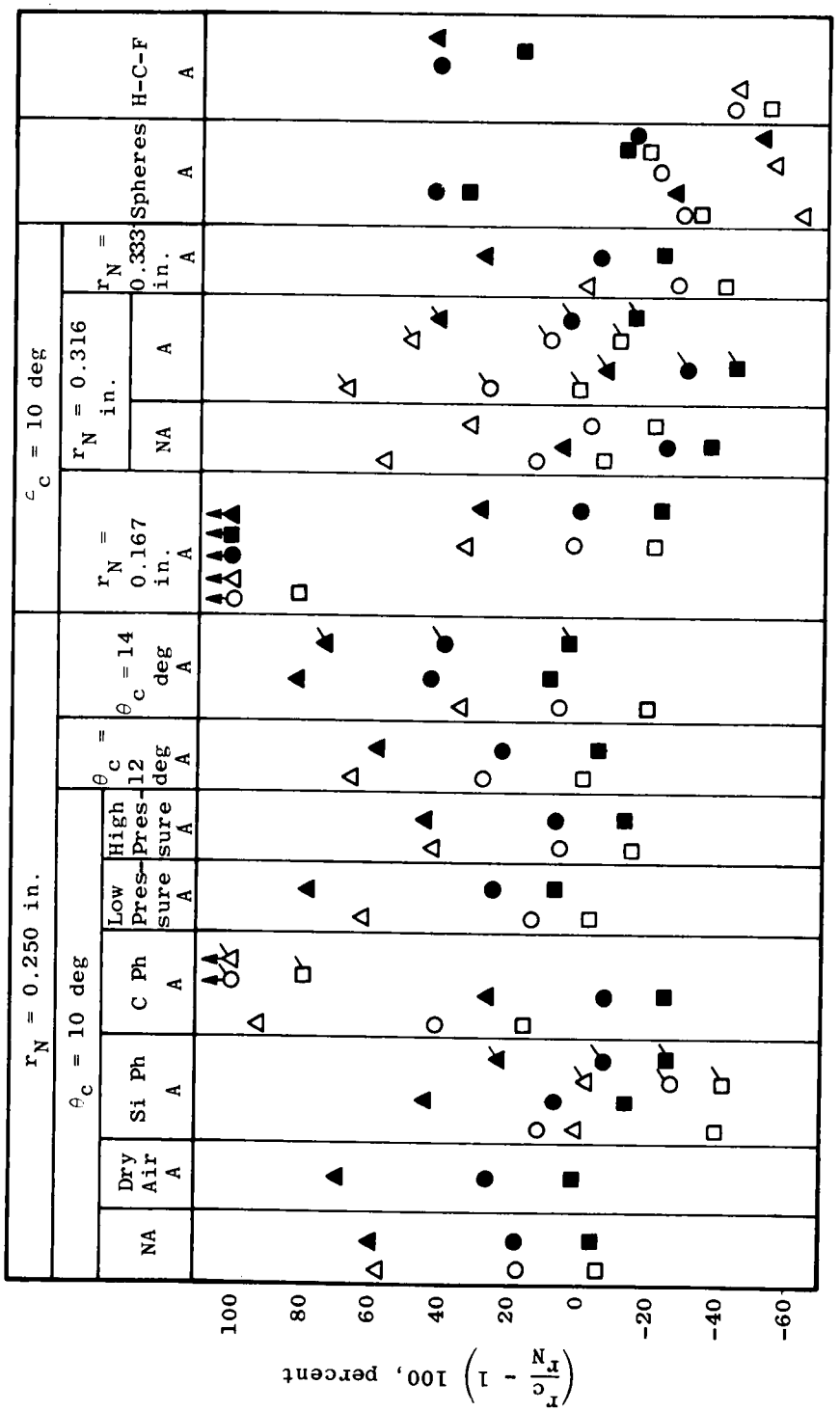


Figure 24. Visible data summary, log-log plots.

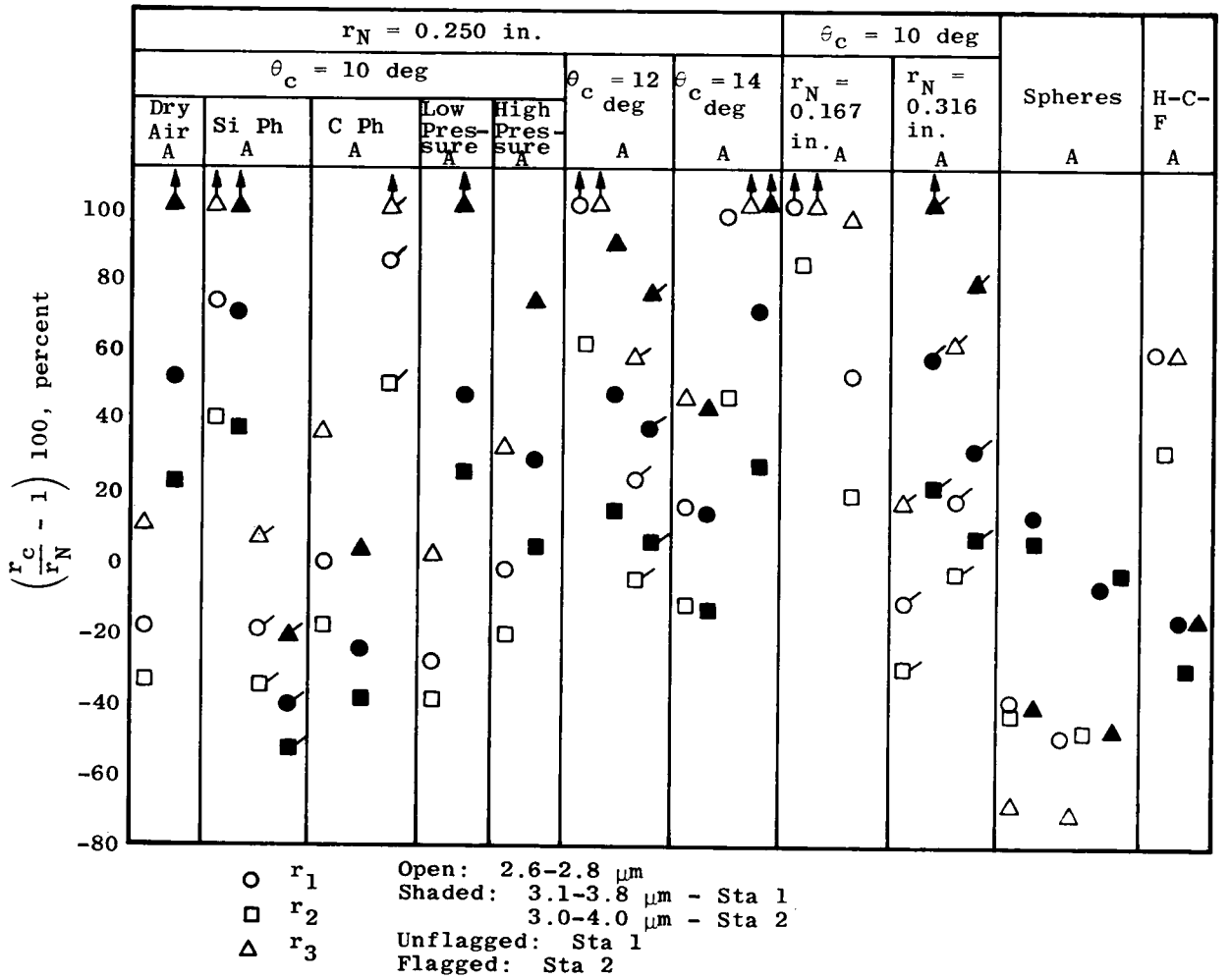


Figure 25. Infrared data summary, Method 1, log-log plots.

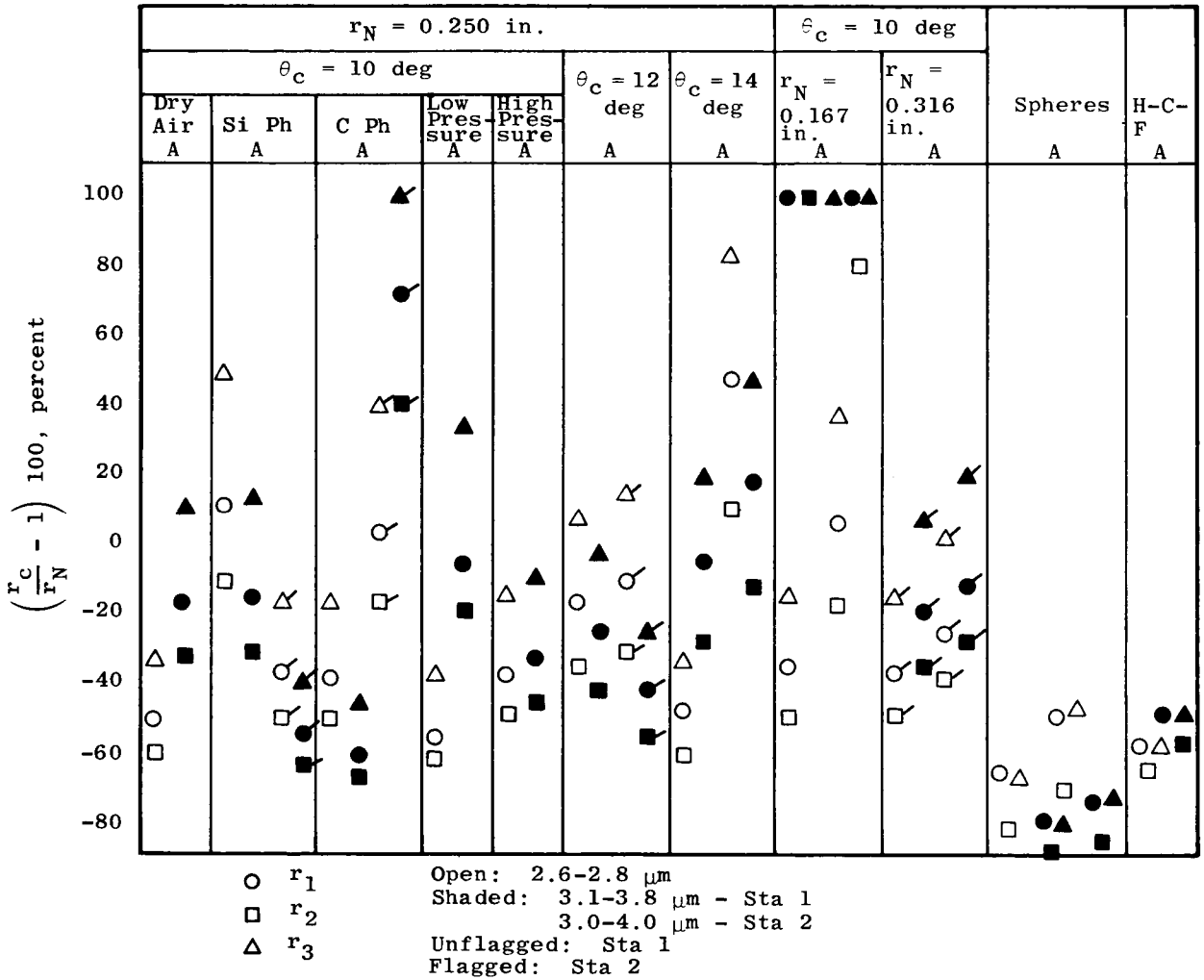


Figure 26. Infrared data summary, Method 2, log-log plots.

Table IX. Data Summary

Wavelength Regime	Plotted Data	Data Reduction Method[a]	Ref. Figure	Model Category	$\left\|\frac{r_c}{r_N} - 1\right\| 100 \leq 30\%$ (% of cases) r_1	r_2	r_3	1σ (% of 0.25) r_1	r_2	r_3
Visible	Log-Linear	1	21	A	68	66	32	--	--	--
				B	63	74	21	51	30	91
				C	79	93	31	38	27	76
Infrared	Log-Linear	1	22	A	47	61	17	--	--	--
				B	55	71	21	48	26	87
				C	57	73	14	41	26	83
Infrared	Log-Linear	2	23	A	47	11	69	--	--	--
				B	55	23	77	32	44	24
				C	43	14	71	35	45	26
				D	57	23	80	--	--	--
Visible	Log-Log	1	24	A	76	71	26	--	--	--
				B	79	84	21	37	25	71
Infrared	Log-Log	1	25	A	45	55	21	--	--	--
				B	48	52	24	52	33	90
Infrared	Log-Log	2	26	A	39	22	44	--	--	--
				B	45	27	50	38	44	40
				D	47	27	53	--	--	--

[a] 1: three straight line curve fits; 2: two straight line curve fits.

1. Figure 21: Visible log-linear plotted data.

   a. All data (Case A):

      Bauer's theory (r_1 calculation) and the Textoris and Stankevics theory (r_2 calculation) result in a calculated nose radius that is within ±30 percent of the actual nose radius in about two-thirds of the cases. It is to be noted that the r_1 calculated nose radii are high for the 12-degree and 14-degree cases, and r_1 and r_2 are high for the 0.167-inch r_N case.

   b. Data from 0.250-inch r_N (Case B):

      The r_1 and r_2 calculations predict r_N with ±30 percent in 63 percent and 74 percent of the cases, respectively. A one-sigma (1σ) calculation determined that the r_1 calculation predicts r_N within ±51 percent in 67 percent of the time, whereas the r_2 calculation predicts r_N within ±30 percent in 67 percent of the time.

   c. Data from 0.250-inch r_N, θ_c = 10 degrees (Case C):

      The r_1 and r_2 calculations predict r_N within ±30 percent in 79 percent and 93 percent of the cases, respectively. The

r_1 and r_2 calculations predict r_N with a 1σ band (67 percent of the time) within ±38 percent and ±27 percent, respectively. Even though deletion of the 12-degree and 14-degree cases caused the r_2 calculations to predict r_N ±30 percent in significantly more cases (93 percent versus 74 percent), the 1σ value of r_N was not improved much (27 percent versus 30 percent).

2. Figure 22: Infrared log linear plotted data, Data Reduction Method 1.

   a. All data (Case A):

      The r_2 calculation predicts r_N ±30 percent in 61 percent of the time. The r_1 calculations are high for the 14-degree case.

   b. Data from 0.250-inch r_N (Case B):

      The r_1 and r_2 calculations improve somewhat from Case A and predict r_N ±30 percent in 55 percent and 71 percent of the time. The 1σ values again show that the r_2 calculation (r_N ±26 percent in 67 percent of the time) predicts better than r_1 (r_N ±48 percent in 67 percent of the time).

c. Data from 0.250-inch r_N, θ_c = 10 degrees (Case C):

The r_1 and r_2 calculations predict r_N about the same as Case B.

3. Figure 23: Infrared log linear plotted data, Data Reduction Method 2.

a. All data (Case A):

Heyda's theory (r_3 calculation) predicts r_N ±30 percent in 69 percent of the time. Nose radii calculations are generally low for the low-pressure, spheres, and H-C-F cases.

b. Data from 0.250-inch r_N (Case B):

The r_3 calculations improve somewhat from the Case A ones and predict r_N ±30 percent in 77 percent of the time. The 1σ calculation gives r_N ±24 percent in 67 percent of the time. The r_1 calculations are not as good as those of the r_3; they predict r_N ±30 percent in little more than half the time, but the 1σ calculation gives r_N ±32 percent in 67 percent of the time, which is good.

c. Data from 0.250-inch r_N, θ_c = 10 degrees (Case C):

The r_3 and r_1 calculations predict r_N a little worse than Case B, but still good.

d. All data less the spheres and H-C-F (Case D):

The r_3 and r_1 predictions of r_N ±30 percent improved somewhat over Case C; they are essentially the same as Case B. Because of the different nose radii involved, the 1σ calculations were not made.

4. Figure 24: Visible log-log plotted data.

a. All data (Case A):

The r_1 and r_2 calculations predict r_N ±30 percent in 76 percent and 71 percent of the time, respectively. The 0.167-inch r_N data are high, as they were for the visible log-linear plotted data.

b. Data from 0.250-inch r_N (Case B):

The r_1 and r_2 predictions of r_N ±30 percent are about the same as Case A. The 1σ calculations show the r_2 calculations to be better than those of r_1, as r_2 predicts r_N ±25 percent in 67 percent of the time, whereas r_1 predicts r_N ±37 percent in that time.

5. Figure 25: Infrared log-log plotted data, Data Reduction Method 1.

   a. All data (Case A):

      The r_2 prediction is best, as it calculates r_N ±30 percent in 55 percent of the time.

   b. Data from 0.250-inch r_N (Case B):

      The r_2 prediction calculates r_N ±30 percent a little better than r_1 does, 52 percent of the time compared to 48 percent; however, r_2 predicts r_N ±33 percent in 67 percent of the time, whereas r_1 predicts r_N ±52 percent in that time.

6. Figure 26: Infrared log-log plotted data, Data Reduction Method 2.

   a. All data (Case A):

      None of the nose radii calculations predict r_N ±30 percent more than half the time. The sphere and H-C-F nose radii calculations are all low.

   b. Data from 0.250-inch r_N (Case B):

      Again, no calculations predict r_N ±30 percent more than half the time. The r_1 calculations are best in that they predict r_N ±38 percent in 67 percent of the time.

c. All data less the spheres and H-C-F (Case D):

The r_3 calculations predict r_N ±30 percent more than half the time (53 percent), but this is still not good.

CHAPTER V

CONCLUSIONS AND RECOMMENDATIONS

The nose radii of blunted reentry vehicles were calculated by curve fitting radiometric wake data and using equations from existing theories. The calculated nose radii were compared to the actual nose radii, and the conclusions from the study are:

1. Textoris' and Stankevics' modification to Bauer's Kink theory predicted the actual nose radius very well from both visible and infrared data, when the data were fitted by three straight lines. The kink distance used was derived from fitting log intensity versus distance data. For the 0.250-inch nose radius, the nose radius calculation predicted the actual nose radius within 30 percent in 67 percent of the time.
2. When the data were curve fitted as log intensity versus log distance, which is a modification to Bauer's method for determining kink distance, again, very good results were obtained from Textoris' and Stankevics' predictions, for three straight line fits. For r_N = 0.250 inch, r_2 predicted r_N ±33 percent in 67 percent of the time. The log-log plotted

data gave slightly better results with visible data, whereas the reverse was true for infrared data.

3. Heyda's modification to Bauer's Kink theory gave very good predictions with infrared log-linear plotted data, and it gave fair-to-good predictions with infrared log-log plotted data, when the infrared data were curve fitted with two straight lines. For r_N = 0.250 inch, r_3 predicted r_N ±26 percent in 67 percent of the time for log-linear plotted data, and r_N ±40 percent in 67 percent of the time for log-log plotted data.
4. Bauer's theory predicted the actual nose radius fair-to-good in all cases. The 0.250-inch nose radius was predicted to within ±32 percent to ±52 percent in 67 percent of all cases. In those cases where Textoris' and Stankevics' predictions were not very good, that is, when infrared data were curve fitted by two straight lines, fair results were still obtained.
5. No configuration-unique conclusions could be made; that is, no model parametric effects were determined. The configurations tested included: 10-degree half-angle, non-ablative blunt cones of two different nose radii; 10-degree half-angle, ablative blunt cones of three different

nose radii and two different heat shields; 12- and 14-degree half-angle, ablative blunt cones; ablative spheres; and an ablative hemisphere-cylinder-flare. Some of the configurations included one model only. The results given in the previous items are applicable to all the configurations together.

In view of the complex and not well understood chemistry in the wake of reentry vehicles, it is recommended that in those applicable bandpasses, data in air of the same water vapor content and/or same constituency be analyzed. It is also recommended that more data be obtained for specific model configurations. Then the validity of the theories considered can be ascertained systematically for different configurations, independent of range air constituency effects. Additional and/or modified data analysis methodology can be used with the data contained herein and with newly acquired data to possibly discover new theories or modify existing ones.

BIBLIOGRAPHY

BIBLIOGRAPHY

1. Lykoudis, Paul S. "Review of Hypersonic Wake Studies," AIAA Journal, 4:577-590, April, 1966.

2. Steiger, Martin. "A Review of Hypersonic Reentry Wakes and Auxiliary Studies, Part 1, Base Flow and Near Wake Fluid Dynamics," Heliodyne Corporation Research Note 40, Van Nuys, California, July, 1967.

3. Gold, Harris. "Course Notes for High Speed Aerodynamics with Emphasis on the Physics of High Temperature Gases." Unpublished classroom notes, The University of Tennessee Space Institute, Tullahoma, Tennessee, March, 1968.

4. Reis, V. H. "Chemiluminescent Radiation from the Far Wake of Hypersonic Spheres," AIAA Journal, 5:1928-1933, November, 1967.

5. Burns, J. C., and T. R. Reithof. "The Status of Optical Diagnostics on Wakes Behind Hypersonic Vehicles," General Electric Company N68-18094, Philadelphia, Pennsylvania, January, 1968.

6. Taylor, R. L., and others. "Techniques for Radiation Measurement and Flow Visualization of Self-Luminous Hypersonic Wakes," AVCO-Everett Research Laboratory AMP 84, Everett, Massachusetts, June, 1962.

7. Steiner, Bruce. "Optical Radiation Measurements: The Present State of Radiometry and Photometry," NBS Technical Note 594-6, U. S. Department of Commerce, Washington, D. C., March, 1974.

8. Hudson, D. H., Jr. Infrared System Engineering. New York: John Wiley and Sons, Inc., 1973.

9. Chapman, G. T., and D. B. Kirk. "A Method for Extracting Aerodynamic Coefficients from Free Flight Data," AIAA Journal, 8:753-758, April, 1970.

10. Textoris, A. T., and J. O. A. Stankevics. "Analysis of FTD/AEDC Wake Measurements." Report prepared under U. S. Air Force Contract No. F33657-75-C-0306 by AVCO-Everett Research Laboratory, Everett, Massachusetts, November, 1975.

11. Lees, L., and T. Kubota. "Inviscid Hypersonic Flow Over Blunt-Nosed Slender Bodies," Journal of the Aeronautical Sciences, 24:195-202, March, 1957.

12. Heyda, J. F. "Some Comments and Observations on the Wake Kink Formula for Determination of the Nose Radius of an RV." Unpublished report, Foreign Technology Division, Air Force Systems Command, Wright-Patterson Air Force Base, Ohio, November, 1975.

13. Lykoudis, P. S. "Ionization Trails," Proceedings of the 1961 Heat Transfer and Fluid Mechanics Institute. Stanford, California: Stanford University Press, 1961. Pp. 176-192.

14. Scarborough, J. B. Numerical Mathematical Analysis. Baltimore, Maryland: The John Hopkins Press, 1966.

APPENDIXES

APPENDIX A

FIELD OF VIEW GEOMETRY

The field of view for radiometers is defined by the geometrical system shown in Figure A-1. This optical system obviously produces penumbral areas fringing the field of view. The assumption is made that one-half the radiance from the penumbral areas is intercepted by the area S_2, or, in other words, that the effective field of view includes one-half of the total penumbral area.

Let a and c designate the widths of areas S_1 and S_2, respectively, and w the width of the penumbral region on each side. If x is the width of the clear field of view, the total field of view width is then:

$$f_w = x + 2w/2 = x + w = \overline{AC} = \overline{AB} + \overline{BC} \ .$$

Using triangle OAB,

$$\frac{\overline{AB}}{d_1 + d_2} = \frac{a + c}{2d_2}$$

$$\overline{AB} = \frac{(d_1 + d_2)(a + c)}{2d_2} \ .$$

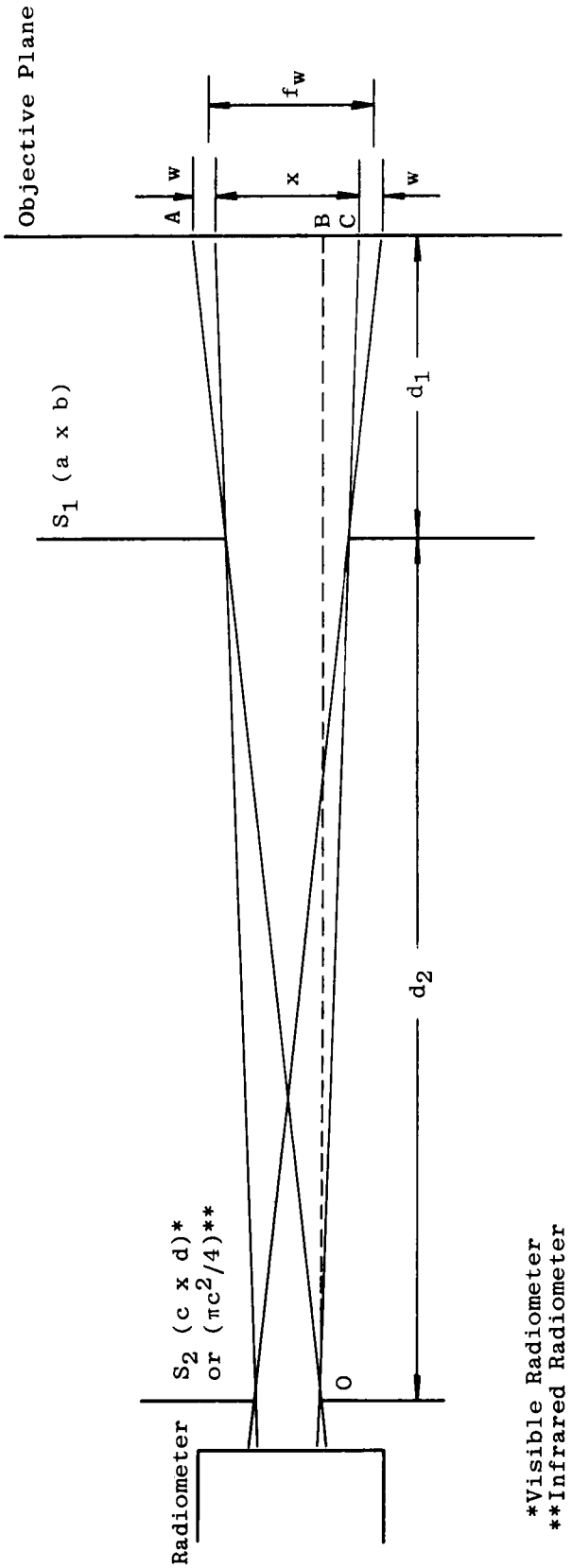


Figure A-1. Field of view schematic.

Using triangle OBC,

$$\frac{\overline{BC}}{d_1 + d_2} = \frac{a - c}{2d_2}$$

$$\overline{BC} = \frac{(d_1 + d_2)(a - c)}{2d_2} ,$$

then

$$f_w = \overline{AB} + \overline{BC}$$

$$= \frac{(d_1 + d_2)(a + c)}{2d_2} + \frac{(d_1 + d_2)(a - c)}{2d_2}$$

$$= \left(\frac{d_1 + d_2}{d_2} \right) a \quad .$$

APPENDIX B

UNCERTAINTY ANALYSIS

I. INTRODUCTION

Let

$$Q = F(q_1, q_2, \ldots q_n)$$

represent any function of directly measured quantities, $q_1, q_2, \ldots q_n$, and let the probable errors of $Q, q_1, q_2, \ldots q_n$ be denoted by $S, s_1, s_2, \ldots s_n$, respectively. Then the relative error of Q is

$$\frac{S}{Q} = \left\{ \left(\frac{\partial Q}{\partial q_1} \right)^2 \frac{s_1^2}{Q^2} + \left(\frac{\partial Q}{\partial q_2} \right)^2 \frac{s_2^2}{Q^2} + \ldots + \left(\frac{\partial Q}{\partial q_n} \right)^2 \frac{s_n^2}{Q^2} \right\}^{1/2}$$

([14], Eq. (161.2)).

When Q is a product of several functions, as

$$Q = K x^m y^n z^p ,$$

then

$$\frac{S}{Q} = \left\{ m^2 \left(\frac{s_1}{x} \right)^2 + n^2 \left(\frac{s_2}{y} \right)^2 + p^2 \left(\frac{s_3}{z} \right)^2 \right\}^{1/2} \qquad \text{(B-1)}$$

([14], Eq. (161.4)).

Thus, the relative error of Q is expressed as a function of the relative errors of the directly measured quantities.

II. CALCULATION OF UNCERTAINTY OF VISIBLE RADIOMETER DATA

Let

$$\int_0^\infty R(\lambda)\ I_\lambda\ d\lambda = N\ .$$

From Chapter II, Eq. (1),

$$K = \frac{V_C}{A_D N}\ \frac{d_d^2}{d_c^2}\ .$$

From Chapter III, Eq. (3),

$$J_{OBS} = \frac{V_S/K}{(A_D/d_S^2)\ f_w}$$

combining,

$$J_{OBS} = \left(\frac{d_c^2}{d_d^2}\ \frac{N}{V_C}\right)\ \frac{d_s^2}{f_w}\ V_S\ .$$

The terms in parentheses are associated with calibration; the other terms with data acquisition.

Precision Error

Using Eq. (B-1), one calculates the precision error of J_{OBS} as follows:

$$\left(\frac{S_{J_{OBS}}}{J_{OBS}}\right)^2 = 2^2\left(\frac{S_{d_c}}{d_c}\right)^2 + 2^2\left(\frac{S_{d_d}}{d_d}\right)^2 + \left(\frac{S_N}{N}\right)^2 + \left(\frac{S_{V_c}}{V_c}\right)^2 + 2^2\left(\frac{S_{d_s}}{d_s}\right)^2 + \left(\frac{S_{f_w}}{f_w}\right)^2 + \left(\frac{S_{V_s}}{V_s}\right)^2 , \quad \text{(B-2)}$$

where the precision errors, specified on a relative basis as $\frac{S_x}{x}$, are in percent to be in agreement with Table B-I.

Looking at each precision error, term by term:

1. From Table B-I,

$$\frac{S_{d_c}}{d_c} = \pm 0.26 \text{ percent} .$$

2. From Table B-I,

$$\frac{S_{d_d}}{d_d} = \pm 0.26 \text{ percent} .$$

3. For the precision error of N, for simplicity, let $N = R_E\ I_E\ \Delta\ \lambda_E$, where the subscript, E, represents effective values resulting from the integration.

   Radiant output, V_{o_1}, varies approximately as the ninth power of filament current, i.

   So, let $V_{o_1} = K\ i^9$.

Table B-I. Errors

Error Category	Item No.	Error Sources	Source Symbol	Bias Errors (±%)	Precision Errors (±%)
Calibration-Infrared	1	Black Body Temperature	T	0.17	0.83
	2	Black Body Aperture Diameter	d_{bb}	0	0
	3	Distance between Black Body and Radiometer	d	0.04	0.26
	4	Digital Voltmeter	V_C	0.10	10.0
Calibration-Visible	5	Q.I. Lamp Current	i	0	0.25
	6	Power Supply	V_I	0.10	0.10
	7	Distance between Q.I. Lamp and Radiometer	d_d	0.04	0.26
	8	Q.I. Lamp Calibration Distance	d_c	0.04	0.26
	9	Transmission of Plexiglass Window	T_{pw}	0.25	5.0
	10	Transmission of Neutral Density Filter	T_{ND}	0.10	0
	11	Digital Voltmeter	V'_C	0.10	5.0

Table B-I. (continued)

Error Category	Item No.	Error Sources	Source Symbol	Bias Errors (±%)	Precision Errors (±%)
Calibration-General	12	Effective Relative Spectral Response	R_E	0	5.0
	13	Effective Wavelength Interval	$\Delta\lambda_E$	0	5.0
Data Acquisition	14	Oscilloscope	SF1	0	3.0
	15	Preamplifier	SF2	0	3.0
	16	Power Supply	SF3	0.25	0.10
	17	Distance between Model and Radiometer	d_s	0.04	0.7
	18	Distance between Radiometer and Front Slit	d_2	0.04	0.7
	19	Slit Width	a	0.04	12.5
	20	Film Reader	$S_{F_{V_{FR}}}$	0	0.34

From Table B-I, $\frac{S_i}{i} = \pm 0.25$ percent; thus,

$$\left(\frac{S_{V_{o_1}}}{V_{o_1}} \right)^2 = 9^2 \ (0.25)^2 = (2.25)^2 \ .$$

Also, the anode sensitivity of a photomultiplier tube, V_{o_2}, was found to be proportional to the ninth power of the applied voltage, V_I. So, let

$$V_{o_2} = K \ V_I^9 \ .$$

From Table B-I,

$$\frac{S_{V_I}}{V_I} = \pm 0.1 \text{ percent} \ .$$

Thus,

$$\left(\frac{S_{V_{o_2}}}{V_{o_2}} \right)^2 = 9^2 \ (0.1)^2 = (0.9)^2 \ .$$

Then,

$$\left(\frac{S_{I_E}}{I_E} \right)^2 = (2.25)^2 + (0.9)^2 \ .$$

From Table B-I,

$$\frac{S_{R_E}}{R_E} = \pm 5.0 \text{ percent} ; \frac{S_{\Delta\lambda_E}}{\Delta\lambda_E} = \pm 5.0 \text{ percent} .$$

Then,

$$\left(\frac{S_N}{N} \right)^2 = (5.0)^2 + (2.25)^2 + (5.0)^2 .$$

4. For the precision error of V_C,

$$V_C = \frac{V_C' \, T_{pw}}{T_{ND}} ,$$

where,

T_{pw} = transmission of plexiglass window,

T_{ND} = transmission of neutral density filter.

From Table B-I,

$$\frac{S_{V_C'}}{V_C'} = \pm 5.0 \text{ percent} ; \frac{S_{T_{pw}}}{T_{pw}} = \pm 5.0 \text{ percent} ;$$

$$\frac{S_{T_{ND}}}{T_{ND}} = 0 .$$

Then,

$$\left(\frac{S_{V_C}}{V_C} \right)^2 = (5.0)^2 + (5.0)^2 .$$

5. From Table B-I,

$$\frac{S_{d_s}}{d_s} = \pm 0.7 \text{ percent} .$$

6. For the precision error of f_w, from Appendix A,

$$f_w = 2.54\ a \left(\frac{d_1 + d_2}{d_2} \right) = 2.54\ a\ \frac{d_s}{d_2} .$$

From Table B-I,

$$\frac{S_a}{a} = \pm 12.5 \text{ percent} ; \frac{S_{d_s}}{d_s} = \pm 0.7 \text{ percent} ;$$

$$\frac{S_{d_2}}{d_2} = \pm 0.7 \text{ percent} .$$

Then,

$$\left(\frac{S_{f_w}}{f_w} \right)^2 = (12.5)^2 + (0.7)^2 + (0.7)^2 .$$

7. For the precision error of V_S,

$$V_S = \frac{SF_{V_S}\ C_V\ (5)}{SF_{V_{FR}}} ,$$

where,

SF_{V_S} = scale factor of the amplitude of the oscilloscope data trace,

C_V = oscilloscope data trace vertical counts read on the film reader,

$SF_{V_{FR}}$ = scale factor on film reader for amplitude of the oscilloscope data trace.

For the precision error of SF_{VS}, the oscilloscope, preamplifier, and power supply all have error contributions. From Table B-I,

$$\frac{S_{SF1}}{SF1} = \pm 3.0 \text{ percent} ; \frac{S_{SF2}}{SF2} = \pm 3.0 \text{ percent} ;$$

$$\frac{S_{SF3}}{SF3} = \pm 0.1 \text{ percent} .$$

Then,

$$\left(\frac{S_{SF_{V_S}}}{SF_{V_S}} \right)^2 = (3.0)^2 + (3.0)^2 + (0.1)^2 .$$

From Table B-I,

$$\frac{S_{SF_{V_{FR}}}}{SF_{V_{FR}}} = \pm 0.34 \text{ percent} .$$

Then,

$$\left(\frac{S_{V_S}}{V_S}\right)^2 = (3.0)^2 + (3.0)^2 + (0.1)^2 + (0.34)^2 + \left(\frac{S_{C_v}}{C_v}\right)^2 .$$

The precision error associated with C_V varies from trace to trace. For a particular trace, the one sigma (1σ) precision error is:

$$\left(\frac{S_{C_v}}{C_v}\right)^2 = \left(\frac{100}{C_v}\right)^2 \left[\left(\frac{Z_t/2}{3}\right)^2 + \left(\frac{D_t/2}{3}\right)^2\right] ,$$

where Z_t is the measured or estimated thickness of the oscilloscope trace at time zero in counts, and D_t is the measured thickness of the data trace in counts.

After substituting the individual precision error contributions into Eq. (B-2),

$$\left(\frac{S_{J_{OBS}}}{J_{OBS}}\right)^2 = 284 + \left(\frac{S_{C_v}}{C_v}\right)^2 .$$

If the precision error associated with C_v is ±5.0 percent, then the precision error associated with J_{OBS} is ±17.5 percent.

Bias Error

Using the same methodology with Table B-I, page 99, bias errors as was used with the precision error determination, the bias error associated with J_{OBS} is calculated to be negligible; that is, less than ±1 percent.

Uncertainty

The total uncertainty is the ±1σ precision error.

III. CALCULATION OF UNCERTAINTY OF INFRARED RADIOMETER DATA

Let

$$\int_0^\infty R(\lambda)\ W_\lambda\ d\lambda = I\ .$$

From Chapter II, Eq. (2),

$$K = \frac{V_C}{\frac{A_{bb}}{\pi}\ \frac{A_D}{d^2}\ I}\ .$$

From Chapter III, Eq. (3),

$$J_{OBS} = \frac{V_S/K}{(A_D/d_s^2)\ f_w}\ .$$

Combining,

$$J_{OBS} = \left(\frac{1}{4} \frac{d_{bb}^2}{d^2} \frac{I}{V_C} \right) \frac{d_s^2}{f_w} V_S \ .$$

The terms in parentheses are associated with calibration; the other terms with data acquisition.

Precision Error

Using Eq. (B-1), the precision error of J_{OBS} is calculated as follows:

$$\left(\frac{S_{J_{OBS}}}{J_{OBS}} \right)^2 = 2^2 \left(\frac{S_{d_{bb}}}{d_{bb}} \right)^2 + 2^2 \left(\frac{S_d}{d} \right)^2 + \left(\frac{S_I}{I} \right)^2 + \left(\frac{S_{V_C}}{V_C} \right)^2$$

$$+ 2^2 \left(\frac{S_{d_s}}{d_s} \right)^2 + \left(\frac{S_{f_w}}{f_w} \right)^2 + \left(\frac{S_{V_s}}{V_s} \right)^2 \ ,$$

where the precision errors, specified on a relative basis as $\frac{S_x}{x}$, are in percent to be in agreement with Table B-I, page 99.

Looking at each precision error, term by term:

1. From Table B-I,

$$\frac{S_{d_{bb}}}{d_{bb}} = 0.$$

2. From Table B-I,

$$\frac{S_d}{d} = \pm 0.26 \text{ percent} \ .$$

3. For the precision error of I.

For simplicity, let $I = R_E W_E \Delta \lambda_E$, where the subscript, E, represents effective values resulting from the integration.

Also, let $W_E = \sigma T^4$, the Stefan-Boltzmann law.

From Table B-I, page 99,

$$\frac{S_T}{T} = \pm 0.83 \text{ percent} .$$

Then,

$$\left(\frac{S_{W_E}}{W_E} \right)^2 = 4^2 \ (0.83)^2 = (3.32)^2 .$$

From Table B-I,

$$\frac{S_{R_E}}{R_E} = \pm 5.0 \text{ percent} , \frac{S_{\Delta\lambda_E}}{\Delta\lambda_E} = \pm 5.0 \text{ percent} .$$

Then,

$$\left(\frac{S_I}{I} \right)^2 = (5.0)^2 + (3.32)^2 + (5.0)^2 .$$

4. From Table B-I,

$$\frac{S_{V_C}}{V_C} = \pm 10.0 \text{ percent} .$$

5. From Table B-I,

$$\frac{S_{d_s}}{d_s} = \pm 0.7 \text{ percent} .$$

6. For the precision error of f_w,

$$\left(\frac{S_{f_w}}{f_w}\right)^2 = (12.5)^2 + (0.7)^2 + (0.7)^2 ,$$

as derived in Section II of this appendix.

7. For the precision of V_S,

$$\left(\frac{S_{V_S}}{V_S}\right)^2 = (3.0)^2 + (3.0)^2 + (0.1)^2 + (0.34)^2 + \left(\frac{S_{C_v}}{C_v}\right)^2 .$$

This was derived in Section II of this appendix. After substituting the individual precision error contributions into Eq. (B-1),

$$\left(\frac{S_{J_{OBS}}}{J_{OBS}}\right)^2 = 339 + \left(\frac{S_{C_v}}{C_v}\right)^2 .$$

If the precision error associated with C_v is ±5 percent, then the precision error associated with J_{OBS} is ±19 percent.

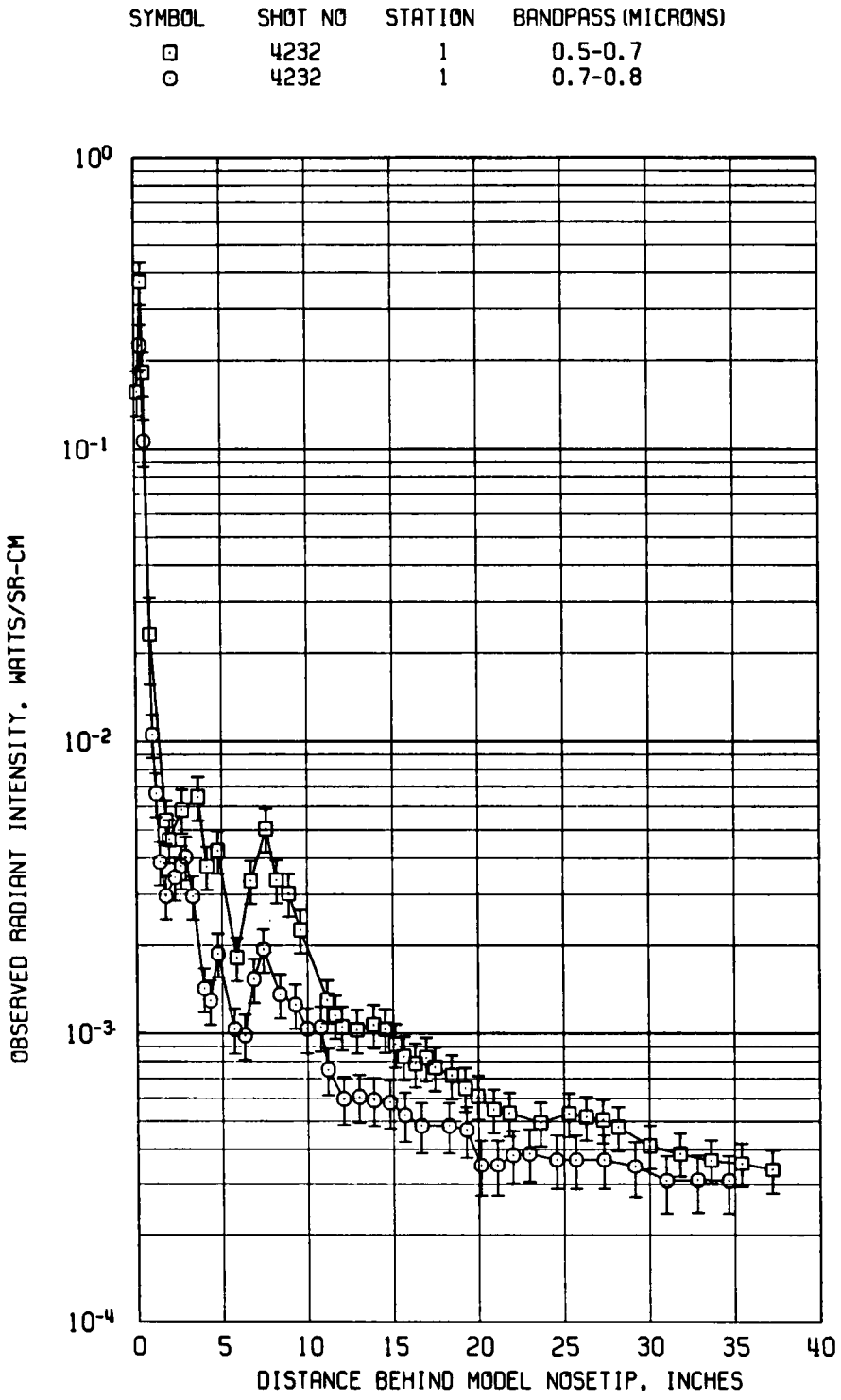
Uncertainty

Similar to the Section II reasoning, the bias error associated with J_{OBS} is negligible, and the total uncertainty is the ±1σ precision error.

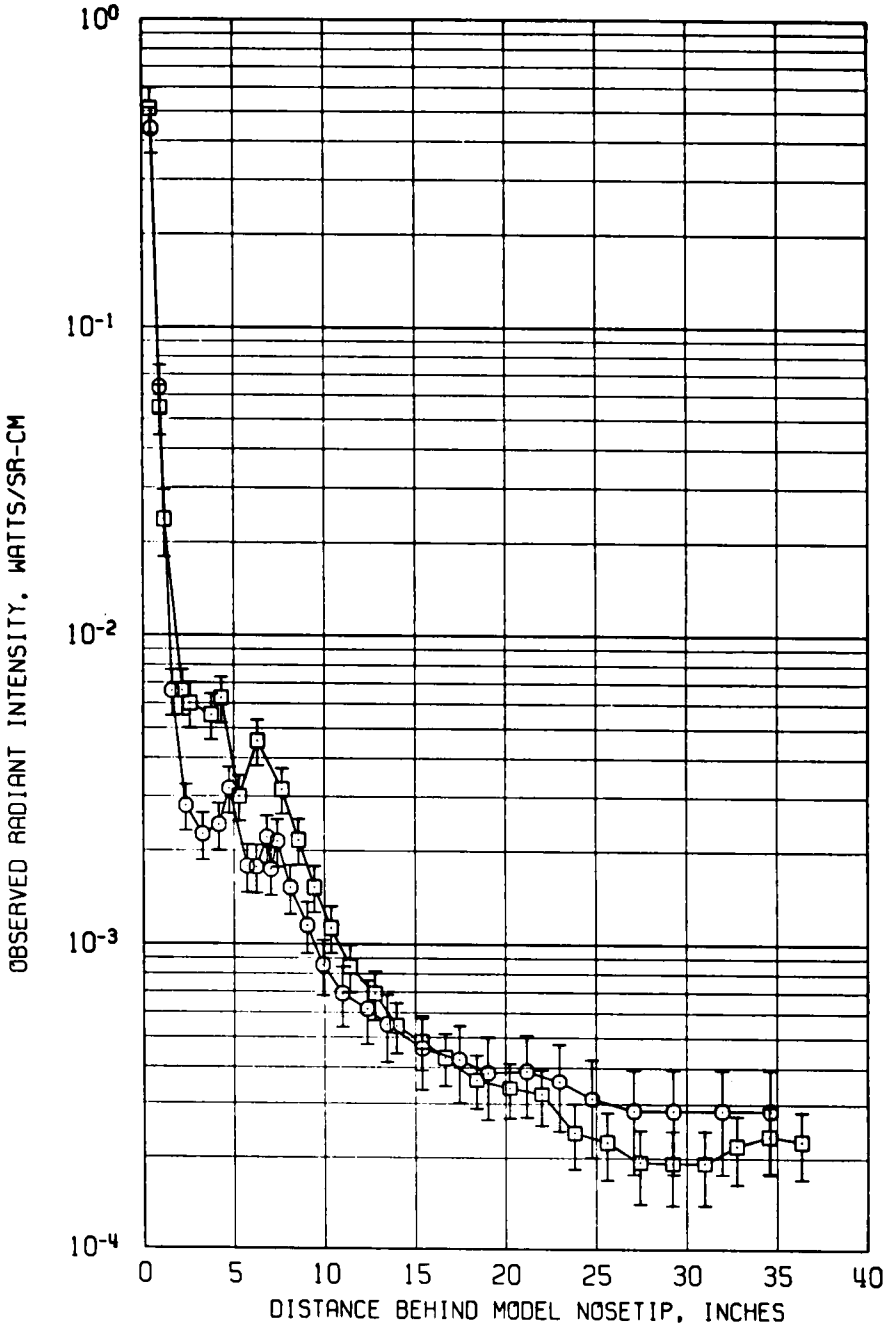
APPENDIX C

LOG INTENSITY VERSUS DISTANCE DATA

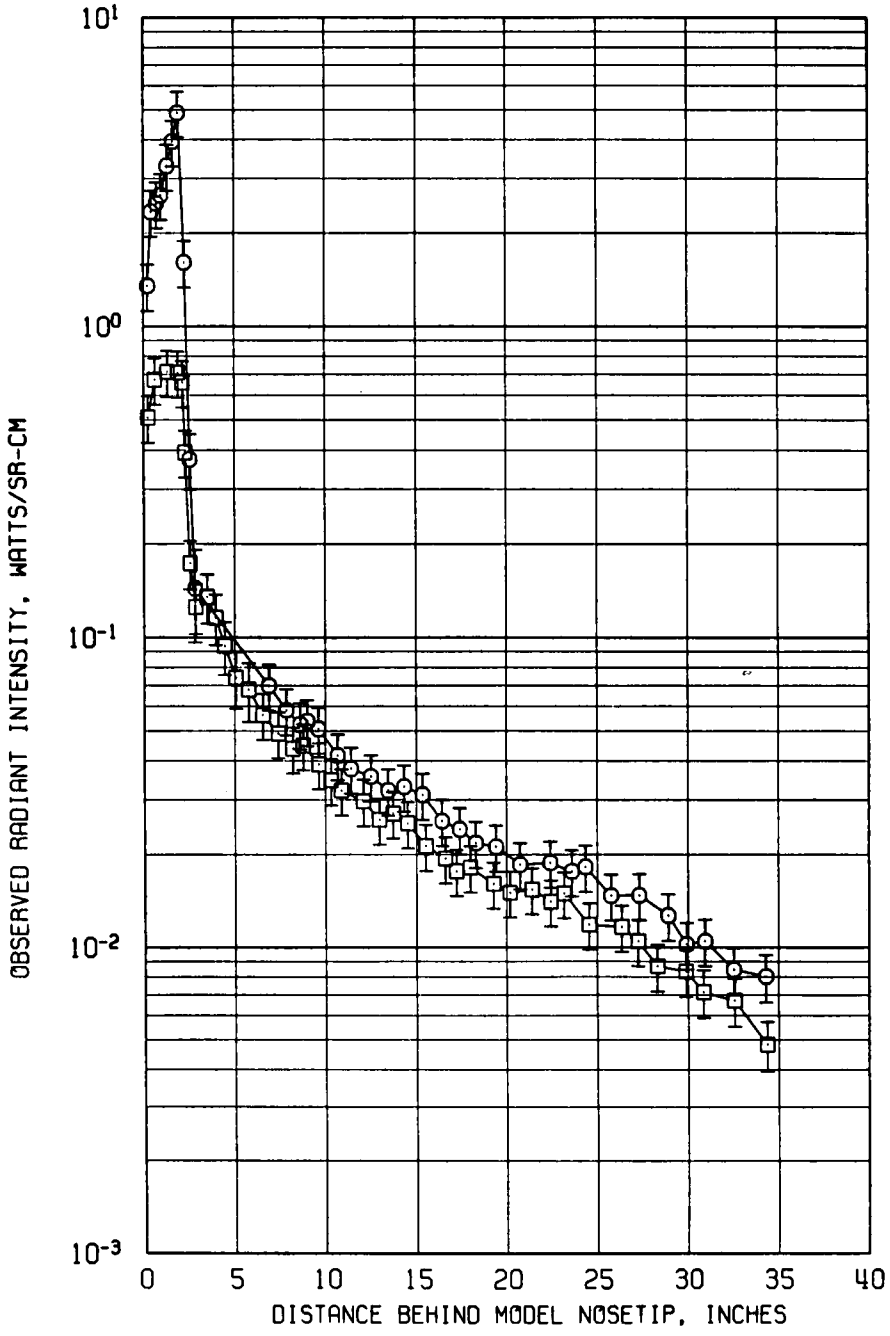
The radiometric test data are plotted as log intensity versus distance in this appendix. The data are presented sequentially by shot number. For a shot number, data from Radiometer Station 1 (noted as Station 1 on the plots) appear first--visible, then infrared; then data from Radiometer Station 2 (noted as Station 19 on the plots, as this denotes the Range G station) appear--visible, then infrared.


SYMBOL SHOT NO STATION BANDPASS (MICRONS)
4232 1 0.5-0.7
4232 1 0.7-0.8
10^0
10^{-1}
10^{-2}
10^{-3}
10^{-4}
OBSERVED RADIANT INTENSITY, WATTS/SR-CM
0 5 10 15 20 25 30 35 40
DISTANCE BEHIND MODEL NOSETIP, INCHES

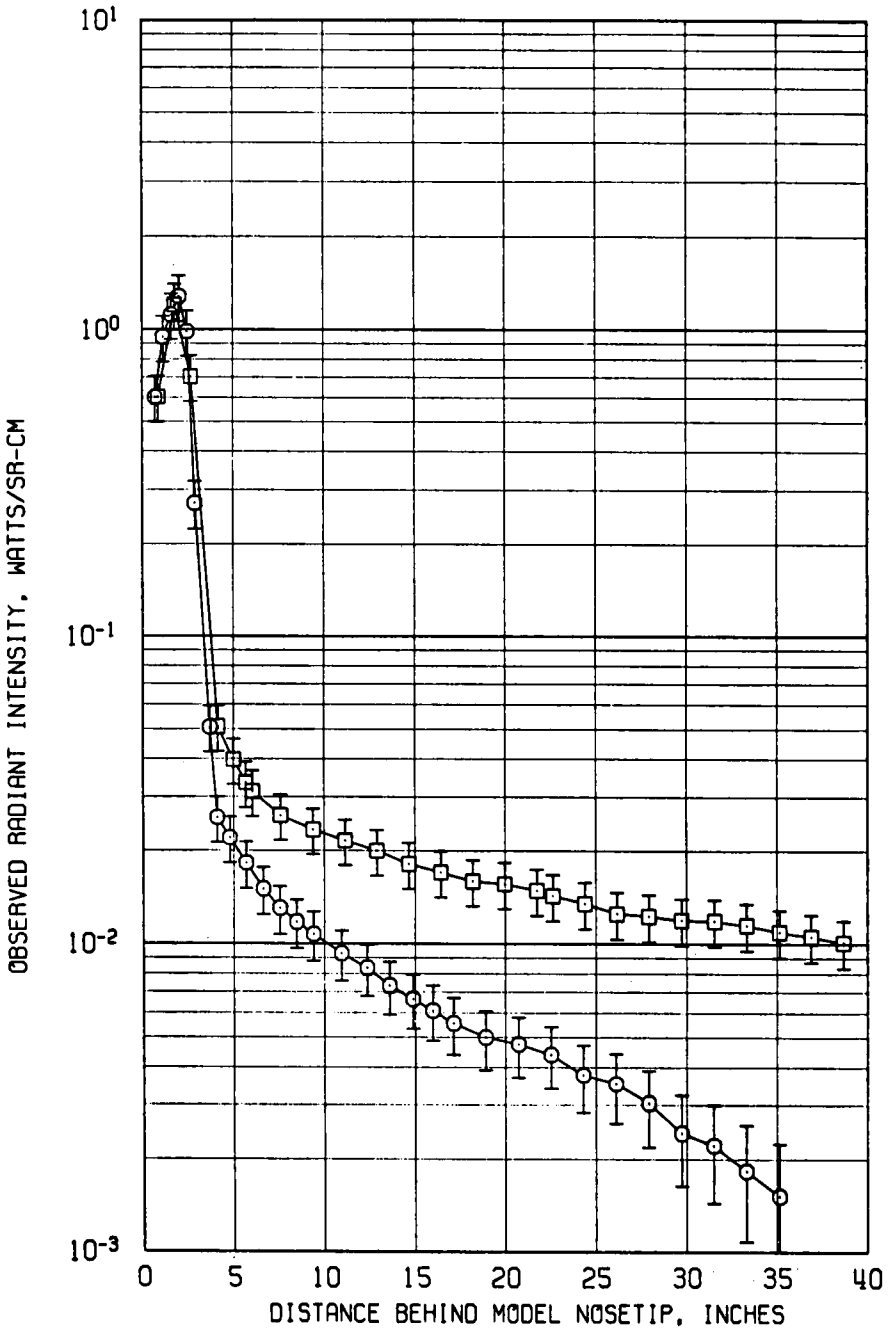
SYMBOL	SHOT NO	STATION	BANDPASS (MICRONS)
⊡	4271	1	0.5-0.7
⊙	4271	1	0.7-0.8



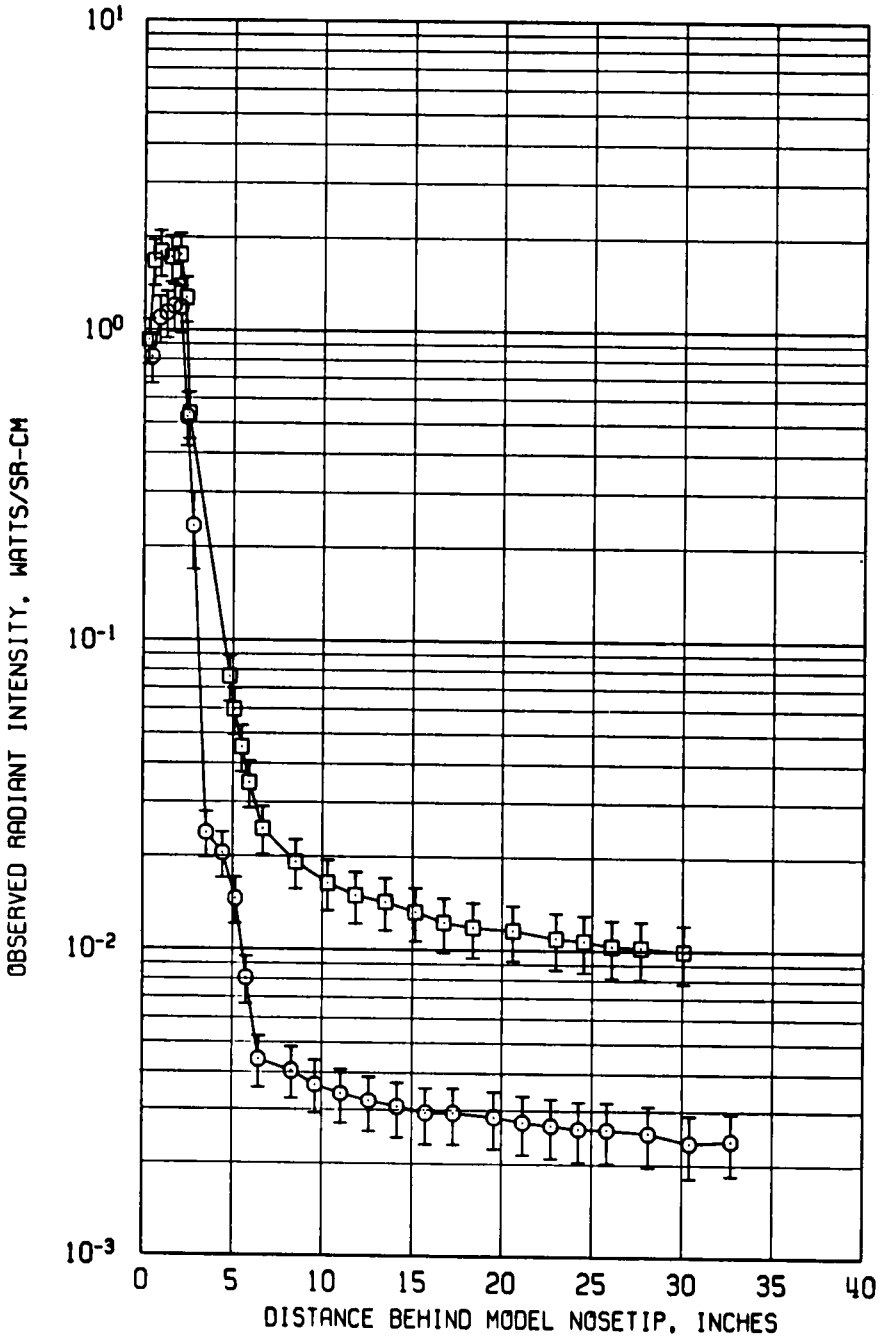
SYMBOL	SHOT NO	STATION	BANDPASS (MICRONS)
⊡	4398	1	0.5-0.7
⊙	4398	1	0.7-0.8



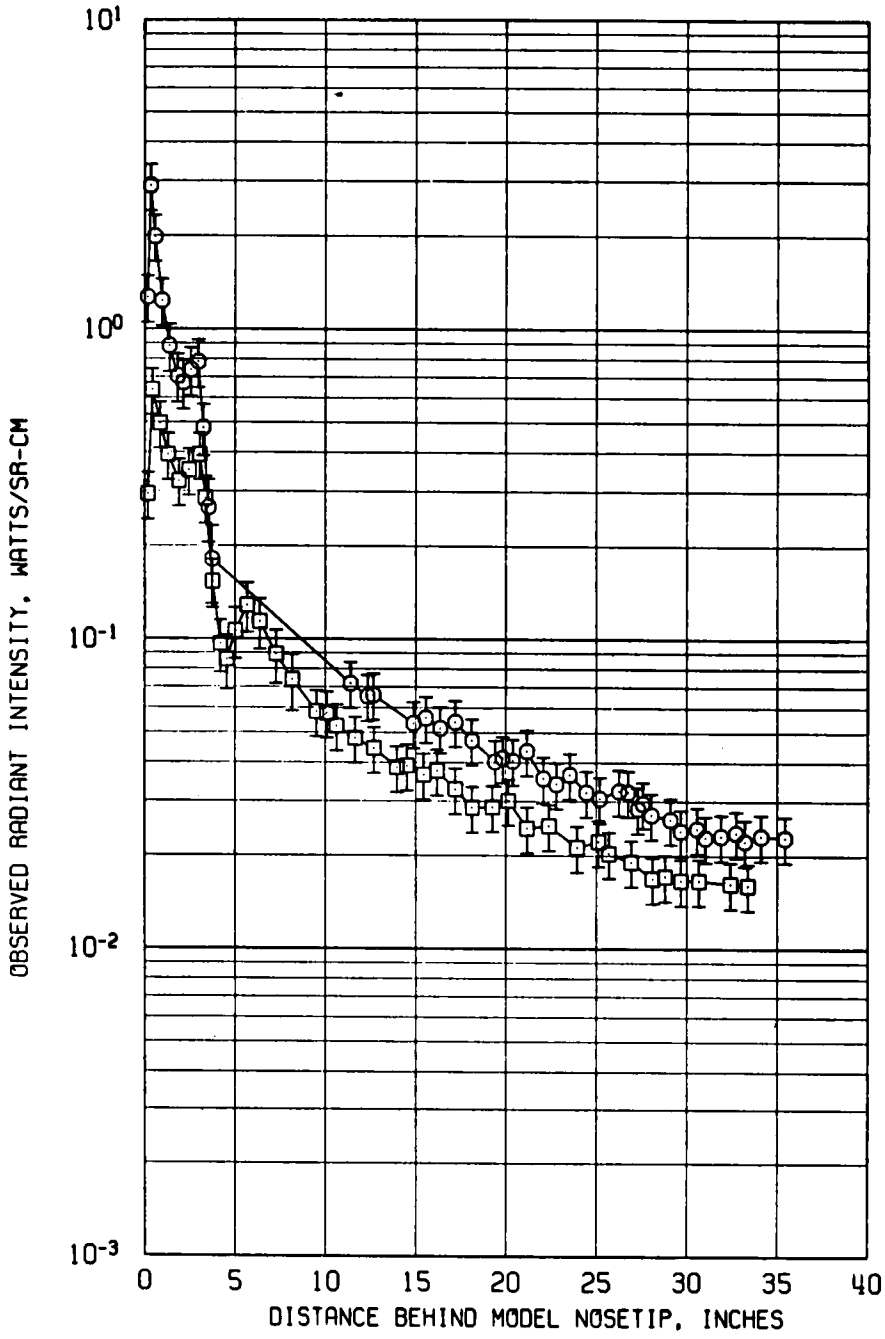
SYMBOL	SHOT NO	STATION	BANDPASS (MICRONS)
⊡	4398	1	2.6-2.8
⊙	4398	1	3.1-3.8



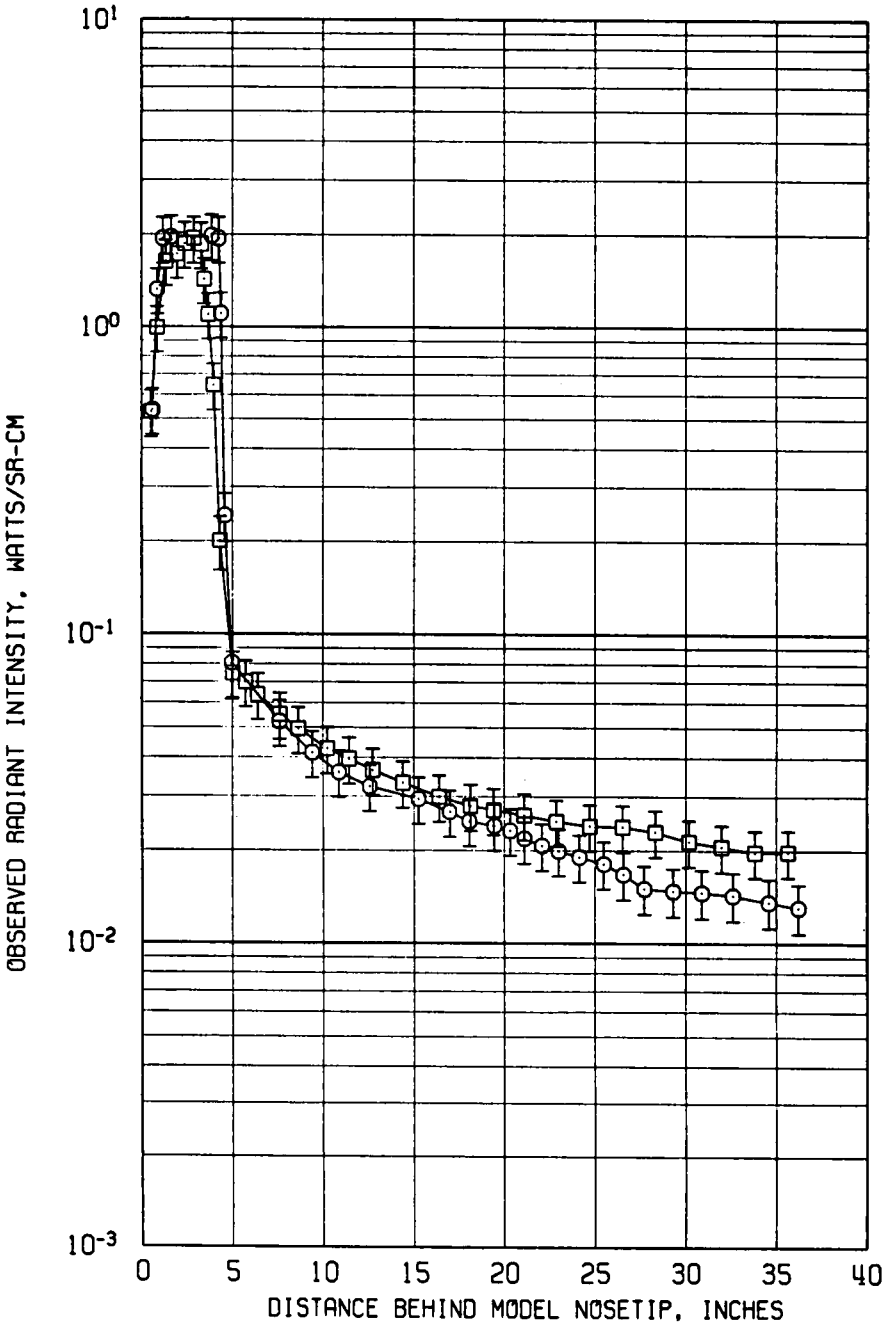
SYMBOL	SHOT NO	STATION	BANDPASS (MICRONS)
⊡	4398	19	0.5-0.7
⊙	4398	19	0.7-0.9

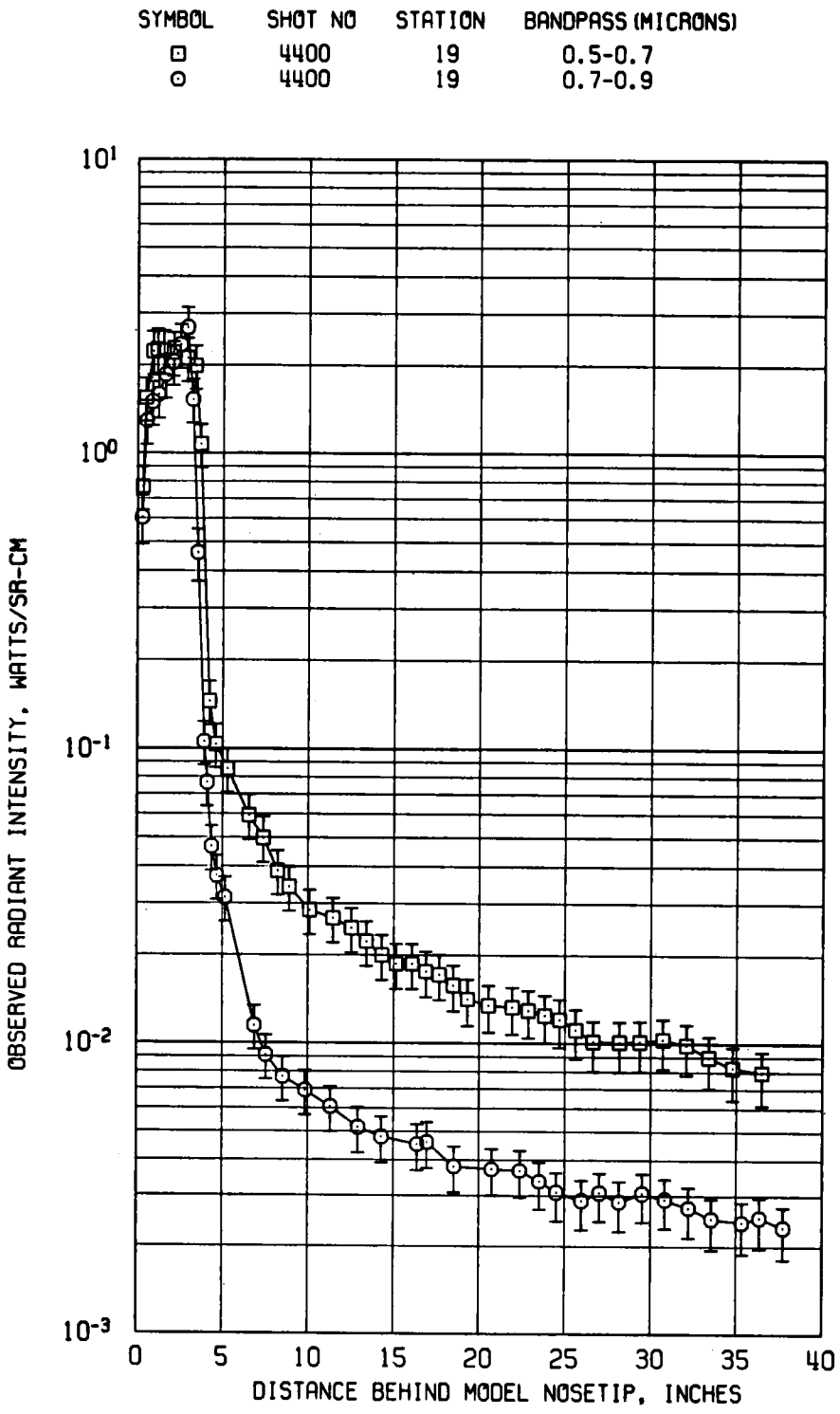


SYMBOL	SHOT NO	STATION	BANDPASS (MICRONS)
⊡	4400	1	0.5-0.7
⊙	4400	1	0.7-0.8

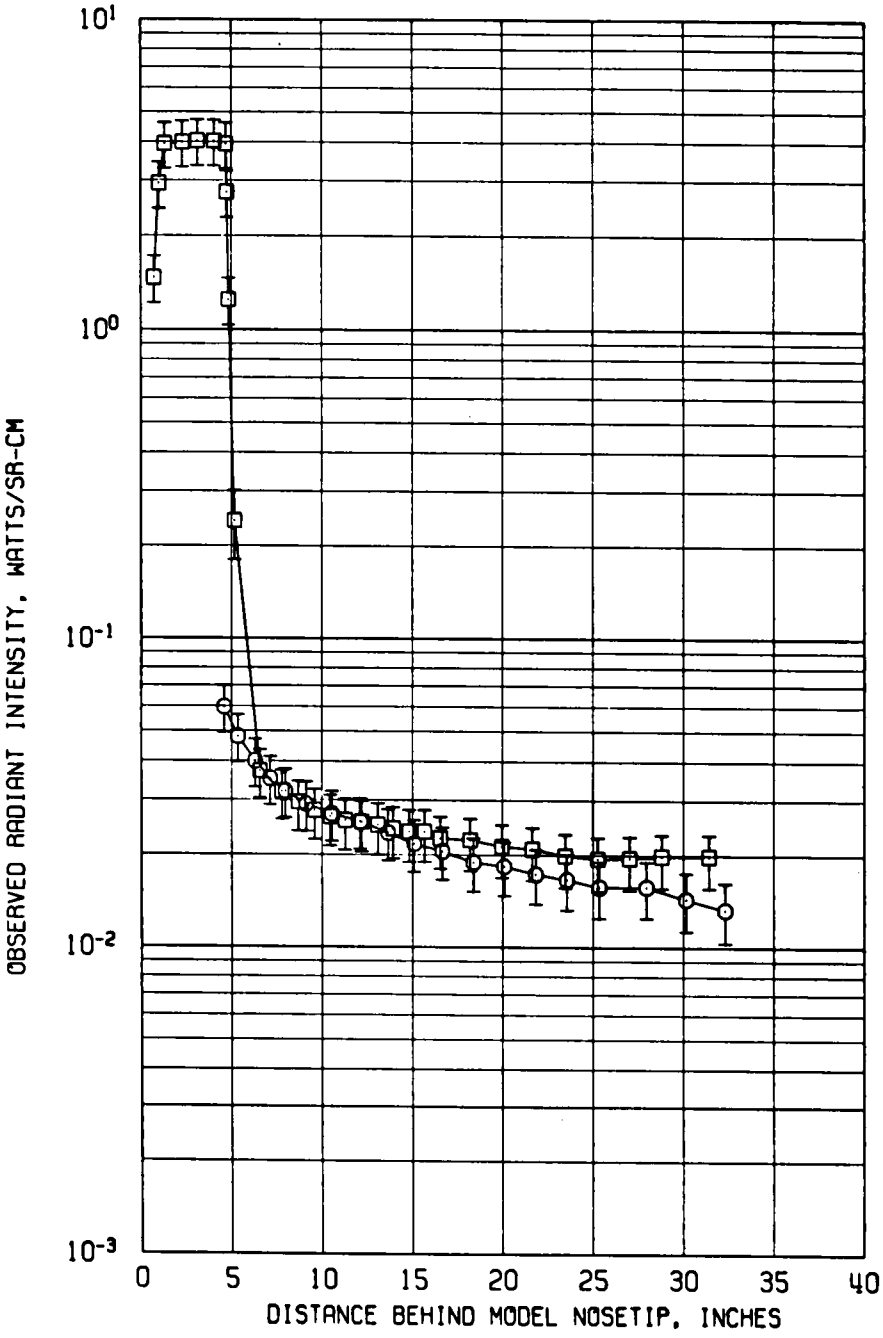


SYMBOL	SHOT NO	STATION	BANDPASS (MICRONS)
⊡	4400	1	2.6-2.8
⊙	4400	1	3.1-3.8

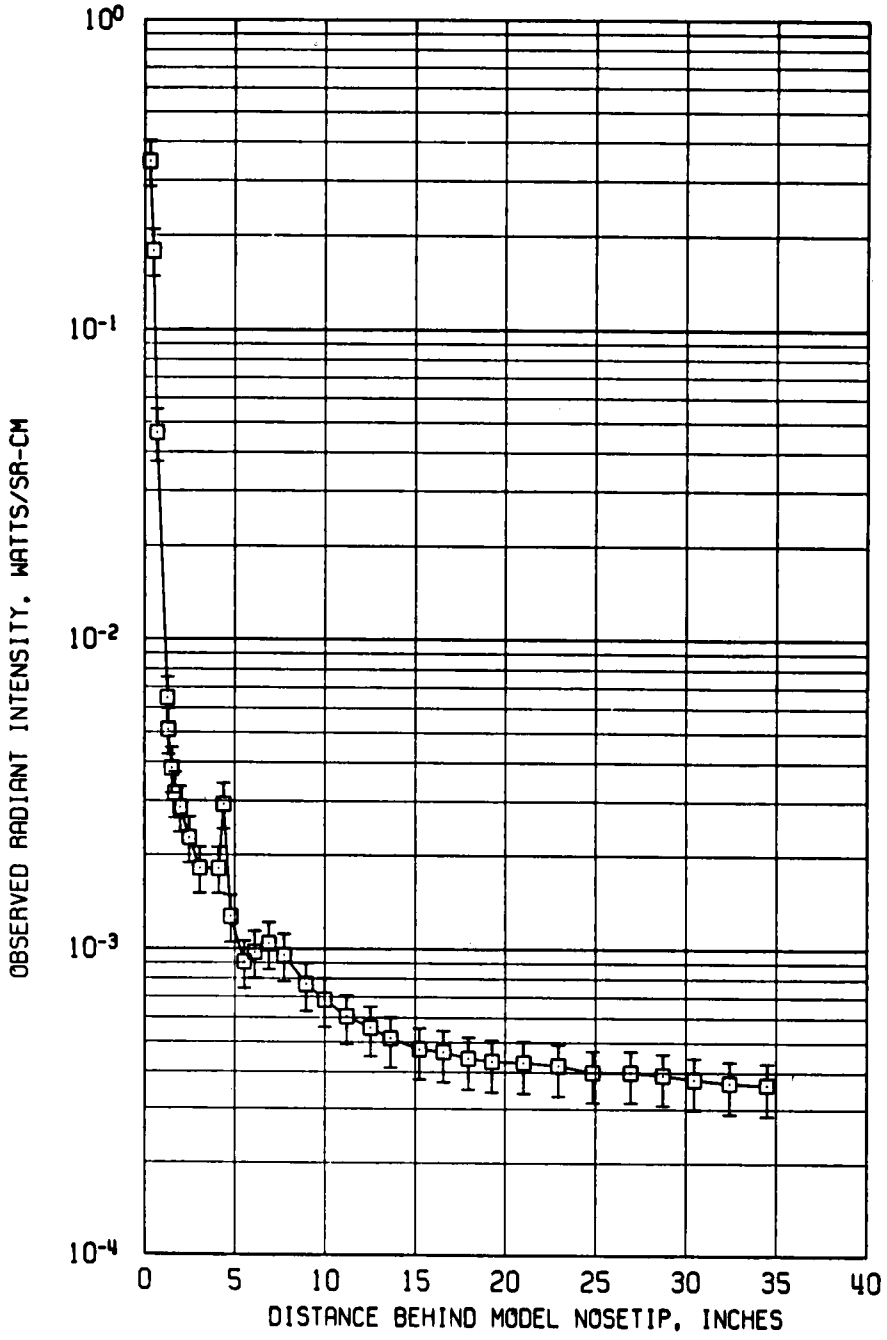



SYMBOL SHOT NO STATION BANDPASS (MICRONS)
⊡ 4400 19 0.5-0.7
⊙ 4400 19 0.7-0.9
OBSERVED RADIANT INTENSITY, WATTS/SR-CM
10^{1}
10^{0}
10^{-1}
10^{-2}
10^{-3}
0 5 10 15 20 25 30 35 40
DISTANCE BEHIND MODEL NOSETIP, INCHES

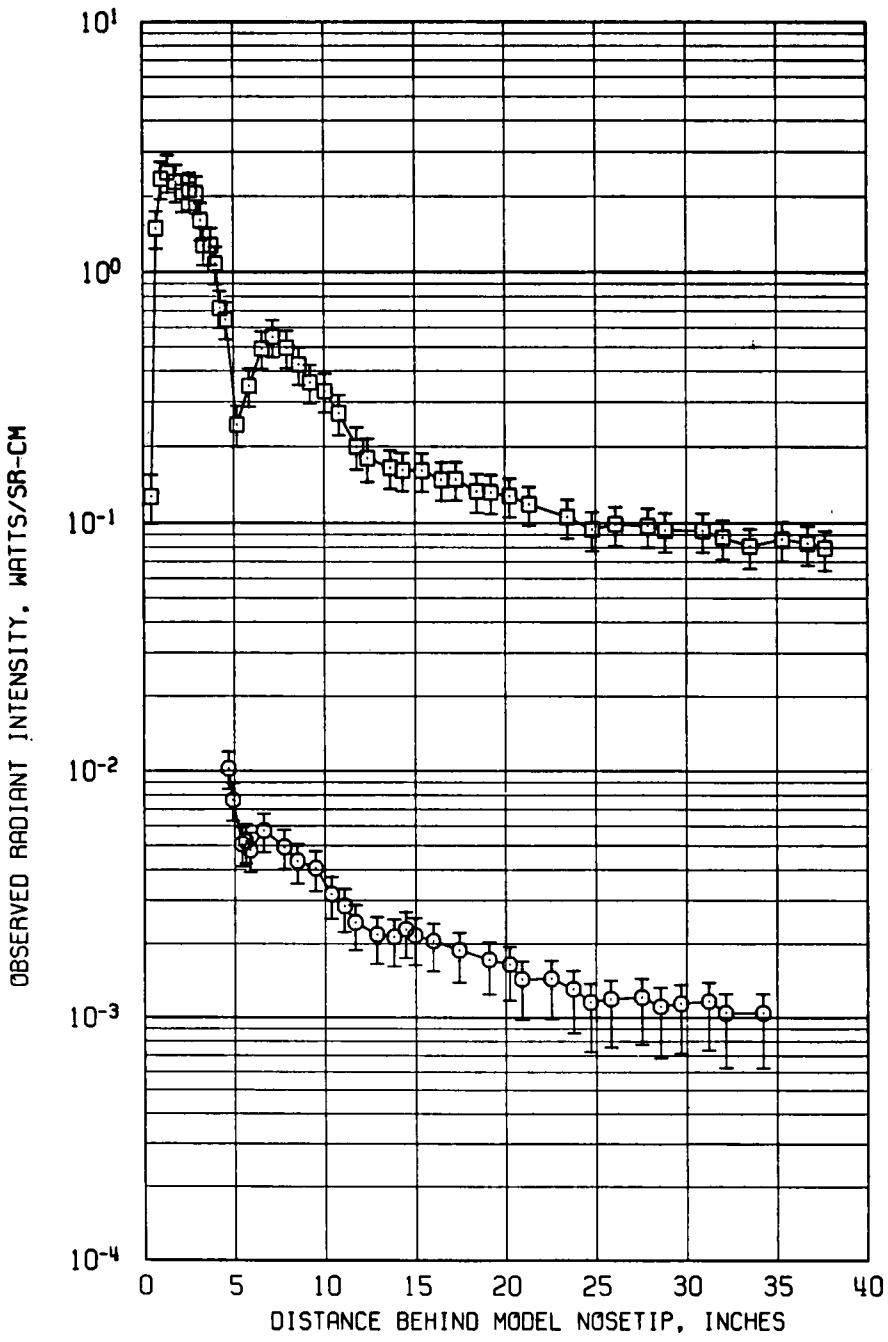
SYMBOL	SHOT NO	STATION	BANDPASS (MICRONS)
⊡	4400	19	2.6-2.8
⊙	4400	19	3.0-4.0



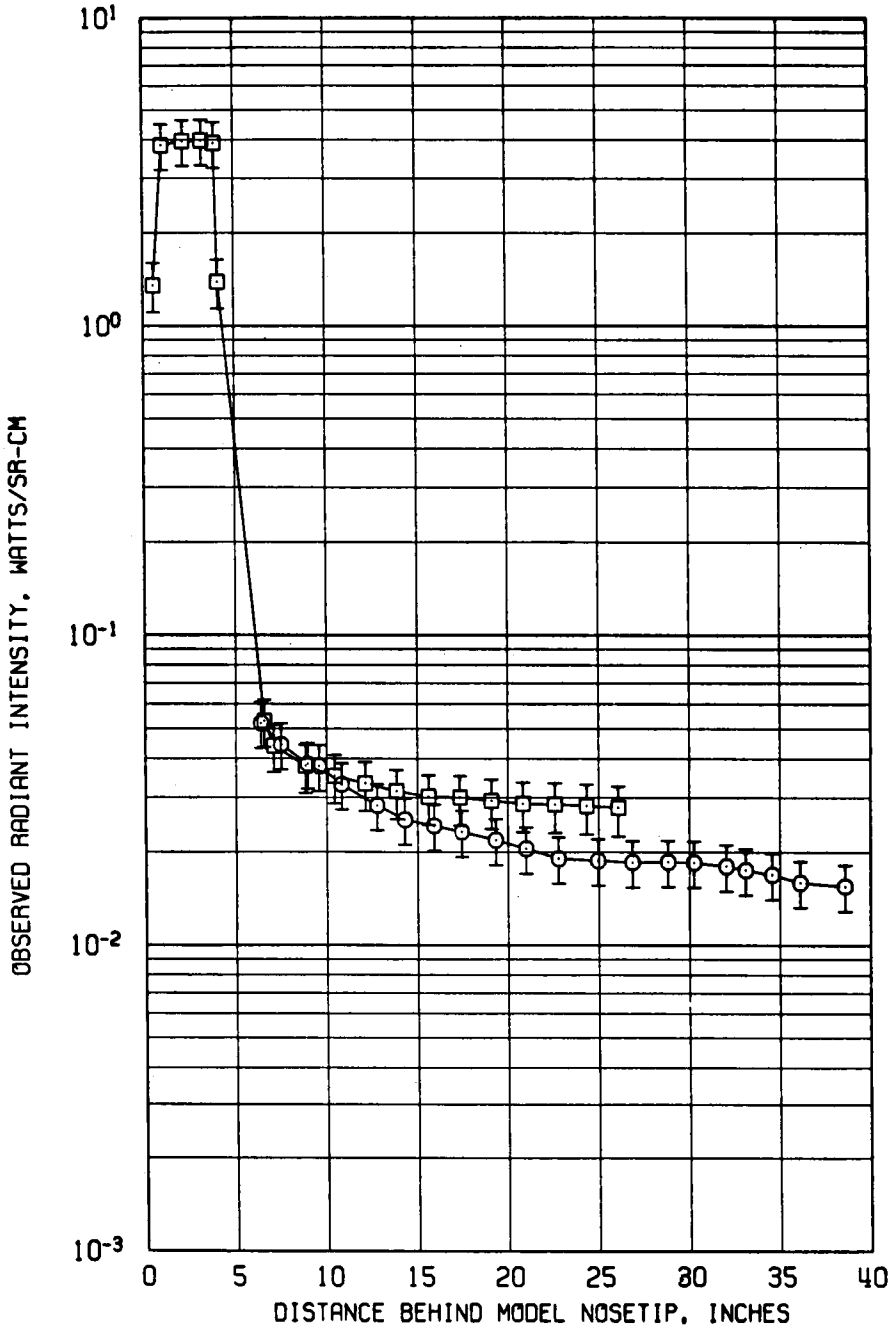
SYMBOL	SHOT NO	STATION	BANDPASS (MICRONS)
⊡	4401	1	0.5-0.7



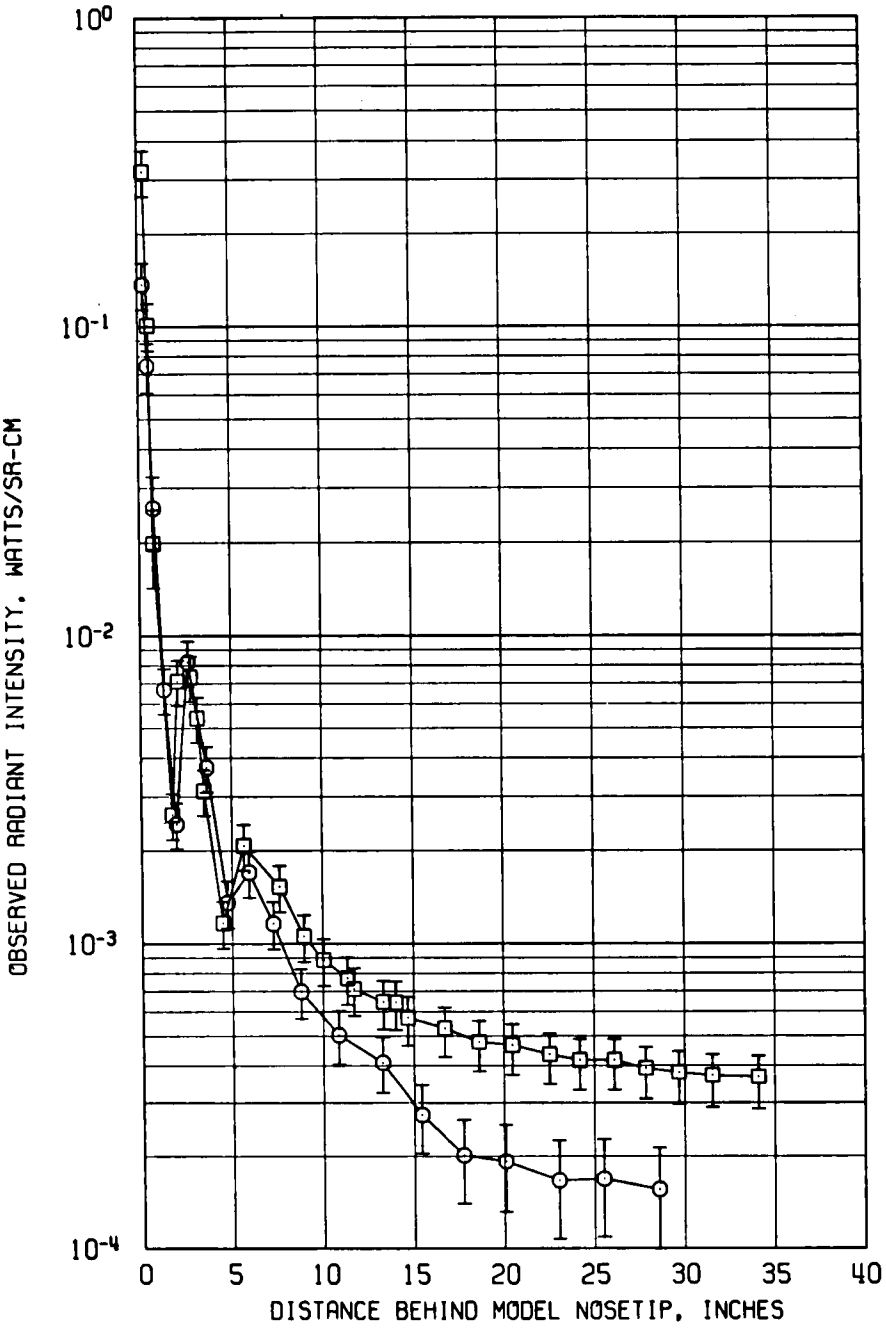
SYMBOL	SHOT NO	STATION	BANDPASS (MICRONS)
⊡	4402	19	0.5-0.7
⊙	4402	19	0.7-0.9



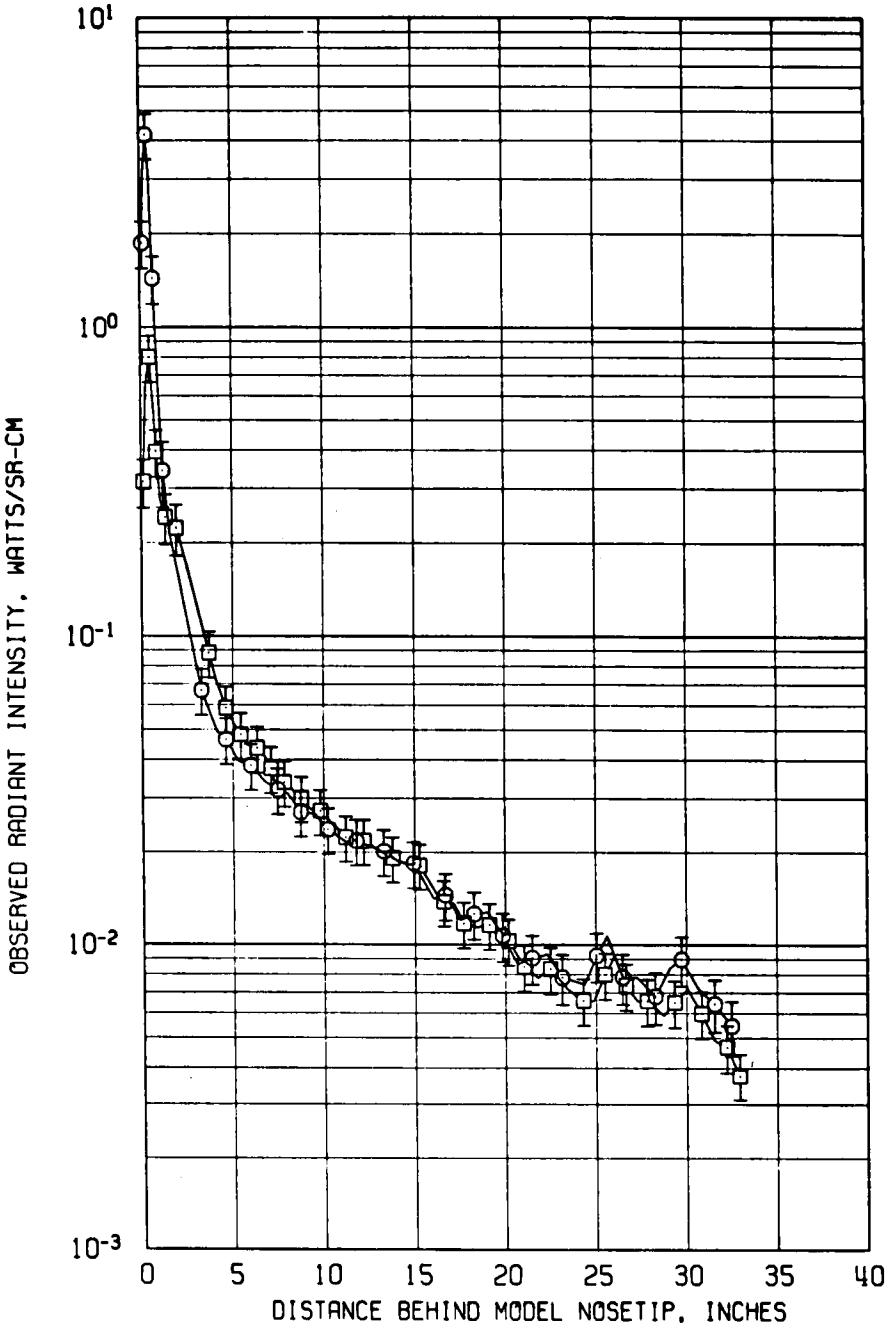
SYMBOL	SHOT NO	STATION	BANDPASS (MICRONS)
⊡	4402	19	2.6-2.8
⊙	4402	19	3.0-4.0



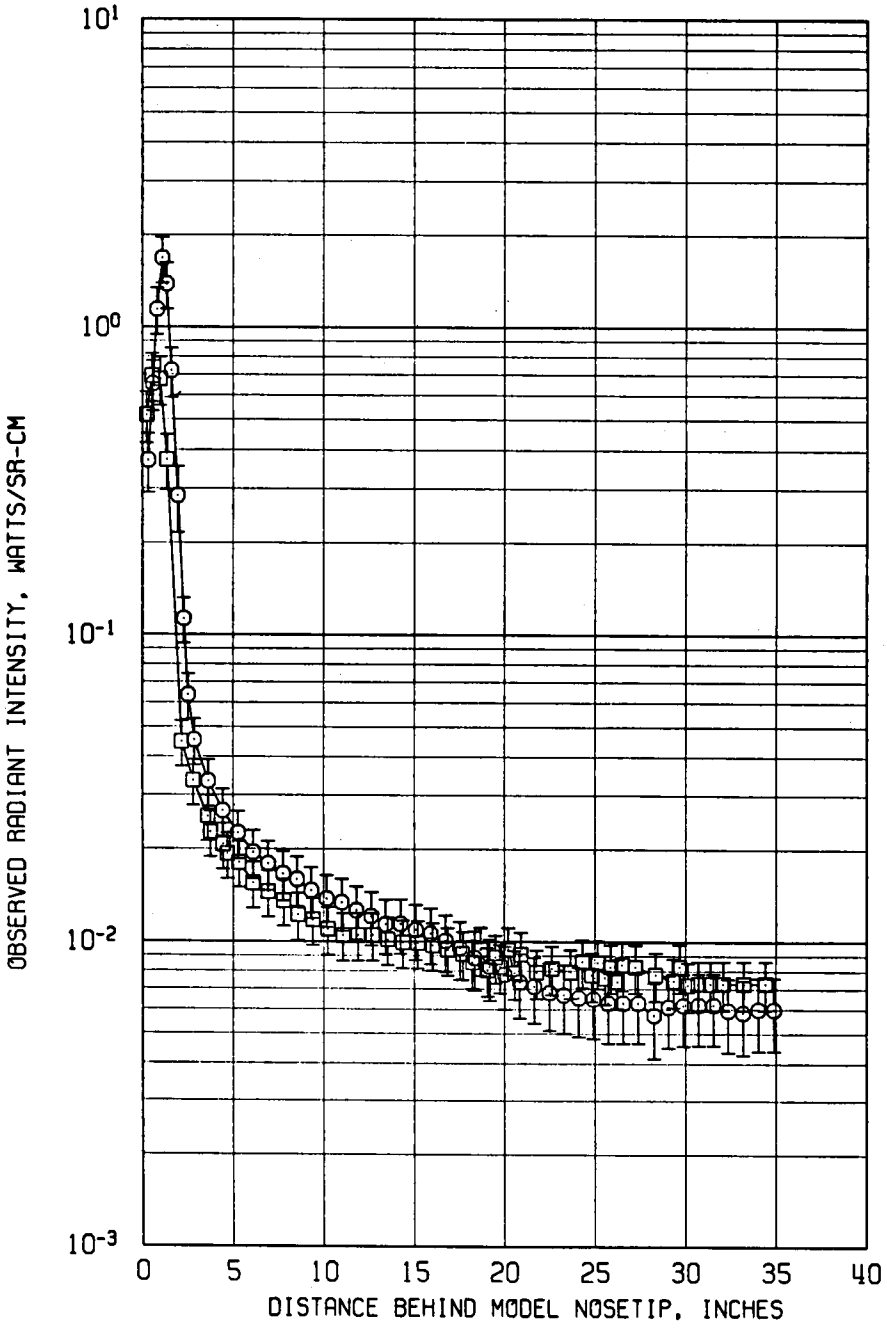
SYMBOL	SHOT NO	STATION	BANDPASS (MICRONS)
⊡	4403	1	0.5-0.7
⊙	4403	1	0.7-0.8



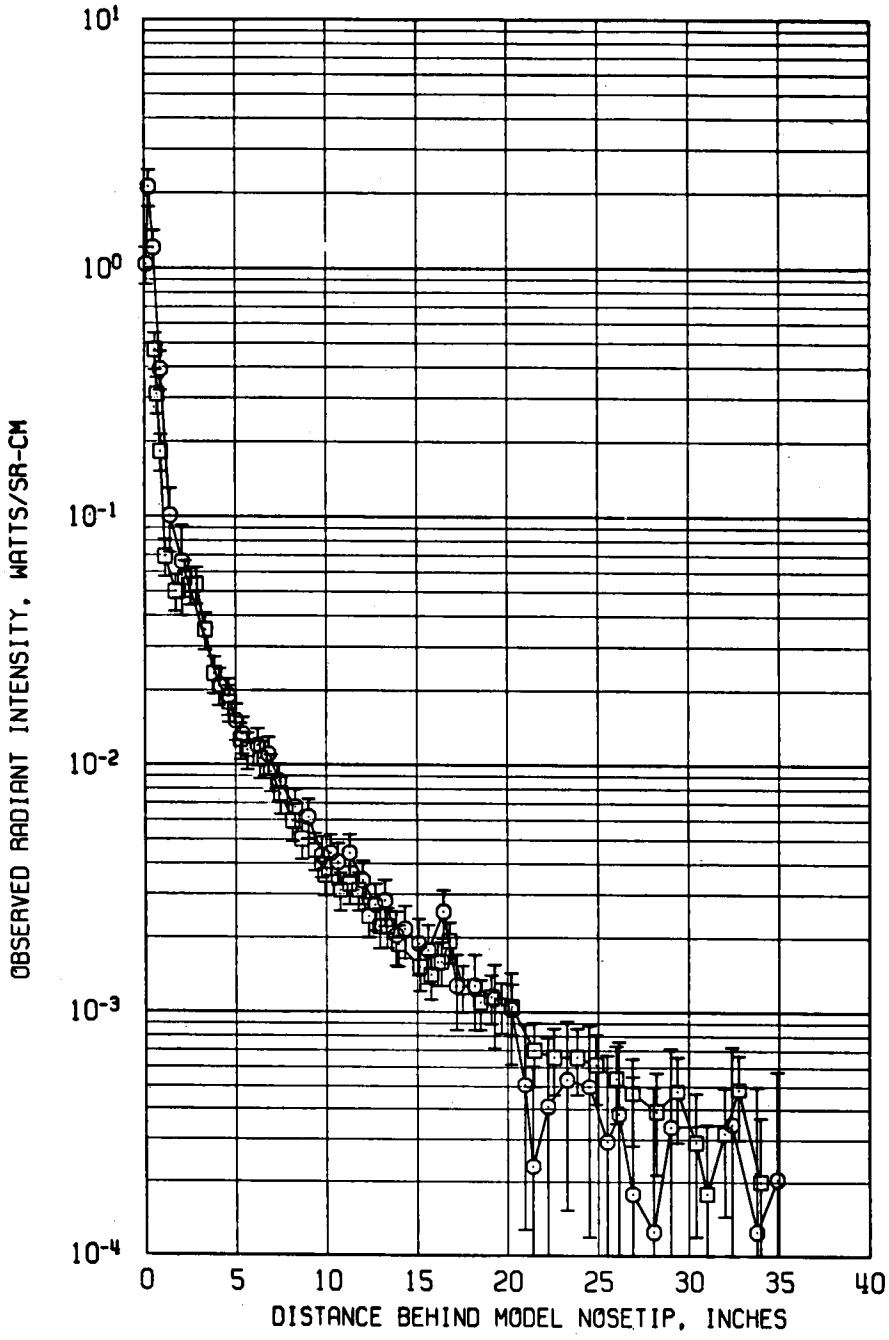
SYMBOL	SHOT NO	STATION	BANDPASS (MICRONS)
⊡	4498	1	0.5-0.7
⊙	4498	1	0.7-0.8



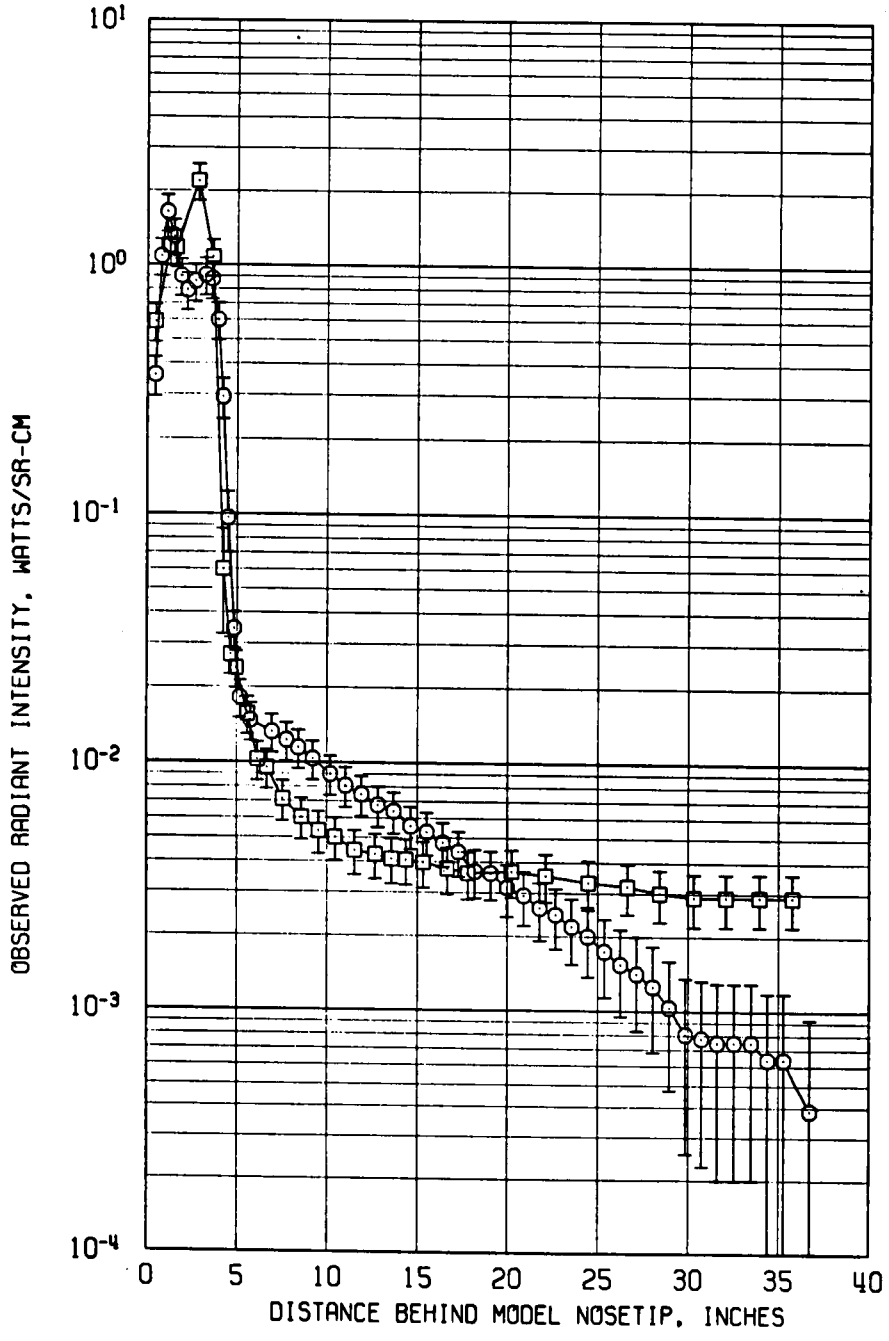
SYMBOL	SHOT NO	STATION	BANDPASS (MICRONS)
⊡	4498	1	2.6-2.8
⊙	4498	1	3.1-3.8

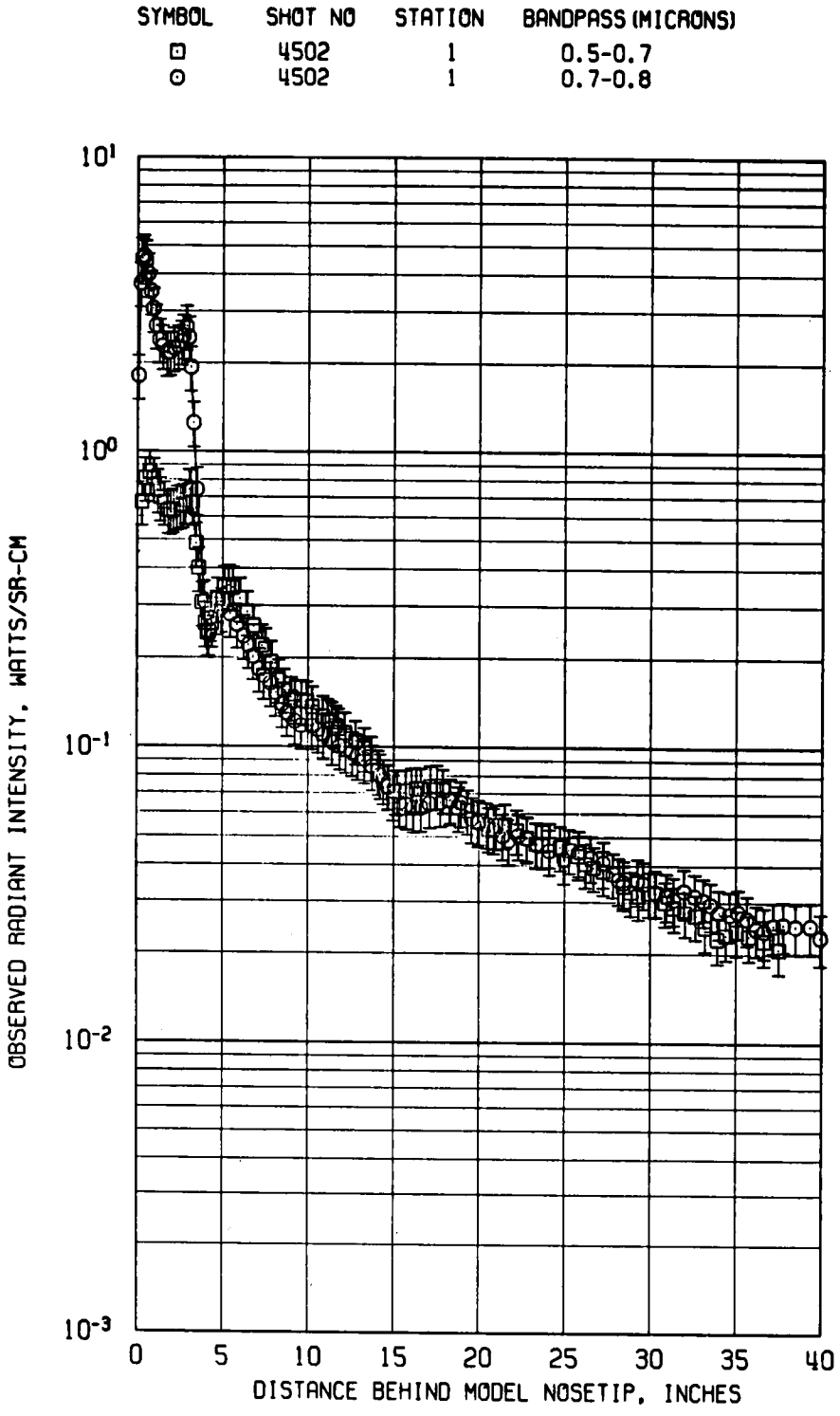


SYMBOL	SHOT NO	STATION	BANDPASS (MICRONS)
⊡	4500	1	0.5-0.7
⊙	4500	1	0.7-0.8

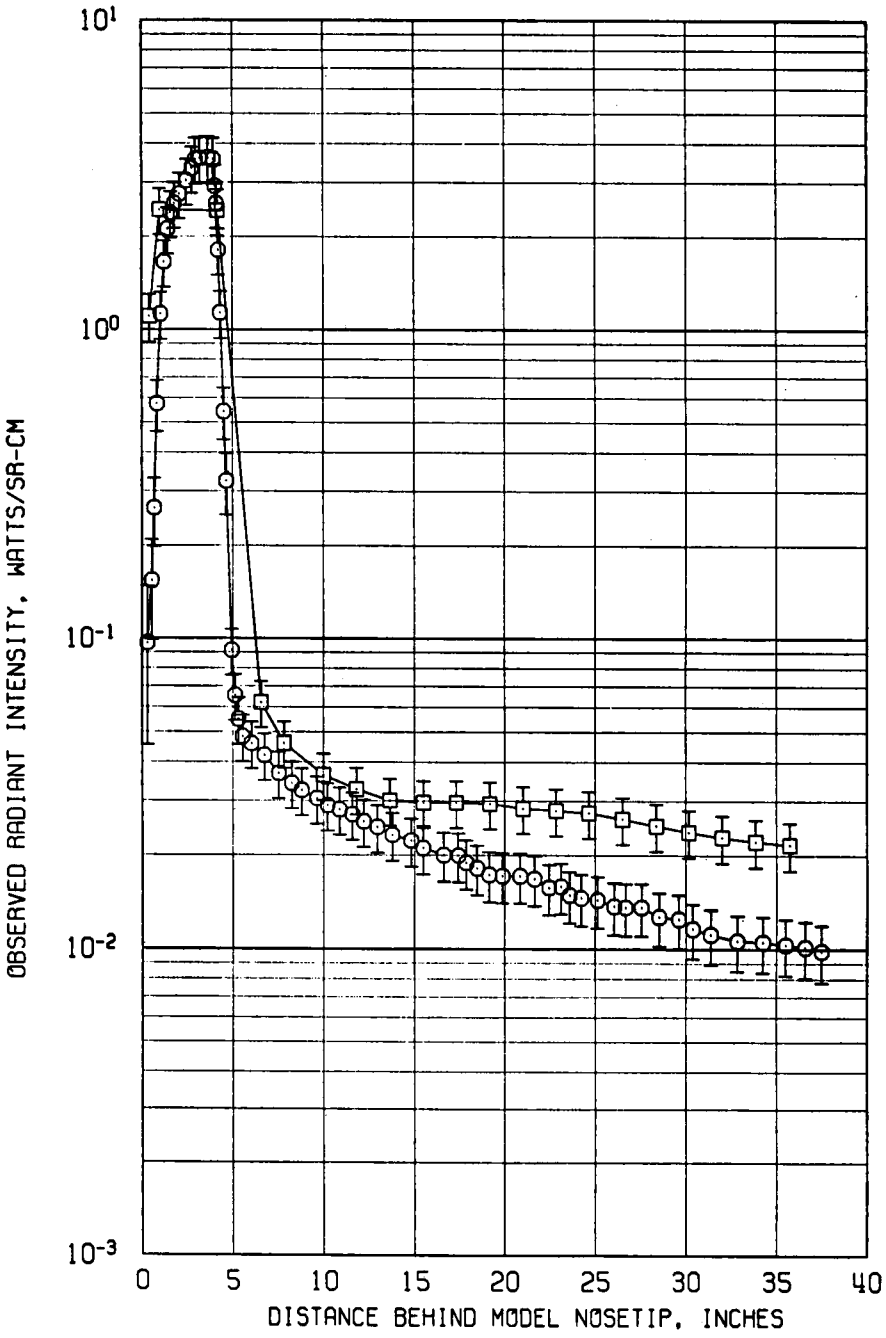


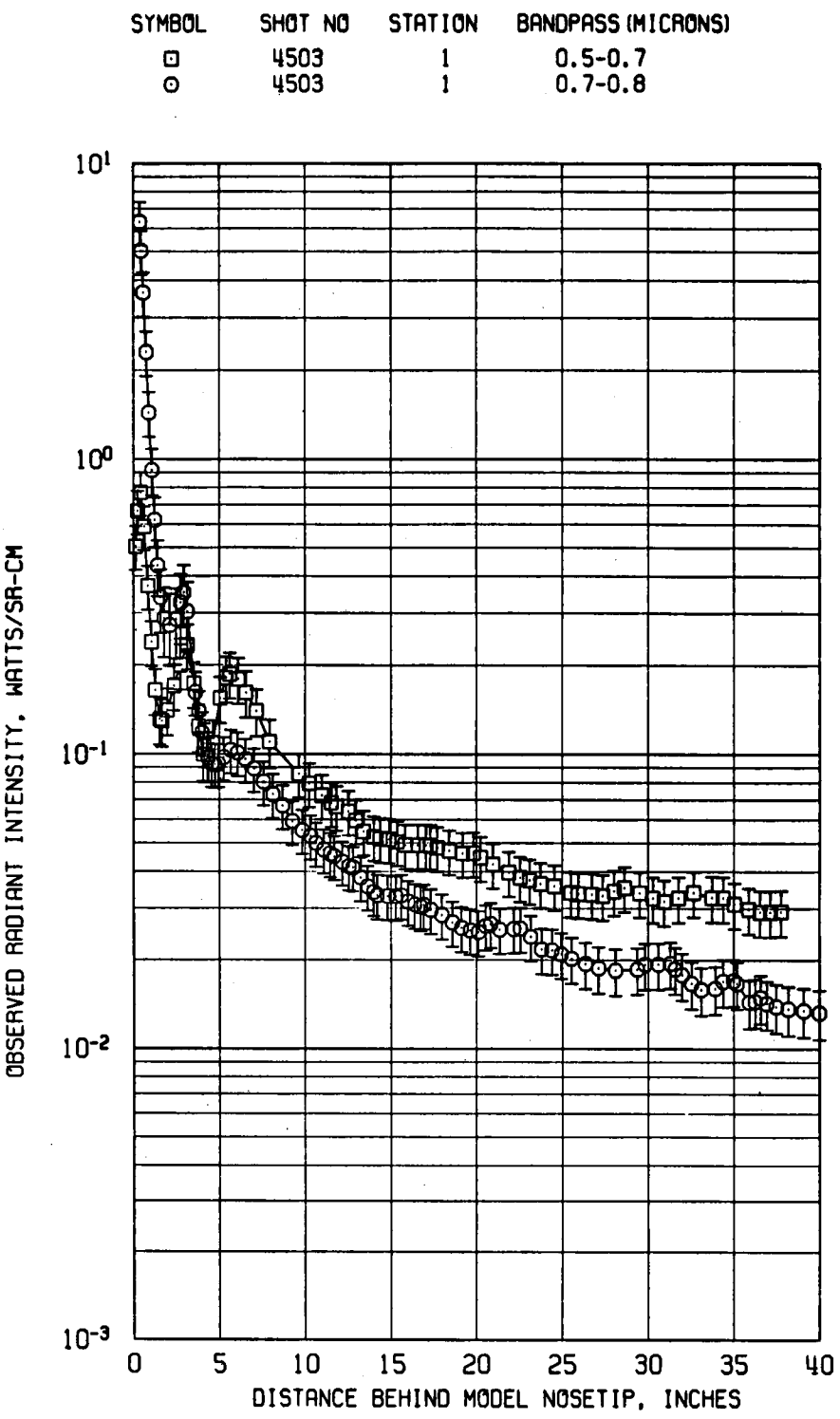
SYMBOL	SHOT NO	STATION	BANDPASS (MICRONS)
⊡	4500	1	2.6-2.8
⊙	4500	1	3.1-3.8



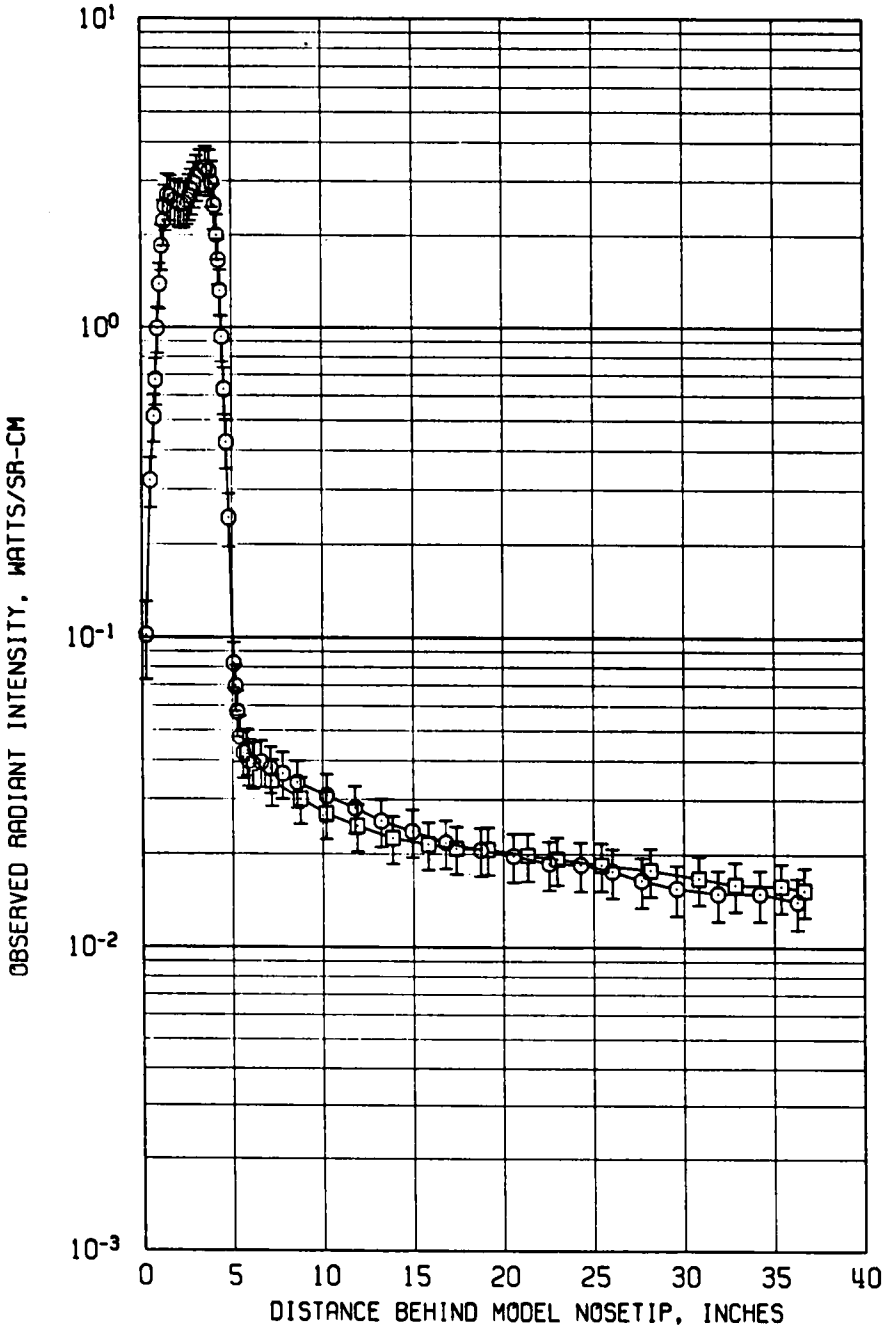

SYMBOL SHOT NO STATION BANDPASS (MICRONS)
⊡ 4502 1 0.5-0.7
⊙ 4502 1 0.7-0.8
OBSERVED RADIANT INTENSITY, WATTS/SR-CM
10¹
10⁰
10⁻¹
10⁻²
10⁻³
0 5 10 15 20 25 30 35 40
DISTANCE BEHIND MODEL NOSETIP, INCHES

SYMBOL	SHOT NO	STATION	BANDPASS (MICRONS)
⊡	4502	1	2.6-2.8
⊙	4502	1	3.1-3.8

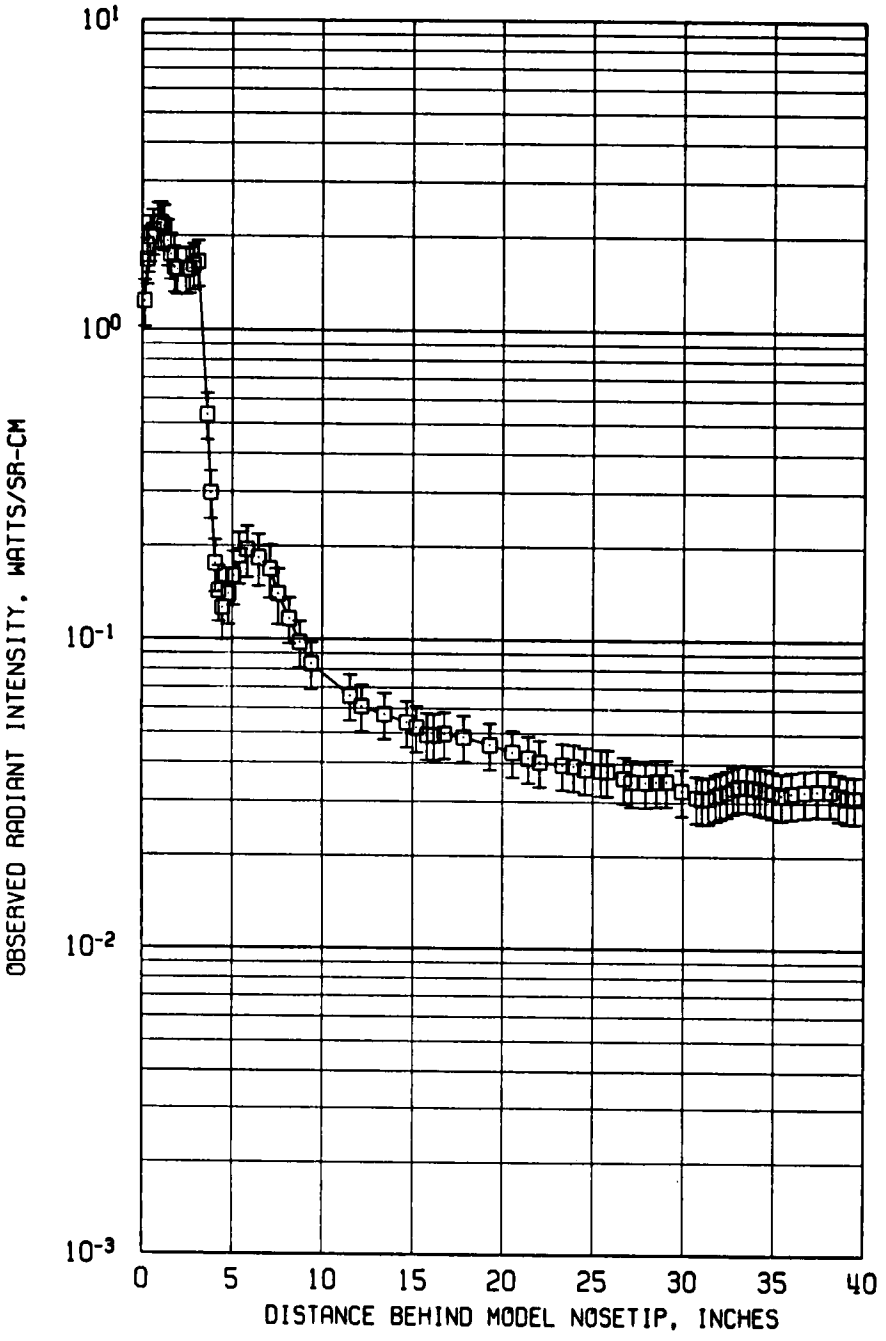



SYMBOL SHOT NO STATION BANDPASS (MICRONS)
0.5-0.7
4503 1
0.7-0.8
4503 1
10^1
10^0
10^{-1}
10^{-2}
10^{-3}
OBSERVED RADIANT INTENSITY, WATTS/SR-CM
0 5 10 15 20 25 30 35 40
DISTANCE BEHIND MODEL NOSETIP, INCHES

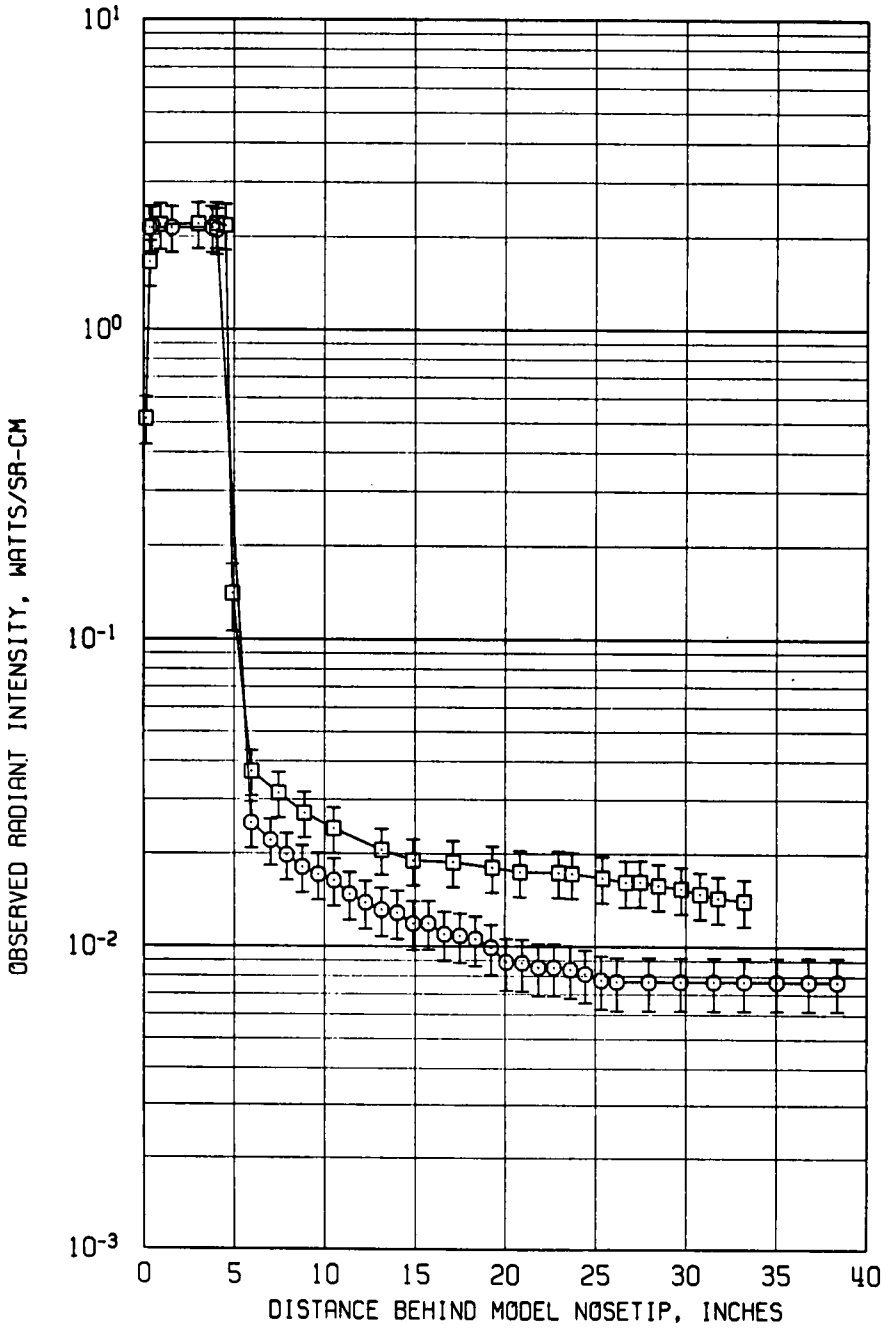
SYMBOL	SHOT NO	STATION	BANDPASS (MICRONS)
⊡	4503	1	2.6-2.8
⊙	4503	1	3.1-3.8



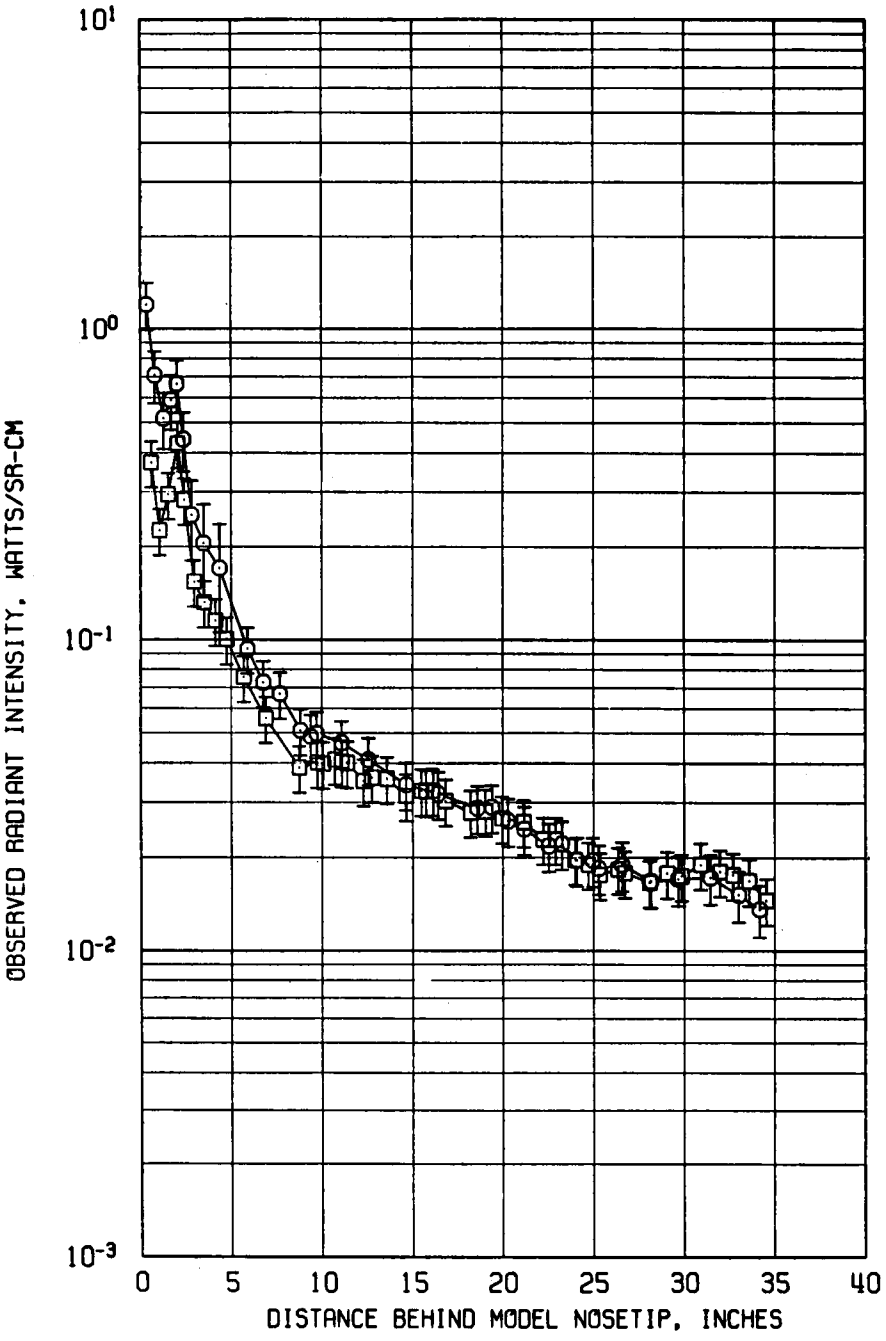
SYMBOL	SHOT NO	STATION	BANDPASS (MICRONS)
⊡	4503	19	0.5-0.7



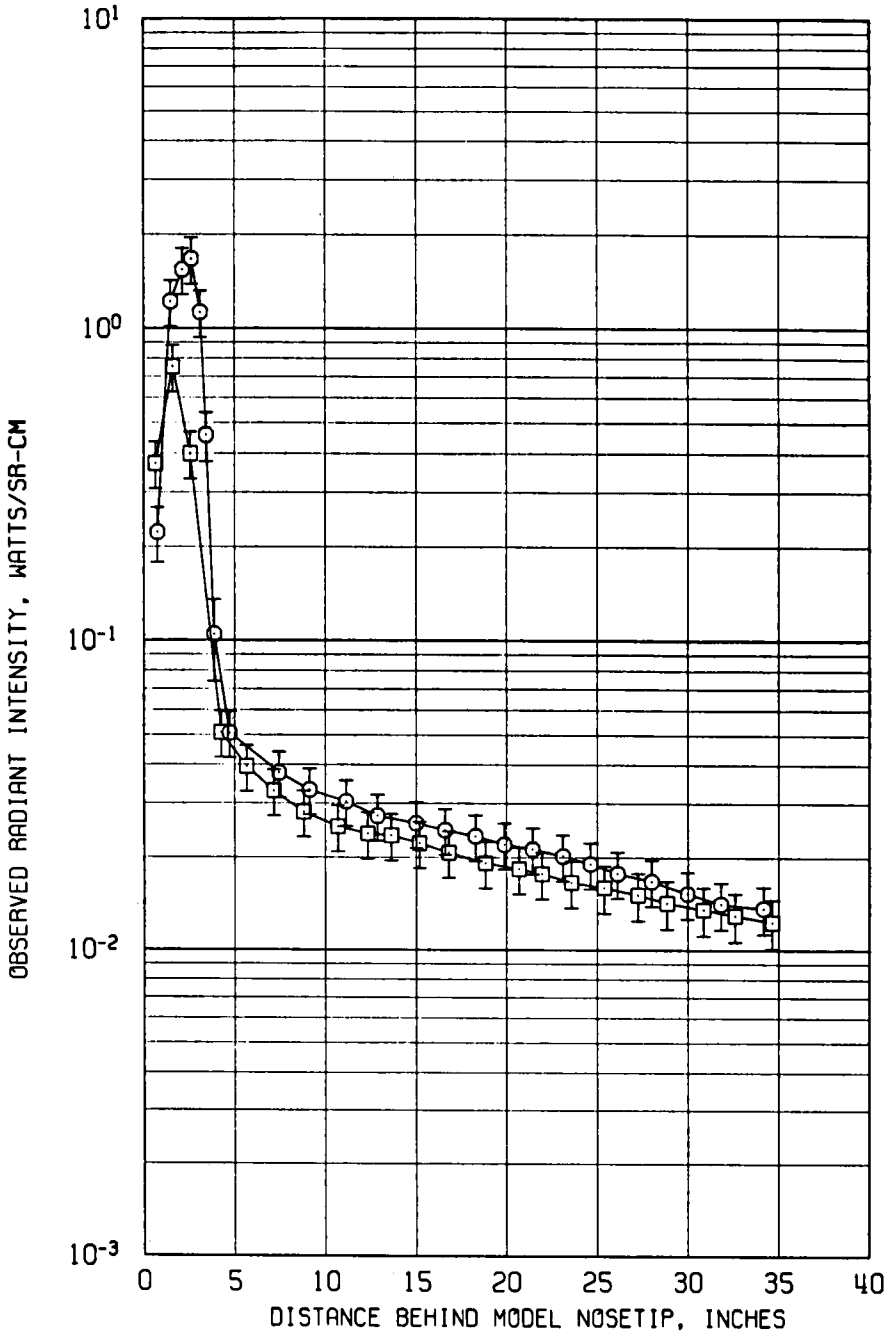
SYMBOL	SHOT NO	STATION	BANDPASS (MICRONS)
⊡	4503	19	2.6-2.8
⊙	4503	19	3.0-4.0



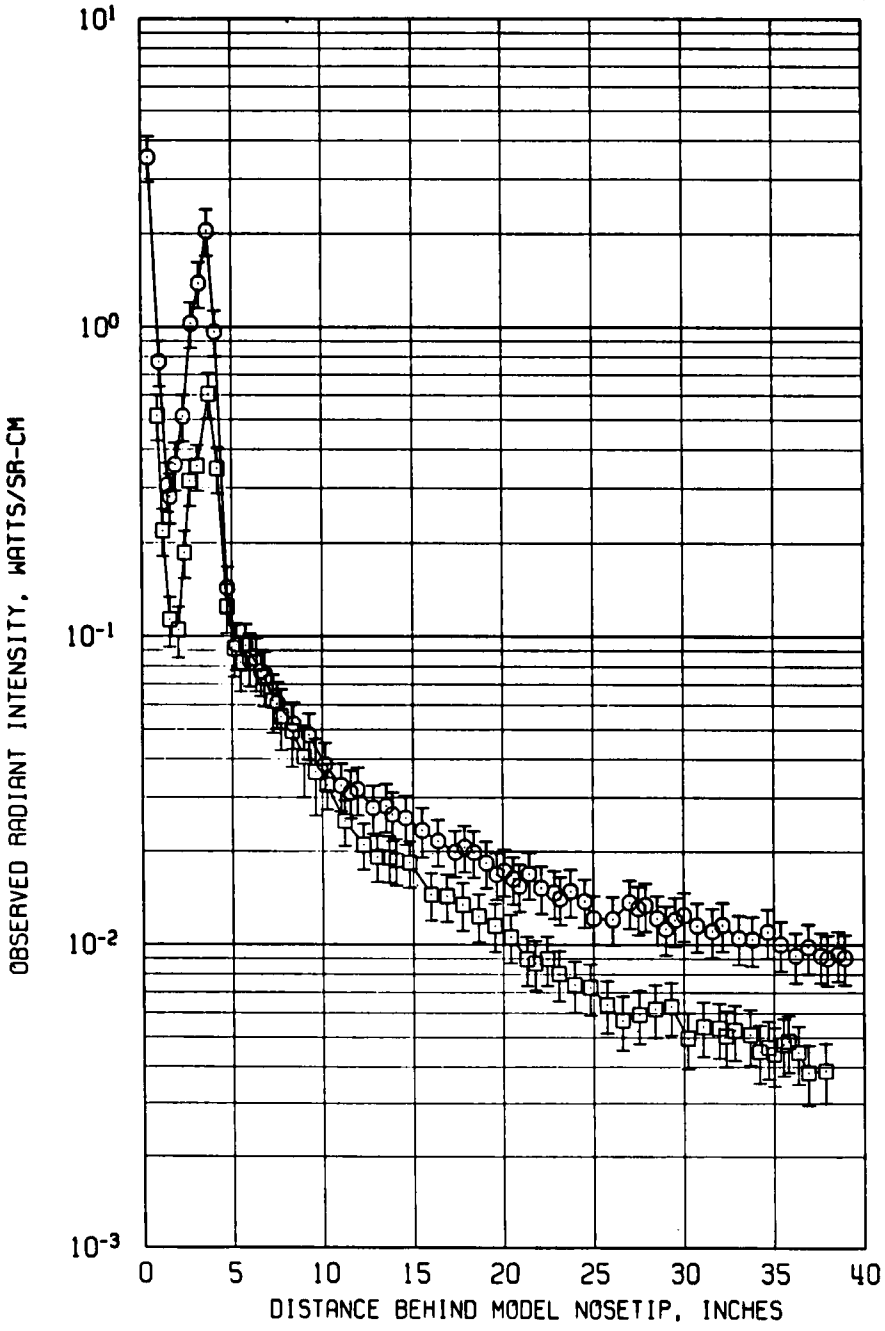
SYMBOL	SHOT NO	STATION	BANDPASS (MICRONS)
⊡	4504	1	0.5-0.7
⊙	4504	1	0.7-0.8



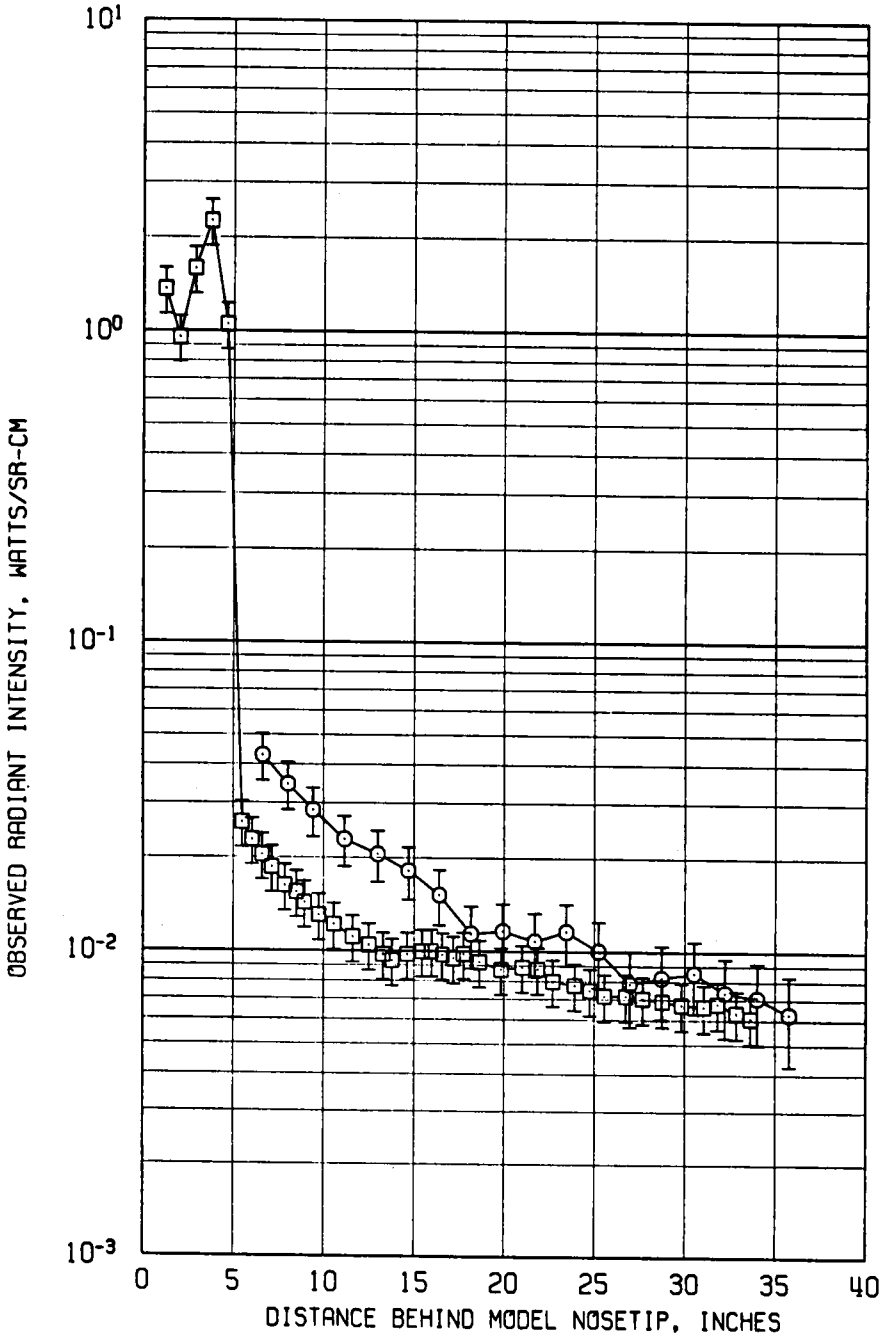
SYMBOL	SHOT NO	STATION	BANDPASS (MICRONS)
⊡	4504	1	2.6-2.8
⊙	4504	1	3.1-3.8



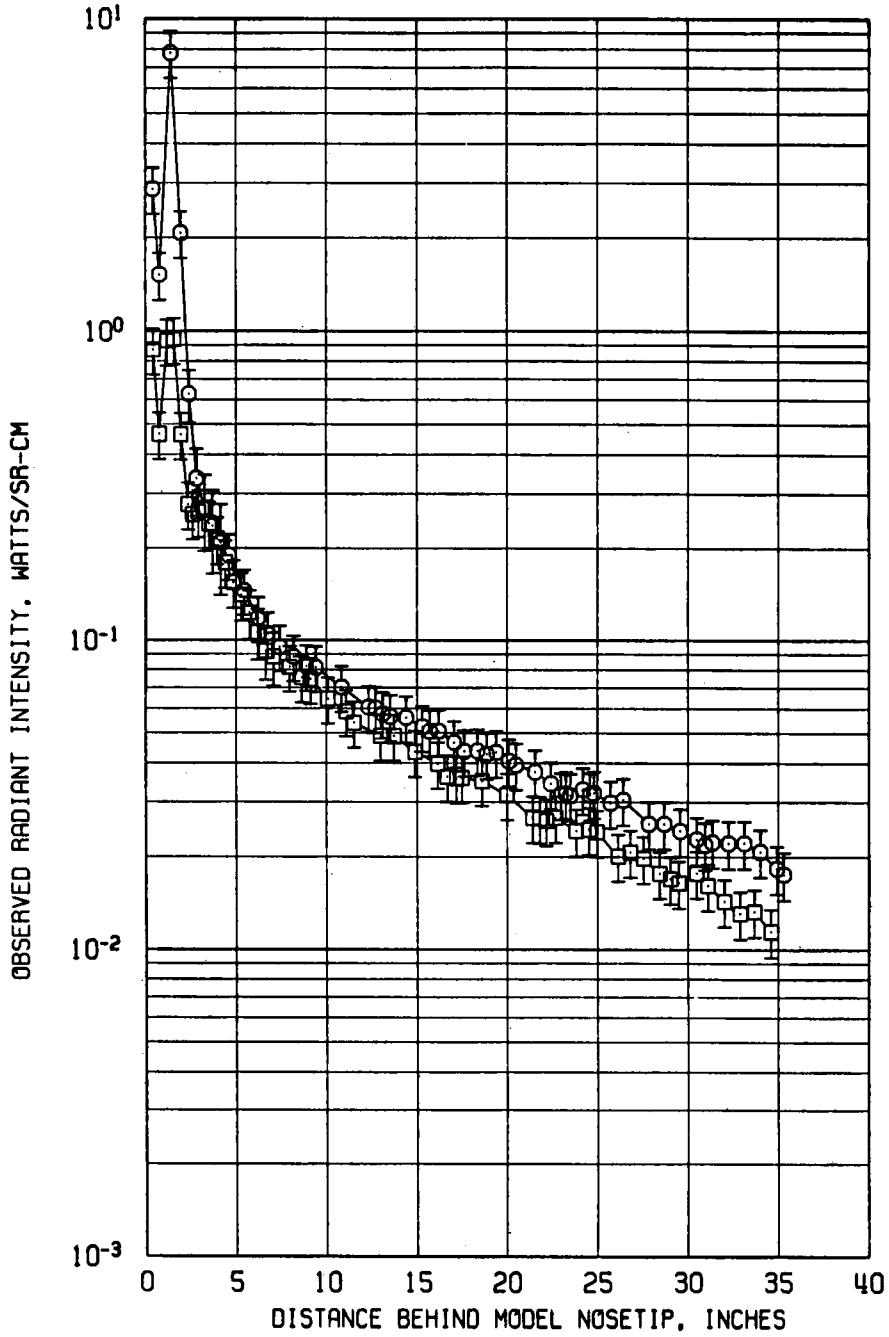
SYMBOL	SHOT NO	STATION	BANDPASS (MICRONS)
⊡	4505	19	0.5-0.7
⊙	4505	19	0.7-0.9

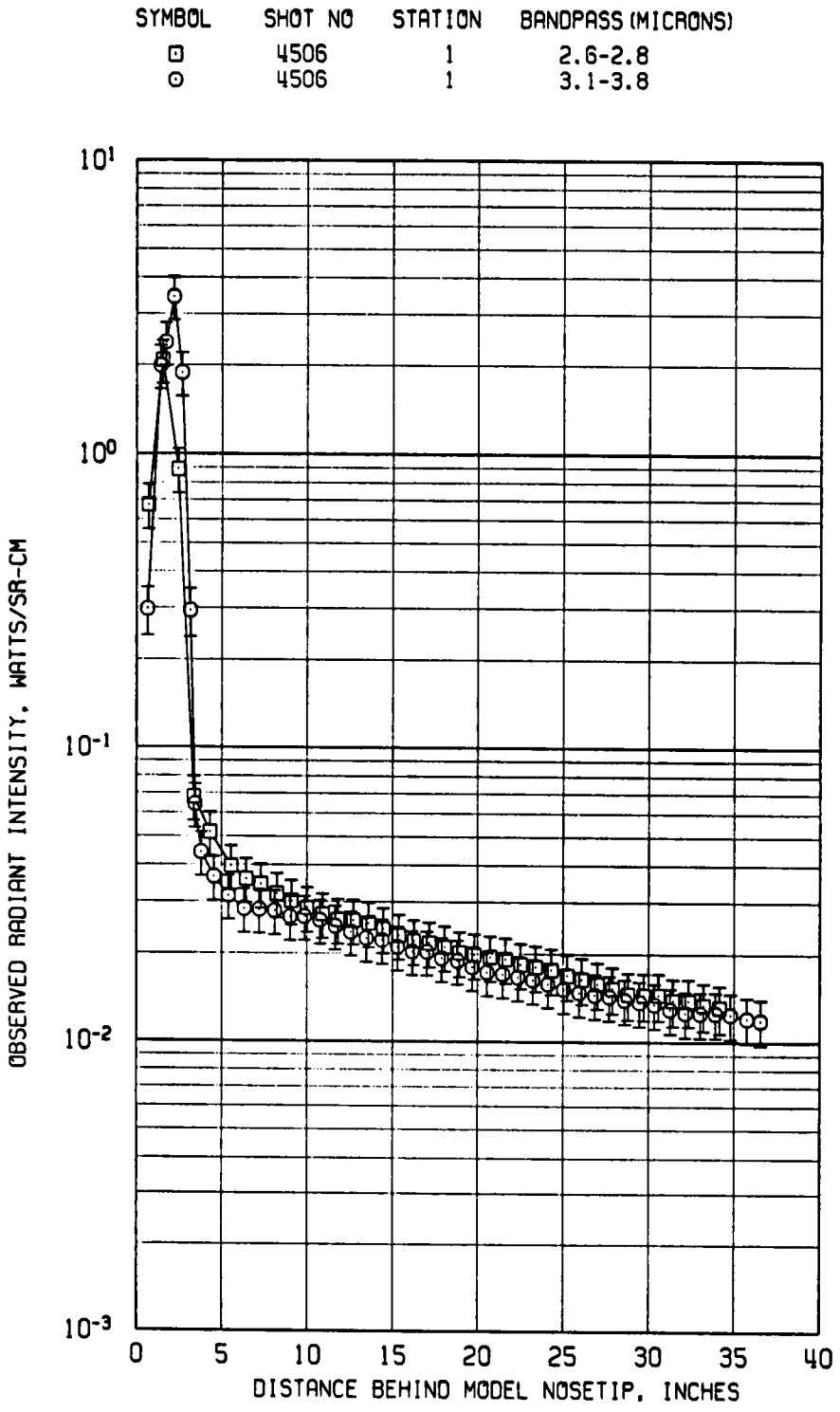


SYMBOL	SHOT NO	STATION	BANDPASS (MICRONS)
⊡	4505	19	2.6-2.8
⊙	4505	19	3.0-4.0

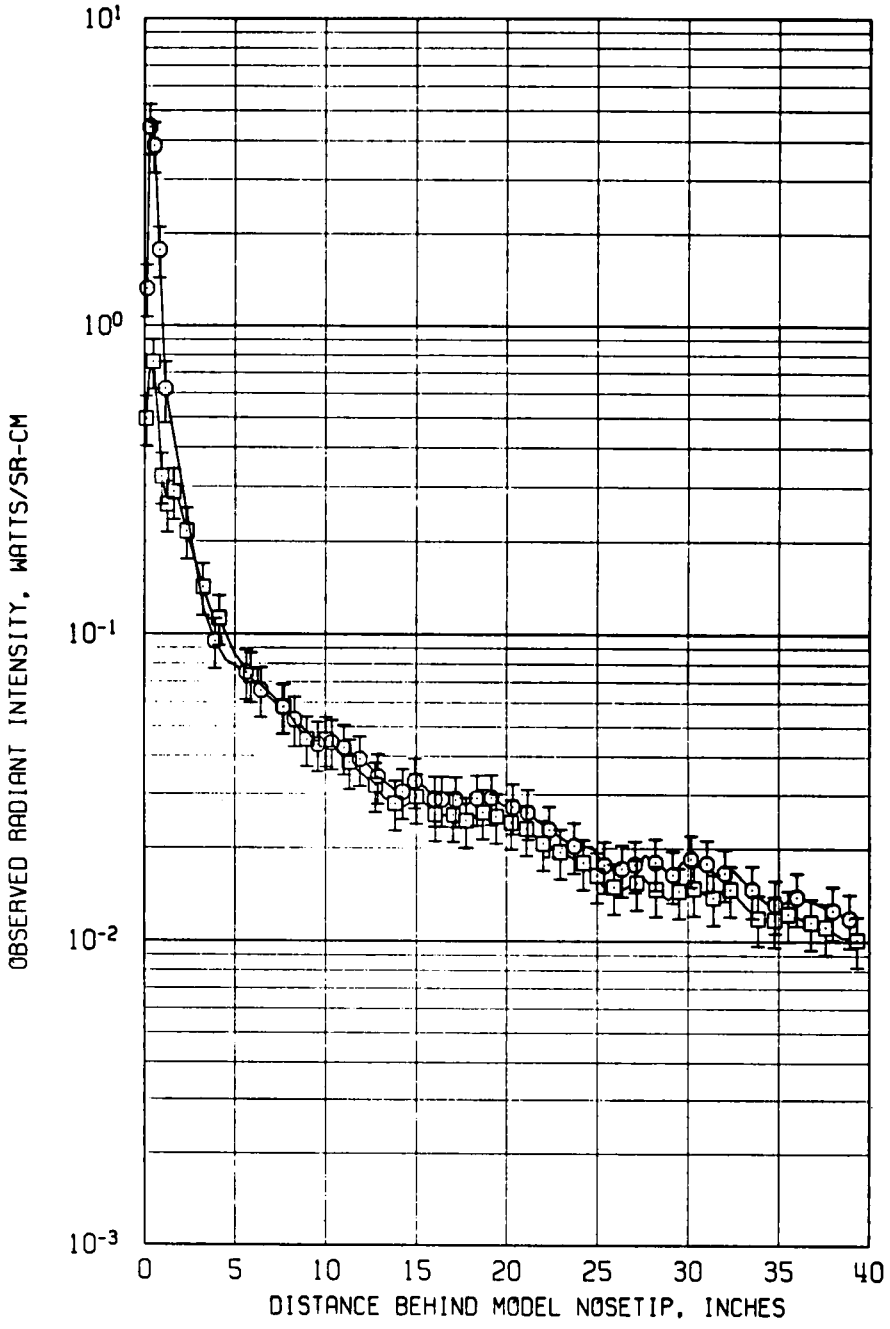


SYMBOL	SHOT NO	STATION	BANDPASS (MICRONS)
⊡	4506	1	0.5-0.7
⊙	4506	1	0.7-0.8

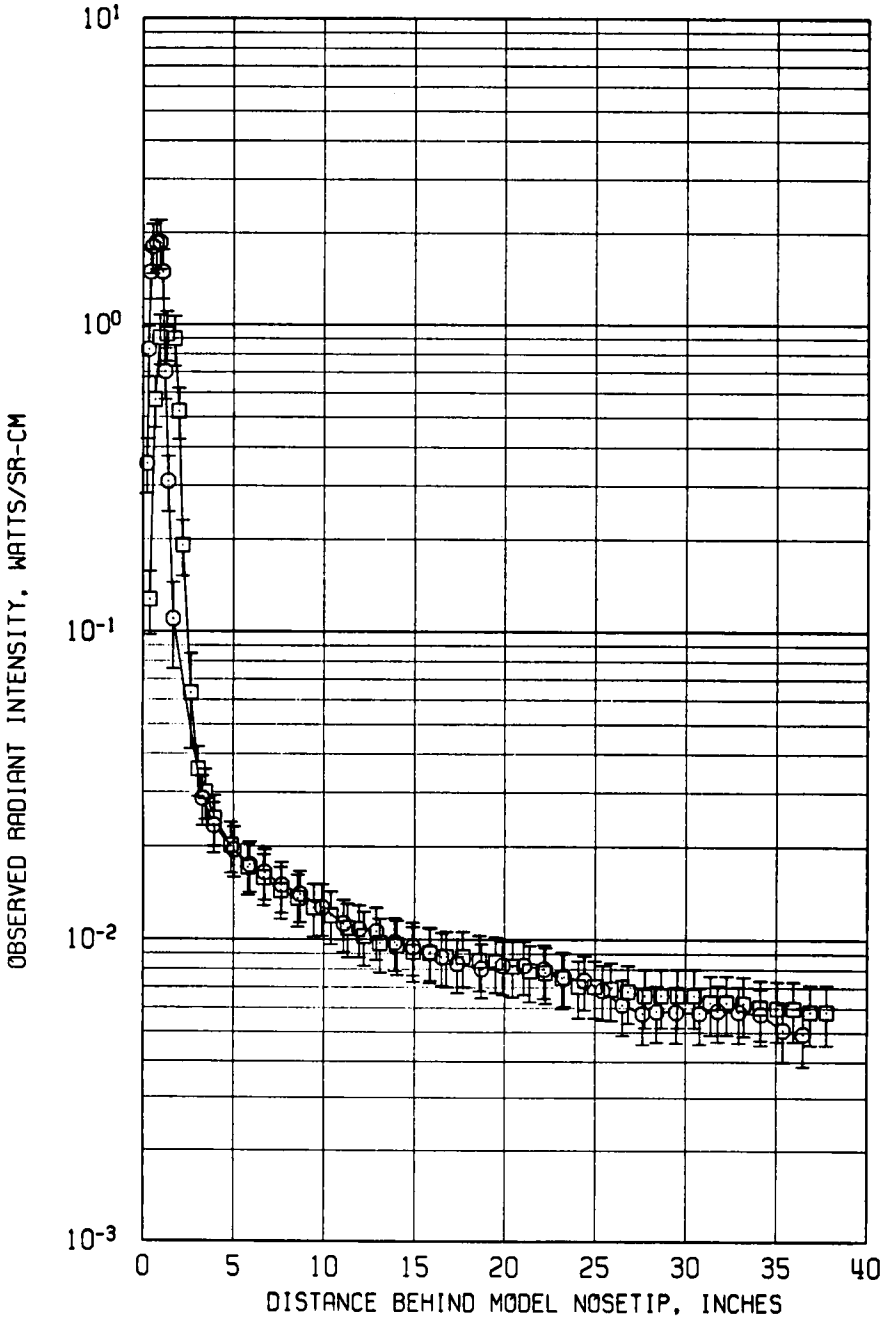



SYMBOL SHOT NO STATION BANDPASS (MICRONS)
4506 1 2.6-2.8
4506 1 3.1-3.8
OBSERVED RADIANT INTENSITY, WATTS/SR-CM
10^{1}
10^{0}
10^{-1}
10^{-2}
10^{-3}
0 5 10 15 20 25 30 35 40
DISTANCE BEHIND MODEL NOSETIP, INCHES

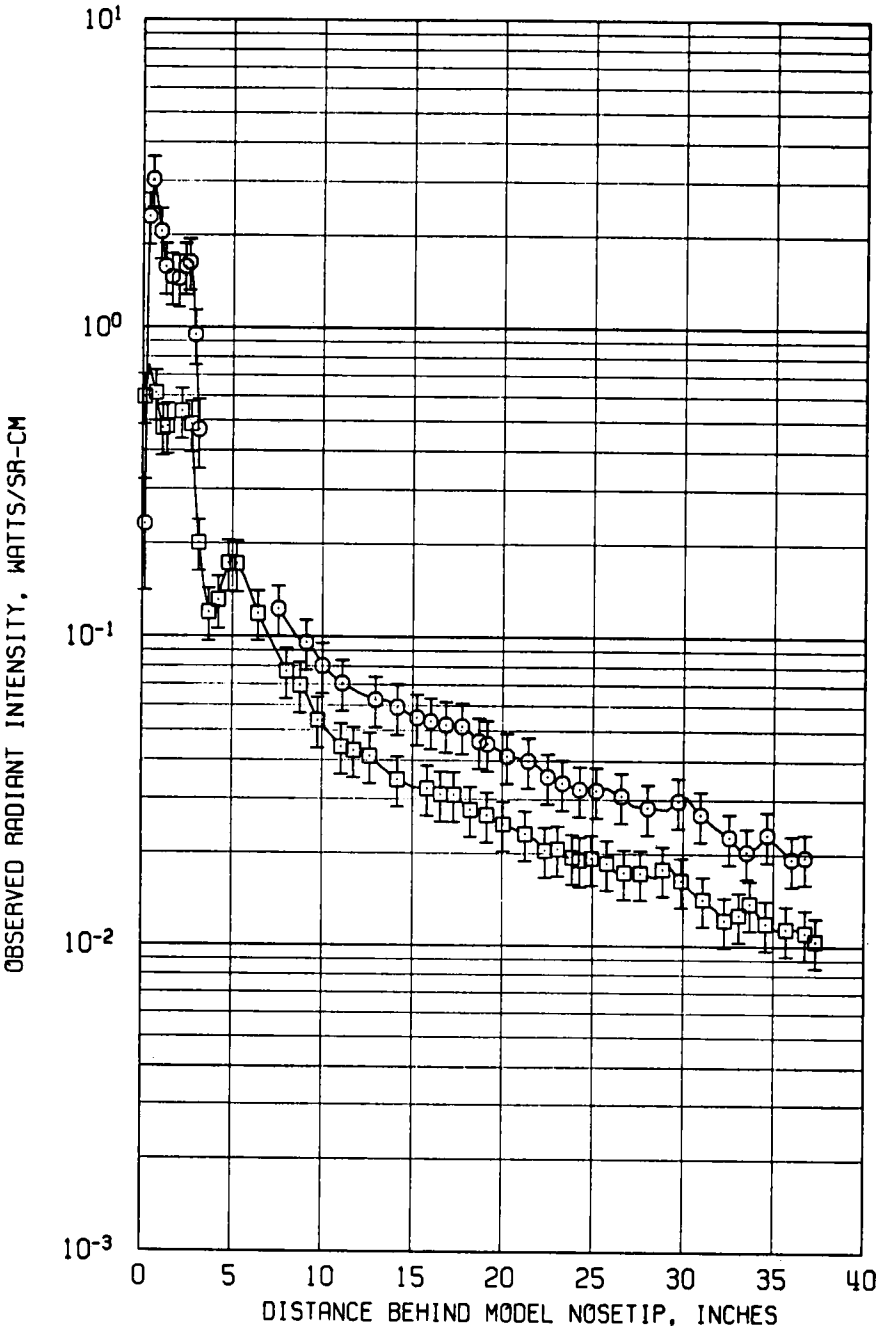
SYMBOL	SHOT NO	STATION	BANDPASS (MICRONS)
⊡	4657	1	0.5-0.7
⊙	4657	1	0.7-0.8



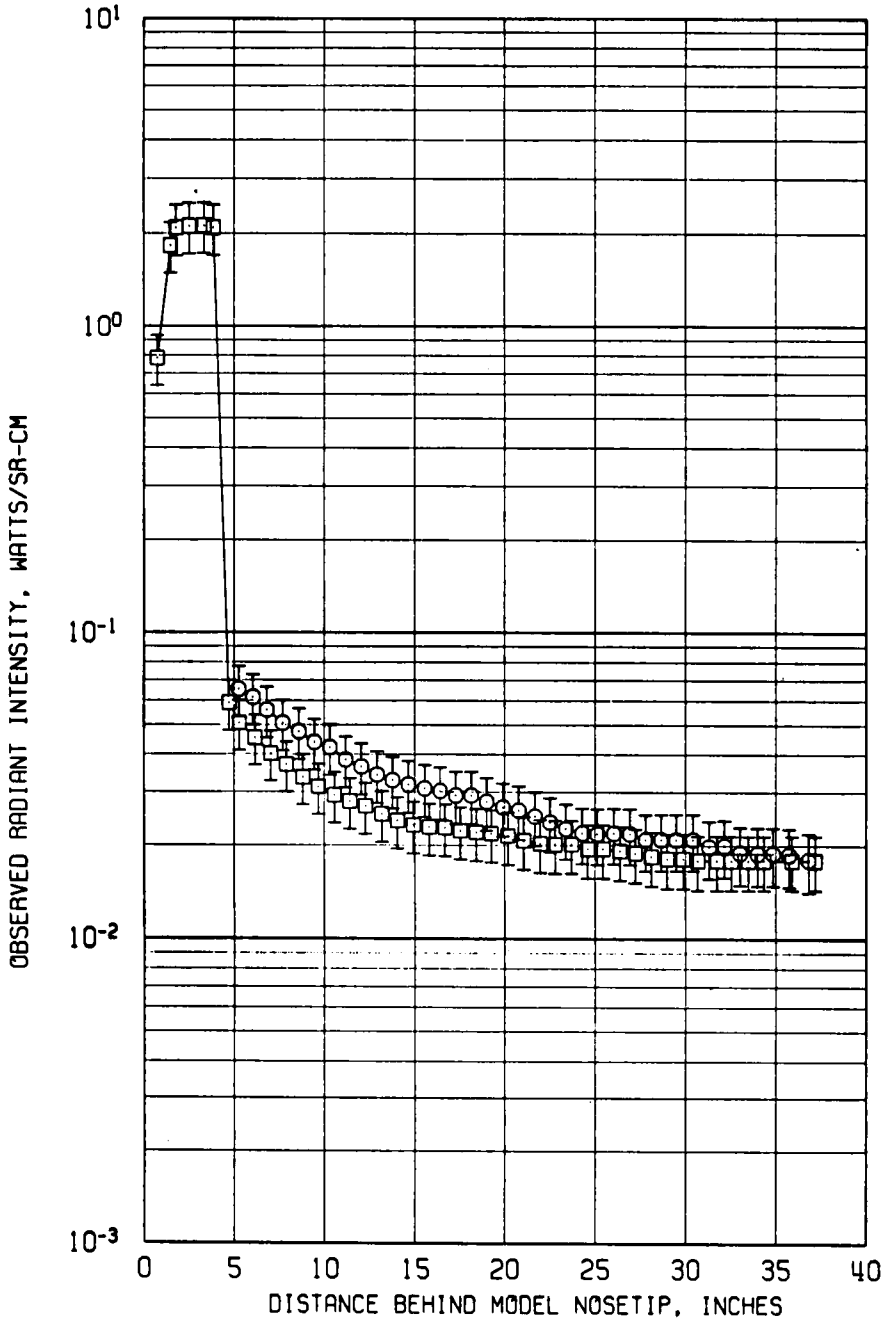
SYMBOL	SHOT NO	STATION	BANDPASS (MICRONS)
⊡	4657	1	2.6-2.8
⊙	4657	1	3.1-3.8



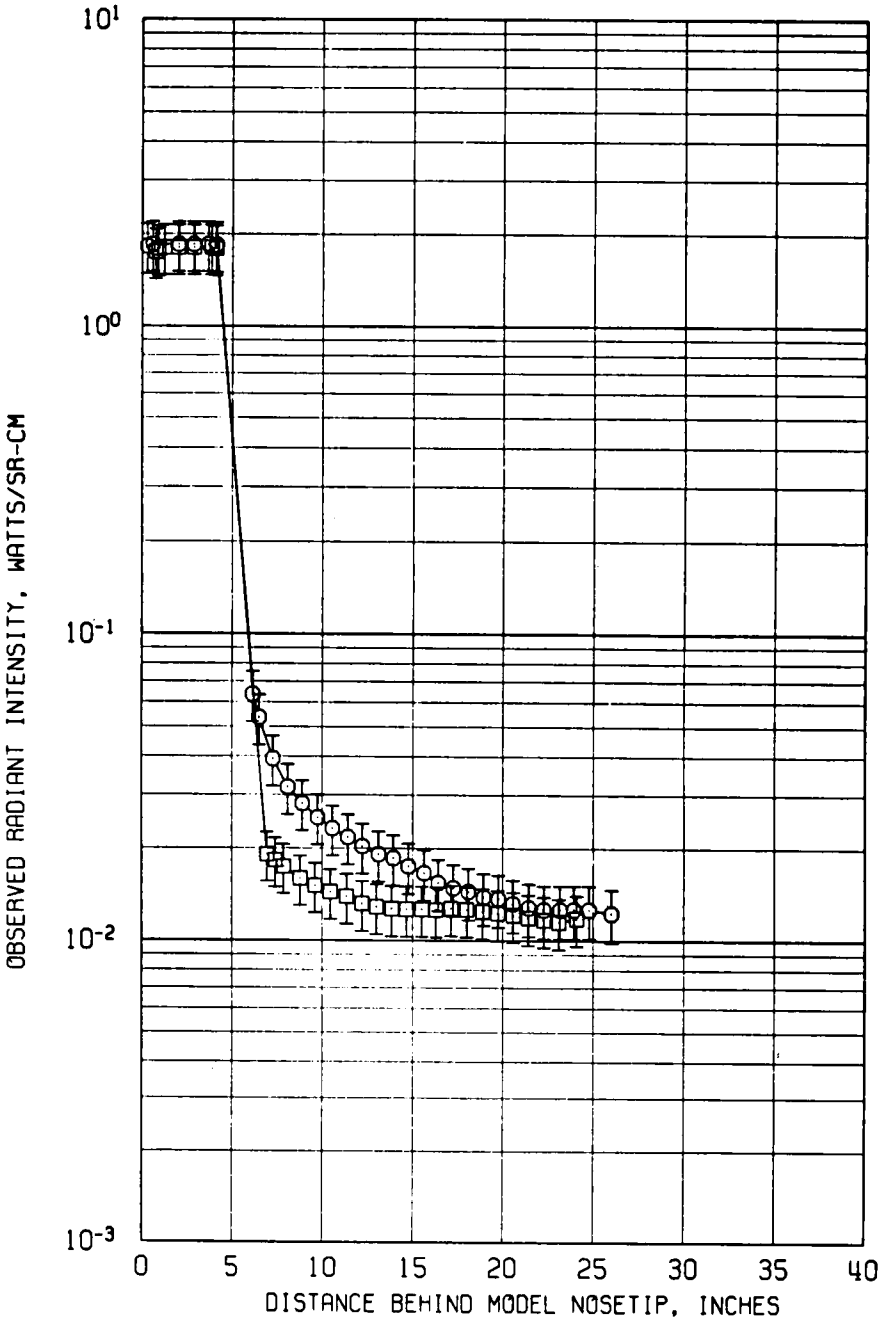
SYMBOL	SHOT NO	STATION	BANDPASS (MICRONS)
⊡	4659	1	0.5-0.7
⊙	4659	1	0.7-0.8



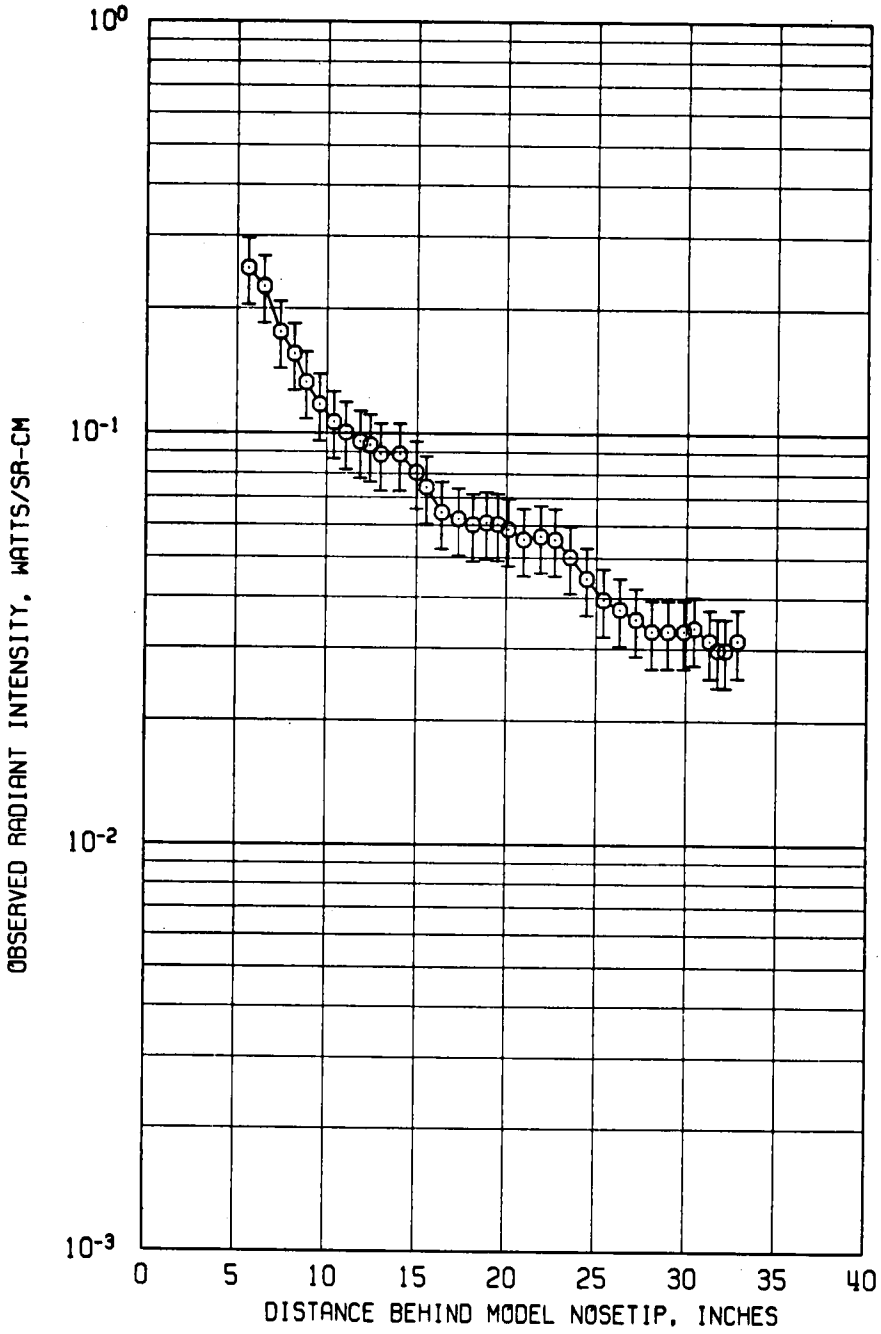
SYMBOL	SHOT NO	STATION	BANDPASS (MICRONS)
⊡	4659	1	2.6-2.8
⊙	4659	1	3.1-3.8

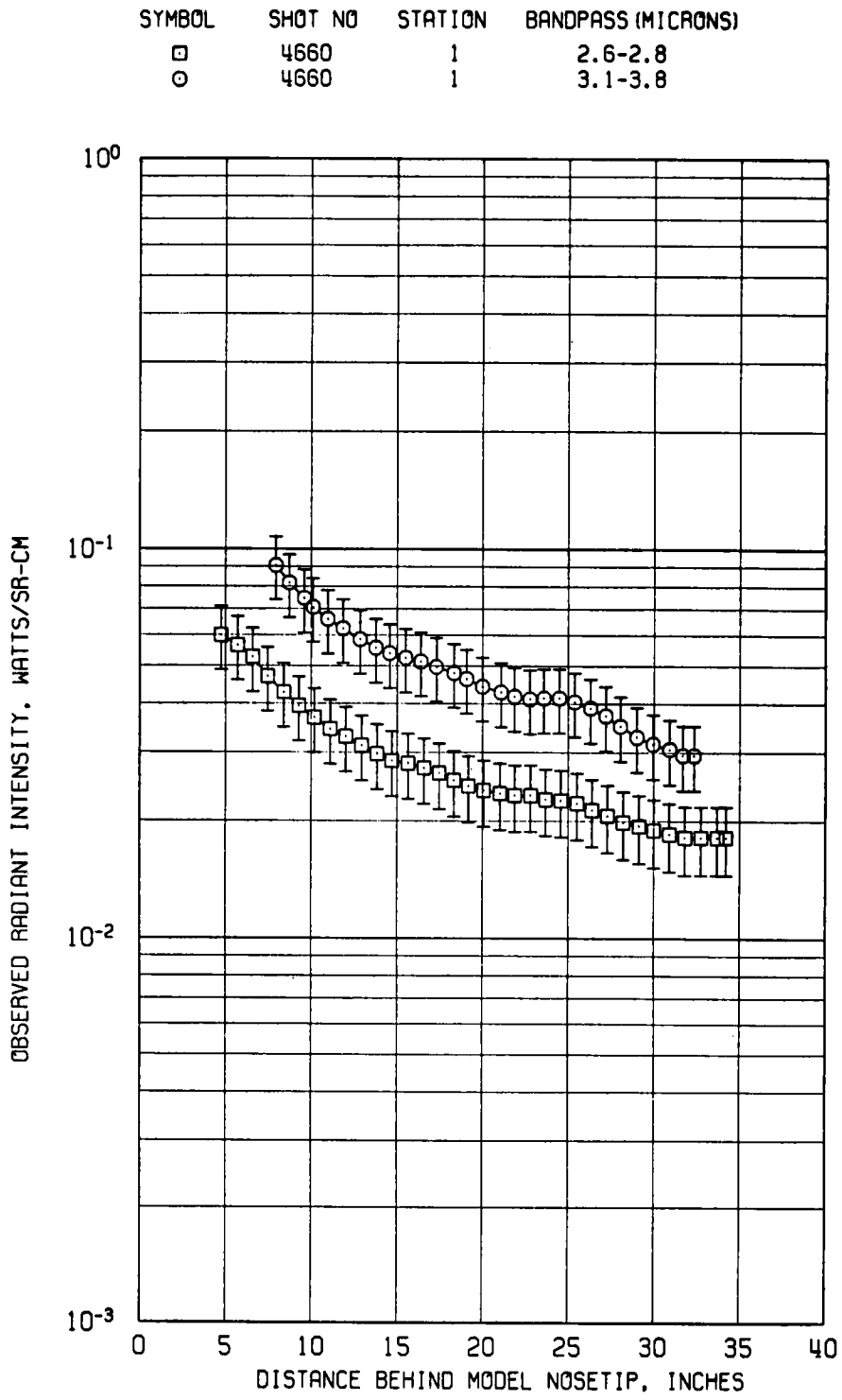


SYMBOL	SHOT NO	STATION	BANDPASS (MICRONS)
⊡	4659	19	2.6-2.8
⊙	4659	19	3.0-4.0

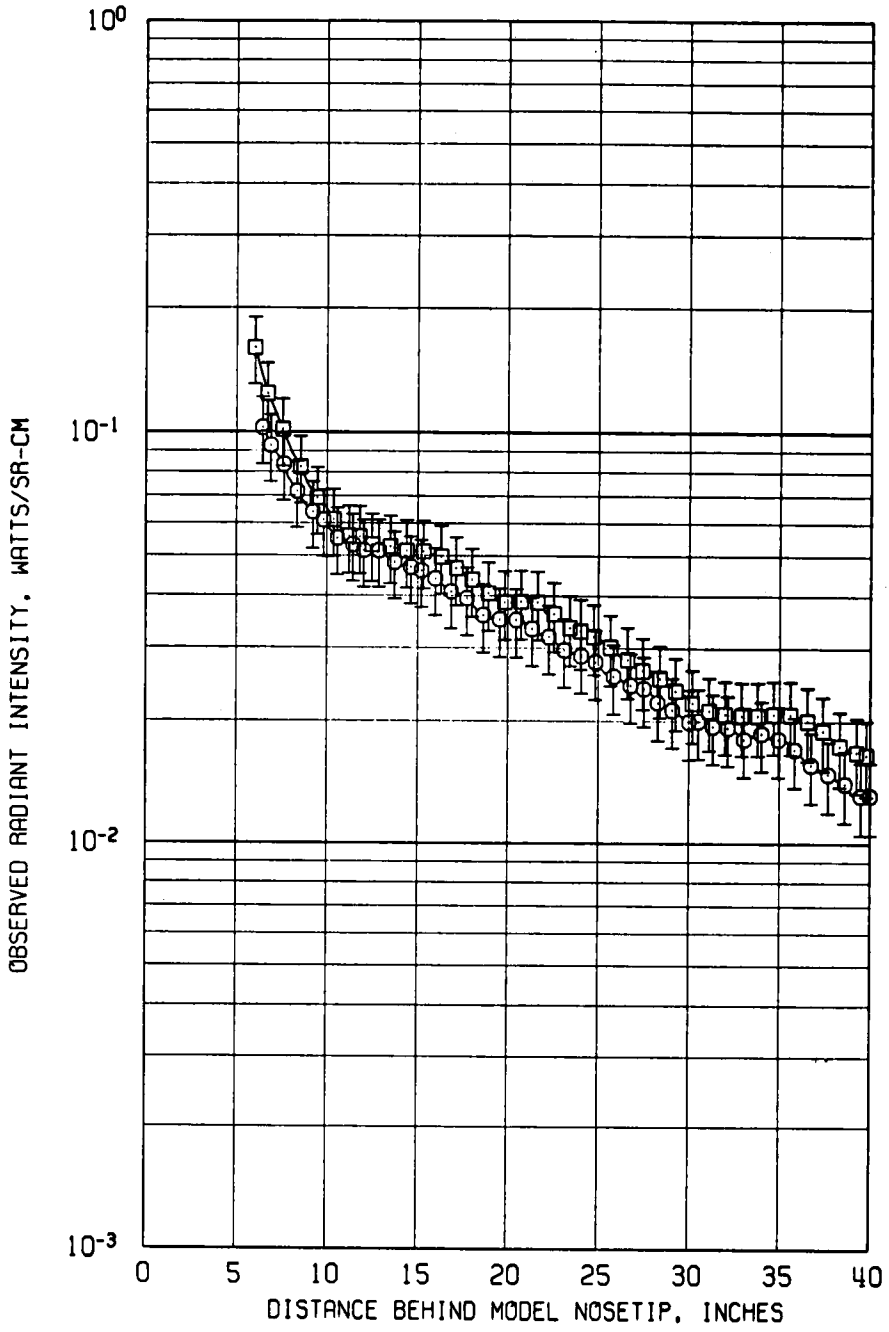


SYMBOL	SHOT NO	STATION	BANDPASS (MICRONS)
⊙	4660	1	0.7-0.8

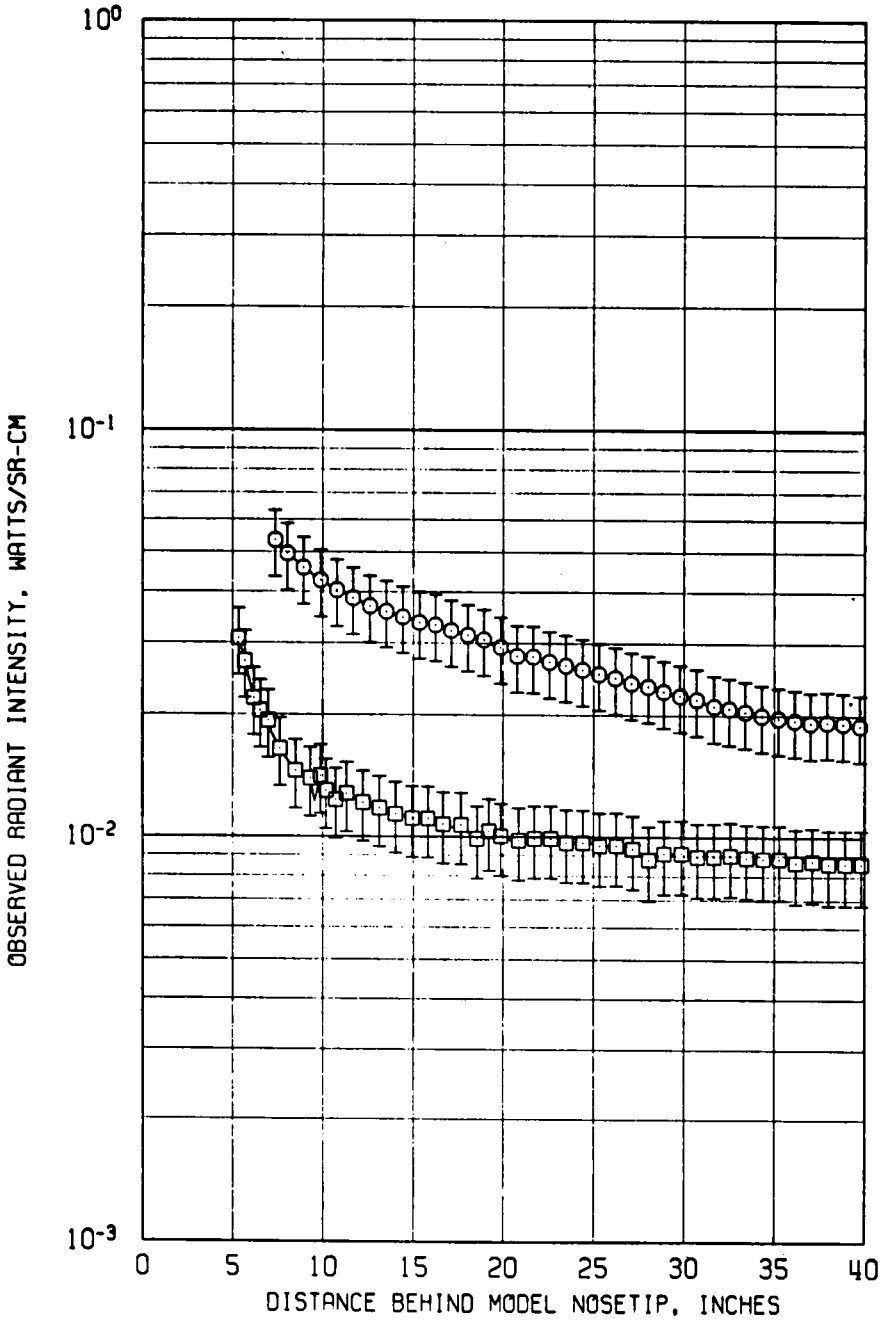



SYMBOL SHOT NO STATION BANDPASS (MICRONS)
4660 1 2.6-2.8
4660 1 3.1-3.8
10^0
10^{-1}
10^{-2}
10^{-3}
OBSERVED RADIANT INTENSITY, WATTS/SR-CM
0 5 10 15 20 25 30 35 40
DISTANCE BEHIND MODEL NOSETIP, INCHES

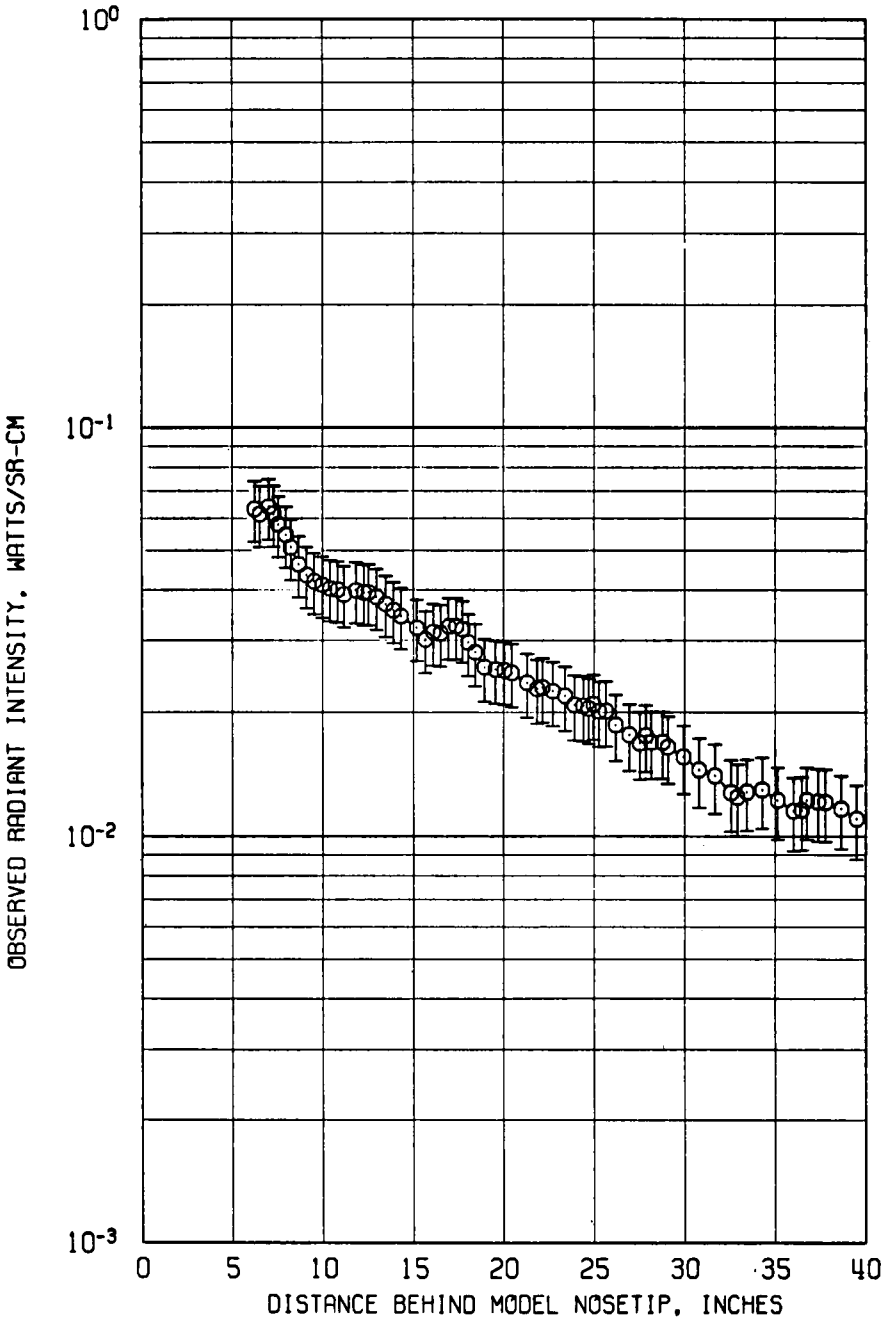
SYMBOL	SHOT NO	STATION	BANDPASS (MICRONS)
⊡	4810	1	0.5-0.7
⊙	4810	1	0.7-0.8



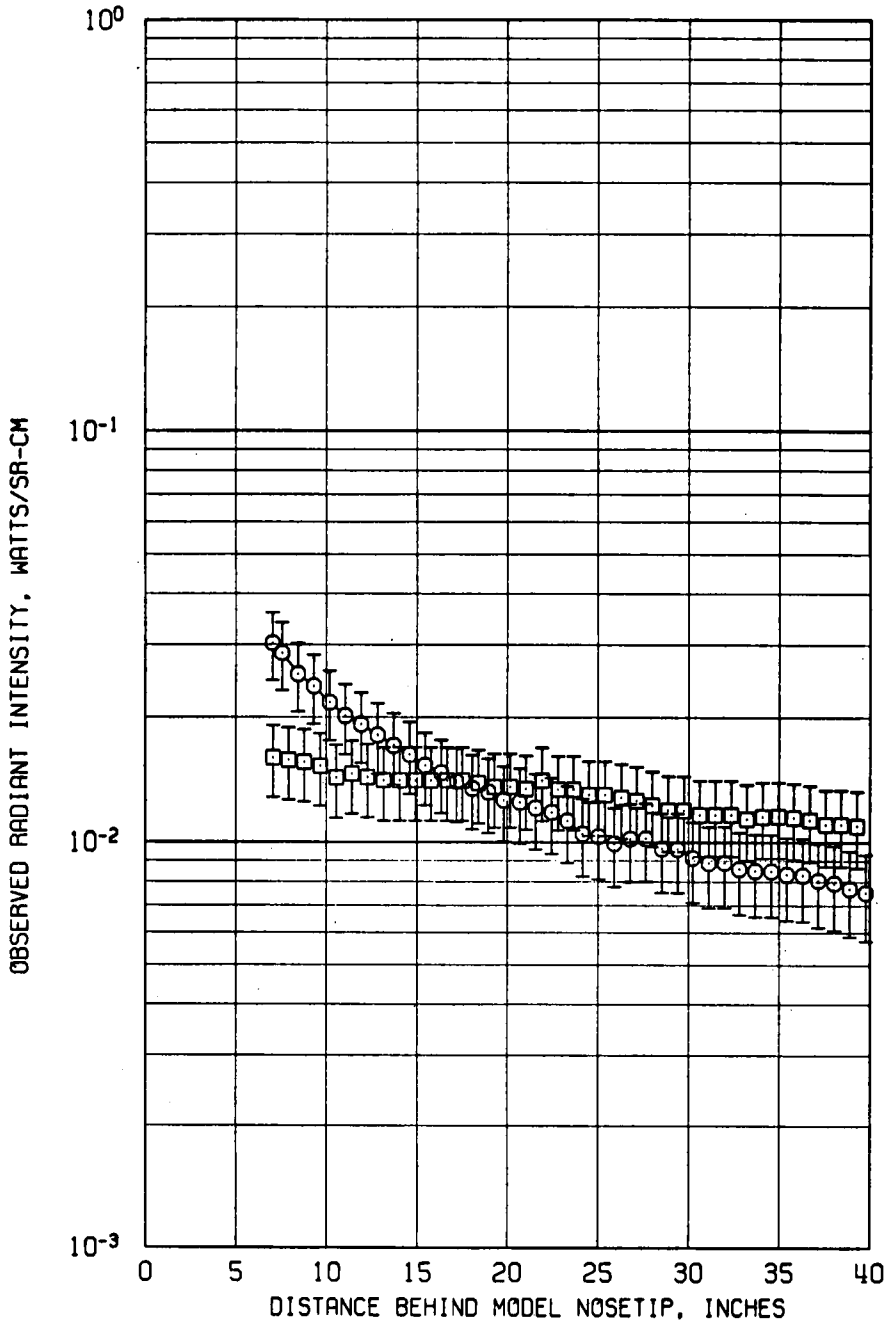
SYMBOL	SHOT NO	STATION	BANDPASS (MICRONS)
⊡	4810	1	2.6-2.8
⊙	4810	1	3.1-3.8



SYMBOL	SHOT NO	STATION	BANDPASS (MICRONS)
⊙	4810	19	0.7-0.9



SYMBOL	SHOT NO	STATION	BANDPASS (MICRONS)
⊡	4810	19	2.6-2.8
⊙	4810	19	3.0-4.0

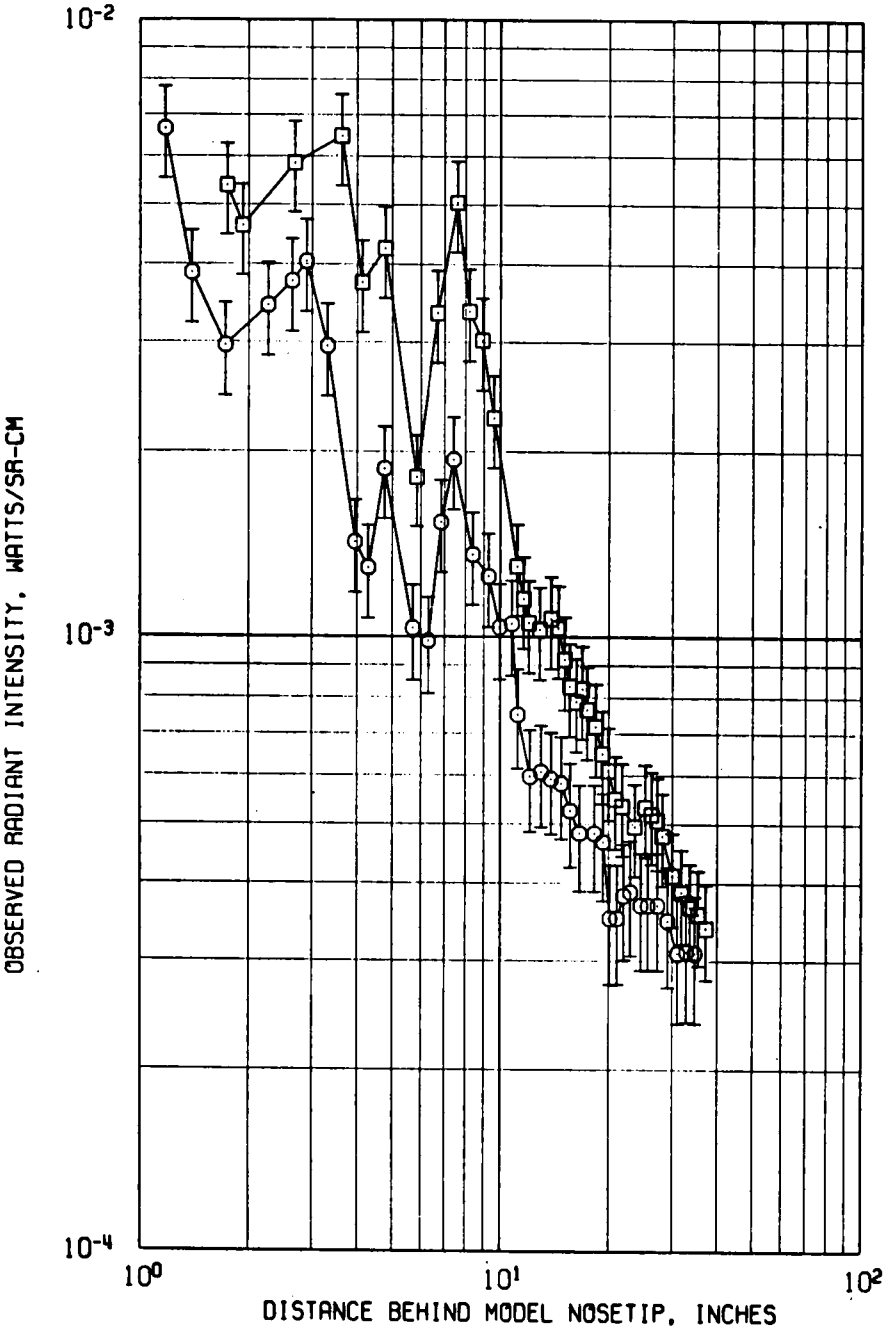


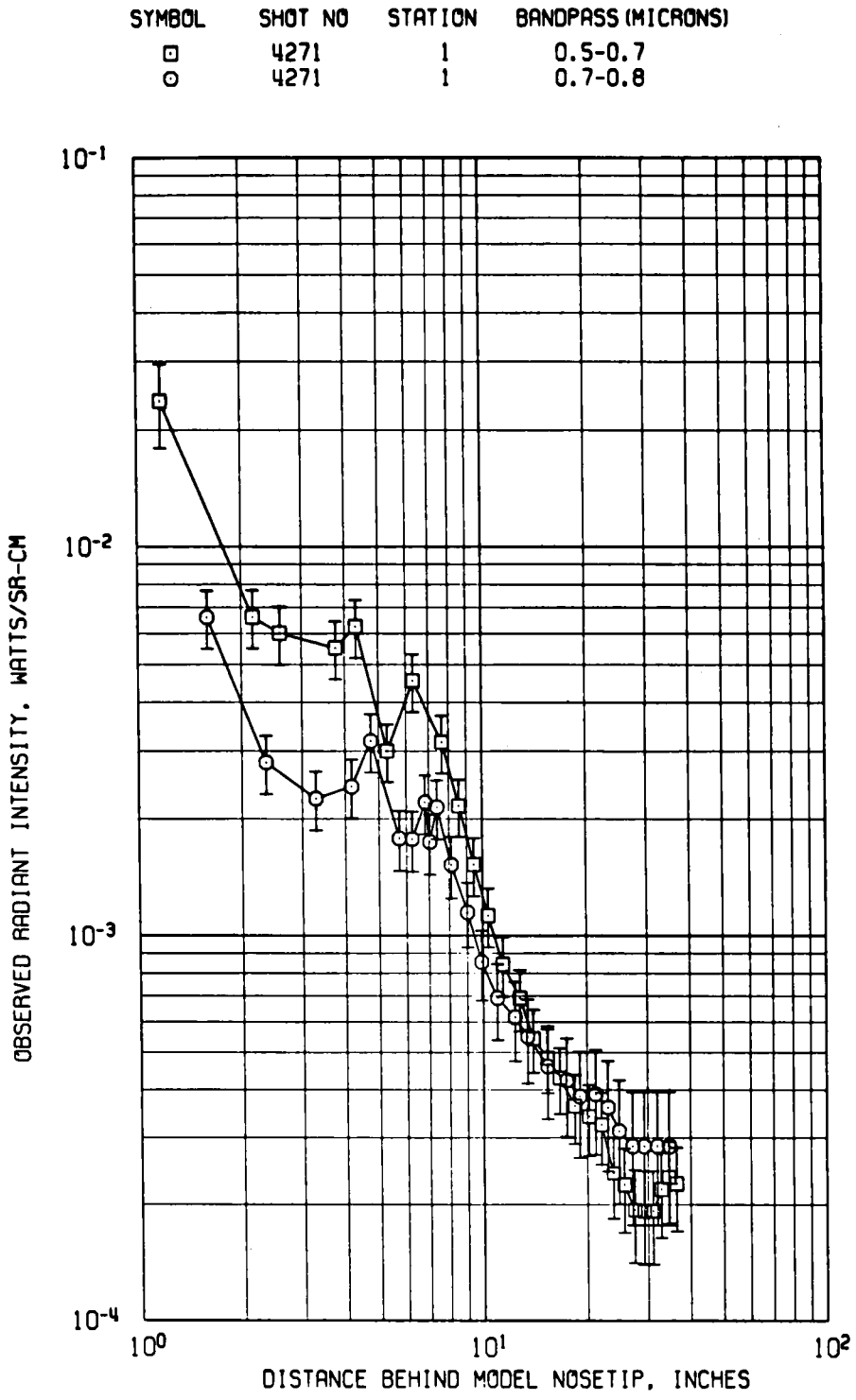
APPENDIX D

LOG INTENSITY VERSUS LOG DISTANCE DATA

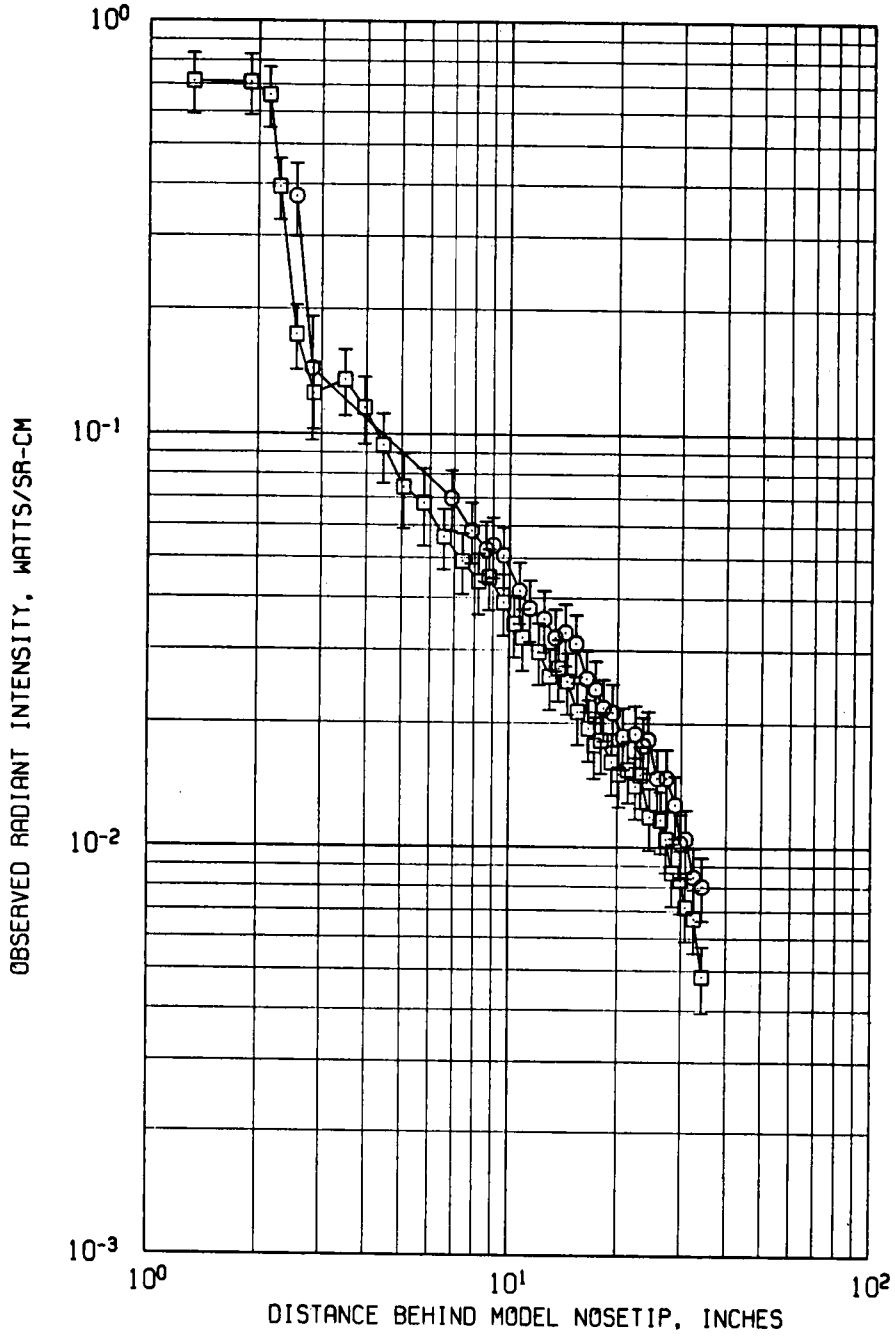
The radiometric test data are plotted as log intensity versus log distance in this appendix and are arranged in the same manner as the Appendix C data.

SYMBOL	SHOT NO	STATION	BANDPASS (MICRONS)
□	4232	1	0.5-0.7
○	4232	1	0.7-0.8

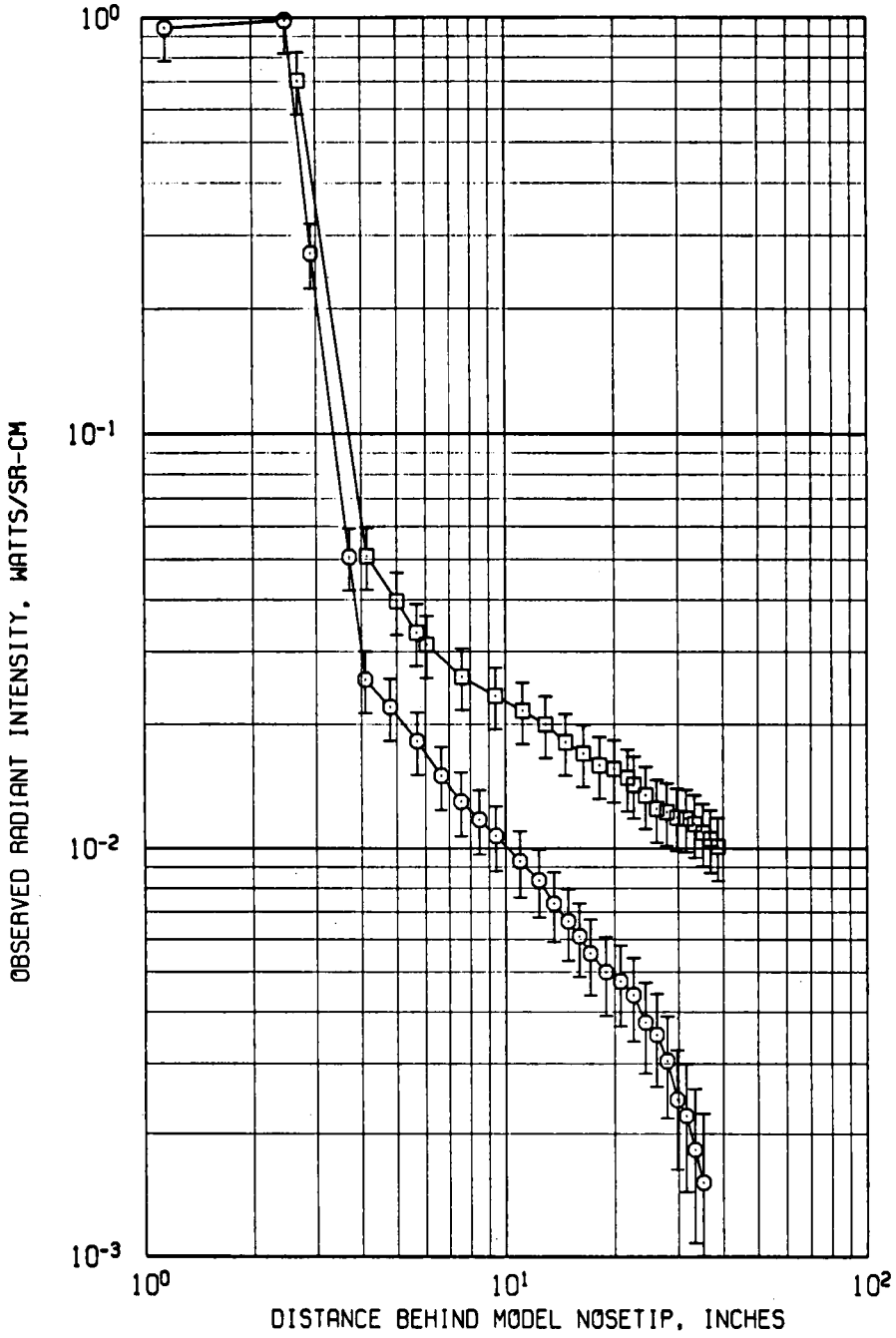



SYMBOL SHOT NO STATION BANDPASS (MICRONS)
4271 1 0.5-0.7
4271 1 0.7-0.8
10^{-1}
10^{-2}
10^{-3}
10^{-4}
OBSERVED RADIANT INTENSITY, WATTS/SR-CM
10^{0}
10^{1}
10^{2}
DISTANCE BEHIND MODEL NOSETIP, INCHES

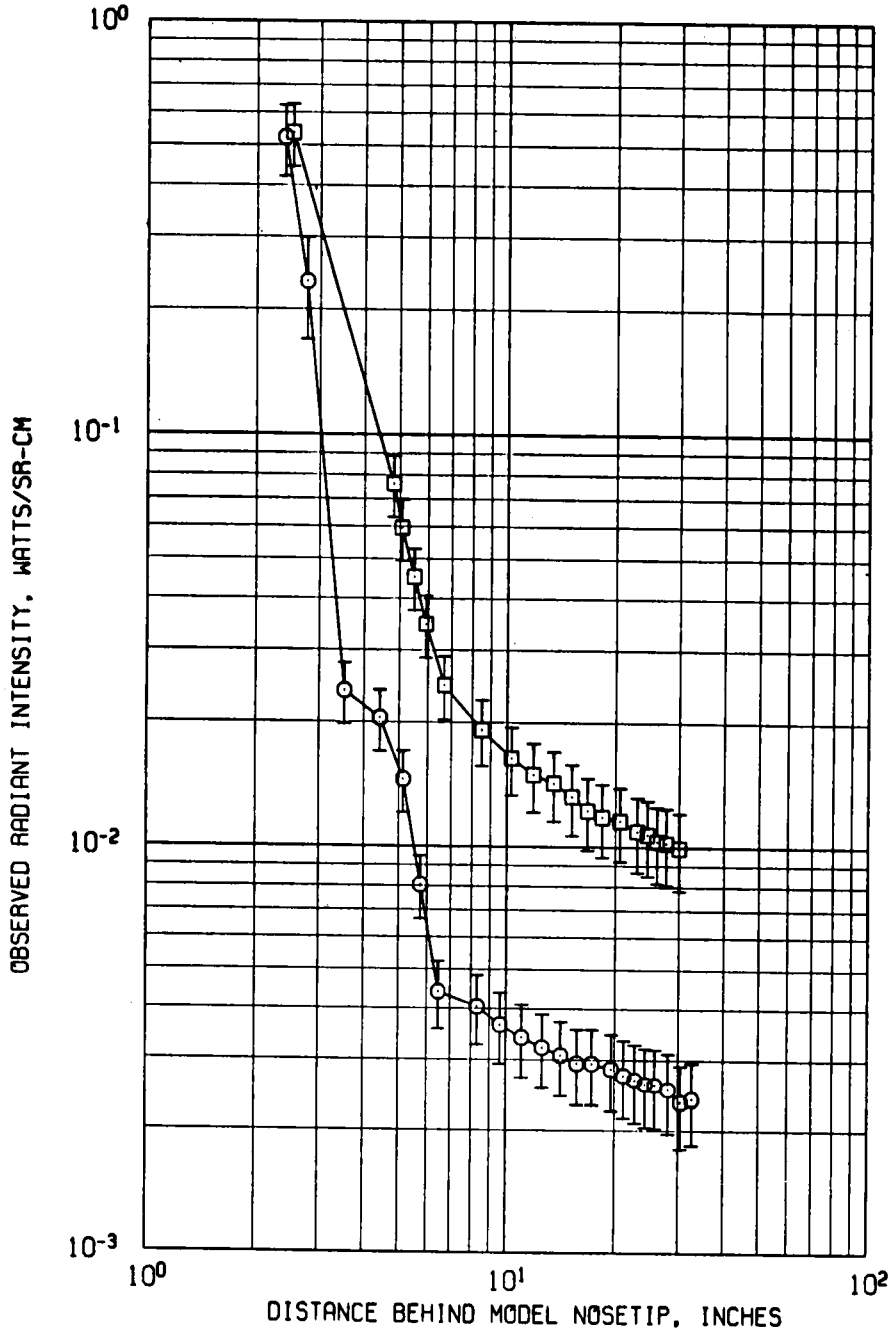
SYMBOL	SHOT NO	STATION	BANDPASS (MICRONS)
⊡	4398	1	0.5-0.7
⊙	4398	1	0.7-0.8



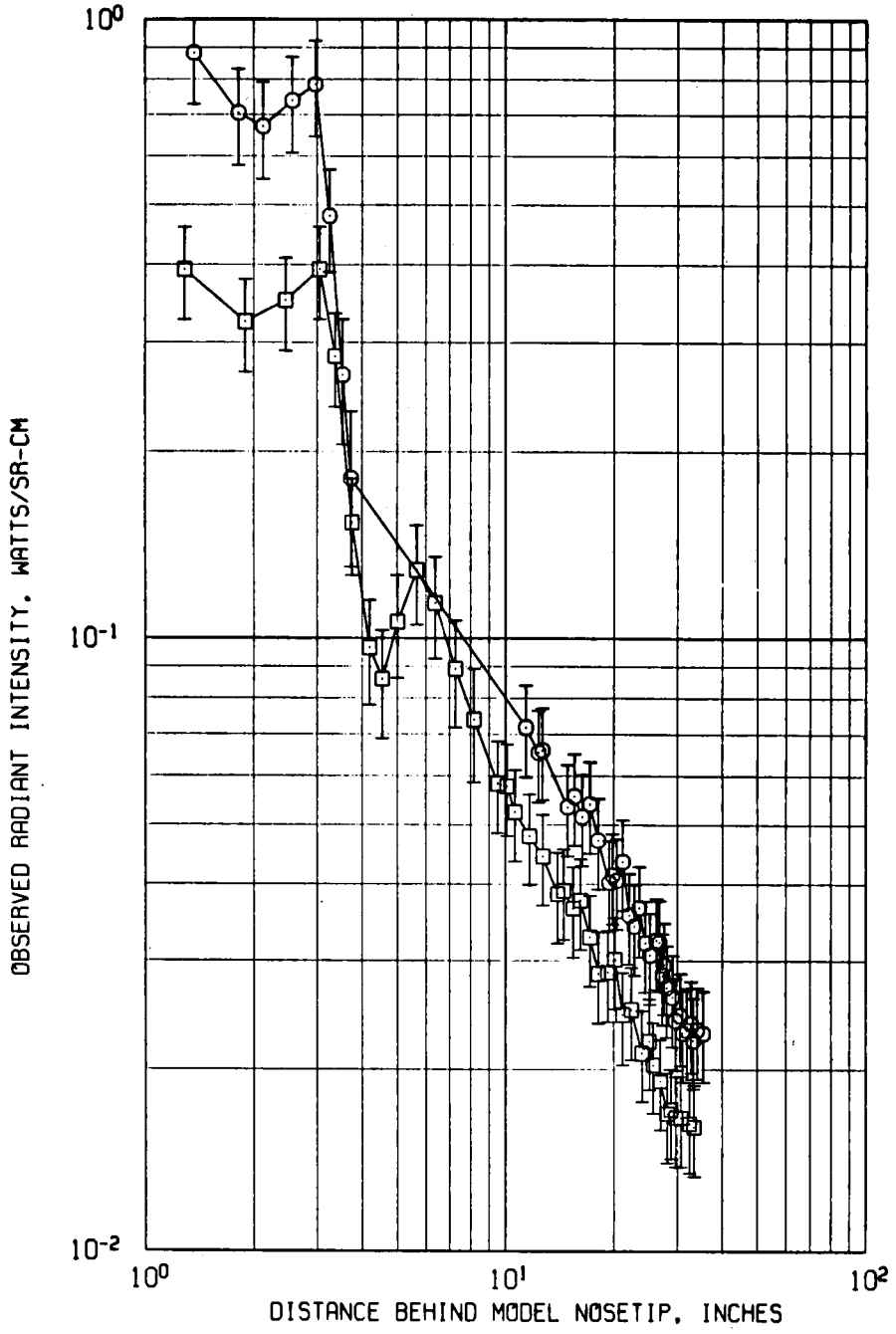
SYMBOL	SHOT NO	STATION	BANDPASS (MICRONS)
⊡	4398	1	2.6-2.8
⊙	4398	1	3.1-3.8



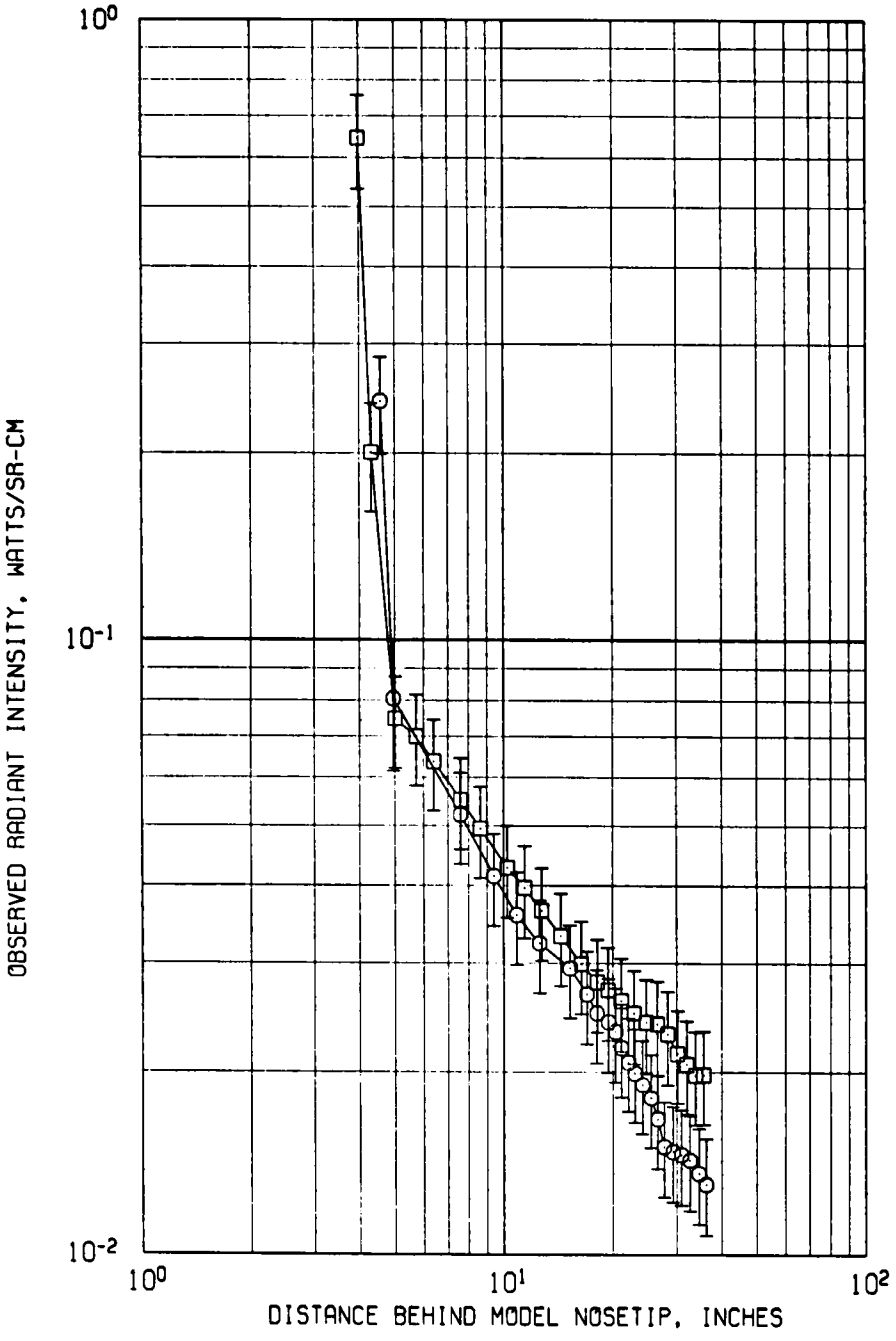
SYMBOL	SHOT NO	STATION	BANDPASS (MICRONS)
⊡	4398	19	0.5-0.7
⊙	4398	19	0.7-0.9



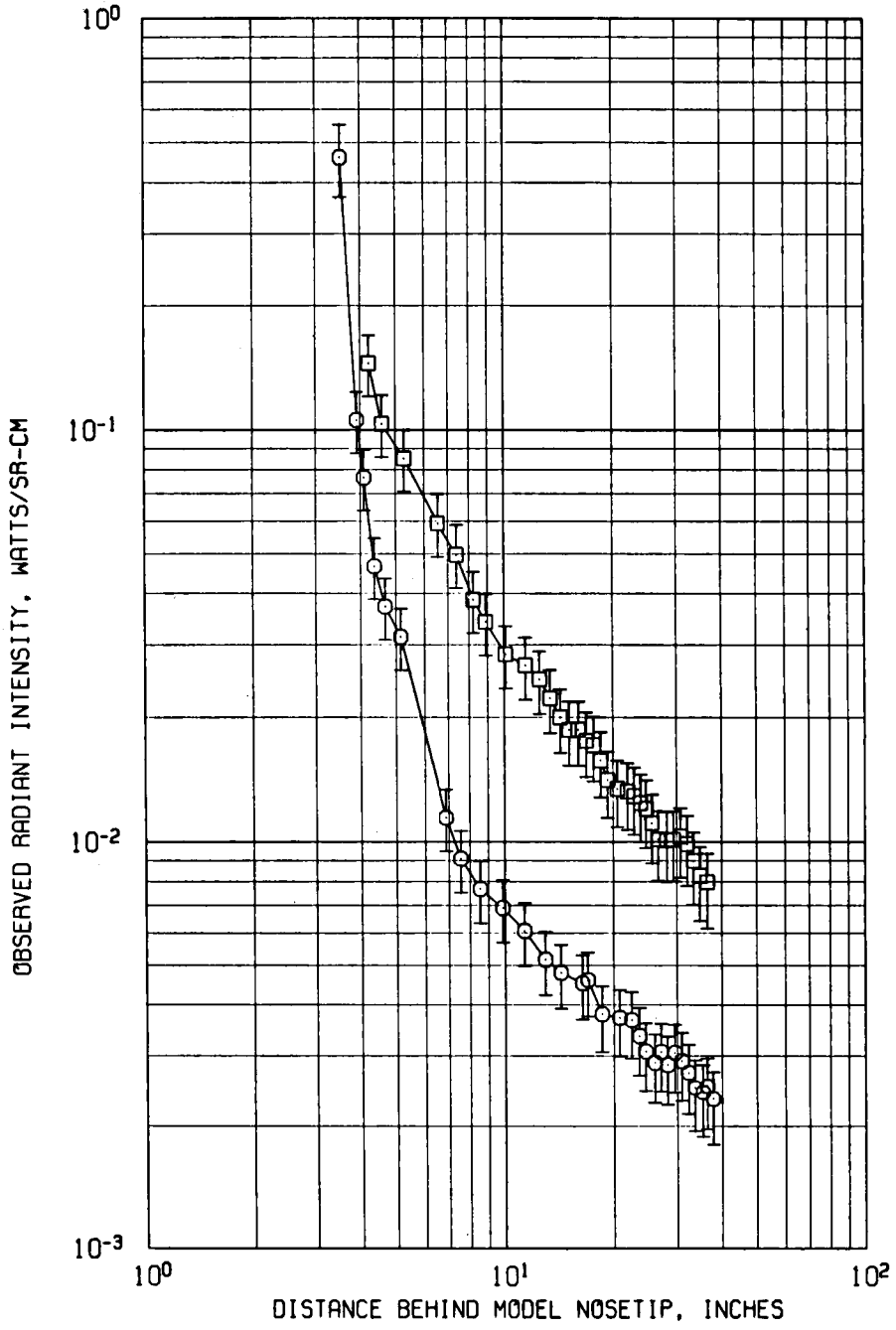
SYMBOL	SHOT NO	STATION	BANDPASS (MICRONS)
⊡	4400	1	0.5-0.7
⊙	4400	1	0.7-0.8



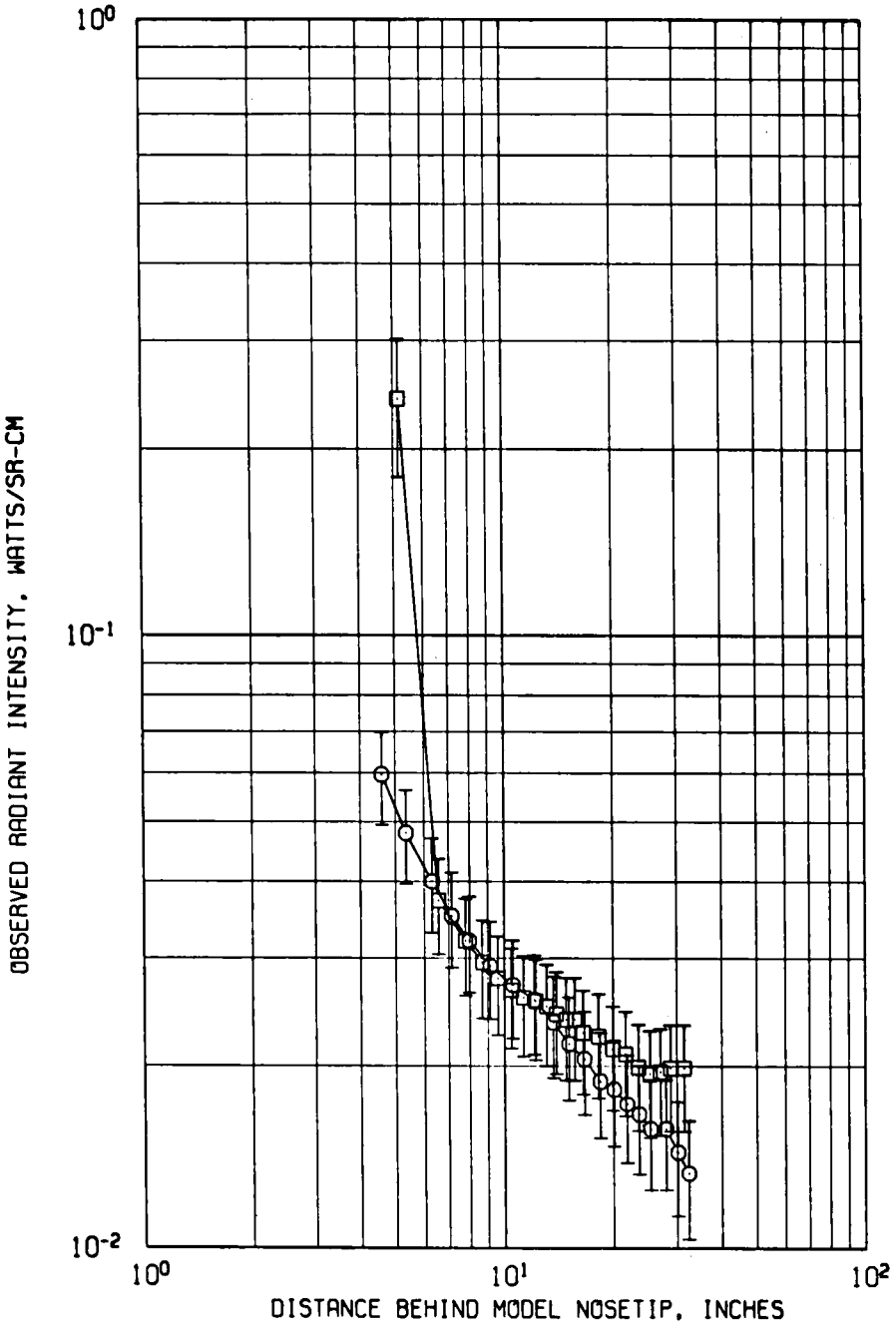
SYMBOL	SHOT NO	STATION	BANDPASS (MICRONS)
⊡	4400	1	2.6-2.8
⊙	4400	1	3.1-3.8



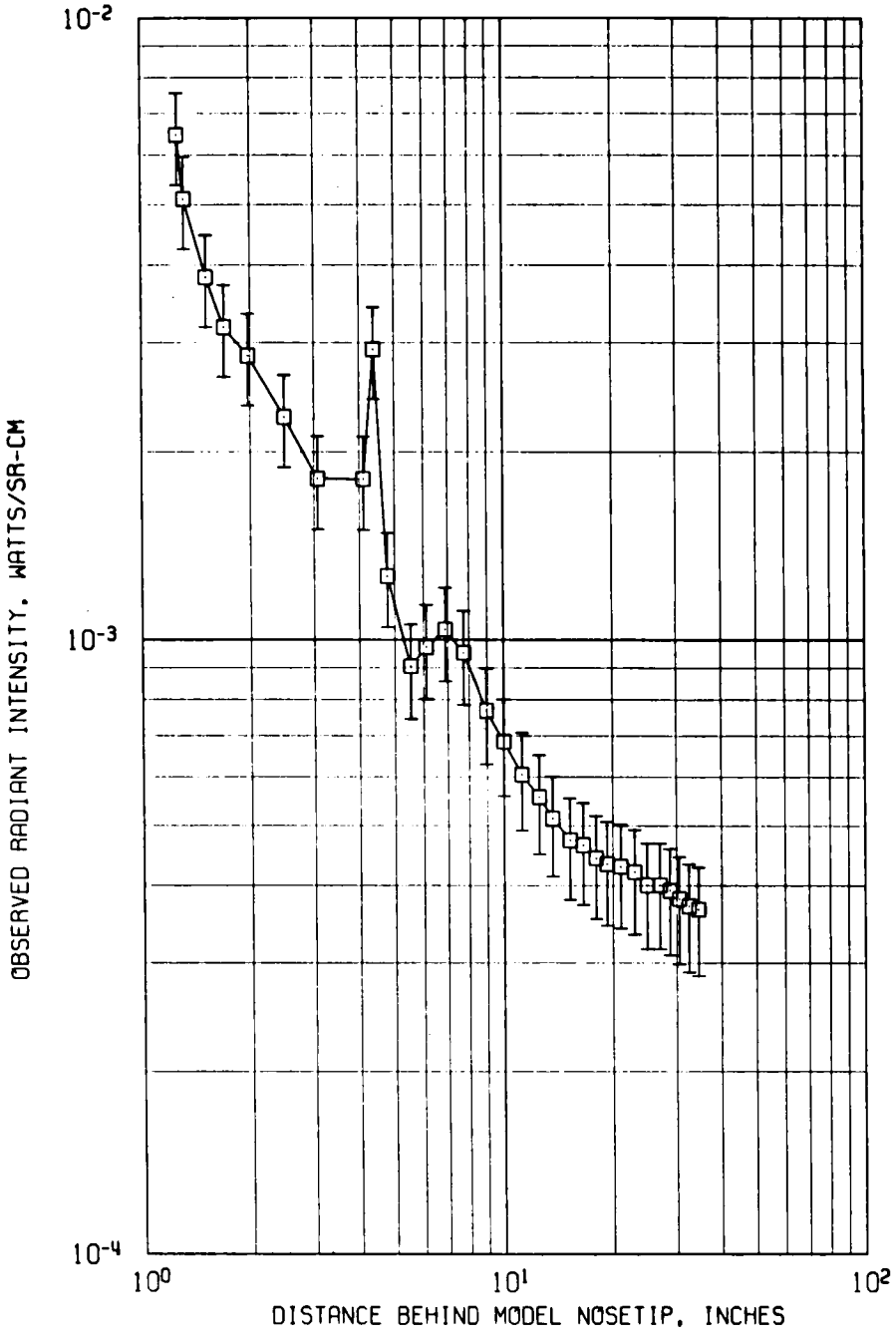
SYMBOL	SHOT NO	STATION	BANDPASS (MICRONS)
⊡	4400	19	0.5-0.7
⊙	4400	19	0.7-0.9



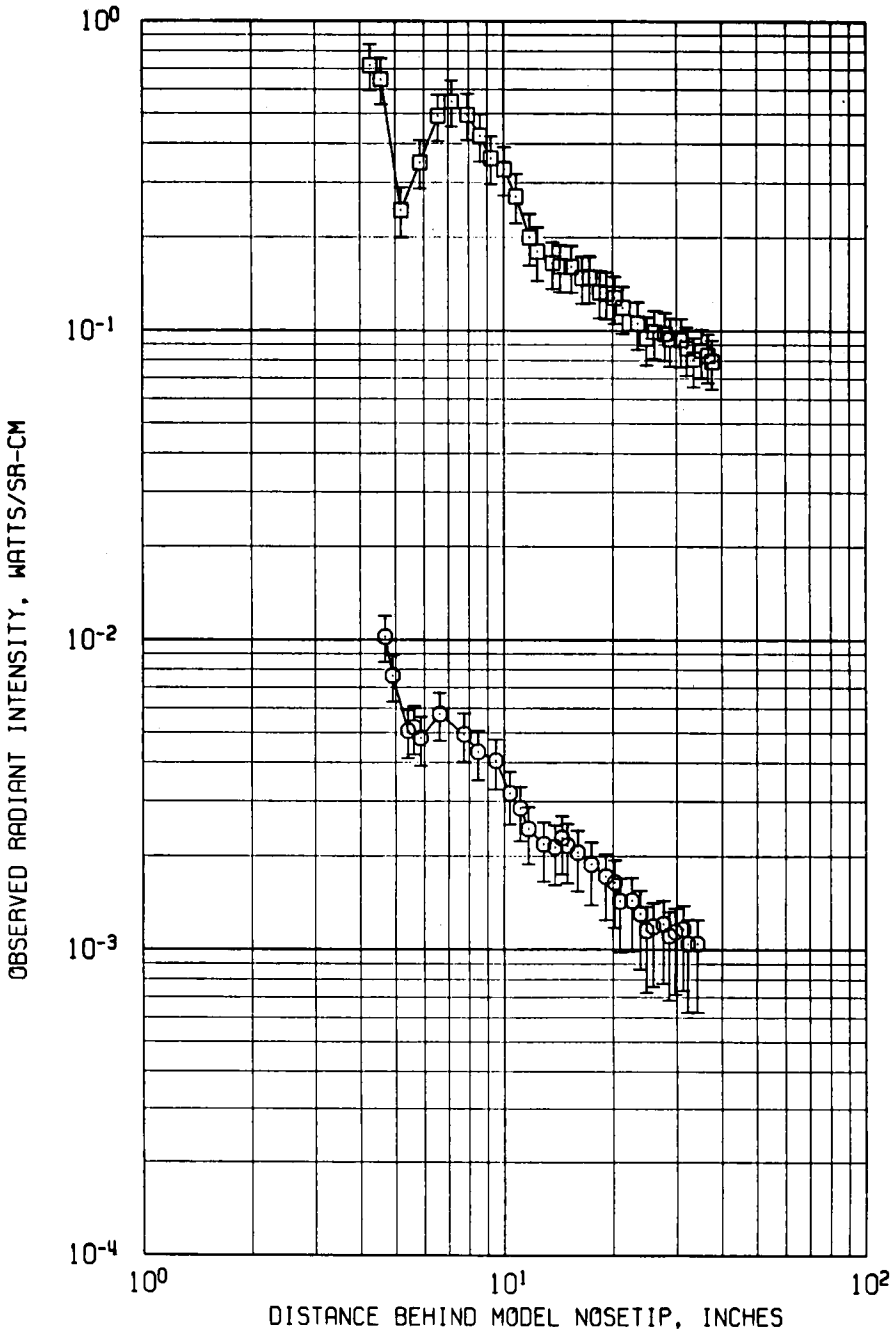
SYMBOL	SHOT NO	STATION	BANDPASS (MICRONS)
⊡	4400	19	2.6-2.8
⊙	4400	19	3.0-4.0



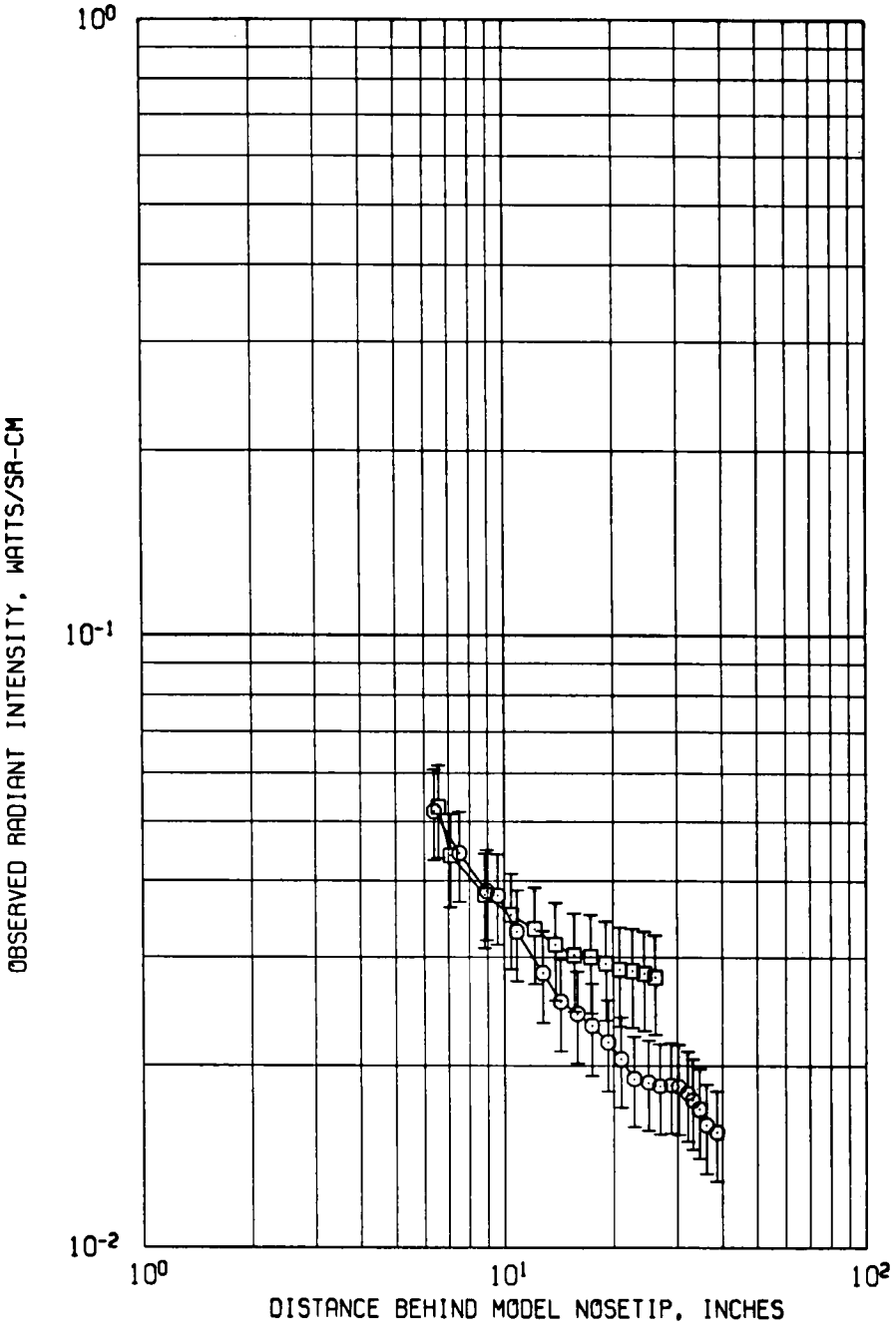
SYMBOL	SHOT NO	STATION	BANDPASS (MICRONS)
□	4401	1	0.5-0.7



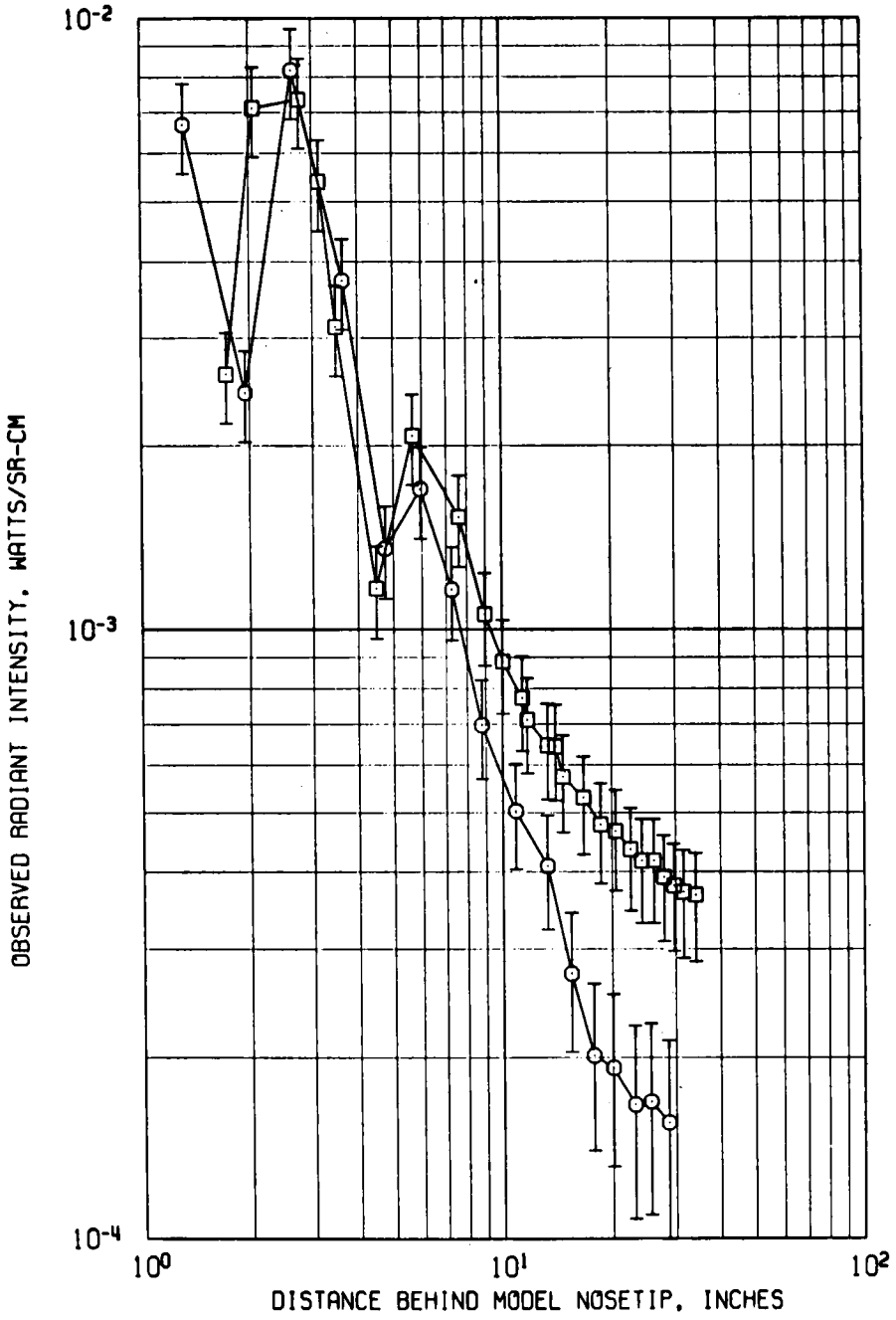
SYMBOL	SHOT NO	STATION	BANDPASS (MICRONS)
⊡	4402	19	0.5-0.7
⊙	4402	19	0.7-0.9



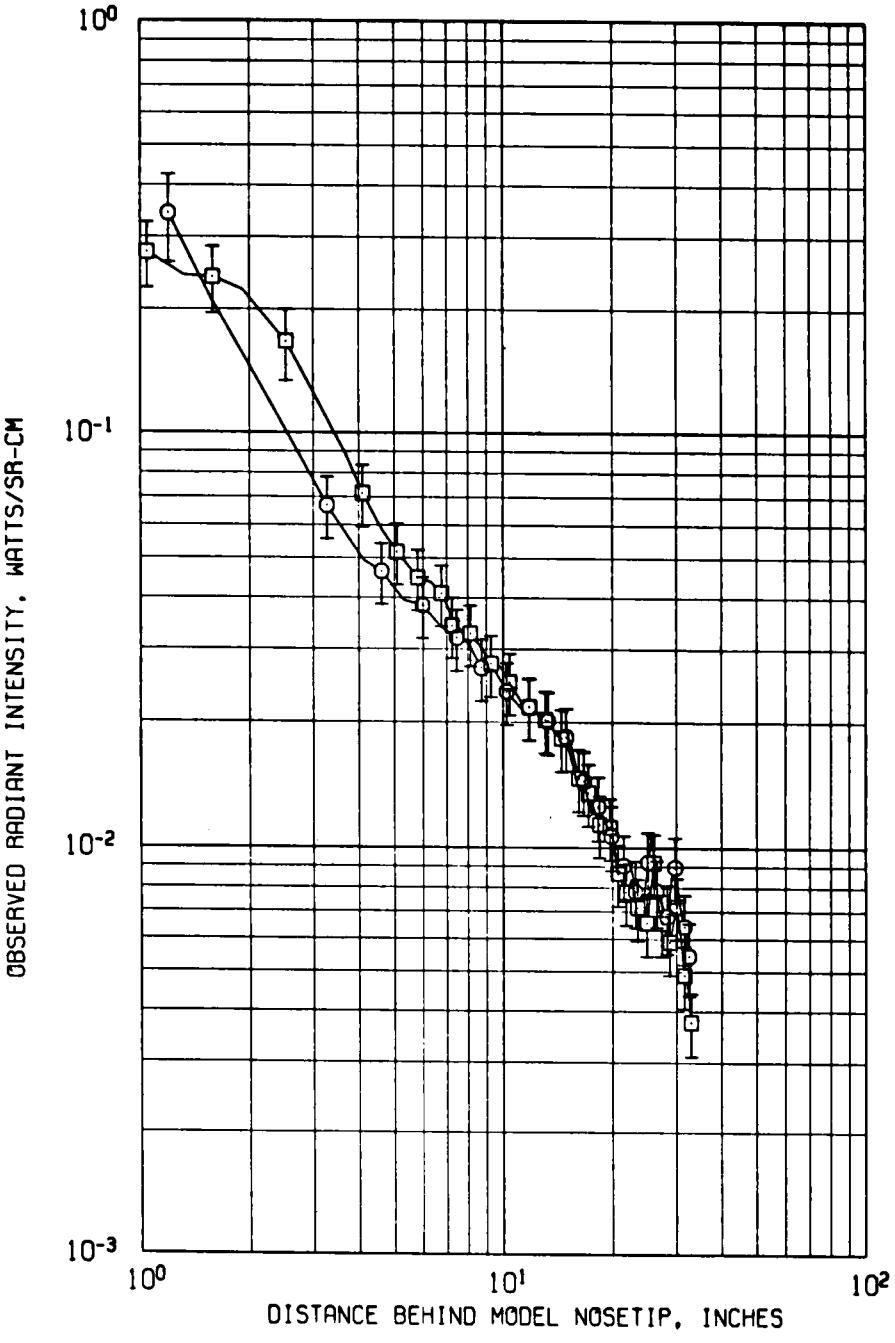
SYMBOL	SHOT NO	STATION	BANDPASS (MICRONS)
⊡	4402	19	2.6-2.8
⊙	4402	19	3.0-4.0



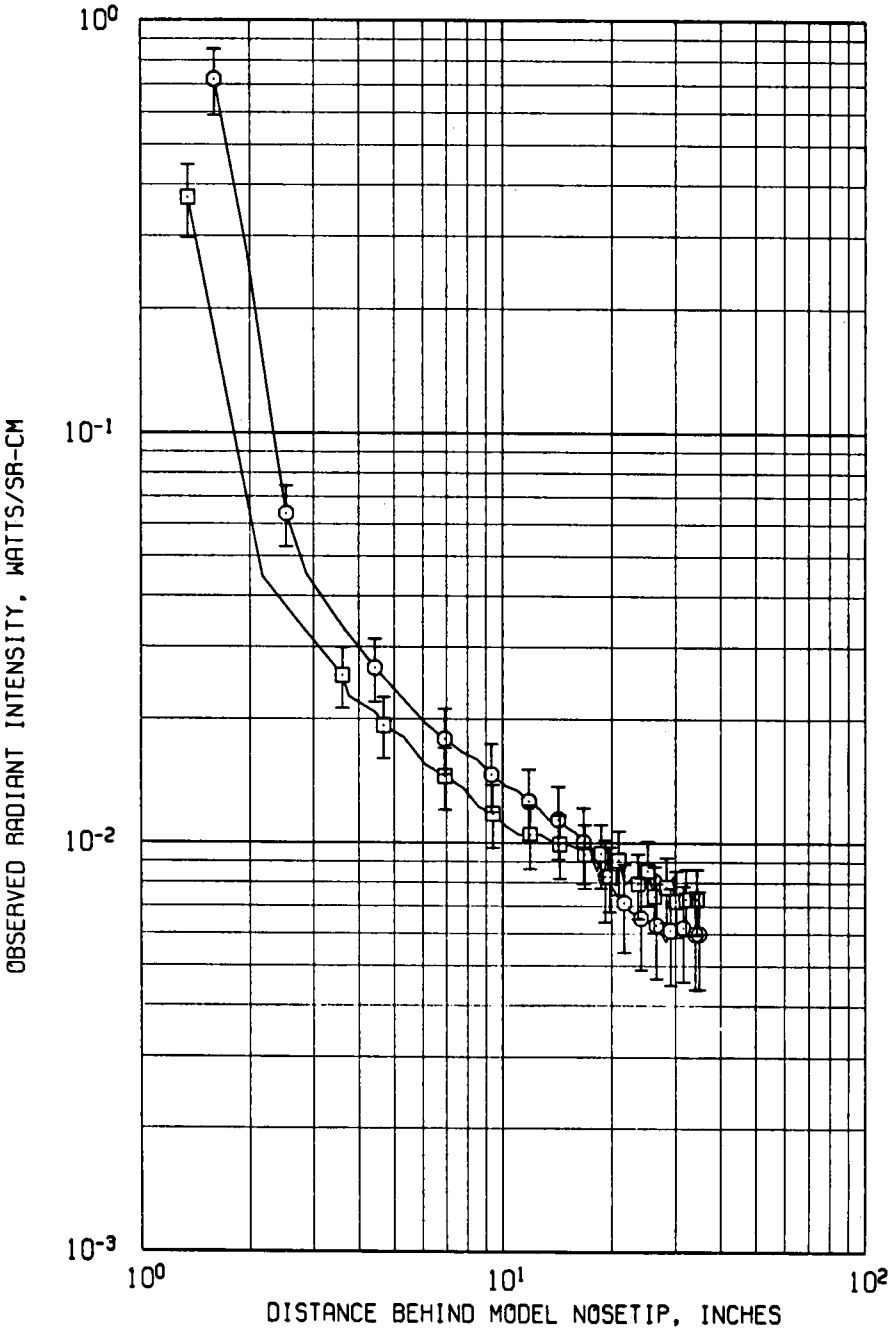
SYMBOL	SHOT NO	STATION	BANDPASS (MICRONS)
⊡	4403	1	0.5-0.7
⊙	4403	1	0.7-0.8



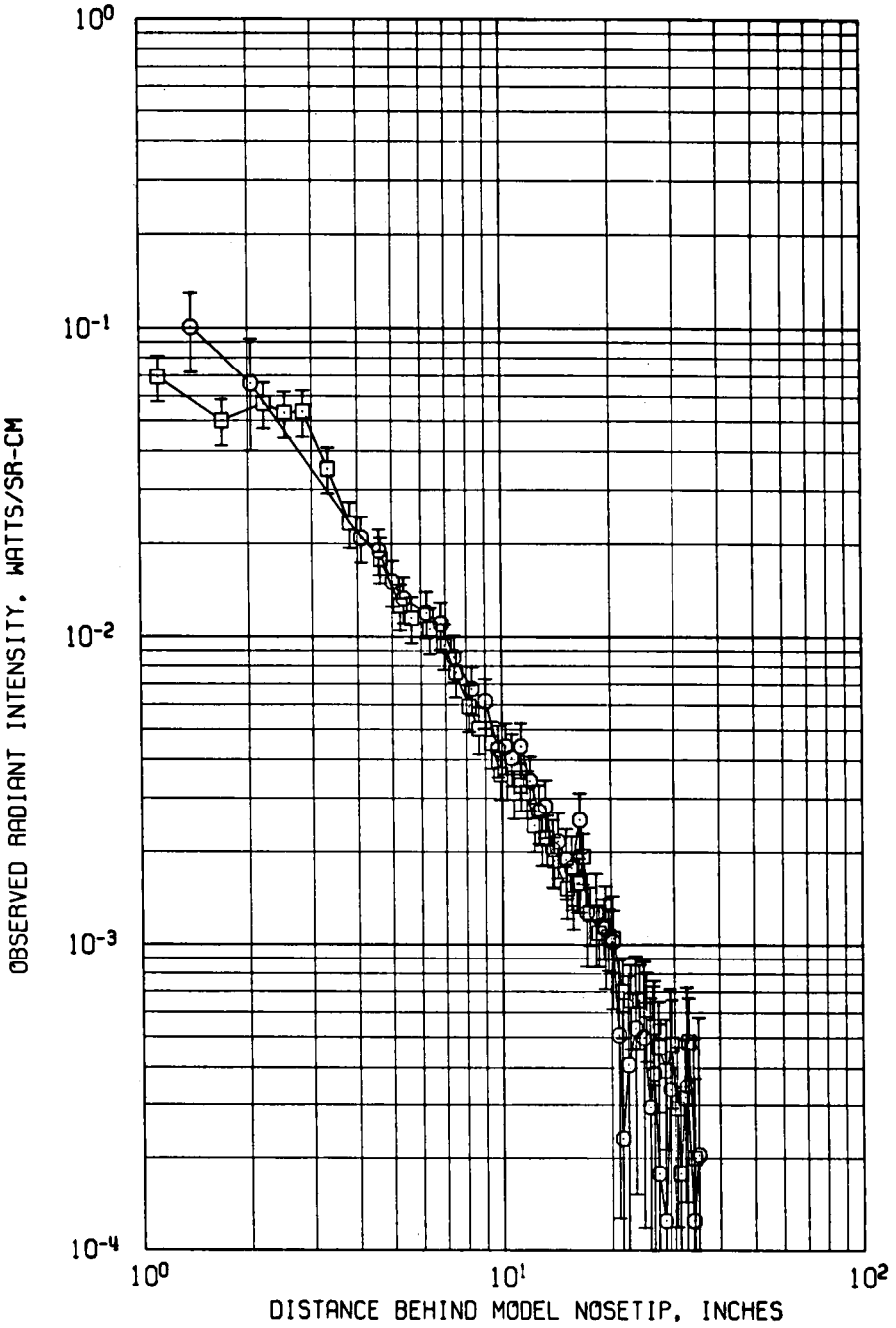
SYMBOL	SHOT NO	STATION	BANDPASS (MICRONS)
⊡	4498	1	0.5-0.7
⊙	4498	1	0.7-0.8



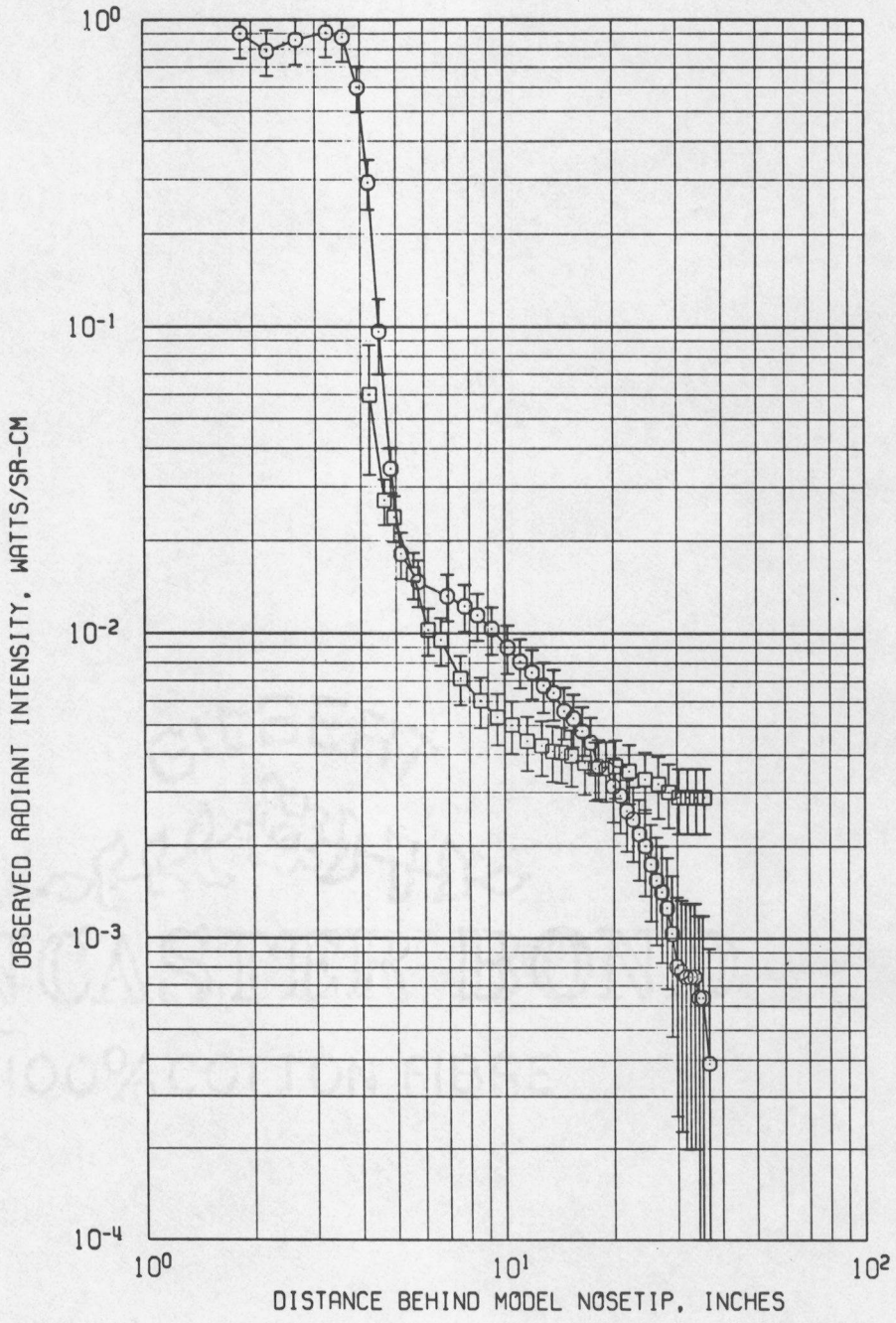
SYMBOL	SHOT NO	STATION	BANDPASS (MICRONS)
⊡	4498	1	2.6-2.8
⊙	4498	1	3.1-3.8



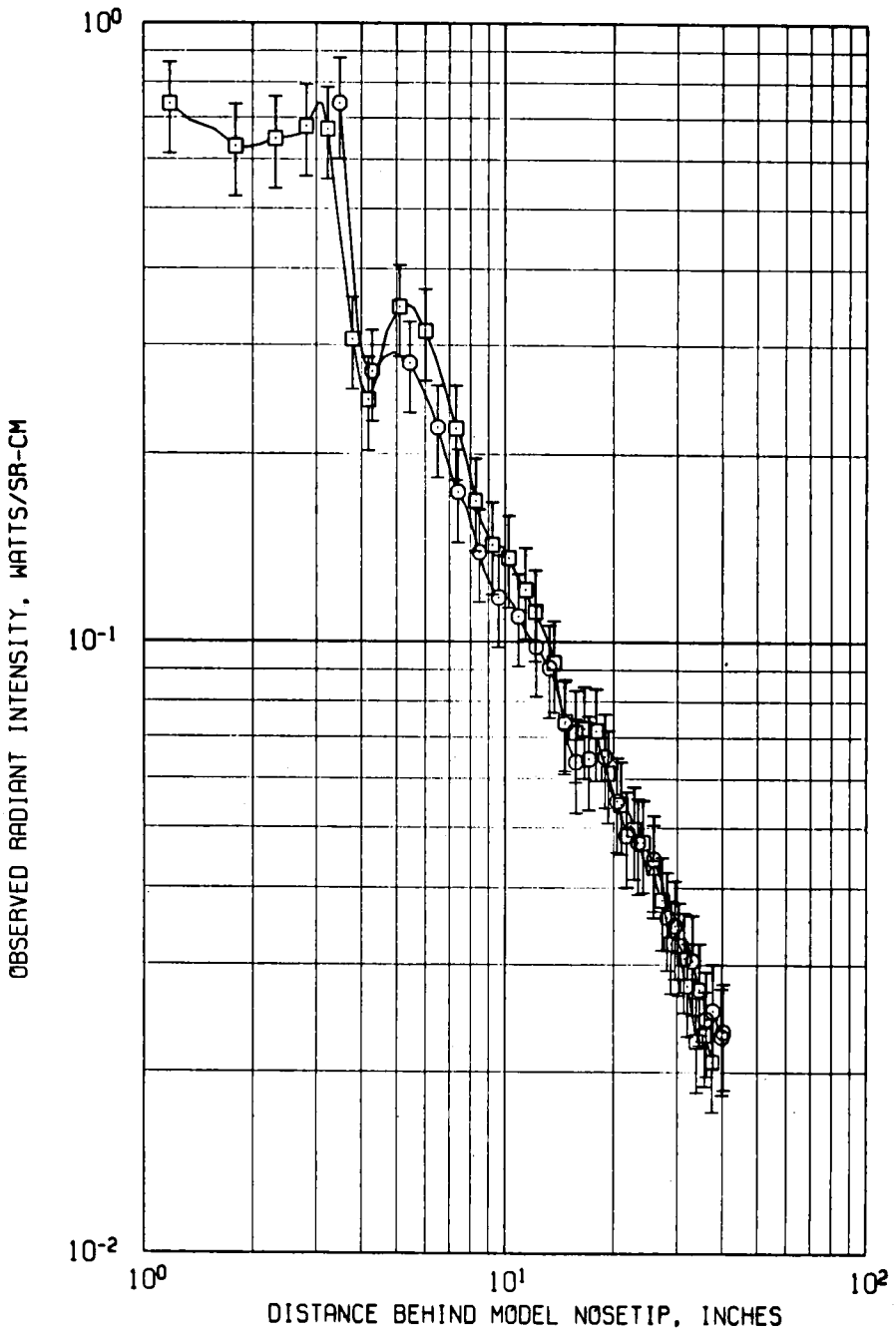
SYMBOL	SHOT NO	STATION	BANDPASS (MICRONS)
⊡	4500	1	0.5-0.7
⊙	4500	1	0.7-0.8



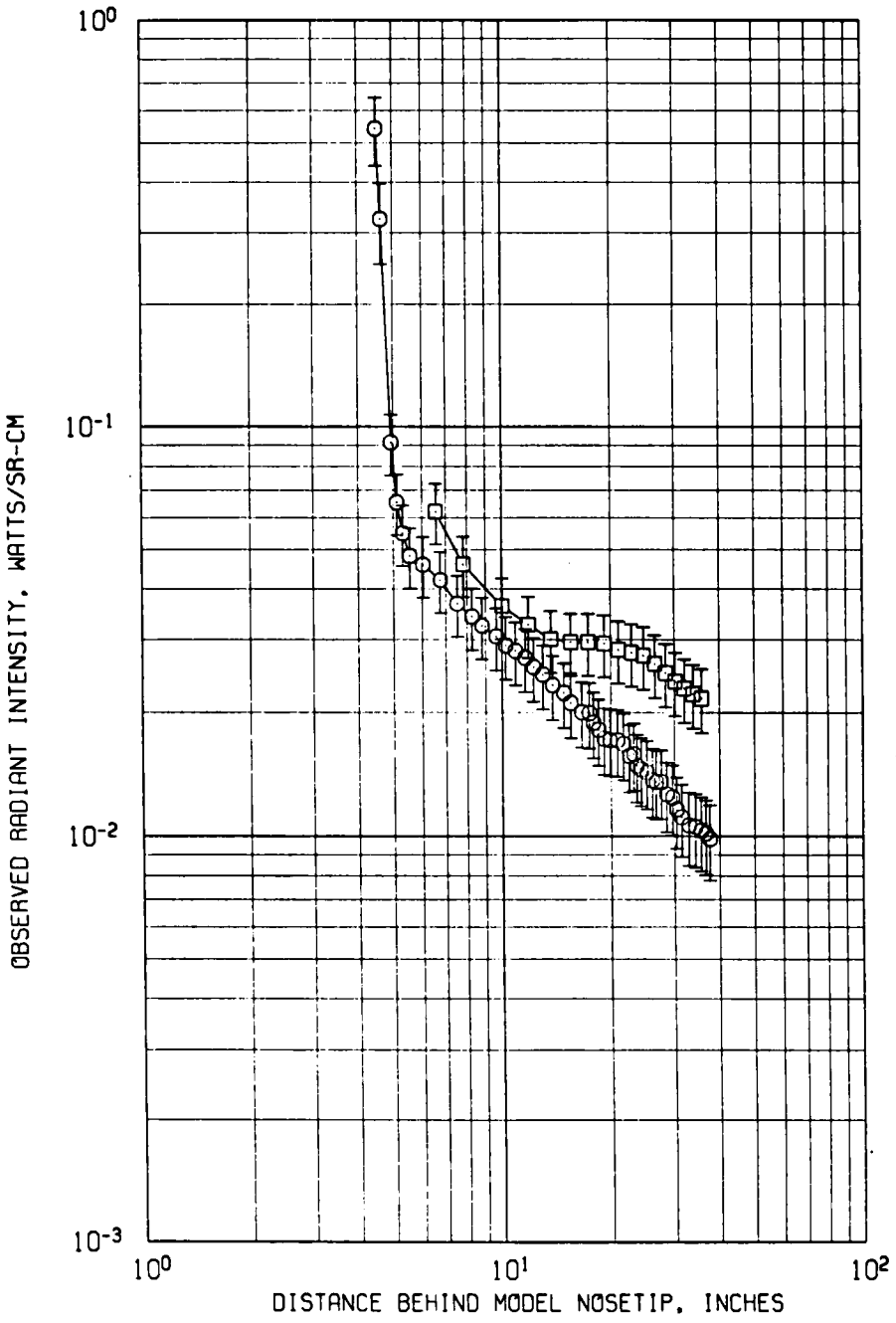
SYMBOL	SHOT NO	STATION	BANDPASS (MICRONS)
⊡	4500	1	2.6-2.8
⊙	4500	1	3.1-3.8



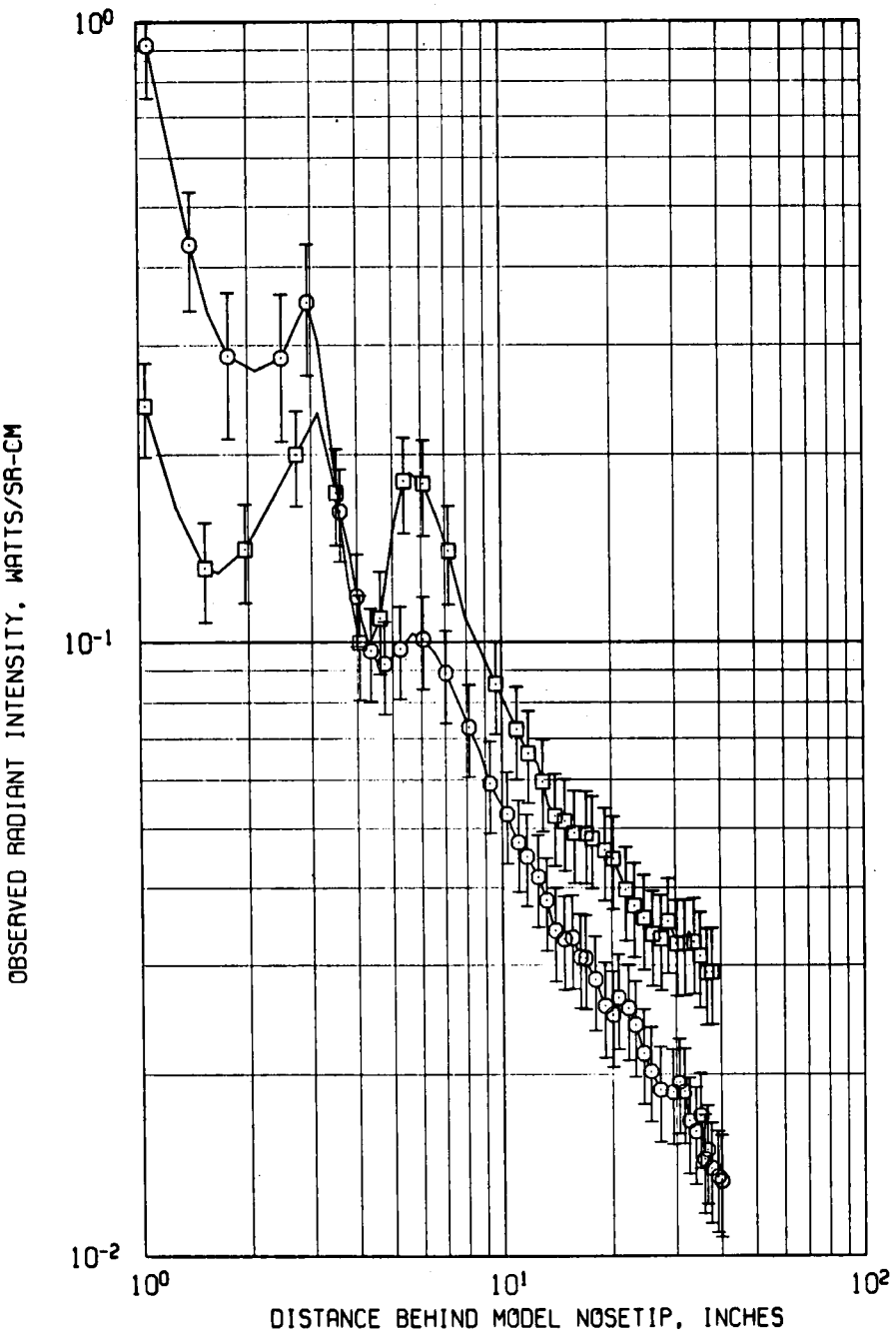
SYMBOL	SHOT NO	STATION	BANDPASS (MICRONS)
⊡	4502	1	0.5-0.7
⊙	4502	1	0.7-0.8



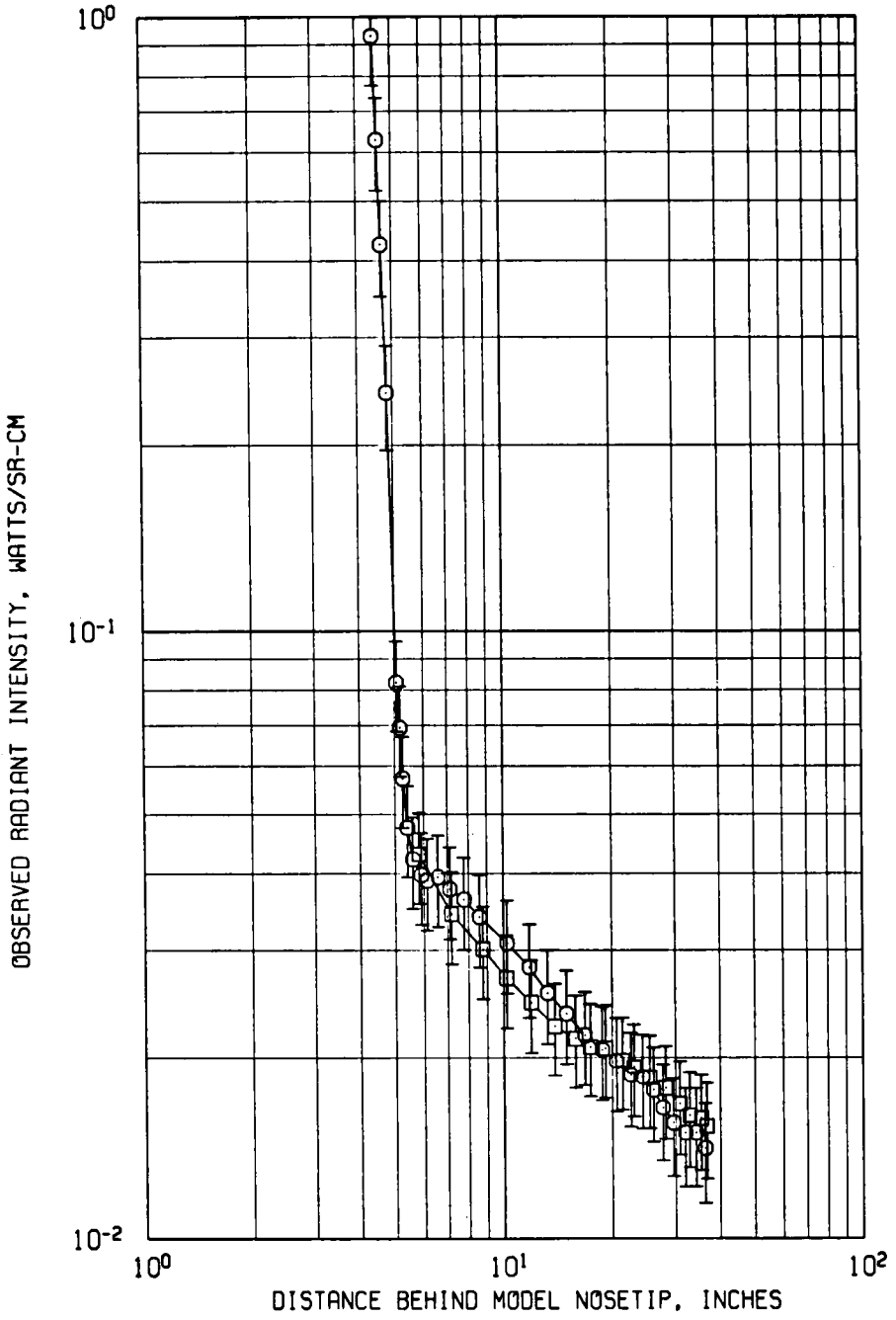
SYMBOL	SHOT NO	STATION	BANDPASS (MICRONS)
⊡	4502	1	2.6-2.8
⊙	4502	1	3.1-3.8



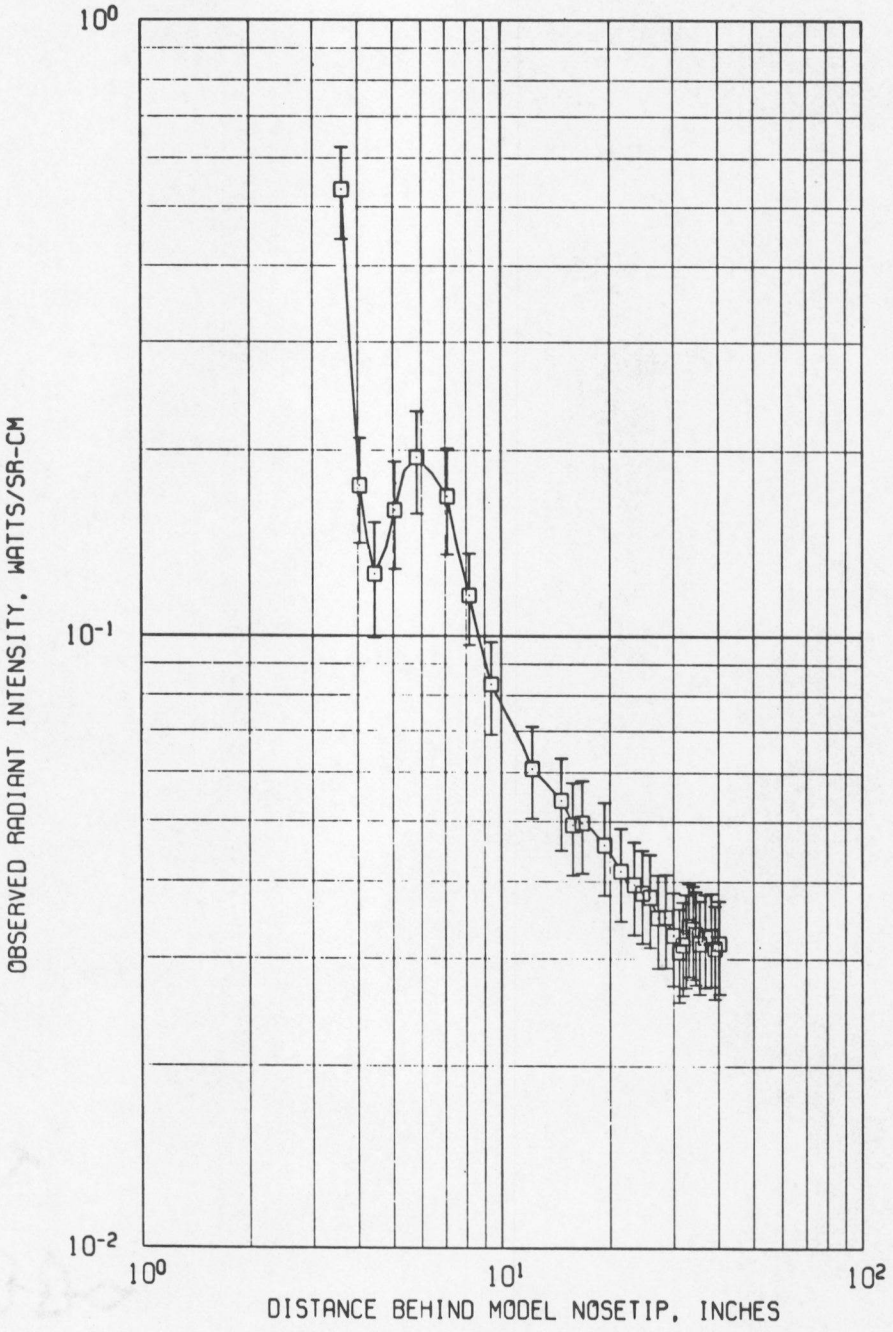
SYMBOL	SHOT NO	STATION	BANDPASS (MICRONS)
⊡	4503	1	0.5-0.7
⊙	4503	1	0.7-0.8



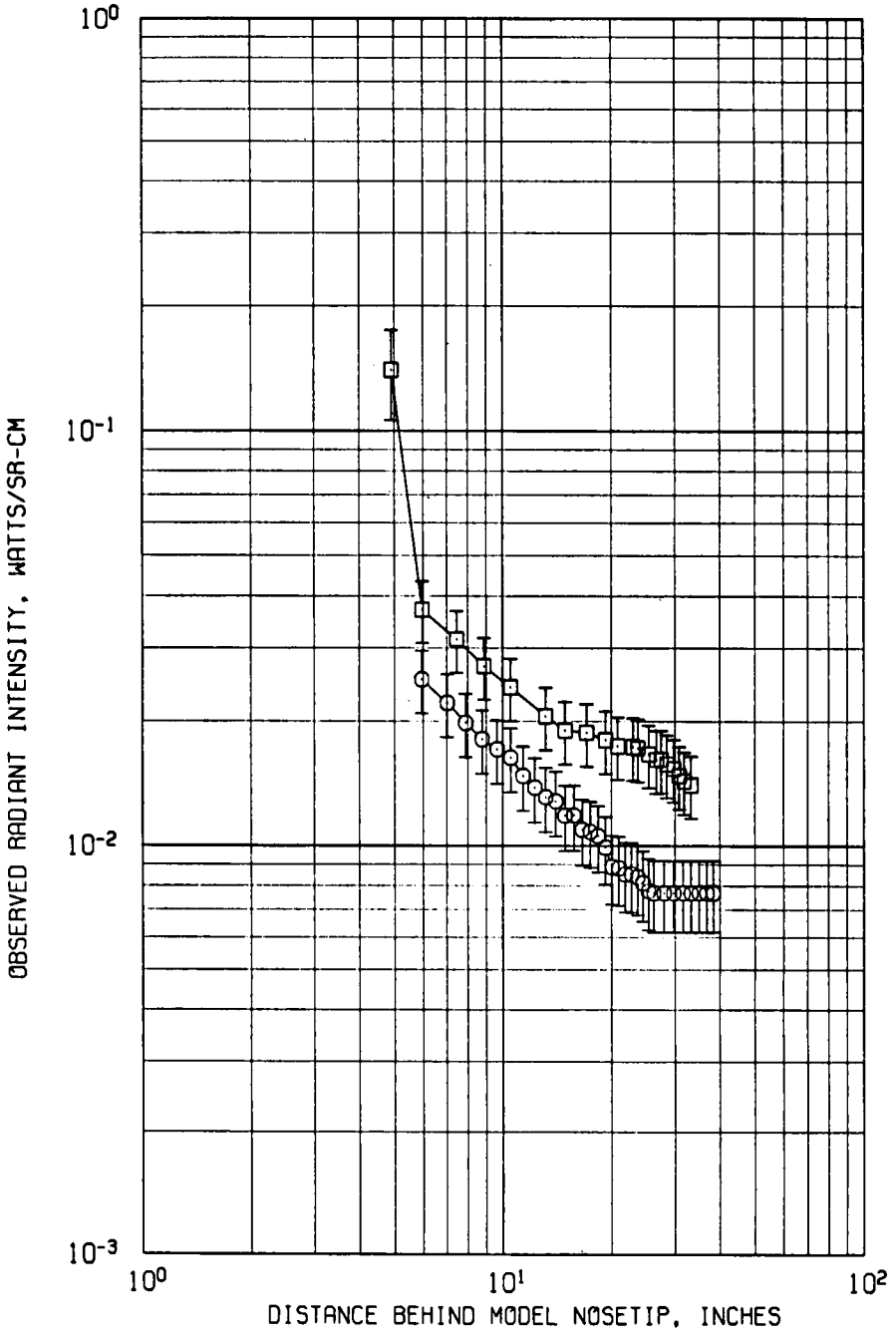
SYMBOL	SHOT NO	STATION	BANDPASS (MICRONS)
⊡	4503	1	2.6-2.8
⊙	4503	1	3.1-3.8



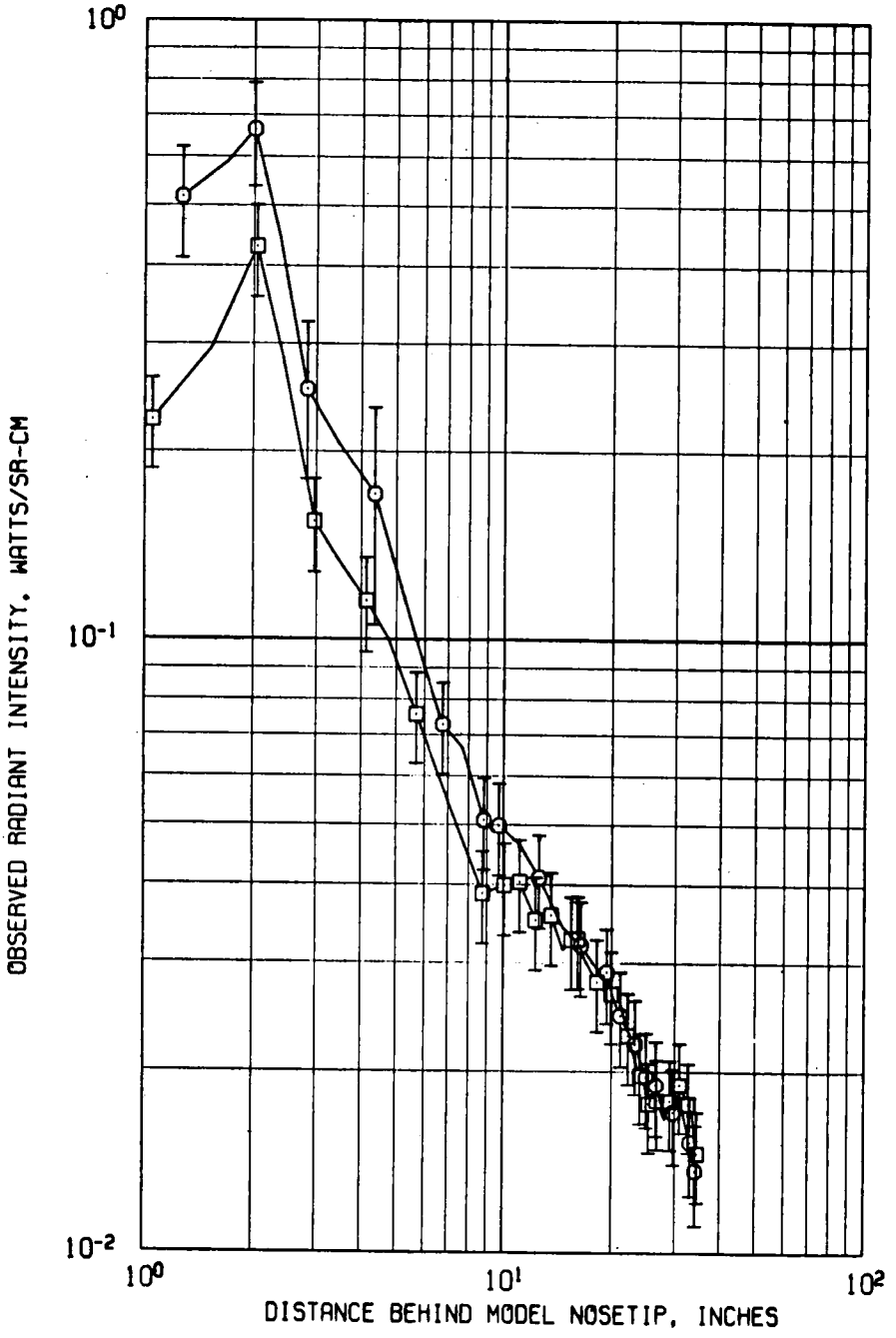
SYMBOL	SHOT NO	STATION	BANDPASS (MICRONS)
⊡	4503	19	0.5-0.7



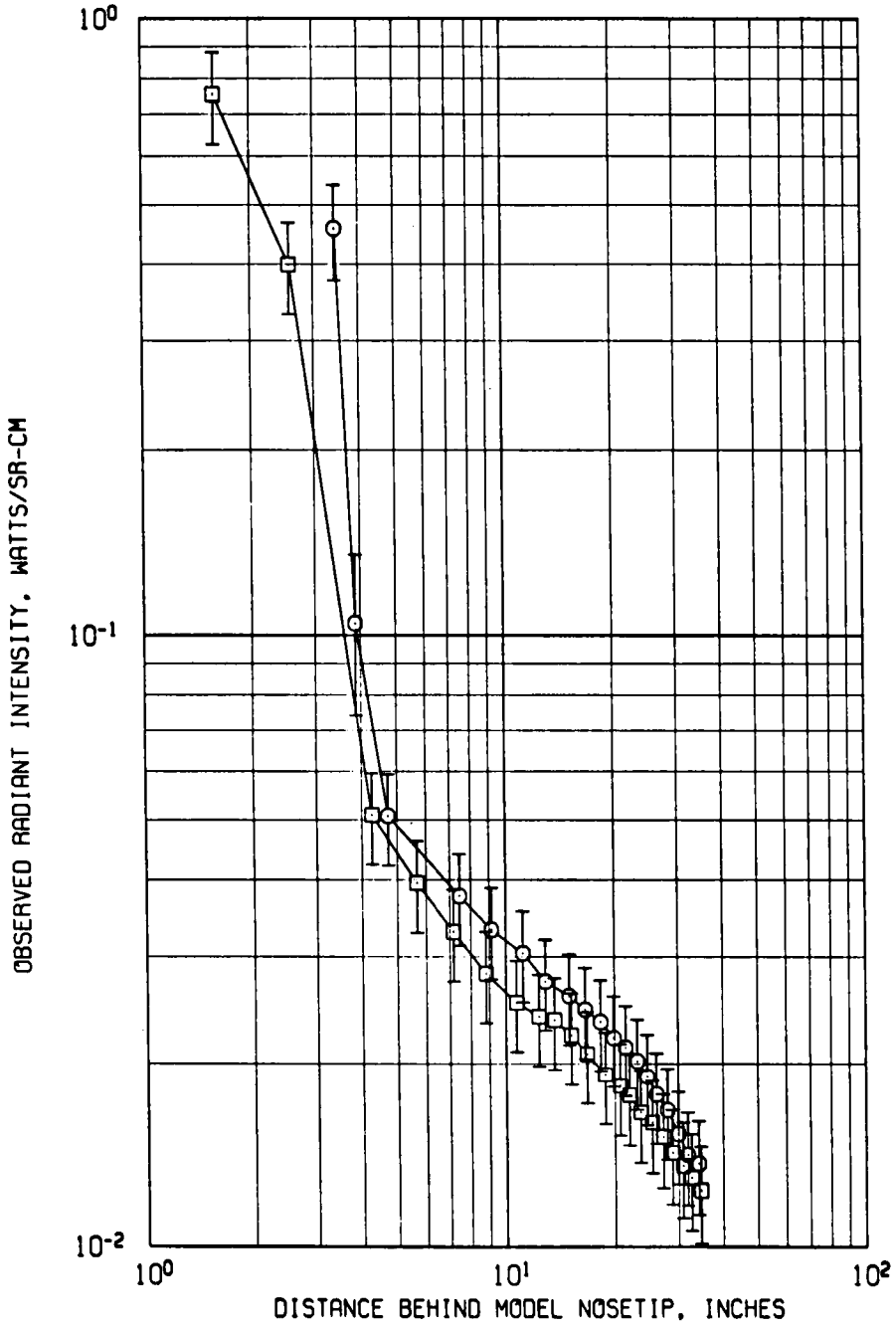
SYMBOL	SHOT NO	STATION	BANDPASS (MICRONS)
⊡	4503	19	2.6-2.8
⊙	4503	19	3.0-4.0



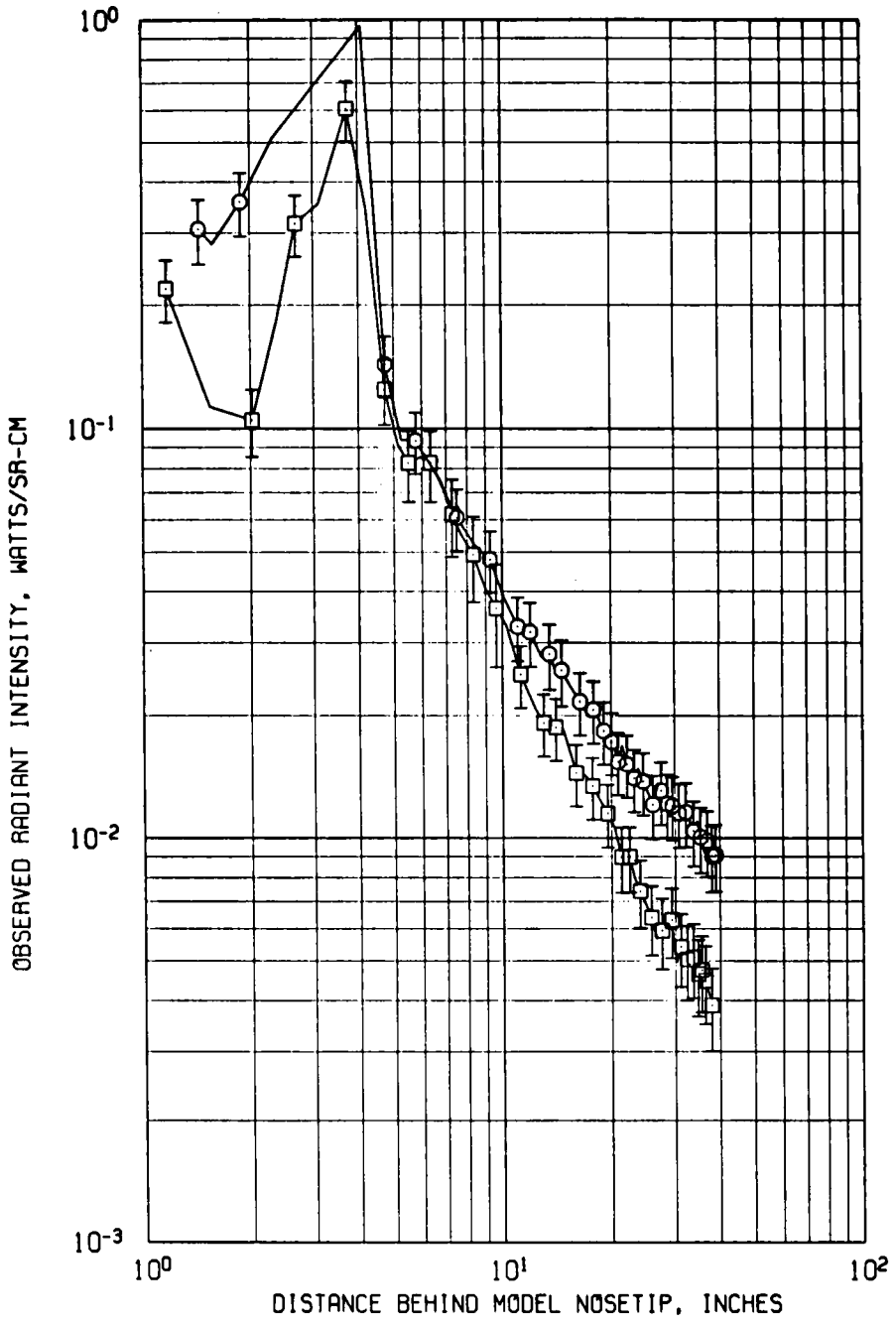
SYMBOL	SHOT NO	STATION	BANDPASS (MICRONS)
⊡	4504	1	0.5-0.7
⊙	4504	1	0.7-0.8



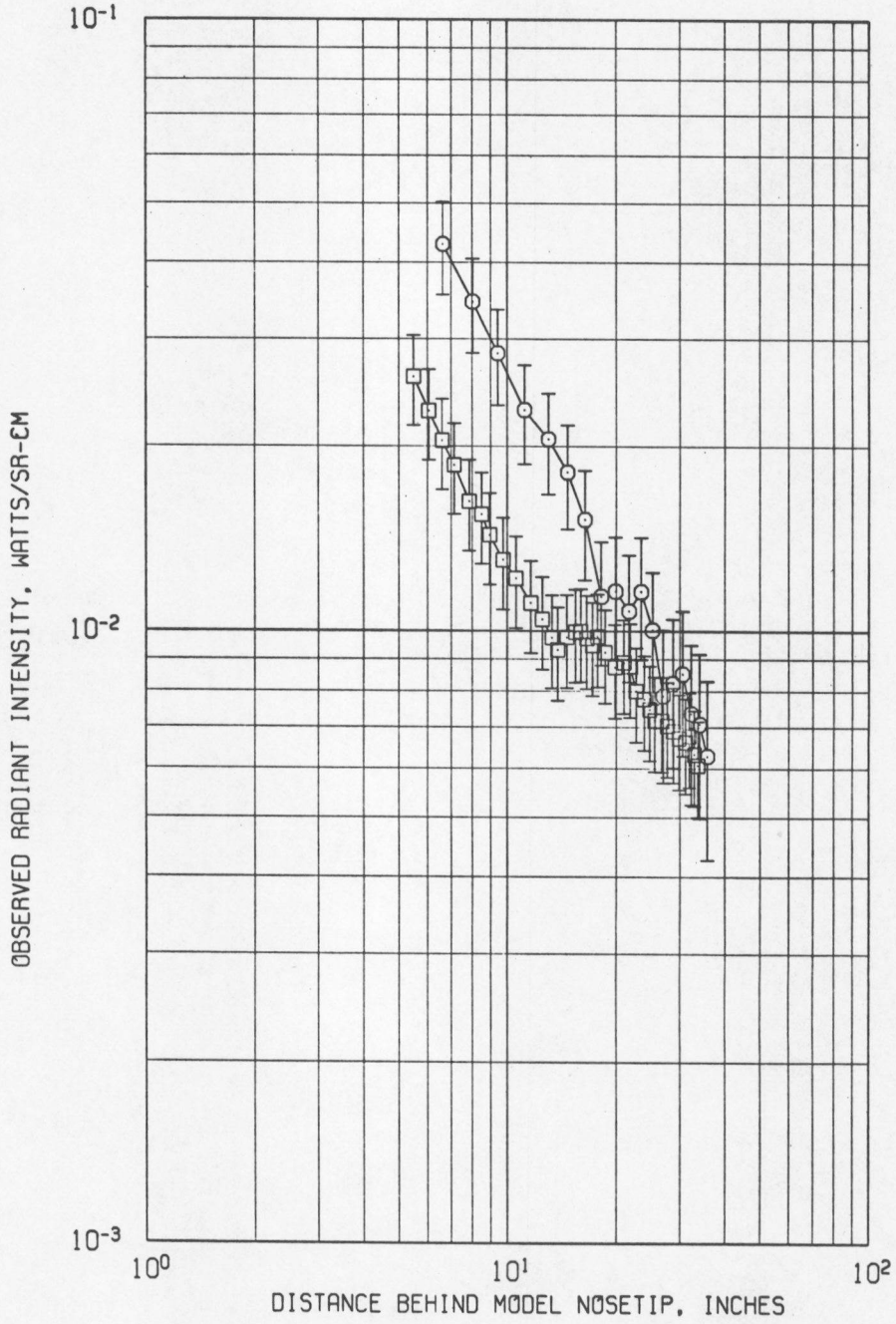
SYMBOL	SHOT NO	STATION	BANDPASS (MICRONS)
⊡	4504	1	2.6-2.8
⊙	4504	1	3.1-3.8



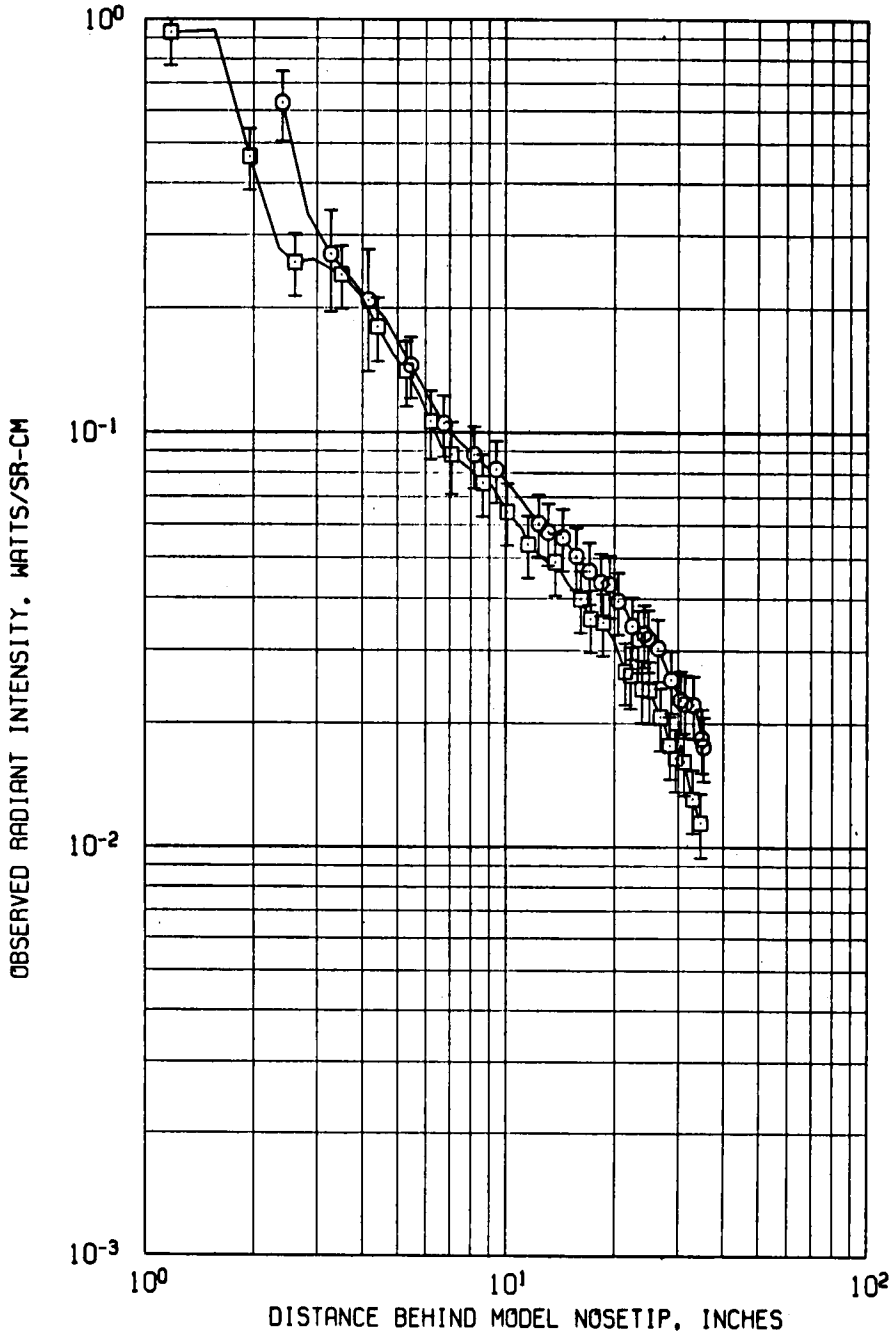
SYMBOL	SHOT NO	STATION	BANDPASS (MICRONS)
⊡	4505	19	0.5-0.7
⊙	4505	19	0.7-0.9



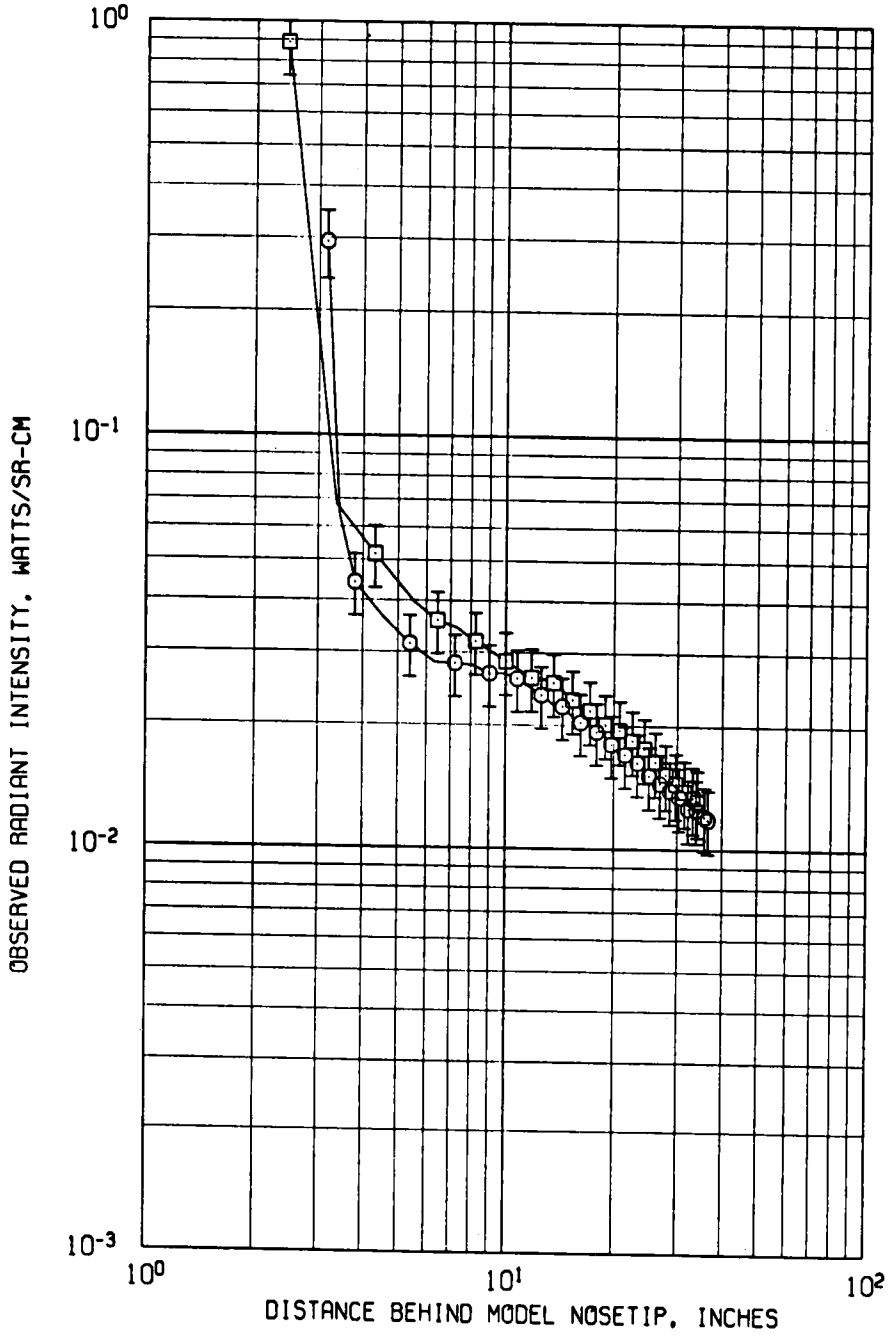
SYMBOL	SHOT NO	STATION	BANDPASS (MICRONS)
⊡	4505	19	2.6-2.8
⊙	4505	19	3.0-4.0



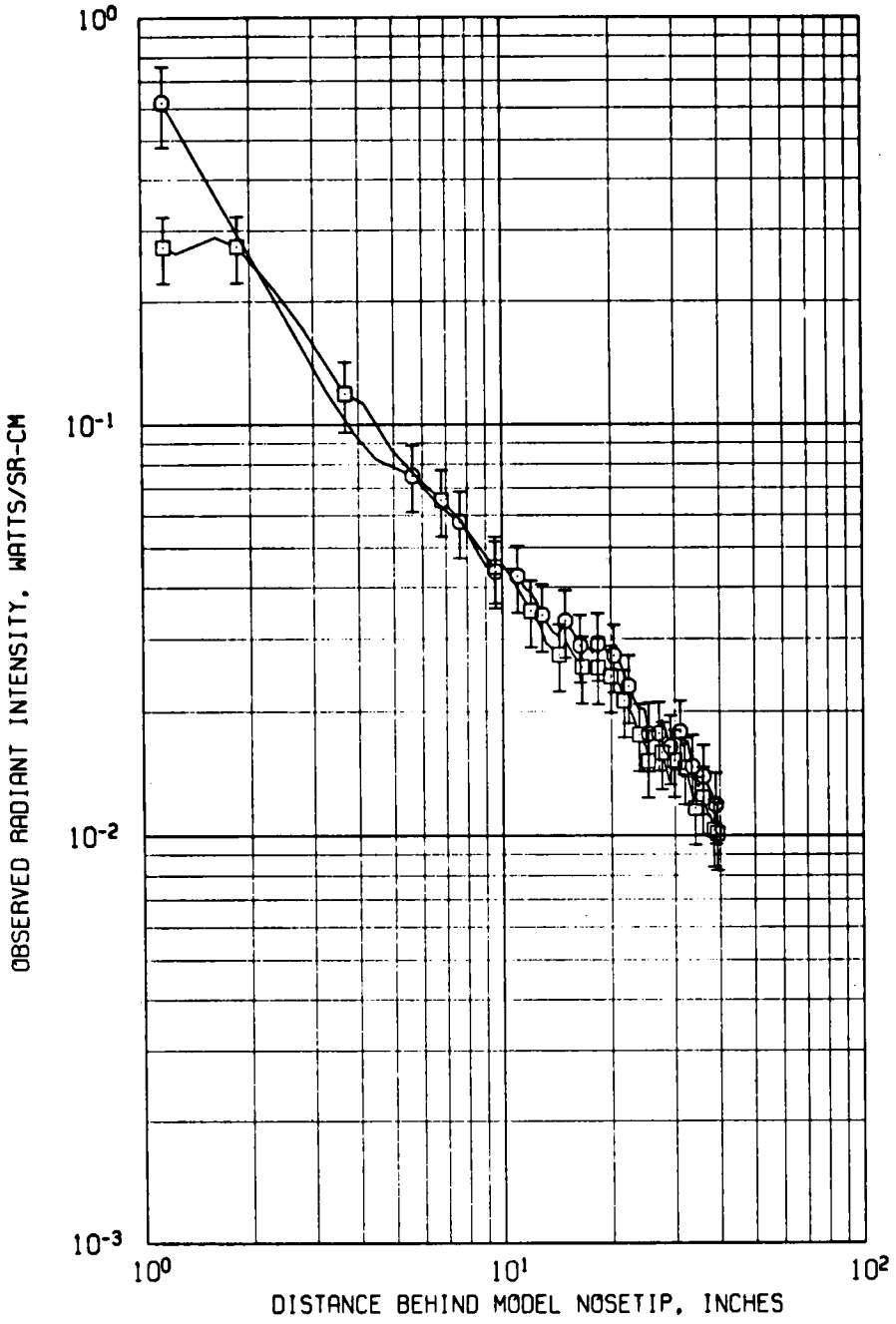
SYMBOL	SHOT NO	STATION	BANDPASS (MICRONS)
⊡	4506	1	0.5-0.7
⊙	4506	1	0.7-0.8



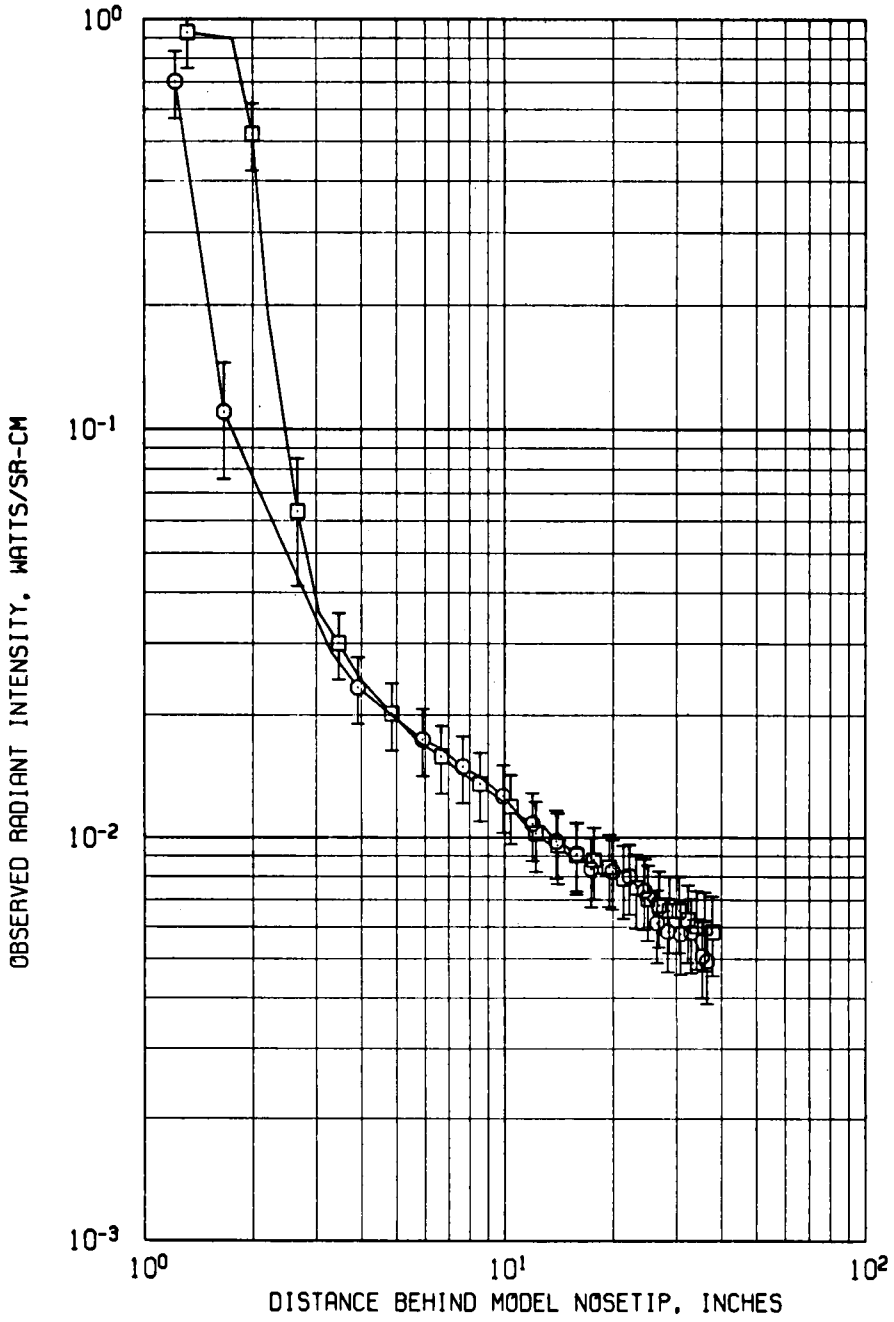
SYMBOL	SHOT NO	STATION	BANDPASS (MICRONS)
⊡	4506	1	2.6-2.8
⊙	4506	1	3.1-3.8

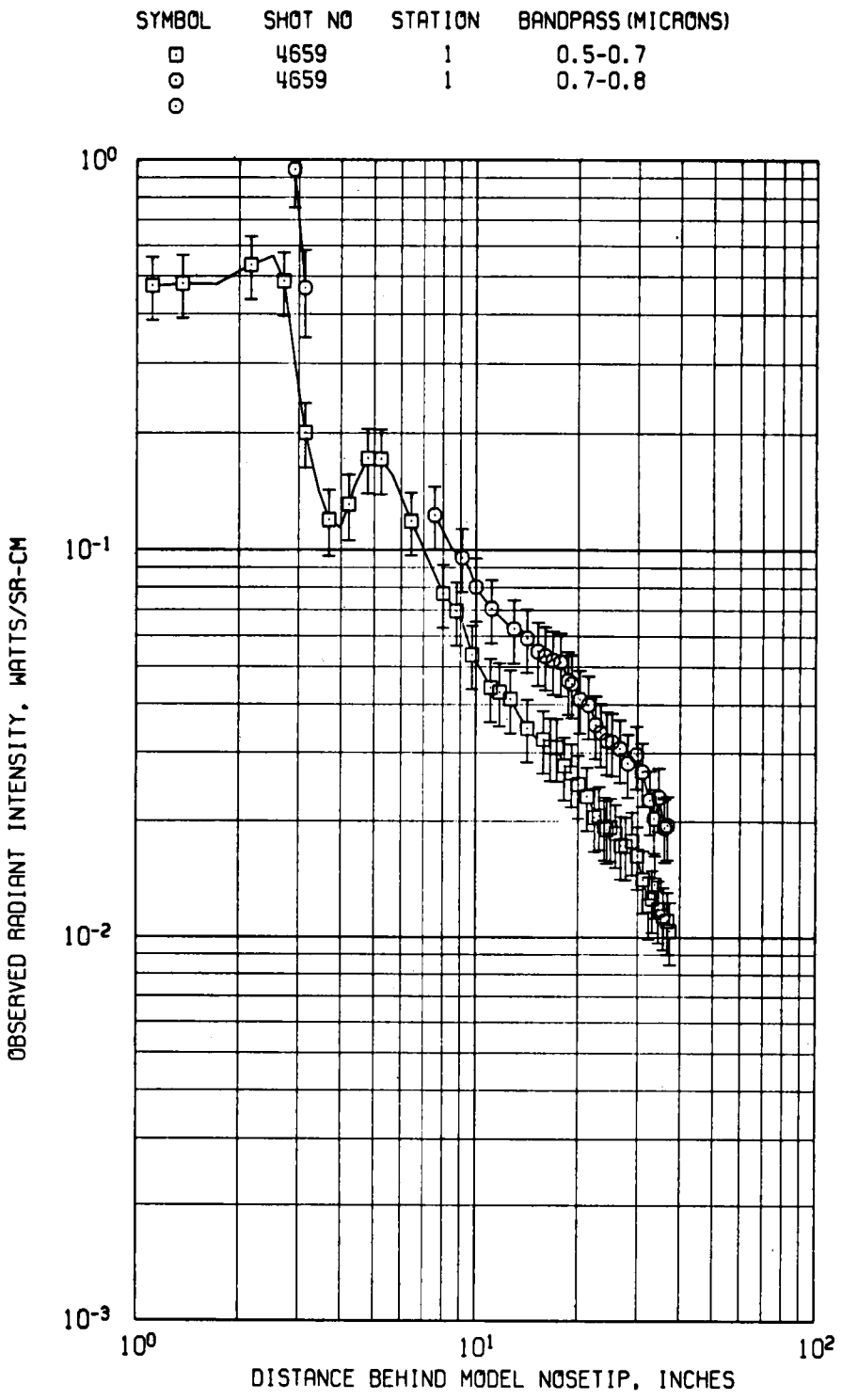


SYMBOL	SHOT NO	STATION	BANDPASS (MICRONS)
□	4657	1	0.5-0.7
⊙	4657	1	0.7-0.8

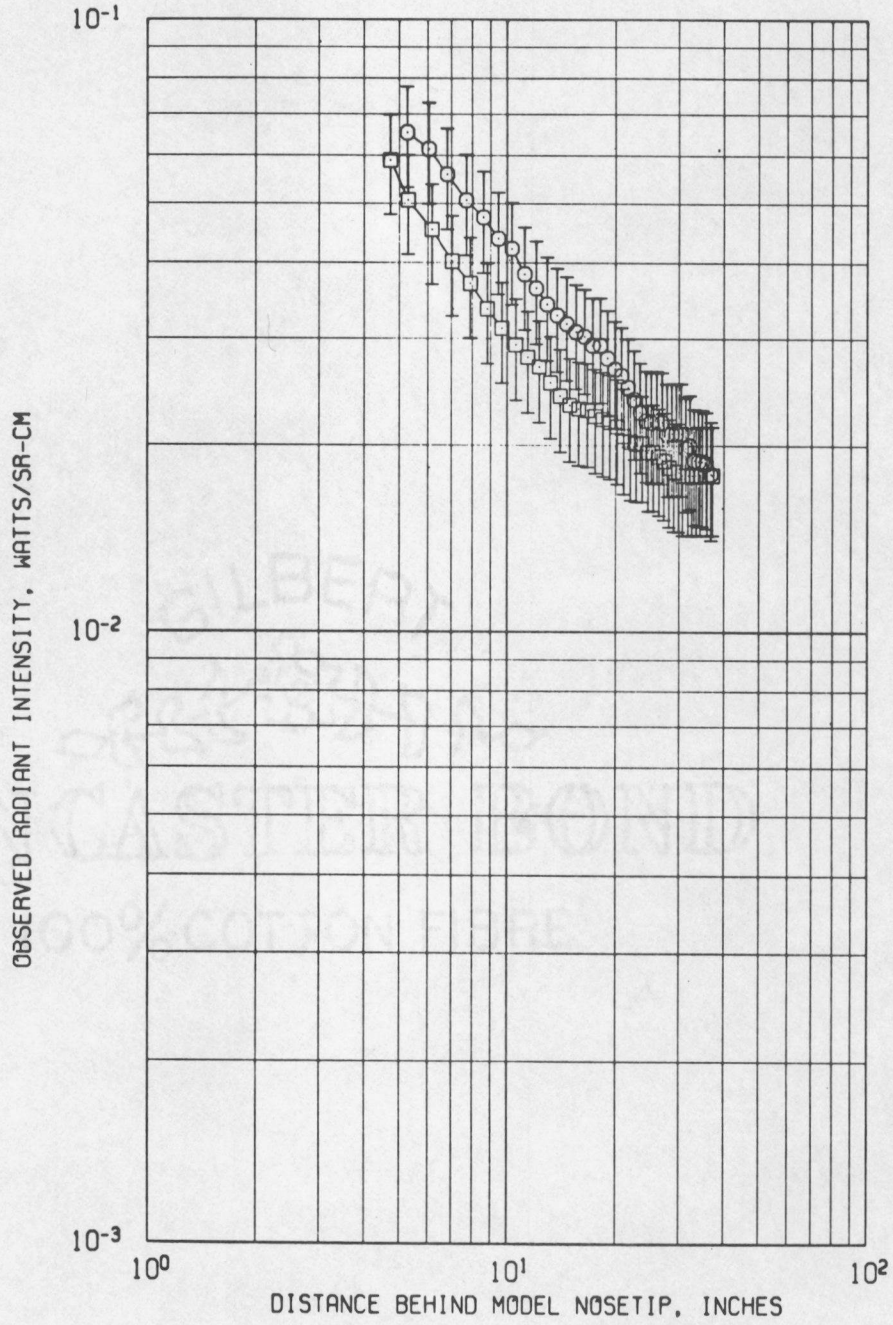


SYMBOL	SHOT NO	STATION	BANDPASS (MICRONS)
⊡	4657	1	2.6-2.8
⊙	4657	1	3.1-3.8

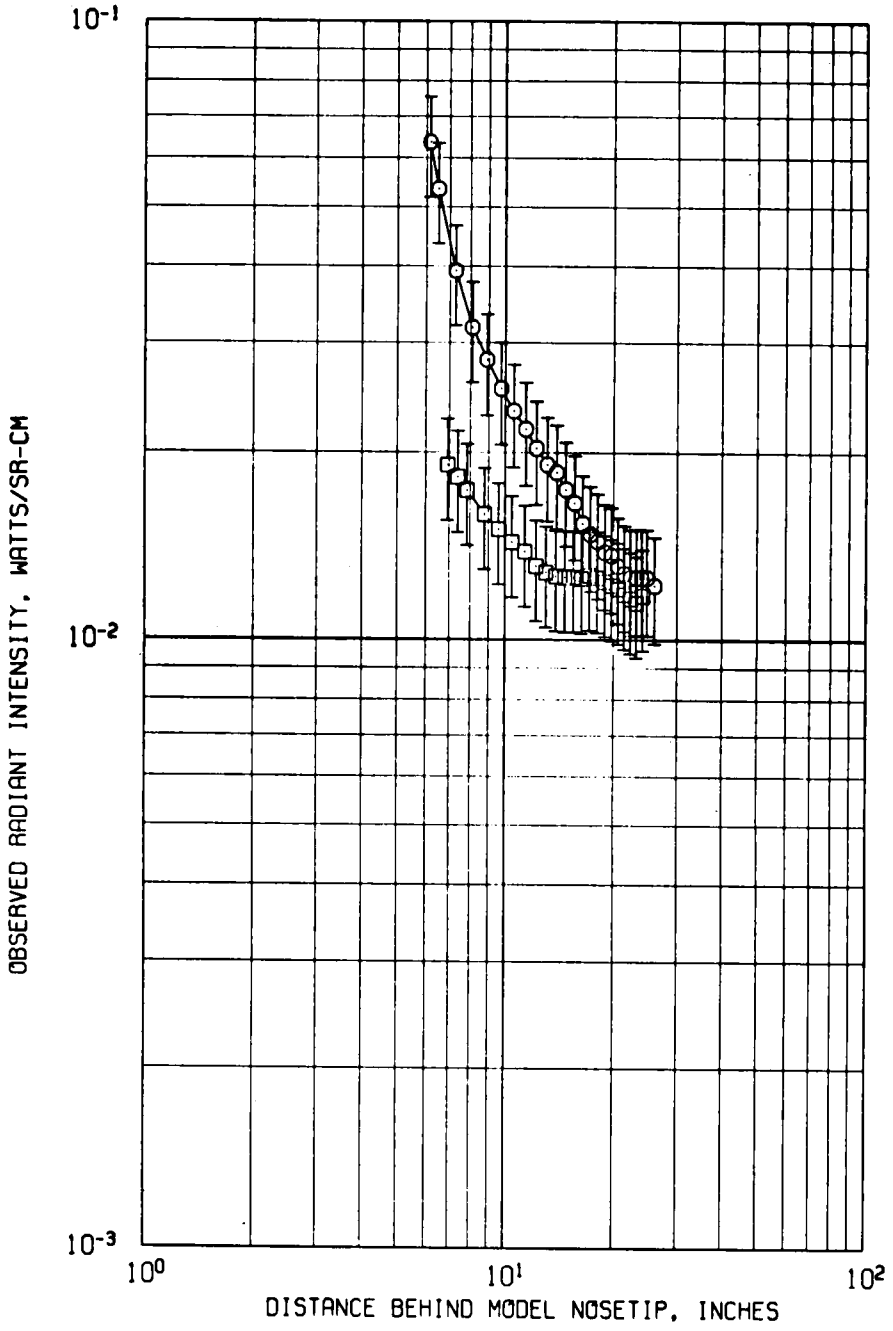



SYMBOL
SHOT NO
STATION
BANDPASS (MICRONS)
4659
1
0.5-0.7
4659
1
0.7-0.8
10^0
10^{-1}
10^{-2}
10^{-3}
10^0
10^1
10^2
OBSERVED RADIANT INTENSITY, WATTS/SR-CM
DISTANCE BEHIND MODEL NOSETIP, INCHES

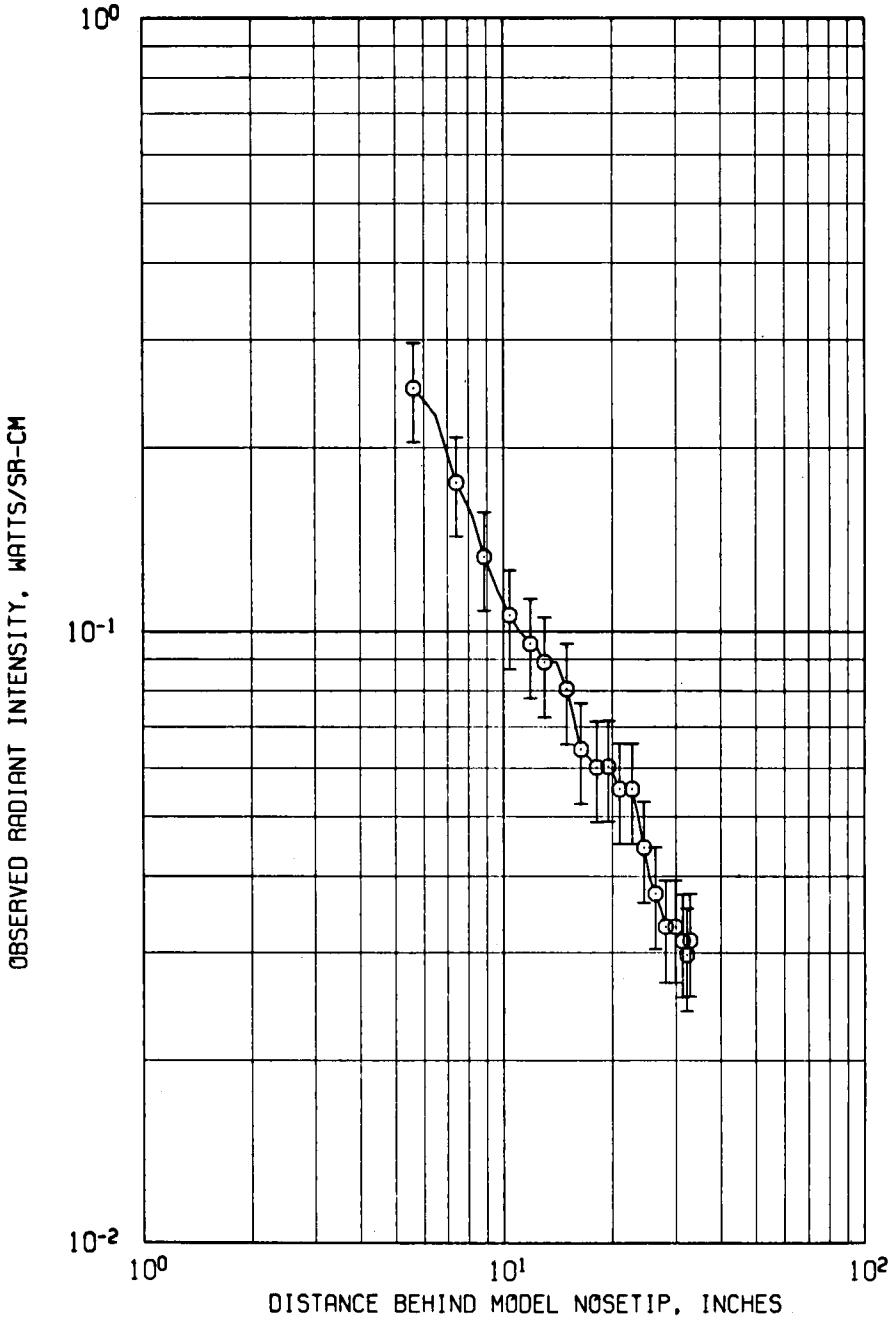
SYMBOL	SHOT NO	STATION	BANDPASS (MICRONS)
⊡	4659	1	2.6-2.8
⊙	4659	1	3.1-3.8



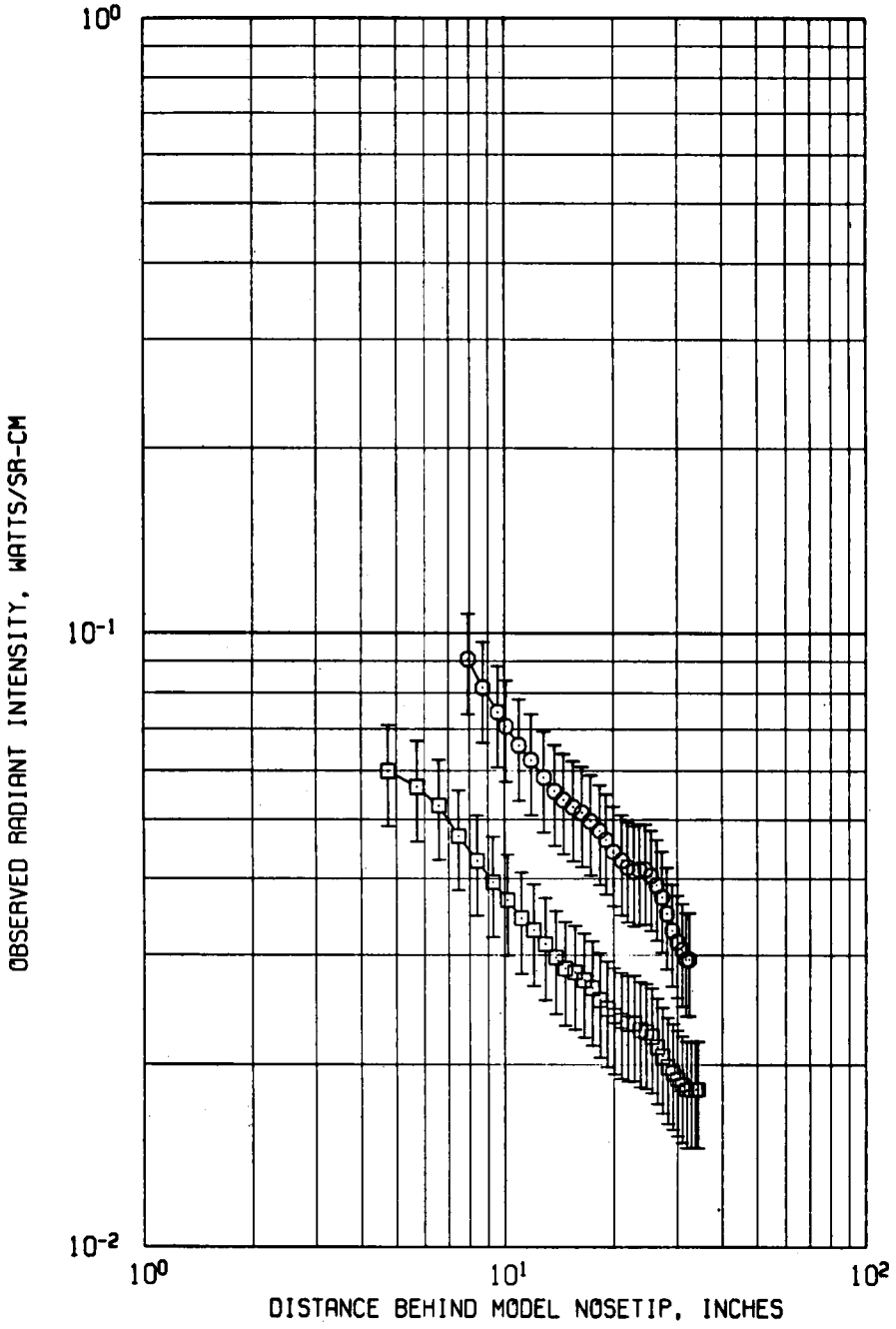
SYMBOL	SHOT NO	STATION	BANDPASS (MICRONS)
⊡	4659	19	2.6-2.8
⊙	4659	19	3.0-4.0



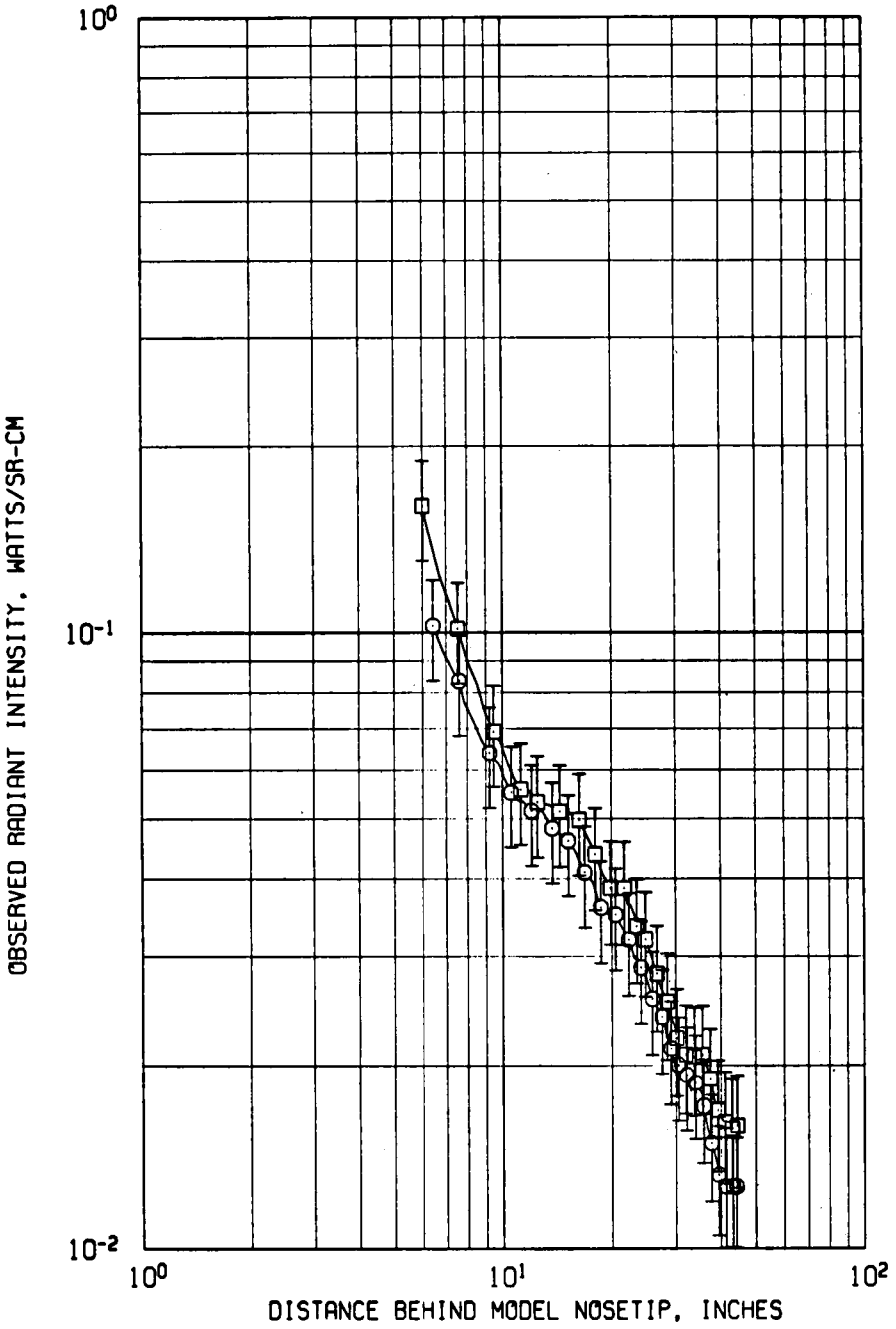
SYMBOL	SHOT NO	STATION	BANDPASS (MICRONS)
⊙	4660	1	0.7-0.8



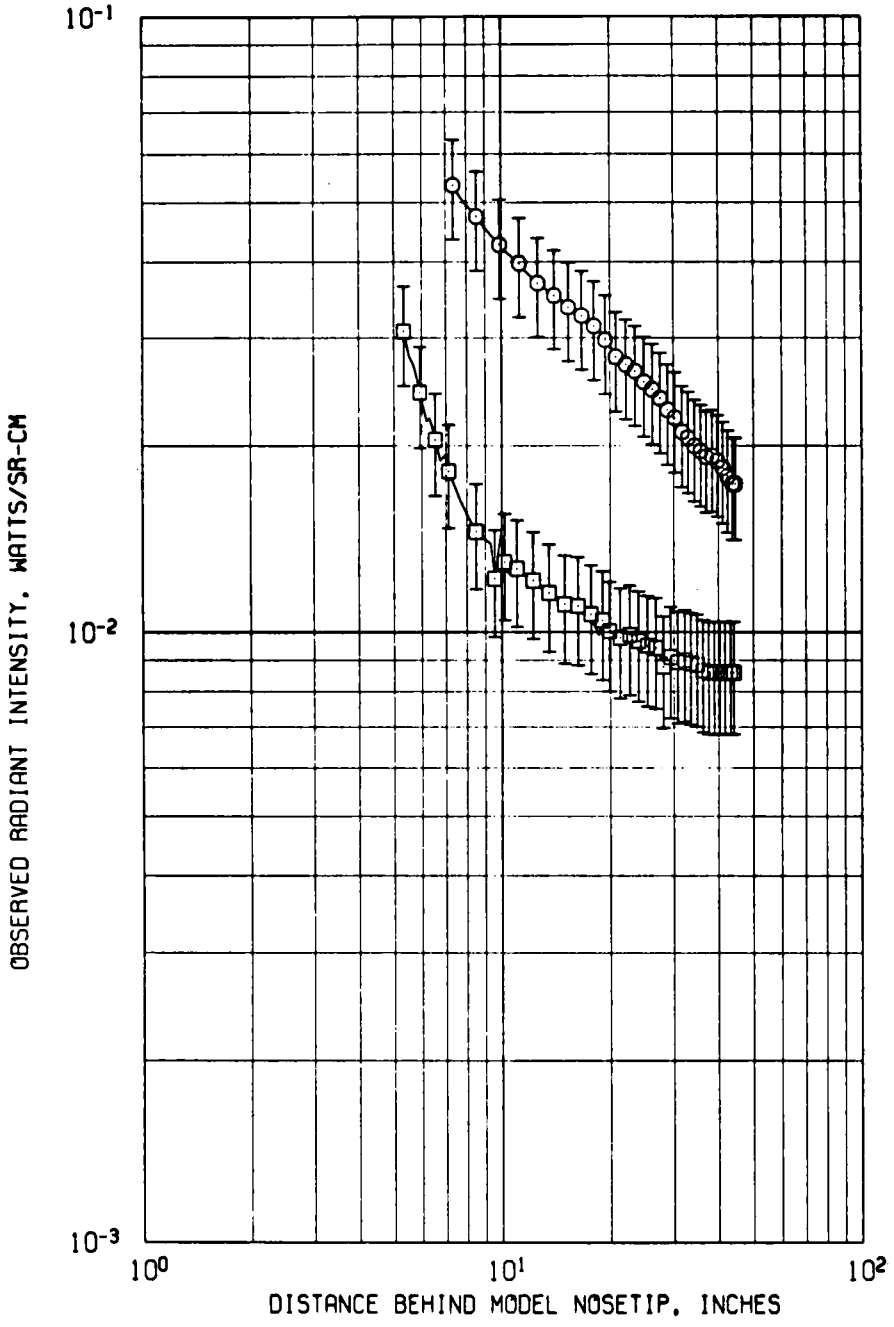
SYMBOL	SHOT NO	STATION	BANDPASS (MICRONS)
⊡	4660	1	2.6-2.8
⊙	4660	1	3.1-3.8



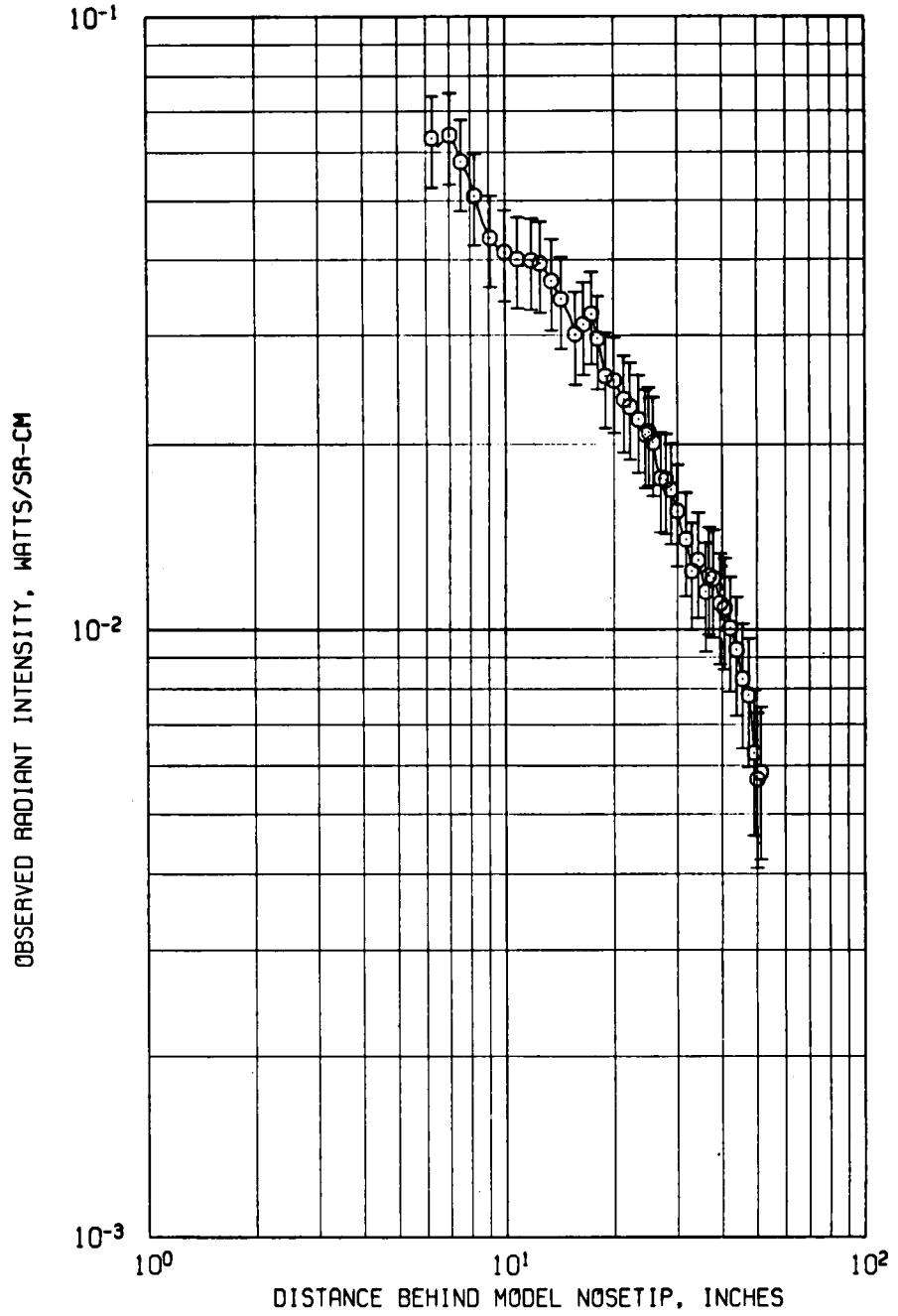
SYMBOL	SHOT NO	STATION	BANDPASS (MICRONS)
⊡	4810	1	0.5-0.7
⊙	4810	1	0.7-0.8



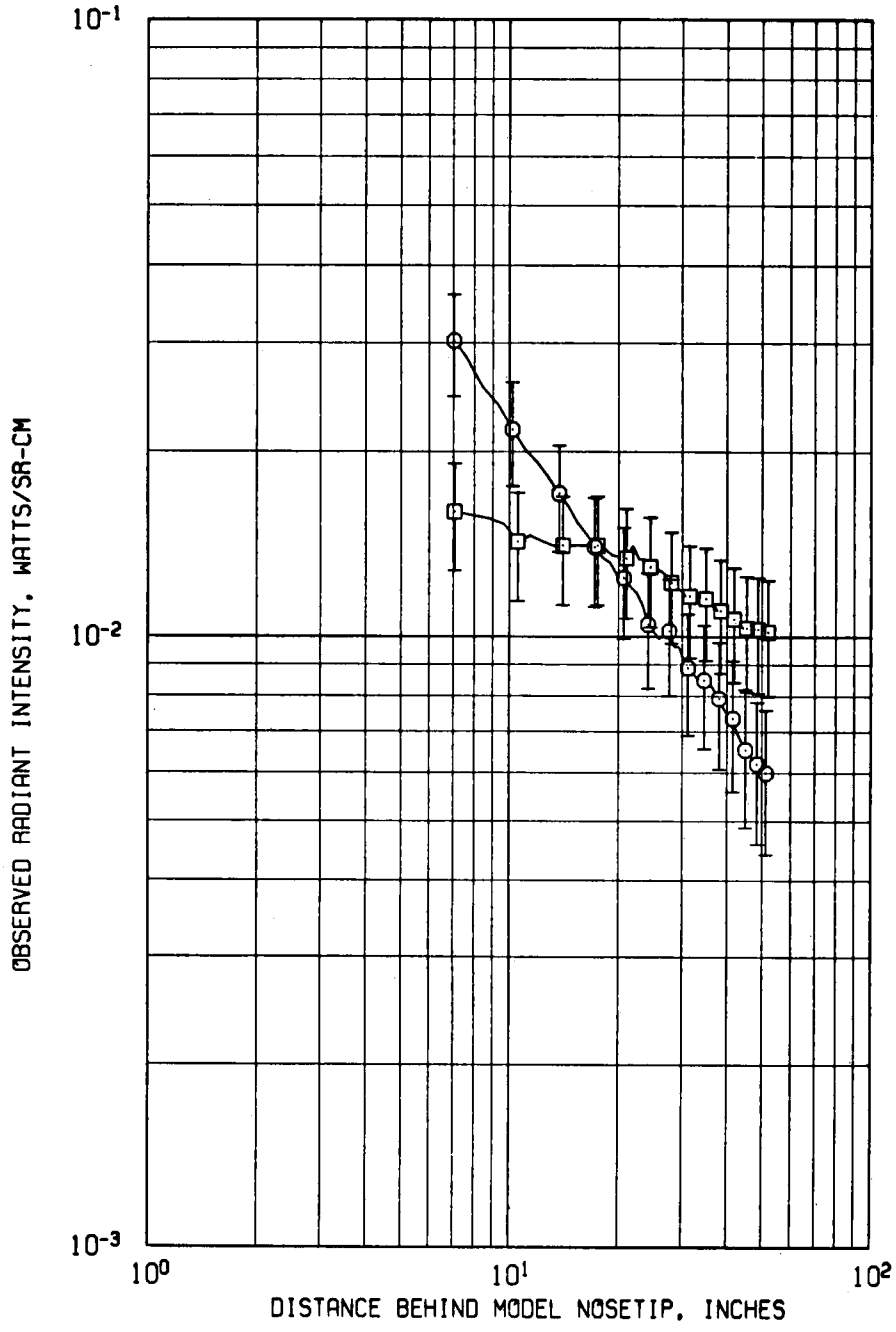
SYMBOL	SHOT NO	STATION	BANDPASS (MICRONS)
□	4810	1	2.6-2.8
○	4810	1	3.1-3.8



SYMBOL	SHOT NO	STATION	BANDPASS (MICRONS)
⊙	4810	19	0.7-0.9



SYMBOL	SHOT NO	STATION	BANDPASS (MICRONS)
⊡	4810	19	2.6-2.8
⊙	4810	19	3.0-4.0



VITA

Norman S. Weinberg was born in Providence, Rhode Island, on June 25, 1942. He attended elementary schools in that city and graduated from Classical High School in 1960. In 1964 he received a Bachelor of Science degree in Aeronautical Engineering from Boston University. Upon graduation, the author was employed by Pratt & Whitney, West Palm Beach, Florida. Later, he worked at The Boeing Company, Cape Kennedy, Florida, and then in Kent, Washington. In November, 1973, he accepted a position with ARO, Inc., Arnold Engineering Development Center, Arnold Air Force Station, Tennessee, as a project engineer. In September, 1974, he enrolled as a part-time student in the graduate program at The University of Tennessee Space Institute. In December, 1977, he received the Master of Science degree in Mechanical Engineering.

Mr. Weinberg presently resides in Manchester, Tennessee, with his wife, Sandra, and three children, Andrea, Natalie, and Kenneth.